

Universität  
Rostock



Traditio et Innovatio



# Structural and Electrochemical Investigation of $\text{BaZr}_{0.7}\text{Ce}_{0.2}\text{Y}_{0.1}\text{O}_{3-\delta}$ Proton Conducting Ceramics synthesized by Spark Plasma Sintering

Dissertation

zur Erlangung des akademischen Grades

doctor rerum naturalium (Dr. rer. nat.)

der Mathematisch-Naturwissenschaftlichen Fakultät

der Universität Rostock

Vorgelegt von

Jan Wallis, geb. am 30.09.1991 in Rostock

aus Greifswald

Rostock



## **Reviewer:**

Professor Dr. Eberhard Burkel, University of Rostock, Faculty of Mathematical and Natural Sciences, Institute of Physics – Physics of New Materials

Professor Dr. Ronny Brandenburg, Leibniz Institute for Plasma Science and Technology – Plasma Chemical Processes

Professor Dr. Angelika Heinzl, University Duisburg Essen, Institute for Energy and Environmental Process Technology – Energy Technology

**Date of submission:** 19.10.2020

**Date of defense:** 26.02.2021

## **Parts of this work have been published:**

Structural and electrical properties of  $\text{BaZr}_{0.7}\text{Ce}_{0.2}\text{Y}_{0.1}\text{O}_{3-\delta}$  proton conducting ceramic fabricated by spark plasma sintering

J. Wallis, L. Urban, C. Grimmer, W. Bodnar, R. Zimmermann, S. Ricote, K.-D. Weltmann, E. Burkel, A. Kruth  
*Solid State Ionics*, 345, p. 115118 (2020)

Nuclear dynamics in  $\text{BaZr}_{0.7}\text{Ce}_{0.2}\text{Y}_{0.1}\text{O}_{3-\delta}$  proton conductor as observed by neutron diffraction and Compton scattering

J. Wallis, A. Kruth, I. da Silva, M. Krzystyniak  
*J. Phys. Commun.*, 4 p. 045004 (2020)

The influence of the sintering temperature on  $\text{BaZr}_{0.7}\text{Ce}_{0.2}\text{Y}_{0.1}\text{O}_{3-\delta}$  proton conductors prepared by spark plasma sintering

J. Wallis, S. Ricote, K.-D. Weltmann, E. Burkel, A. Kruth  
*Ceramics International*, In Press Journal Pre-proof (2021)





# ABSTRACT

Barium zirconate-based proton conducting materials are promising candidates for solid electrolytes in fuel cells, electrolysers, hydrogen pumps and hydrogen sensors. As such, they could pave the way for the future hydrogen-based economy to reduce our dependence on fossil fuels and the associated environmental impact. In this thesis,  $\text{BaZr}_{0.7}\text{Ce}_{0.2}\text{Y}_{0.1}\text{O}_{3-\delta}$  (BZCY72) was synthesized by spark plasma sintering (SPS) from a lab-produced and commercial precursor powder. Microstructural, crystallographic and electrical properties were investigated by X-ray diffraction, electron microscopy, Raman spectroscopy as well as impedance spectroscopy and compared to state-of-the-art materials. Samples prepared by SPS showed up to 99.7 % of relative density that cannot be reached by any other synthesis techniques at 1450 °C. Significant barium evaporation, typically occurring at high sintering temperatures and limiting overall electric performance, could be prevented. The bulk conductivity for samples prepared by SPS was up to 10 % higher compared to state-of-the-art synthesis routes. In an extensive study, SPS process parameters were varied in a systematic way. The effects of sintering temperature, pressure, heating rate and holding time on the resulting material properties were investigated. The result of this study provides a better understanding of the sintering mechanisms occurring during SPS. A total conductivity of  $1.25 \cdot 10^{-3} \text{ S}\cdot\text{cm}^{-1}$  was observed at 600 °C.

Quasi-elastic neutron scattering (QENS) and neutron Compton scattering (NCS) were employed at ISIS RAL (UK) for synthesized BZCY72 to investigate the proton diffusion and confinement of protons within the crystal structure. The experiments confirmed a Grotthuss mechanism for this proton conductor and phase transitions could be observed in agreement with modern understanding of the protonic diffusion in perovskite ceramics. The analysis of the proton momentum distribution reveals that the concentration of hydrogen in the BZCY72 lattice is constant across the orthorhombic to rhombohedral phase transition and further down to room temperature.

As an outlook, SPS was applied to synthesize stable membrane-electrode-assemblies (MEAs) composed of two 60 wt% NiO/40 wt% BZCY72 electrodes and a dense BZCY72 electrolyte. A proof of concept with an SPS process for cosintering of MEAs with a possible application in protonic ceramic electrolysers is given.



# Zusammenfassung

Protonenleitende Materialien auf der Basis von Bariumzirkonat sind vielversprechende Kandidaten für die Anwendung als Elektrolyt in Brennstoffzellen, Elektrolyseuren, Wasserstoffpumpen und Sensoren. Diese gelten als wesentliche Meilensteine einer zukünftigen umweltfreundlichen Wasserstoffwirtschaft. In dieser Doktorarbeit wurde der Protonenleiter  $\text{BaZr}_{0.7}\text{Ce}_{0.2}\text{Y}_{0.1}\text{O}_{3-\delta}$  (BZCY72) aus einem lab-synthetisierten und aus einem kommerziellem Pulver mittels des Spark Plasma Sinterns (SPS) hergestellt. Seine kristallographischen, mikrostrukturellen und protonenleitenden Eigenschaften wurden dabei mittels Röntgenbeugung, Elektronenmikroskope, Raman-Spektroskopie und Impedanzspektroskopie untersucht und mit Proben verglichen, welche durch aktuelle Syntheserouten hergestellt wurden. Durch SPS synthetisierte Proben zeichnen sich durch relative Dichten bis zu 99.7 % bei einer Temperatur von 1450 °C aus, was durch andere Methoden nicht erreicht werden kann. Dadurch konnte der Barium-Verlust, der typischerweise bei hohen Sintertemperaturen die Leitfähigkeit von BZCY72 drastisch reduziert, vermieden werden. Die ermittelte Bulkleitfähigkeit der SPS-Probe war um ca. 10 % höher als für Proben, die mittels State-of-the-Art-Sinterverfahren hergestellt wurden. In einer umfangreichen Studie wurden die Prozessparameter Sintertemperatur, Druck, Heizrate und Haltezeit variiert und deren Auswirkungen auf die Eigenschaften des Protonenleiters untersucht. Die Ergebnisse dieser Untersuchungen leisten einen Beitrag zum besseren Verständnis der dem Sinterprozess zugrundeliegenden Mechanismen. Die durch Optimierung der Prozessparameter erzielte Gesamtleitfähigkeit von BZCY27 betrug  $1.25 \cdot 10^{-3} \text{ S}\cdot\text{cm}^{-1}$  bei 600 °C.

Es wurden erstmals quasi-elastischer Neutronenstreuung (QENS) und Neutron Comptonstreuung (NCS) am ISIS RAL (UK) zur Untersuchung der zugrundeliegenden Diffusionsprozesse der Protonen in BZCY72 eingesetzt. Der Grotthuss-Mechanismus zur Beschreibung der Protonenbewegung, sowie die zuvor durch Neutronendiffraktion charakterisierten Phasenübergänge des Materials wurden dabei experimentell bestätigt. Die Analyse der Protonen-Impulsverteilung zeigte eine konstante Protonenkonzentration innerhalb des BZCY72-Kristallgitters von 70 K über die Phasentransformation bis zur Raumtemperatur.

Schließlich wird als ein erster Schritt auf dem Weg zur Herstellung von Membran-Elektroden-Einheiten (MEAs) die Synthese eines Hybrides aus poröser Elektrode und dichtem Elektrolyt mittels Co-Sintern beschrieben. Dabei wurden zwei 60 wt% NiO/40 wt% BZCY72 Elektroden zusammen mit einem BZCY72 Elektrolyten erfolgreich gesintert. Auf dieser Basis liegt ein erstes Proof-of-Concept für eine Fabrikation von MEAs vor, z.B. für zukünftige Elektrolyseure auf der Basis von protonenleitenden Keramiken.



## List of symbols and abbreviations

A	electrode area
Å	angstrom, $1 \text{ Å} = 10^{-10} \text{ m}$
BZY	Y-doped barium zirconate
BCY	Y-doped barium cerate
BZCY	Y and Ce-doped barium zirconate
C	capacitance
CTE	coefficient of thermal expansion
D	diffusion coefficient or diffusivity
$\rho$	density
DINS	deep inelastic neutron scattering
E	energy, electric field
e	elementary charge, $1 e = 1.60219 \times 10^{-19} \text{ C}$
$\epsilon_0$	vacuum permittivity
$\epsilon$	dielectric constant or relative permittivity
EDX	energy-dispersive X-ray spectroscopy
$E_A$	activation energy
eV	electron-Volt, $1 \text{ eV} = 1.60219 \times 10^{-19} \text{ J}$
F	force, Faraday's constant $F = 96485 \text{ C/mol}$
$f$	frequency
FWHM	full width at half maximum
$\Delta G^0$	Gibbs energy
GB	grain boundary
h	Planck's constant $h = 6.62607004 \times 10^{-34} \text{ m}^2 \text{ kg / s}$
IS	impedance spectroscopy
$j$	imaginary unit
$k_B$	Boltzmann constant, $k_B = 1.38066 \times 10^{-23} \text{ J K}^{-1}$
L	sample thickness
$\lambda$	wavelength
M	electric modulus
MEA	Membrane-electrode-assembly
$\mu$	mobility
NCS	neutron Compton scattering
NMD	nuclear momentum distribution
$\sigma$	conductivity
PEMFC	polymer electrolyte membrane fuel cell
p	pressure

PCFC	protonic ceramic fuel cell
$p_x$	partial pressure of gas x
Q	constant phase element
QENS	quasi-elastic neutron scattering
r	ionic radius
R	resistance
sccm	standard cubic centimeters per minute
SEM	scanning electron microscopy
SOFC	solid oxid fuel cell
SPS	spark plasma sintering
SSRS	solid-state reaction sintering
T	temperature
$\tau$	residence time
TEM	transmission electron microscopy
TGA	thermogravimetric analysis
$\nu$	stretching frequency, nodes
XRD	X-ray diffraction
$\omega$	angular frequency
Z	impedance

## Acknowledgements

Behind every PhD project stands a group of people to whom the PhD student is much indebted to. This work was carried out at the Leibniz-Institute for Plasma Science and Technology (INP) and the University of Rostock. I am deeply grateful to my supervisor Prof. Eberhard Burkel at University of Rostock who paved the way for this dissertation and gave scientific advice. I am also thankful to Prof. Ronny Brandenburg for taking over the supervision in the last month of the dissertation. Along the same line, I am very thankful to my advisor Dr. Angela Kruth, who provided a lot of scientific advice and guidance for my project work and encouraged me to network and collaborate with other research groups within the proton conductor community during my PhD project. I am also very grateful to the INP for funding my PhD project and the help and advice given by Prof. Klaus-Dieter Weltmann.

My thanks are also due to my colleagues in the research group for Materials for Energy Technology (MET) and the department of Plasma Process Techniques (PPT) at INP. In particular, I am thankful to Dr. Kerstin Witte and Dr. Wiktor Bodnar who helped me in questions related to SPS, Miguel Dias for support with Raman measurements, Dr. Volker Brüser for administrative assistance and Kirsten Anklam and Anja Albrecht, both for their technical support. Further thanks are given to Udo Nehmzow and the glassblower workshop at University of Greifswald who assisted with glass containment manufacturing.

I am thankful to my friend and colleague Christoph Grimmer and Prof. Ralf Zimmerman at University of Rostock for the TGA measurements. I also thank Laurence Urban for his preparation of the lab-produced powder and Bärbel Przybill for the collection of the dilatometry data.

I am very grateful to the INP for giving me the opportunity to visit the Colorado School of Mines (CSM) in the US for a research exchange over a period of three weeks. Special thanks are due to Dr. Sandrine Ricote at CSM who has been a constant source of help and collaboration from the beginning, who did a lot of proof-reading and prepared samples by solid-state reaction sintering. I am grateful to David Diercks at CSM who studied a selection of my samples by TEM. Further thanks are due to Dr. Canan Karakaya, Benjamin Kee and Prof. Ryan O' Hayre who provided interesting discussions and allowed further insights in proton conducting ceramics.

Experimental work was conducted at the ISIS Rutherford Appleton Laboratory. I am very thankful to Prof. Martin Owen Jones who supported me with application for beam time and had valuable ideas on how to conduct experiments. Furthermore, I am grateful to Dr. Franz Demmel and Dr. Matthew Krzystynaik at ISIS who advised me in quasi-elastic neutron scattering and neutron Compton scattering experiments, respectively, as beam line scientists and also provided astonishing results for my work. Further thanks is due to Ivan da Silva for the Rietveld refinement of neutron diffraction data.

I also would like to thank Jens Wartmann at Zentrum for BrennstoffzellenTechnik (ZBT) in Duisburg for very interesting discussions on the hydrogen technologies, giving me great motivation for my work with regard to later applications.

Above all, I am very grateful to my beloved wife Sandra, for her love, patience, and encouragement during my PhD work. I also thank my family for their constant support, their interest in my work and encouragement over the years. They never doubted on my decision to become a material scientist and kept me going though all times. It would not have been possible without your support!





# TABLE OF CONTENTS

1	INTRODUCTION .....	1
1.1	Project context .....	1
1.2	Electrochemical energy devices .....	3
1.3	Perovskite structure .....	4
1.4	Selection of material and defect chemistry.....	6
1.5	Proton incorporation and conductivity .....	8
1.6	Spark plasma sintering.....	11
1.7	Aim of the thesis and overview .....	13
2	SYNTHESIS AND CHARACTERISATION METHODS .....	15
2.1	Powder synthesis and sintering.....	15
2.1.1	Synthesis of precursor powder .....	15
2.1.2	Solid state reactive sintering .....	16
2.1.3	Spark plasma sintering setup.....	16
2.1.4	Process protocol for synthesis of BZCY72 samples .....	17
2.1.5	SPS-cosintering of membrane-electrode-assemblies (MEAs) .....	18
2.2	Scattering Experiments.....	19
2.2.1	Static light scattering.....	19
2.2.2	X-Ray diffraction .....	20
2.2.3	Raman spectroscopy.....	21
2.2.4	Quasi elastic neutron scattering.....	22
2.2.5	Neutron Compton scattering .....	24
2.3	Electron microscopy .....	26
2.3.1	Scanning electron microscopy.....	26
2.3.2	Transmission electron microscopy.....	26
2.4	Impedance spectroscopy.....	26
2.4.1	Fundamentals .....	26
2.4.2	Experimental setup.....	28
2.4.3	Data interpretation.....	29
2.4.4	Transport study for different oxygen partial pressures .....	30
3	STRUCTURAL AND ELECTRICAL PROPERTIES OF BZCY72 .....	31
3.1	Investigation of precursor powders .....	31

3.2	Properties of sintered pellets.....	32
3.3	Crystallographic investigation .....	34
3.4	Microstructure.....	37
3.5	Electrical properties .....	39
3.6	Thermal expansion.....	43
4	CORRELATION BETWEEN SPS PARAMETERS AND PROPERTIES OF BZCY72 ....	45
4.1	Influence of sintering temperature and pressure.....	45
4.1.1	Densification and pellet stability.....	45
4.1.2	Crystallographic structure .....	48
4.1.3	Microstructure .....	52
4.1.4	Conductivity .....	55
4.2	Influence of heating rate .....	62
4.2.1	Densification.....	62
4.2.2	Crystallographic structure .....	63
4.2.3	Microstructure .....	65
4.2.4	Conductivity .....	68
4.3	Influence of holding time.....	72
4.3.1	Densification.....	72
4.3.2	Crystallographic structure .....	73
4.3.3	Microstructure .....	74
4.3.4	Conductivity .....	76
4.4	Chapter summary.....	77
5	NEUTRON STUDIES OF THE PROTON TRANSPORT .....	81
5.1	Proton diffusion by QENS.....	81
5.2	Neutron Compton scattering and proton transports in BZCY72 .....	86
5.3	Comparison with results from impedance spectroscopy .....	89
6	CO-SINTERING OF A MEMBRANE-ELECTRODE-ASSEMBLY .....	91
6.1	Structural investigations .....	91
6.2	Electrical investigations.....	95
7	CONCLUSIONS.....	97
7.1	Summary.....	97
7.2	Outlook and future work.....	99

8	APPENDIX.....	100
8.1	Introduction .....	100
8.2	Sample preparation .....	104
8.3	Rietveld refinement .....	107
8.4	Neutron scattering experiments .....	108
8.5	Impedance spectroscopy .....	111
8.6	Properties of BZCY72 .....	113
8.7	Influence of SPS parameters on BZCY72 .....	117
8.8	Neutron studies of BZCY72 .....	127
8.9	Co-sintering of a membrane-electrode-assembly .....	130
9	References .....	131



# 1 INTRODUCTION

This work contributes to the synthesis and characterization of yttrium and cerium doped barium zirconate. This proton conducting ceramic is used as electrolyte in intermediate temperature fuel cells and electrolysers and plays a key role for the future energy transition. The following section will provide the reader with the general social and political context, before covering the fundamentals of the thesis.

## 1.1 Project context

The increasing energy demand of our modern society causes major challenges for our generation. According to the IEA World Energy Balances database, in the year 2016, 81.1% of the world total primary energy supply relied on fossil fuels [1]. Mineral oil and coal are the backbone of the world's economy and enabled our predecessor generations to overcome technological challenges, unmindful of any risks. This allowed for rapid growth of the world's population and increased societal polarization as the poorest typically suffer the greatest impact from climate change, referred to as global warming. The carbon dioxide emission of any given country is a direct evidence of its economic status. Today, the relation between human activity, such as greenhouse gas emission, and global warming is well established and widely accepted (see **appendix 8.1.1**). Effects of climate change observed today are the increase of endangered and extinct species [2], glacial recession and associated rise of sea levels [3], extended droughts that lead to water shortages in some regions [4] as well as increased number of severe weather events [5]. Also due to the limited nature of fossil resources as well as their environmental impact, the search for alternative and renewable energy supplies is of economic, environmental and social interest. The energy transition is not a matter of "if", but rather a matter of "how" it will be implemented.

In the past decade, many companies and governments invested in a rapid expansion of wind turbines and photovoltaic cells. However, most of the renewable energies do not provide a consistent power supply or generate electricity where it is not necessarily needed. They also lack the required power densities to support urban population and it is hard to imagine that the whole primary energy consumption can be covered directly by renewable energies without any form of long-term storage.

The most promising approach to overcome this challenge is in chemicals such as hydrogen and power-to-X fuels and the implementation of hydrogen technologies. Up to 95 % of H<sub>2</sub> is synthesized by steam reforming today [6]. This process provides cheap hydrogen, however, a large volume of carbon dioxide is released into the atmosphere ("gray hydrogen") or is released and cost-intensively captured ("blue hydrogen") during the process. For hydrogen to become a true zero-carbon fuel, it needs to be produced from renewable energies ("green hydrogen"). The storage of hydrogen can be realized by compression, liquefaction or by means of hydration of materials and compounds such as metal hydrides or liquid organic hydrocarbons, LOHC. Research and development of new technologies and materials for production, storage and transportation of hydrogen has become a wide field of interest and is enabling new market routes for various industrial branches.

## Project context

The possible future implementation of hydrogen technologies to support a decentralized energy grid is shown in **figure 1.1**. Electricity is generated from renewable energy sources at different locations with short supply and distribution chains. Oversupply of electricity is used to produce green hydrogen by means of electrolysis. Produced hydrogen can either be stored for utilization during shortages or be transported to locations in need of higher energy demand, such as industrial or urban areas. The utilization of hydrogen as an energy storage medium may be by fuel cells for

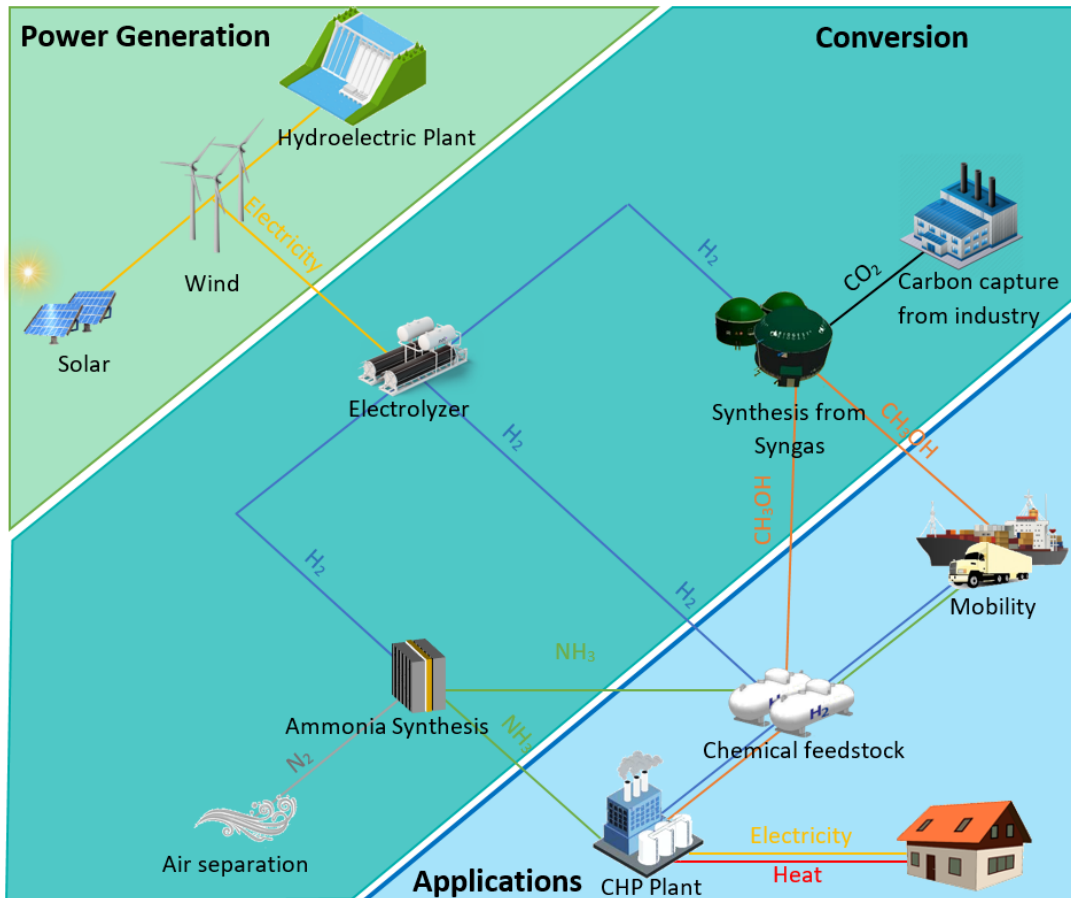


**Figure 1.1:** Schematics of a decentralized future power grid. Electricity is generated locally from fluctuating renewable energy sources. The local power grid is complemented by a power-to-X infrastructure to ensure a constant power supply and long-term storage. For improvement of energy security as well as provision of areas with high energy demand, such as industrial or urban regions, the renewable power is supplied from multiple sources.

direct conversion into electricity or by combustion for heat generation in mobile and stationary energy applications.

Hydrogen is the key component in sector coupling, replacing the traditional separation of the energy sectors of electricity, heating and cooling, transport and chemical industry and enabling flexibility potential for producers and consumers as well as the storage of energy in its various forms. Conversion of hydrogen into nitrogen- or carbon-based products such as ammonia or methanol, power-to-X is a crucial route to enable cost-efficient storage and transport as well as easy handling of hydrogen.

## 1.2 Electrochemical energy devices

Electrochemical energy devices such as electrolyzers and fuel cells are essential technologies for the implementation of the hydrogen economy. Solid oxide electrolyzers and fuel cells that are based on protonic conducting membranes may be operated at intermediate temperatures between 300 and 600 °C and are increasingly gaining significant attention. Electrolyte membranes based on proton conducting perovskite oxides are well known to exhibit attractive conductivities while also providing chemical and thermal durability. Since their discovery in the early 1980s, they are wielded as promising candidates for a wide field of applications such as steam electrolysis, gas separation membranes, CO<sub>2</sub> conversion, hydrogen sensors and for the production of green ammonia [7-11].

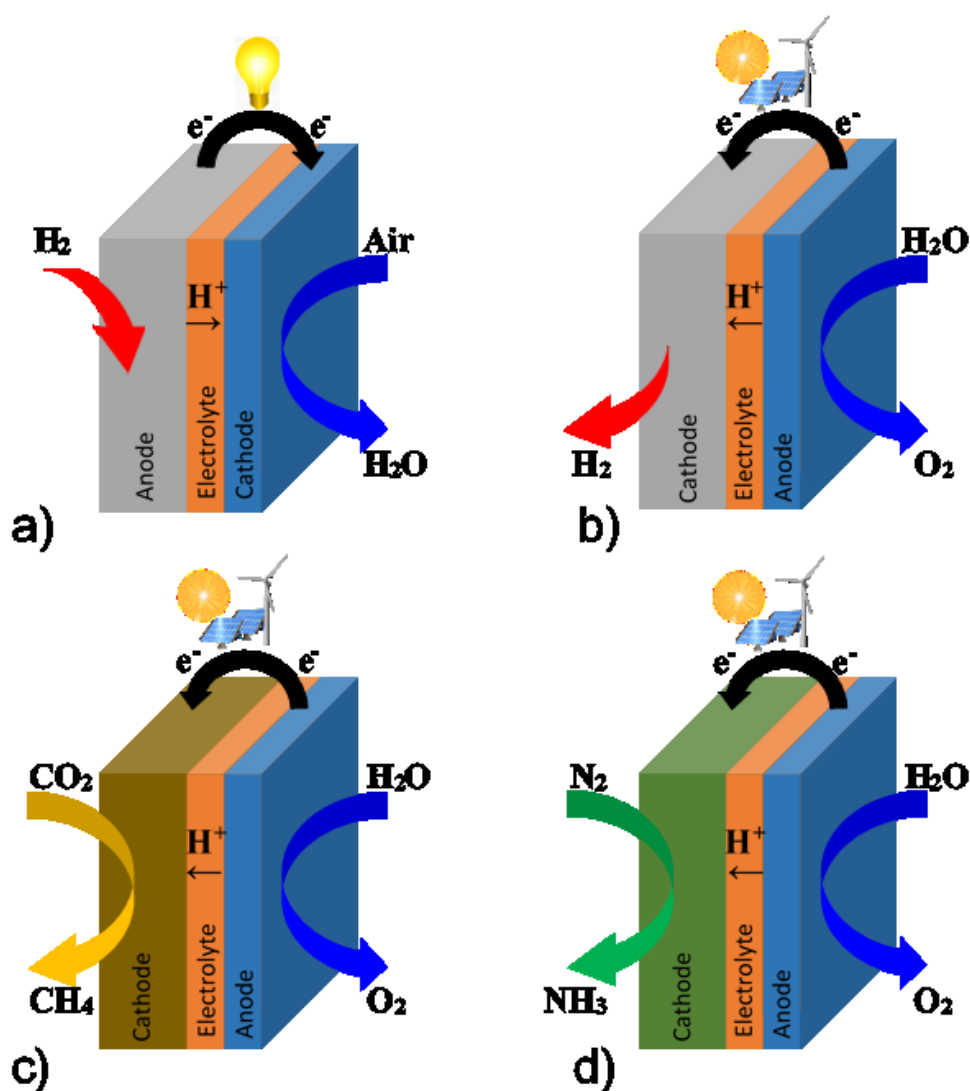


**Figure 1.2:** Schematic illustrations of applications of proton conducting ceramic cells: (a) Fuel cell, (b) Electrolyser, (c) Co-conversion or Methanisation, (d) Solid-state ammonia synthesis. Image recreated from [7].

## Perovskite structure

Potential applications for proton conducting oxides as electrolyte materials in different electrochemical devices for energy conversion are presented in **figure 1.2**. Although, there are many different types and implementation of electrochemical cells today [12], their working principle and setup is similar. As displayed in **figure 1.2**, they consist of anode, electrolyte and cathode. At the electrodes, electrochemical oxidation (anode) or reduction (cathode) occur. An overview of the electrochemical reactions is given in **appendix 8.1.2**. Catalysts are employed to enhance the reaction kinetics. The rate and selectivity of electro-catalytic reactions determine the conversion rates from electricity to product and vice versa.

A fuel cell is an electrochemical device that converts chemical energy of a fuel directly into electrical energy (a). Unlike a battery which stores the chemical energy in metal ions or oxides at electrodes, fuel cells require a continuous supply of fuel (for instance hydrogen) and oxygen (for instance supplied from ambient air) to operate. Since there are no intermediate energy conversion steps, high efficiencies of up to 85% may be obtained by combined heat and power [13]. In fuel cells, the fuel is oxidized at the anode and split into ions and electrons. While the electrons are transported via an external circuit, the ions (such as protons or oxide ions) are diffusing through the electrolyte.

A fuel cell reaction is reversible and is employed for the electrolysis of water (b). In contrast to solid oxide electrolyzers (SOEC) that are based on oxide ion-conducting electrolytes, proton ceramic electrolyzers (PCEC) are utilizing a proton conducting membrane and allow for steam feed at the oxygen evolution electrode, and therefore spatial separation from the hydrogen evolution electrode, thus enabling production of dry hydrogen [14]. Further examples for application of protonic ceramics in power-to-X technologies are co-electrolysis of CO<sub>2</sub> and H<sub>2</sub>O to produce syngas as a feedstock for synthetic fuels such as methanol, kerosene or methane (c) or solid-state ammonia synthesis (SSAS) (d). [14, 15]. Proton conductors are particularly suitable for ammonia production, since their operating temperature regime is favorable with regard to prevention of ammonia decomposition at temperatures above 450 °C [14]. Since proton ceramic electrolyzers are exposed to high partial pressure of steam, thicker electrolytes are typically employed as compared to fuel cells.

For application of proton ceramics in a) to d), protonic conductivities of around 10 mS · cm<sup>-1</sup> [8, 9] and long lifetimes are required, with low cost manufacturing of membranes-electrode-assemblies (MEAs) [10-12].

### 1.3 Perovskite structure

Named after the Russian mineralogist Lev Aleksevich von Perovski, the mineral perovskite was discovered by Gustav Rose in the Ural Mountains, in 1839 [13]. Originally, the name perovskite described the mineral CaTiO<sub>3</sub>, while nowadays, perovskites are a large family of structures exhibiting ABX<sub>3</sub> stoichiometry. The A-site is usually occupied by a 12-fold coordinated cation with a larger ionic radius compared to the smaller 6-fold coordinated B-site cation. Perovskites provide an immense versatility, because both metal cation sites are available for dopant substitutions. Therefore, they exhibit a large range of properties and applications (see **appendix 8.1.3**).



As illustrated in **figure 1.3a**, the ideal perovskite structure is cubic for a perfect match of A- and B- cation radii [13-16]. However, the majority of perovskites deviate from the cubic symmetry, **figure 1.3b,c**. According to K.S. Knight, there are three different main mechanisms of distortions [16, 17]. Firstly, within the perovskite structure, the  $\text{BO}_6$  octahedra may be distorted. Secondly, displacement of the B-site cation from its central site within the octahedra may occur, as well as displacements of A-site cations. Finally, octahedral tilting occurs across one, two or all three crystallographic axes.

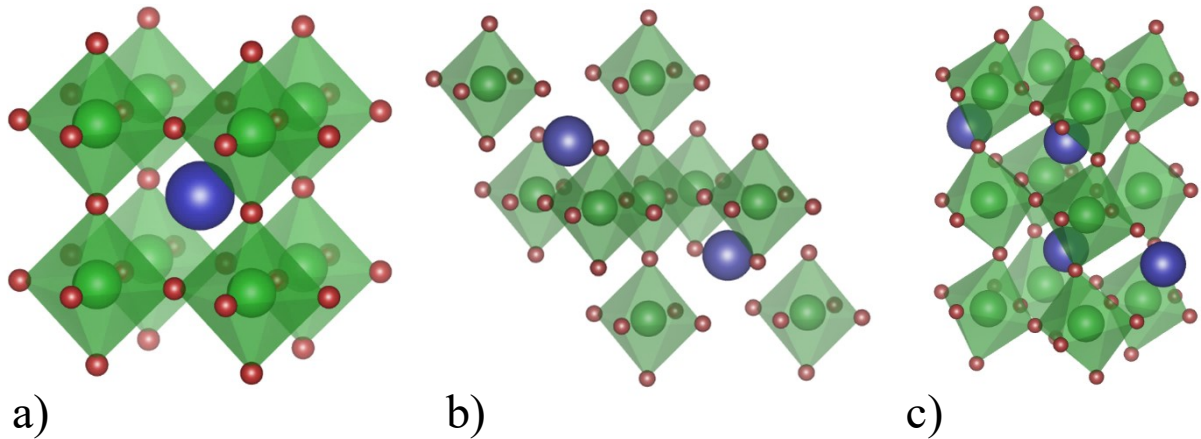


**Figure 1.3:** Different symmetries of perovskite unit cells. Blue spheres represents the A-site, green spheres the B-site and red spheres the anion. a) ideal cubic structure (space group:  $Pm\bar{3}m$ ) for  $\text{BaZrO}_3$ , b) rhombohedral structure (space group:  $R\bar{3}c$ ) and c) orthorhombic structure (space group:  $Pnma$ ) for  $\text{BaCeO}_3$ .

Octahedral tilting is a direct consequence of a geometric mismatch of the ionic radii  $r$  of A- and B-site cations. The mismatch may be expressed by the Goldschmidt tolerance factor, that is calculated in equation 1.1: [18]

$$t = \frac{r_A + r_X}{\sqrt{2} (r_B + r_X)} \quad (1.1)$$

where  $r_A$ ,  $r_B$  and  $r_X$  are the ionic radii of the A-Site, B-Site and oxygen ions, respectively. It should be noted that the perovskites are assumed here as purely ionic crystals [19, 20]. As the tolerance factor shifts away from unity, distortions are more likely to occur. The value of  $t$  for perovskites lies between 0.8 and 1.1[19]. It therefore gives a rough estimation of the occurring perovskite crystal structure. The correlation between the octahedral tilting and resulting space group was described by Glazer [21, 22]. In the Glazer notation, three different letters  $abc$  describe unequal tilt. If there are tilts along one equal axis, they are noted with the same letter. Additional superscripts describe, whether the successive octahedra are tilted in the same sense (+), the opposite sense (-) or no tilt (0). An undistorted system would be noted as  $a^0a^0a^0$  and the rhombohedral system is noted as  $a^-a^-a^-$ . The complete list of possible tilts and their corresponding space group can be found in **appendix 8.1.4**.

## 1.4 Selection of material and defect chemistry

Early evidence of protonic conductivity was reported back in 1956 by Thomas and Lander who observed a correlation between the conductivity of ZnO and the hydrogen pressure [23]. However, the materials investigated were dominated by electron conduction and only minimal amounts of protons could be dissolved [24]. For applications given in **figure 1.2**, a protonic electrolyte must exhibit [25, 26]:

- High protonic conductivity ( $> 1 \text{ mS} \cdot \text{cm}^{-1}$ ) and neglectable electronic conductivity
- Chemical and mechanical stability over a wide temperature range ( $> 5000 \text{ h}$  operation)
- High density to prevent gas diffusion (relative density above 99 %)
- Similar thermal expansion and chemical compatibility with regard to electrodes
- Easy and cost-efficient fabrication and sinterability
- Preferably use inexpensive materials

The first breakthrough was in 1981 when Iwahara and coworkers reported high protonic conductivity in alkaline-earth based perovskites  $\text{SrCeO}_3$  [27]. This gave rise to the new research field of high temperature proton conductors. High protonic conductivity was found in  $\text{BaCeO}_3$ , because of the higher ionic radius of Ba compared to Sr, giving it a more symmetric structure [28, 29]. However,  $\text{BaCeO}_3$  electrolytes are not stable in reducing atmosphere [30, 31]. They form alkaline earth metal carbonates in  $\text{CO}_2$ -containing atmosphere and furthermore decompose in the presence of water to form  $\text{Ba(OH)}_2$  [13, 32]. This results in a fast degradation of the electrolyte. To improve the stability, the B-site should therefore be occupied by a smaller cation as in  $\text{BaZrO}_3$ , which has an excellent conductivity and stability [28]. On the other hand, the fabrication of highly dense membranes of  $\text{BaZrO}_3$  remains challenging, due to the required elevated sintering temperatures [8, 33-36]. Another drawback for  $\text{BaZrO}_3$  electrolytes is a high grain boundary resistivity, even if the grain boundaries are free of secondary phases [9, 34, 37]. Many different approaches in fabrication of a dense and thin electrolyte based on this material were studied and, up to the present day, the fabrication remains a challenge due to barium evaporation [13] or phase separation [38] at the required high sintering temperatures. The solid-state solution of  $\text{BaCeO}_3$  and  $\text{BaZrO}_3$  offers advantages from both endmembers [38-42]. The phase diagram of this solid state solution, according to Pagnier et al., is shown in **figure 1.4** [43].

The introduction of oxygen vacancies and their distribution in the lattice are major requirements for protonic conductivity. Protons are incorporated into oxygen vacancies. Lower-valent dopants are substituted for B-site of the lattice to increase the dissolution of protons [24]. The resulting effective negative charge is compensated for by creation of oxygen vacancies.

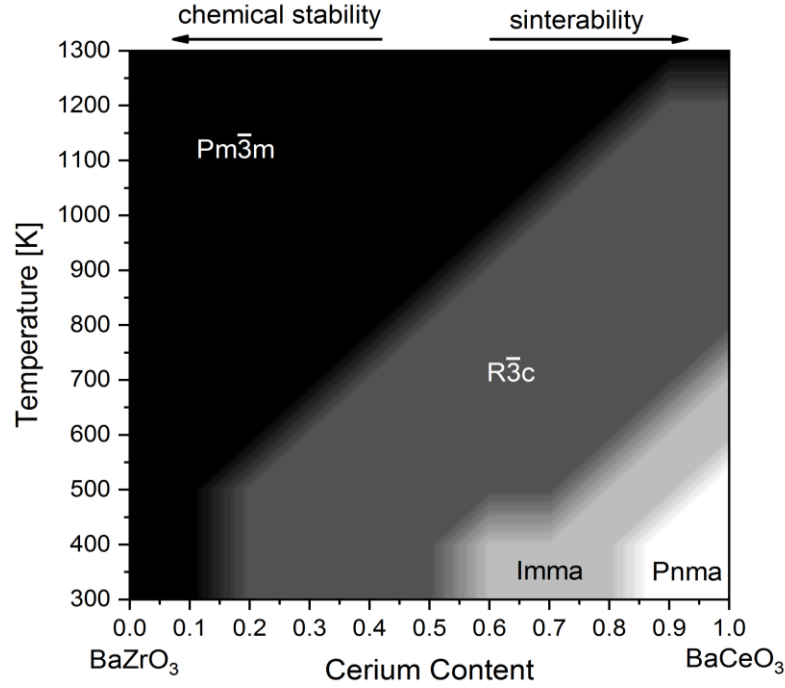
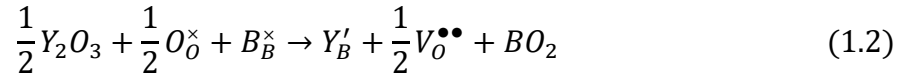
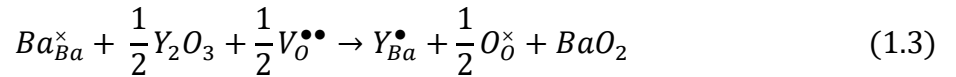


**Figure 1.4:** Phase diagram for the BaZrO<sub>3</sub>-BaCeO<sub>3</sub> solid solution. Recreated from Pagnier et al. [43]

For the BaCeO<sub>3</sub>-BaZrO<sub>3</sub> solid solution, Y<sup>3+</sup> is most often chosen as a dopant, since it has a similar ionic radius as Zr<sup>4+</sup> [29]. The doping and charge compensation mechanisms are shown in Kröger-Vink-Notation [44] in equation 1.2:



where B is either Zr<sup>4+</sup> or Ce<sup>4+</sup> and V<sub>O</sub><sup>••</sup> are oxygen vacancies. Incorporation of two Y-atoms is compensated for by introduction of one oxygen vacancy. Nevertheless, at dopant contents above 25 at%, the bigger sized Y<sup>3+</sup> ion is partially occupying the A-site, leading to reduction of nominal oxygen vacancy concentration, according to equation 1.3 in BaCeO<sub>3</sub> and BaZrO<sub>3</sub>:

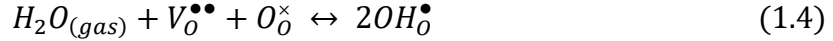


The optimum Y-concentration was reported between 20 and 25 at% [45, 46]. In addition, the fabrication becomes increasingly difficult for increasing Y content due to the potential cross-doping of Y into the A-site [45].

Since the early 1980s, Y-doped zirconium- and cerium-based perovskites remain the most studied and utilized materials for future hydrogen applications [47, 48]. According to Ricote et al., BaZr<sub>0.7</sub>Ce<sub>0.2</sub>Y<sub>0.1</sub>O<sub>3-δ</sub>, referred to as BZCY72, offers the best combination of advantages [41] and is currently applied in demonstrator devices for technology transfer due to its high technological potential [49, 50]. For a complete phase diagram of the ZrO<sub>2</sub>-CeO<sub>2</sub>-BaO-Y<sub>2</sub>O<sub>3</sub> system see **appendix 8.1.5**.

## 1.5 Proton incorporation and conductivity

In perovskite oxides, protons are not a part of the oxide lattice nor its stoichiometry. Instead, they are present as hydroxyl defects, also known as protonic defects, which they form together with oxide ions in equilibrium with an ambient stable hydrogen carrier [24, 51]. Water vapor is absorbed at the surface and dissociates into a hydroxyl ion, which fills an oxygen vacancy, while the remaining proton forms a covalent bond with the surface oxygen [52]. This is expressed in the Stoltz-Wagner equation as:



Formation of protonic defects is an exothermic reaction, meaning that protonic defects are predominant at lower temperatures, while free oxygen vacancies are present at high temperatures [53]. The equilibrium constant is expressed as [13]:

$$K_{OH} = \left( \frac{\Delta S_{OH}^0}{R} \right) \left( \frac{-\Delta H_{OH}^0}{RT} \right) = \frac{[OH_O^\bullet]^2}{[O_O^\times][V_O^{\bullet\bullet}]p_{H_2O}} \quad (1.5)$$

where  $\Delta S_{OH}^0$  is the change in entropy,  $\Delta H_{OH}^0$  is the enthalpy change,  $p_{H_2O}$  is the water vapor partial pressure and  $[O_O^\times]$ ,  $[OH_O^\bullet]$  and  $[V_O^{\bullet\bullet}]$  are concentrations of lattice oxygen ions, protonic defects and oxygen vacancies, respectively. To calculate the protonic defect concentration, two simplifications are made: 1) assuming that protonic defects are the only charge carriers in the perovskites so the electro-neutrality condition reads:  $[Y'_{Zr,Ce}] = 2[V_O^{\bullet\bullet}] + [OH_O^\bullet]$ , where  $Y'_{Zr,Ce}$  denotes the Y acceptor. 2) The number of defects and oxygen vacancies is low compared to the number of oxygen sites  $[O_O^\times] \gg [V_O^{\bullet\bullet}] + [OH_O^\bullet]$ . Turning this into equation 1.5 and solving it for the concentration of protonic defects yields [19, 24]:

$$[OH_O^\bullet] = \frac{1}{4} \left[ [O_O^\times] K_{OH} p_{H_2O} \left( \sqrt{1 + \frac{8[Y'_{Zr,Ce}]}{[O_O^\times] K_{OH} p_{H_2O}}} - 1 \right) \right] \quad (1.6)$$

In reality, however, all perovskite oxides exhibit some degree of mixed conductivity [54]. Under high oxygen partial pressure, electron holes are generated in the lattice according to:



giving rise to p-type electronic conduction. At low oxygen pressure, electrons are formed and n-type electronic conduction is observed, according to the following reaction:



Therefore, it is often meaningful to measure the conductivity as a function of oxygen partial pressure to determine the degree of electronic contribution and its type. In ceramic proton conductors at typical operating temperatures of 600 °C, holes and electrons do not reside in bands. Instead, they are localized within the crystal structure as small polarons [55]. Concentrations of electrons and holes are then noted as polaron defect concentration  $[O_O^\bullet]$  [56]. The concentration of all mobile charge carriers (electrons, electron holes, protonic defects and oxygen vacancies) is well described within the Brouwer diagram (see **appendix 8.1.6**) [54, 57, 58].

Modern understanding of the protonic conductivity arises from quantum molecular dynamics simulations [59], quasi-elastic neutron scattering [60] and muon spin relaxation experiments [61]. Previous work suggest that in solid state electrolytes, protons move via the Grotthuss mechanism [62]. This mechanism is described as a combination of rotational diffusion of the protonic defect and transfer of the proton from oxygen to a nearest neighbor. An illustration of the Grotthuss mechanism is shown in **figure 1.5**. In the model, only the protons show long-range diffusion, while the oxygen ions reside at their lattice positions. The activation energy for the rotation step is low compared to the activation energy for the jumps, with the latter being the rate-determining process for trans-lattice diffusion [32, 63]. Simulations have shown that protons reorientate themselves multiple times before jumping to another oxygen ion, leading to constant stretching of the O-H bond [59]. The time period is in the order of  $10^{-12}$  s and  $\sim 10^{-10}$  s for the rotation and hopping, respectively [13]. During the hopping, the protons form O – H – O bonds for a short time. This strong interaction between the proton and two oxygen ions avoids the need of extra energy to break the O – H bond to the previous oxygen ion. In case of highly-tilted octahedrons, the proton can also directly move between them, which is known as inter-octahedral hopping [24]. However, distortions overall tend to suppress protonic conductivity [19]. In general, smaller lattice constants and higher symmetry enhance protonic conductivity [64-66]. The conductivity of a material depends on the concentration of charge carriers and their mobility. For an ionic species it can be calculated by the equation:

$$\sigma = nq\mu \quad (1.9)$$

where  $n$  is the concentration of mobile species,  $q$  is the elementary charge and  $\mu$  the mobility. Using the Nernst-Einstein equation,  $\mu$  equals [13]:

$$\mu = \frac{qD}{k_B T} = \frac{qf\lambda^2}{6k_B T} = \frac{qz\omega_0 e^{-E_A/k_B T} \lambda^2}{6k_B T} \quad (1.10)$$

where  $k_B$  is the Boltzmann constant, T the temperature and D is the diffusivity, which is a function of the attempt frequency  $f$  and jump distance  $\lambda$ .

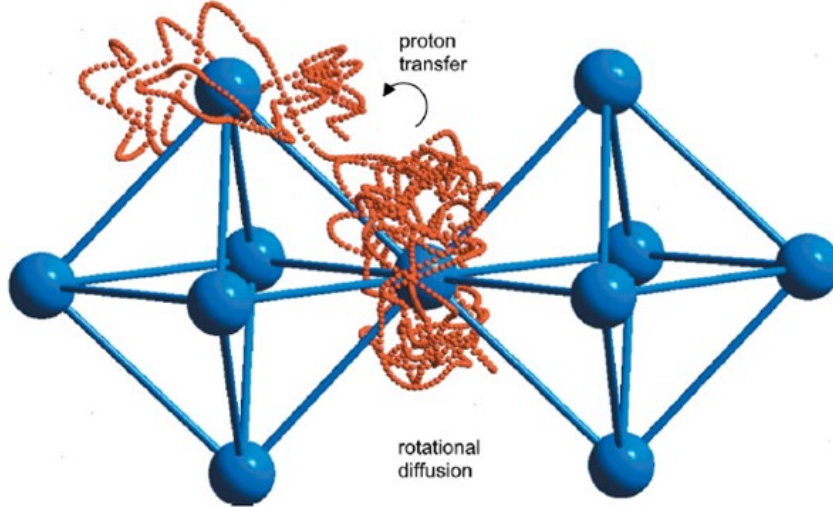


**Figure 1.5:** The trace of a proton in a perovskite showing the two principle features of proton transport: rotational diffusion and proton transfer (data have been obtained by a quantum molecular dynamics simulation of a proton in cubic  $\text{BaCeO}_3$ . Image taken from [32, 59] ).

The attempt frequency itself is dependent on the number of possible jump directions  $z$ , the lattice variation frequency  $w_0$  and the jump activation energy  $E_A$ . Combining equation 1.9 and 1.10 yields:

$$\sigma T = A e^{-E_A/k_B T} \quad (1.11)$$

with the pre-exponential factor

$$A = \frac{z n w_0 q^2 \lambda^2}{6 k_B} \quad (1.12)$$

The activation energy and pre-exponential factor for bulk and grain boundary of proton conductors can be determined experimentally by impedance spectroscopy. For protonic conductivity the value of  $E_A$  varies from 0.4 to 0.6 eV [67, 68], while for oxygen ion conductivity,  $E_A$  was observed in the range of 0.6-1.2 eV [69]. Consequently, proton conducting oxides work at lower temperatures compared to ceramics based on ionic conductivity. Nevertheless, at higher temperatures, parallel protonic and oxygen ionic conduction is observed.

## 1.6 Spark plasma sintering

Spark plasma sintering is a bottom-up synthesis technique, which offers near crystallographic densities of fabricated samples at low sintering temperatures and short process times [70, 71]. The method separates itself from other sintering techniques as a low-voltage and pulsed direct current (DC) is employed under a uniaxial pressure to consolidate the sample. Depending on the conductivity of the sample, it is either directly heated due to Joule heating by the passing DC or heated by thermal conduction from conductive parts of the pressing tools. Because there is no direct evidence of spark discharge [72], SPS is also referred to as Field Assisted Sintering Technique (FAST) [73, 74], Pulse Electric Current Sintering (PECS) [75] or Current-Activated Pressure Assisted Densification (CAPAD) [76]. The original idea of sintering under electric current can be traced back to British and American patents in 1906 and 1913, respectively [77, 78]. However, it took another fifty years for the initially called “spark sintering” method to be invented by Inoue [79]. In the 1970s this technique was used to synthesize functionally graded materials (FGM) for aerospace applications by Lockheed Missile and Space Co [74]. In the early 1990s, Japanese companies started the commercialization of SPS leading to a wide distribution and increase in publications in materials science. More and more companies in Germany, USA, China and Korea implemented this technology to answer the increasing demand in science and industry due to the unique materials that can be fabricated with SPS. Those include metals, alloys, ceramics and all imaginable composites and special material systems such as FGMs [70], as well as porous materials [80].

The driving force of the SPS process is the total reduction of surface energy [81, 82]. This is accomplished by replacing the solid-vapor interfaces with solid-solid interfaces (grain boundaries), grain growth and surfaces smoothing. Those effects are a consequence of the accelerated mass transport at elevated temperatures of typically above 50 % of the melting temperature ( $T_m$ ). In SPS, the mass transport mechanisms are evaporation and surface diffusion which cause particle coarsening, as well as grain boundary diffusion and volume diffusion which lead to densification [76, 83]. While all of them simultaneously determine the sintering progress, one mechanism is usually dominant due to different activation energies [84]. The complexity in the sintering process lies in the interaction between mechanical, thermal and electrical effects, which are often described separately in the literature [74]. This is the reason for the large gap between the fundamental understanding of SPS and its application oriented practical counterpart [85]. Parameters such as temperature, pressure, heating rate and holding time influence the dominating mechanism(s) in the SPS process and, consequently, the sintered sample properties. A typical SPS process profile employed for BZCY72 is seen in **figure 1.6** with all its adjustable critical process parameters. To get a better understanding of the active working mechanisms, it is meaningful to discuss the process in four stages. In stage I the pressure increases within the sample at a controlled rate. The applied force ensures contact between particles and mechanically densifies the powder. Mechanical impact on the sample, attributable to compressive stress, include particle rearrangement, plastic deformation and grain boundary sliding [86]. With increasing pressure the densification rate decreases as more and more cavities between the particles collapse. As indicated by the sample densification progression, most of the densification is due to this contribution because of the porous nature of the precursor powder.

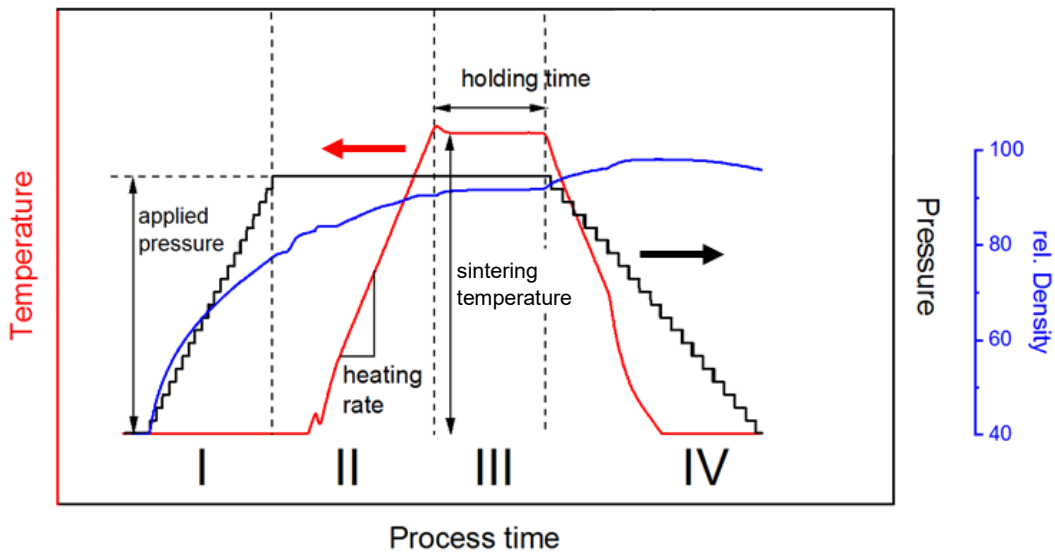


**Figure 1.6:** The SPS process profile used to synthesize BZCY72 ceramics with process parameter profiles. The progression of sintering temperature (red line), applied pressure (black line) and BZCY72 sample densification (blue line) define different sintering stages as described in the text. (The small peak in the heating stage is due to the PID-control reaction time).

At stage II, electric power is applied to the system. Heat is provided either directly due to Joule heating, if the sample is conductive, or via thermal conduction from the surrounding die. This allows for high heating rates of up to 1000 K/min as compared to conventional sintering. As all diffusion related processes scale exponentially with temperature, the thermal effects on the sintering body, especially when combined with high heating rates, lead to unique sample characteristics for SPS. As the temperature rises in the initial sintering stage, particles begin to form necks driven by surface diffusion. The increasingly rounded pores between the particles build a network along the grain boundaries. This leads to coarsening of the grains and delays grain growth [83, 87]. At higher temperatures, pores shrink due to increasing volume diffusion and further densification is reached. In stage III, the maximum sintering temperature and pressure are held for a given holding time to achieve the final densification. During this stage, grains start to grow while smaller grains are eventually consumed by larger grains [83, 88]. Smaller particles sizes in the precursor powder promote densification, while wider particle size distributions generate faster grain growth [83, 89]. Depending on material and sintering conditions, small grains may also evaporate during longer holding times, lowering the density due to emerging nano pores. Depending on the conductivity of the sample, electrical induced mass transport will occur. For ceramics, no current flows though the sample, excluding electro migration. However, there are conflicting results on the effects of the electrical field [90]. Grain growth retardation was reported for yttrium-stabilized zirconia and attributed to an altered grain boundary mobility or solute segregation due to field effects [91, 92]. As for the current pulsing employed in SPS, there is no evidence on an effect attributed to the frequency or pattern of the pulsing [93-95].

In the final stage IV, the system is powered down and the pressure is released, either in an abrupt or continuous manner. The latter is usually preferred, as it reduces the samples internal stress.



## 1.7 Aim of the thesis and overview

Up to this day, the protonic conductivity of  $\text{BaCe}_{1-x}\text{Y}_x\text{O}_3$  (BCY) and  $\text{BaZr}_{1-x}\text{Y}_x\text{O}_3$  (BZY) is unmatched in the temperatures regime of  $400\text{ }^\circ\text{C} - 600\text{ }^\circ\text{C}$ , despite being discovered in the 1980s and 1990s, respectively. Therefore, most material scientists focused on the synthesis and doping of these known compositions.

The aim of this thesis was the development of an SPS process for the synthesis of high-performing and chemically stable BZCY72 protonic ceramics. Conventional sintering techniques at best lead to total conductivities of  $2 \cdot 10^{-4}\text{ S} \cdot \text{cm}^{-1}$  at  $750\text{ }^\circ\text{C}$  for BZY samples [68, 96, 97]. For the synthesis of BZY samples, high temperatures of around  $1650\text{ }^\circ\text{C}$  and long annealing times over 20 h are required [41]. This leads to significant barium evaporation and eventually lower conductivity in addition to comparable low density obtained from these methods. More advanced sintering techniques make excessive use of sintering aids to lower the sintering temperature. However, those introduce unfavorable electronic conductivity into the material and can also lead to mechanical stress within the structure [98]. The following chapter 2 gives an overview about the experimental details for sample preparation and characterization methods for determining crystallographic attributes, microstructure and conductivity as well as neutron scattering setups.

It is well established that the properties of the precursor powder affect the sintering behavior and thus the properties of the sintered specimen. For this reason, two different powder sources were used in the initial SPS processes. Lab-produced solid-state reacted BZCY72 powder was compared with commercial BZCY72 powder to provide solid base conditions for further synthesis. Properties of the SPS processed specimen were directly compared with pellets obtained by conventional sintering and solid-state reaction sintering under the same conditions. Chapter 3 contains a benchmark to provide main sintering characteristics for BZCY72 and its properties as well as comparison with the existing literature.

Further work was carried out to optimize the SPS process with regard to the fabrication of BZCY72. Studies on synthesis of proton conductors often present only one or two sets of sintering conditions [33, 34, 38, 41, 99, 100]. For this reason, much research so far has been trial and error with unquestioned sintering parameters, and frequently conflicting results are obtained [82]. This is due to the complexity of the SPS process. Accordingly, chapter 4 provides a comprehensive data set that correlates SPS process parameters to the resulting material properties. It provides a direction for parameter optimization to determine most suitable sintering conditions for protonic ceramics and assesses given advantages of SPS over state-of-the-art synthesis routes for fabrication of BZCY72. Furthermore, an insight into the SPS mechanisms is given.

For a better understanding of the proton conduction mechanism, neutrons are ideal probes because of their large cross-section for hydrogen and the typical timescales of  $\sim 10^{-8}$  to  $10^{-10}$  s in which these processes occur. In chapter 5, the proton transport in BZCY72 is investigated by means of quasi-elastic neutron scattering. The hopping mechanism of protons in the SPS prepared samples is compared to that of similar proton conductors and to theoretical models. Two different sintering temperatures were chosen in order to answer the question if the fabrication process affects the proton diffusion on a local level. Additional neutron Compton scattering is employed to shed a light on the bonding and amount of hydrogen in the material and their relation to the little known phase transition at low temperatures.

## Aim of the thesis and overview

When used in applications, electrolyte materials are embedded in membrane-electrode-assemblies (MEAs). Since each material layer has different properties, the fabrication of MEAs involves many time consuming steps, such as tempering. A proof-of-principle for the single-step-fabrication of a MEA based on a BZCY72 electrolyte by SPS co-sintering is described in chapter 6, where the properties of the cell and the challenges of its fabrication are briefly enlightened.

The final chapter 7 summarizes the results and gives a prospect on the SPS technique for the synthesis of proton conductors such as BZY, BZCY and similar stoichiometries as well as their possible applications.

## 2 SYNTHESIS AND CHARACTERISATION METHODS

This thesis employs a unique combination of synthesis routes and characterization methods to improve the understanding from the material synthesis to the application, as well from the fundamental physics of the proton diffusion to the fabrication of a membrane-electron-assembly. All experimental methods are described in the upcoming chapter with the main focus on the impedance spectroscopy due to its relevance for the application.

### 2.1 Powder synthesis and sintering

#### 2.1.1 Synthesis of precursor powder

The composition  $\text{BaZr}_{0.7}\text{Ce}_{0.2}\text{Y}_{0.1}\text{O}_{3-\delta}$  was chosen as a high-performance and stable composition. Four different BZCY72 pellets were prepared – two by spark plasma sintering from two different precursor powders, one by conventional sintering and one by solid state reactive sintering. Three different sources of the BZCY72 precursor powders were used as described in what follows:

The first powder synthesis route was performed by a solid state reaction.  $\text{BaCO}_3$  (99.5 %, Alfa Aesar),  $\text{ZrO}_2$  (99.7 %, Alfa Aesar),  $\text{CeO}_2$  (99%, Jenapharm) and  $\text{Y}_2\text{O}_3$  (99.9%, Alfa Aesar) were mixed together in stoichiometric ratios. The resulting powder was ball-milled (Retsch PM 100) in hexane for 12 h in a zirconia container. To ensure homogeneity of the powder, this procedure was repeated twice with an intermediate drying and grinding step at room temperature. Subsequently, the powder was calcined in static air in a tube furnace for 12 h at 1200 °C, at heating and cooling rates of 10 K/min. The powders were ball milled again and dried at room temperature. In the following sections, this powder is referred to as *lab-produced powder*.

The second precursor powder was commercially available BZCY72 (Cerpotech, Norway). This powder was prepared at a large scale based on spray-pyrolysis [101]. The corresponding metal salts are in a precursor solution that is atomized and evaporates, leaving behind a shell of metal salts which eventually decomposes into a mix of metal oxides [102]. BZCY72 powder was obtained after calcination and milling of the metal oxides. An additional calcination was required for the commercial product as explained in section 2.2.2. A similar heat treatment as described for the lab produced powder (12 h at 1200 °C) was used. Subsequently, this powder is referred to as *commercial powder*.

The third source for powder was also synthesized by solid state reaction. Stoichiometric amounts of  $\text{BaCO}_3$  (99.95%),  $\text{ZrO}_2$  (99.7%),  $\text{CeO}_2$  (99.5%) and  $\text{Y}_2\text{O}_3$  (99.9%), all obtained from Alpha-Aesar, were mixed in stoichiometric ratios and ball milled in acetone for 24 hours. The resulting mixture was calcined 24 h at 1400 °C and a few drops of PVA binder was added afterwards. This *benchmark powder* was used for conventional sintering (CS) and solid-state reaction sintering (SSRS) as a benchmark process.

For the CS route, the powder was pressed into a green body ( $\varnothing$  2.5 cm) by uniaxial pressing under a load of 60 MPa. The pellet was then embedded in a Ba excess powder of  $\text{BaZr}_{0.9}\text{Y}_{0.1}\text{O}_{3-\delta} + 20\text{wt}\%$   $\text{BaCO}_3$  to prevent barium evaporation and sintered for 10 h at 1650 °C [103].

### 2.1.2 Solid state reactive sintering

Solid-state reactive sintering (SSRS) was first employed by Babilo and Haile in 2005 [104]. Instead of sintering the pre-reacted powder, samples were directly synthesized from precursor powder with addition of sintering aids, mostly NiO. Precursors such as BaSO<sub>4</sub> or BaCO<sub>3</sub> are reacting with NiO and form a binary eutectic glass-phase lowering the melting point down to 1125 °C [98] (compare **appendix 8.2.1**). With increasing temperature the barium is then extracted from the liquid glass phase since it is more stable and forms the more stable perovskite phase with ZrO<sub>2</sub>, CeO<sub>2</sub> and Y<sub>2</sub>O<sub>3</sub> in the case of BZCY72. The liquid phase sintering terminates around 1500 °C – 1600 °C, depending on the Ba precursor, with the left NiO phase to accumulate within the grain boundaries [105]. The optimal amount of NiO sintering aid was found to be between 0.5 and 1 wt% of NiO [106]. By this method grain boundary diffusion is reduced, since reaction and sintering occur in one step and large grained BZCY72 samples can be obtained (2-5 µm grain size) [98]. However, this synthesis route still requires dwell time over 6 h. Moreover, in reducing atmospheres, NiO is irreversibly reduced to Ni, introducing significant electronic conductivity and significantly lowering electrolyte performance. Therefore, an additional nickel extraction step is required. Solid-state reaction sintering currently qualifies as the state-of-the art recipe to fabricate dense large-grained ceramics based on barium zirconate [42, 107-110]. For the SSRS benchmark pellet 1 wt% of NiO was added to the precursor powder. A green pellet (Ø 2 cm) was pressed at 60 MPa and sintered for 10 h at 1550 °C.

### 2.1.3 Spark plasma sintering setup

All SPS experiments were carried out in the Tycho Sinterlab at the University of Rostock using an HP D5 unit from FCT Systeme GmbH Rauenstein, Germany. The Setup is shown in **figure 2.1** and consists of a mechanical loading system which is part of a high-power electrical circuit. The precursor powder was loaded into a graphite die that closes the circuit. The voltage was approximately 5 V and the current varied from 1 – 2 kA, depending on the sintering conditions. During the initially sintering stage, no current flows through the ceramic sample. Instead, it passes through the die (green path) [93, 111]. According to Guillon et al. most of the energy is dissipated at the sample graphite interface for insulating materials [74]. At higher temperatures, the ceramic become more conductive, allowing a fraction of the current to pass through it (red path) [48]. Sintering is carried out in a rough vacuum at 50 Pa to prevent chemical reactions between oxygen and the graphite die.

In order to enhance the electrical contact and to prevent reactions between the powder and graphite elements, the inner walls of the graphite elements were covered with graphite foil. In addition, the dies were wrapped in carbon felt to reduce the radiation heat loss, thus minimizing temperature gradients inside the system during the process [112]. The device allows for real-time data acquisition of process parameters and system displacement. The temperature was monitored by a pyrometer on top of the die focused on a spot through a hole in the upper punch, approximately 4 mm away from the sample. This temperature reading was used to control the power output via PID (proportional-integral-derivative) controller. In order to observe densification processes during sintering, the position and displacement of the punches were monitored by a capacitive sensor, which was mechanically coupled with the upper punch.

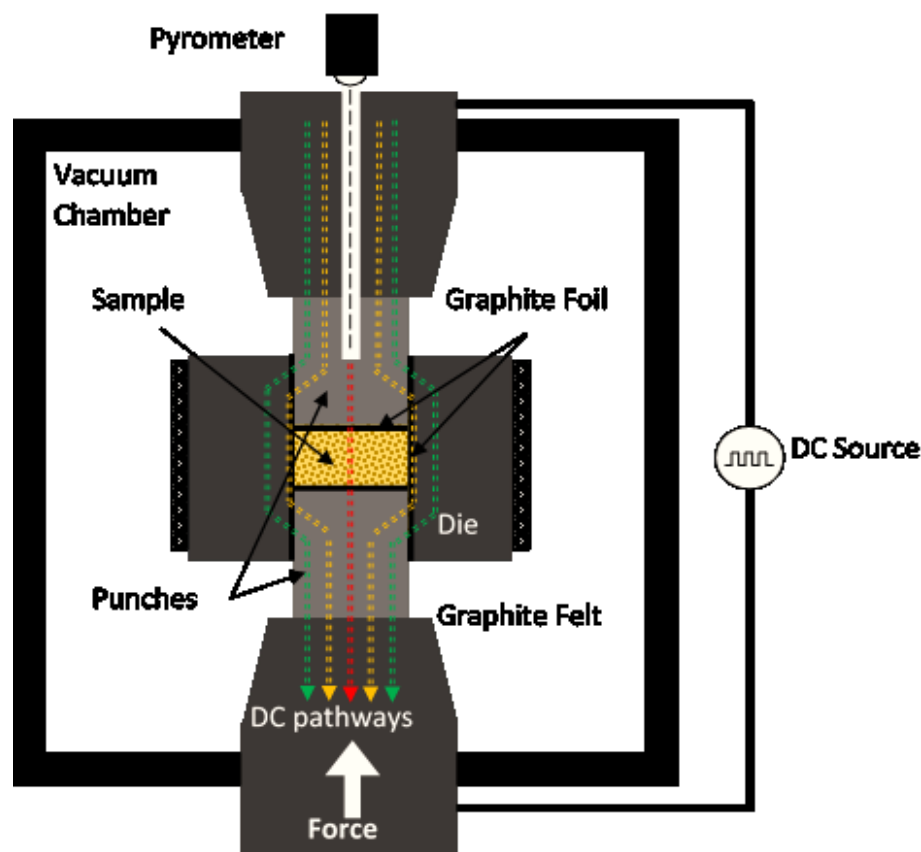


**Figure 2.1:** A schematic representation of the SPS configuration used at the University of Rostock. The DC pathways for a BZCY72 sample illustrate the current flow within the setup, where green indicates high current densities and red indicates low densities. Image recreated from [48].

#### 2.1.4 Process protocol for synthesis of BZCY72 samples

For a final pellet thickness of 2 mm, approximately 4 g of BZCY72 precursor powder was loaded into a graphite die with an inner diameter of 20 mm and positioned between graphite punches. As explained in section 2.2.1, 1 mm thick graphite foil was used to cover the sample facing surfaces. The first sintering experiments were conducted using commercial powder. It was essential to perform a calcination step prior to the sintering process, otherwise, released gas (presumably  $\text{CO}_2$ ) caused damage to the die under pressures of  $\sim 90$  MPa during the heating stage at  $881$  °C. For more details and reasoning behind the chosen parameters see **appendix 8.2.2**.

For synthesis of benchmarking pellets (chapter 3), an axial pressure of approximately 80 MPa was employed. To allow for a better adjustment of the powder particles, the pressure rate was maintained at  $10 \text{ MPa} \cdot \text{min}^{-1}$ . The heating rate was set to  $150 \text{ K} \cdot \text{min}^{-1}$  and the maximal sintering temperature of  $1550$  °C was held for 5 min. After the dwell segment, the sample was cooled to  $800$  °C at  $150 \cdot \text{min}^{-1}$  followed by natural cooling rate averaging  $\sim 100 \text{ K} \cdot \text{min}^{-1}$  to room temperature. The pressure was released at a rate of  $10 \text{ MPa} \cdot \text{min}^{-1}$ . The duty cycle for the DC was 80% with a pulse length of 40 ms. After the sintering process, the pellet was removed from the die using a hydraulic press. The remaining graphite stuck to the surface of the sample was removed

## Powder synthesis and sintering

by manual grinding using SiC-coated abrasive paper.

The same process was used for the lab- produced powder. To remove the last remaining graphite the samples were calcined at 1000 °C for 2 h in static air with heating and cooling rates of 10 K/min.

For the parameter mapping in chapter 4 the SPS process was modified and previously mentioned parameters were varied systematically. The standard parameters were:

- sintering temperature of 1350 °C
- maximum load of 24 kN, (~76 MPa)
- heating rate of 150 K·min<sup>-1</sup>
- holding time of 5 min
- pulse duty cycle was 4:1 with 40 ms pulse time

The investigated parameter ranges are given in **table 2.1**.

**Table 2.1:** Sintering parameter ranges for the BZCY72 sample property investigations. The corresponding color code is applied for all figures in chapter 4.

Sintering parameter	Investigated values					
Maximum temperature	1150 °C	1250 °C	1350 °C	1450 °C	1550 °C	1650 °C
Maximum load	12 kN	16 kN	20 kN	24 kN	28 kN	32 kN
Corresponding pressure	38 MPa	51 MPa	64 MPa	76 MPa	89 MPa	102 MPa
Heating rate	25 K/min	50 K/min	100 K/min	150 K/min	200 K/min	
Holding time	5 min		20 min	40 min	60 min	

The sintering temperature and pressure are considered to be the most influencing parameters for the SPS process [76]. The influence of other parameters has not yet been studied for BZCY72 or related materials to the best of the author's knowledge. Therefore, a complete sample matrix as a function of maximum temperature and pressure within the given values was fabricated. Exemplary samples at 1050 °C and 1750 °C were also produced but were not further investigated due to their extremely fragile nature.

Sintered specimen of 8 mm thickness were prepared for the neutron scattering experiments, corresponding to ca. 8 g of precursor powder. A complete sample overview with basic properties and comments is given in **appendix 8.2.3**.

### 2.1.5 SPS-cosintering of membrane-electrode-assemblies (MEAs)

To investigate the co-sintering behavior of electrode and electrolyte, an electrode with 60 wt% of NiO and 40 wt% BZCY72 mixed precursor was loaded as additional layer into the graphite die. The sintering temperature for this system was 1350 °C for 5 min holding time at a pressure of ~76 MPa and a heating rate of 150 K·min<sup>-1</sup>. The resulting symmetrical NiO-BZCY72/BZCY72/NiO-BZCY72 exhibited good stability in air. After grinding the sample surface with SiC sand paper, mechanical polishing was employed for further investigation.

## 2.2 Scattering Experiments

### 2.2.1 Static light scattering

The particle size distribution is an important property of any precursor powder, since it has a critical effect on the sintering behavior [113, 114]. It can be accessed through Static Light Scattering (SLS) analyzed by means of Fraunhofer diffraction or Mie scattering models [115], where the latter yields more precise results [116]. Mie scattering describes the solution of Maxwell's equation for an electromagnetic plane wave scattered by spherical particles. This model is used when the particle size  $r$  has the same dimensions as the wavelength  $\lambda$  of the scattered light  $0.1 \lambda < r < \lambda$  [117]. Particles of various sizes produce different diffraction patterns. Large particles scatter light in narrow angles at high intensities and more in forward direction while small particles scatter light less intensely at wider angles [118]. Generally, the scattering intensity can be expressed as:

$$I(\theta, \lambda, a) = A \int_{a_{min}}^{a_{max}} K(\theta, \lambda, a) f(a) da \quad (2.1)$$

where  $A$  is a scale form-factor considering the geometry of the setup,  $\theta$  is the scattering angle and  $f(a)$  is the particle size distribution as a function of the particle size  $a$ .  $K(\theta, \lambda, a)$  describes the scattering process. In Mie theory an infinite series of Bessel functions and Legendre functions is employed for the angle dependent scattering amplitude (see [119, 120] for a detailed mathematical description).  $I(\theta, \lambda, a)$  can be measured, however, to calculate the particle size distribution the diffraction index of the sample as well as its imaginary part (absorption index) must be known.

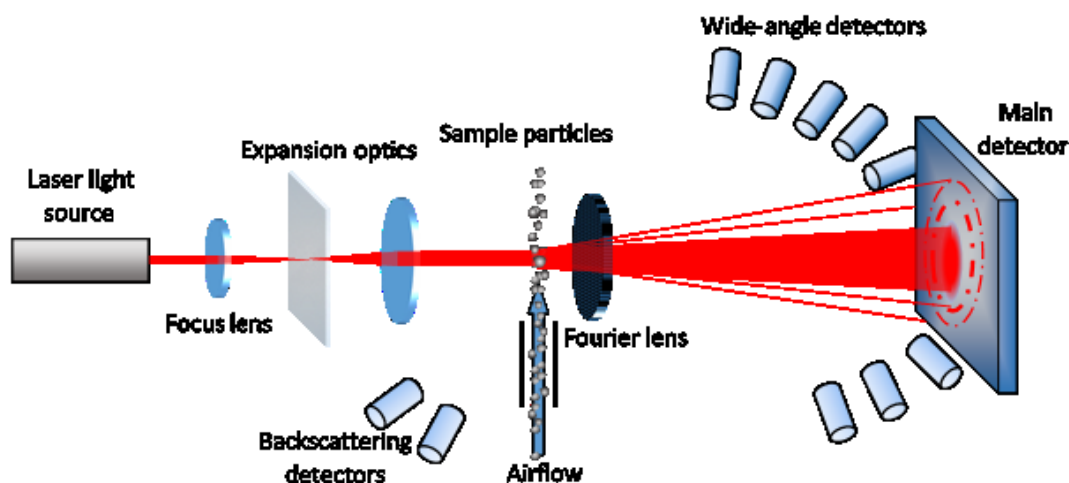


**Figure 2.2:** Scheme to measure particle size distribution using static light scattering (Mastersizer 2000).

All SLS experiments were performed with the Mastersizer 2000 (Malvern) with the setup shown in **figure 2.2**. A helium neon laser ( $\lambda = 633 \text{ nm}$ ) produces the light beam which is expanded to increase the scattering cross section. The light gets scattered by the particles and a Fourier lens is employed to ensure that particles of the same size scatter to the same detector position. The main

## Scattering Experiments

detector has 33 compartments to cover small angle scattering, additional 11 wide-angle detectors cover large angles and 2 backscattering detectors track backscattered light. All detectors are photomultipliers which convert the scattered intensity into a voltage at different scattering angles. The position (angle) of the detector is then converted into a particle size distribution employing the Mie theory.

Approximately 2 g of each precursor sample were used for investigation. Initial particle separation was realized by mechanical vibration. Dry particle dispersion was subsequently achieved by pressured air at 3.2 bar. The refractive index for the BCZY72 sample was assigned to 2.15 according to [121]. On recommendation of the manufacturer Malvern, the absorption factor for slightly dyed particles can be estimated to be 0.1.

### 2.2.2 X-Ray diffraction

X-rays are a part of the electromagnetic spectrum with a wavelength ranging from  $10^{-3}$  to 10 nm which makes them well suited scattering probes for structural investigations on condensed matter [122]. Within a crystal lattice X-rays are reflected at parallel lattice planes made up by the periodically aligned atoms. If the path difference of the waves reflected from the planes with the distance  $d$  is an integer multiple of their wavelength  $\lambda$  constructive interference occurs and generates sample characteristic diffractograms, as described by Bragg's law:

$$n\lambda = 2d \sin \theta \quad (2.2)$$

X-ray diffraction (XRD) was carried out on powders and sintered pellets at room temperature by means of a Bruker D8 Advance X-ray diffractometer in reflection geometry, using Ni-filtered Cu  $K_{\alpha}$  characteristic X-rays. Patterns were collected over a range of  $2\theta$  of 20 to 120°, at a step width of 0.02° and a data collection time of 5 s per step.

XRD patterns were analyzed by the TOPAS software, employing a Rietveld refinement procedure [123]. In a XRD pattern, several Bragg reflections contribute to the observed intensity  $I_{i,obs}$  at any scattering angle  $\theta_i$  in the diffractogram. For the refinement, the structural model of BZCY72 was imported from combined high-resolution neutron and synchrotron XRD diffraction by Mather et al. [124]. The calculated intensity is given by [125]:

$$I_{i,calc} = S_i \sum_K^{N_{peaks}} L_K |F_k|^2 P_k A \phi(2\theta_i - 2\theta_k) + I_{i,bkg} \quad (2.3)$$

where

- $S_i$  is a scale factor for the incident beam,
- $K$  represents a set of Miller indices for a Bragg reflection,
- $L_K$  is the Lorenz-polarization factor
- $F_k$  describes the structure factor for the corresponding Bragg reflection  $K$
- $P_k$  is the texture factor and takes preferred orientations into account
- $A$  represents the absorption factor



- $\phi$  is the reflection profile function for which the modified Thompson-Cox-Hastings pseudo-Voigt “TCHZ” peak type is used in this thesis
- $I_{i,bkg}$  is the background intensity

More detailed information about the Rietveld refinement is listed in **appendix 8.3.1**. For the precursor powders, a quantitative phase analysis and a least square lattice parameter refinement was carried out. For the sintered pellets, the lattice parameters, average crystallite sizes and occupancies for Ba and Ce, Zr metal cations were refined, whereas the occupancy for oxygen was fixed to nominal values according to equation 1.7. Due to the similar electron configurations of Zr and Y, the occupancy of Y was fixed to 0.1 and a constraint for the B-factors of the cations was established. From the refined data, B – O bond lengths and bond angles were calculated.

### 2.2.3 Raman spectroscopy

Raman spectroscopy is a non-destructive analysis technique to determine mainly vibrational modes of molecules or phonons which provide detailed information about the structure, crystallinity and atomic interactions. This method relies upon the interaction between light and the chemical bonds within a material in the form of inelastic scattering or Raman scattering. If monochromatic radiation of a frequency  $\nu_0$  interacts with molecules or phonons and the scattered radiation is dispersed it is found to contain not only the original frequency  $\nu_0$  in Rayleigh scattering but also pairs of new frequencies of the type  $(\nu_0 \pm \nu_M)$  (see **figure 2.3**). In the case of a lower scattered frequency the interacting molecule has a higher vibrational energy, which is known as Stokes Raman scattering. On the other hand, if the final vibrational energy of the molecule is lower, the scattered light has a higher frequency, which is called Anti-Stokes Raman scattering. In Raman Spectroscopy the Raman shifts is always characterized by the frequency shift  $\nu_M$  and are generally reported in wavenumbers.

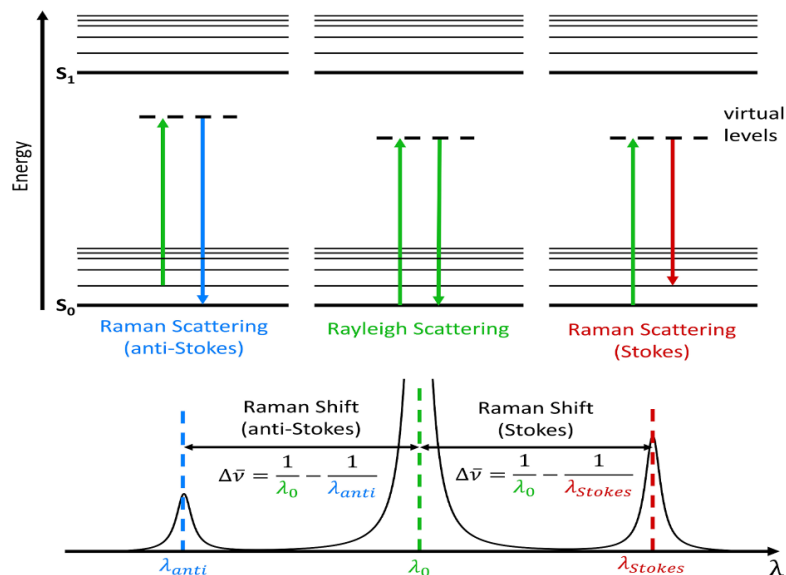


**Figure 2.3:** The origin of Rayleigh scattering, Stokes Raman scattering and Anti-Stokes-Raman scattering [126]. Top: The electronic energy levels  $S_0$  and  $S_1$  and the vibrational energy levels (Energy scale not linear). Bottom: Resulting Raman shift.

## Scattering Experiments

Raman spectroscopy was used on the polished surfaces of the BZCY72 samples in order to detect possible amorphous impurity phases and to determine vibrational modes of the phonons in the crystal. Raman spectroscopy was carried out using a Renishaw inVia Raman microscope with a RL532C100 laser source ( $\lambda = 532$  nm). Spectra were analyzed using Renishaw's WiRE (Windows-based Raman Environment) software using a Pseudo Voigt profile function.

### 2.2.4 Quasi elastic neutron scattering

Neutrons have unique properties for investigating dynamical and geometrical properties of condensed matter. Their energy  $E$  is controlled by passing them through a moderator with a certain temperature  $T$  according to:

$$E = \frac{1}{2}mv^2 = \frac{3}{2}k_B T \quad (2.4)$$

where  $m$ ,  $v$ ,  $k_B$  are the mass, velocity and Boltzmann constant, respectively. Using the de Broglie relation this corresponds to a wavelength of

$$\lambda = \frac{h}{\sqrt{2mE}} \quad (2.5)$$

Neutrons used for Quasi Elastic Neutron Scattering (QENS) are thermal neutrons with wavelengths of  $6 - 10$  Å [127, 128]. The generation of the probing neutrons is explained in **figure 2.4**. The energy of those neutrons is in the same order as the thermal energy inside crystals, allowing to study the motions within the sample. This method focuses on scattering processes at small energy transfers within a timescale of  $10^{-8} - 10^{-13}$  s and is capable to investigate diffusive motion with path lengths of  $10^{-8} - 10^{-11}$  m [129]. Since hydrogen has the highest incoherent scattering cross section for neutron of all elements, this method is well suited for proton diffusion [130]. While most incoming neutrons are scattered by the sample elastically, some neutrons get a small energy and momentum transfer caused by diffuse motions within the sample with a corresponding wave vector  $Q = k - k_0$  where  $k_0$  and  $k$  are the incident and scattered wave vectors, respectively.

In a QENS experiment the measured intensity is proportional to the dynamic structure factor  $S(Q, \omega)$ , which describes the probability that an incident neutron is scattered by the sample with a momentum transfer  $\hbar Q$  and energy transfer  $\hbar \omega$  [130, 131] where  $\hbar$  is the reduced Planck constant.  $S(Q, \omega)$  consist of two contributions: a coherent scattering function and an incoherent scattering function, which hold information on the collective motions of all particles and single particles, respectively (further information is given in **appendix 8.4.1**). For the analysis,  $S(Q, \omega)$  was modelled by the following function:

$$S(Q, \omega) = b(Q) \cdot \delta(\hbar \omega) + a_L(Q) \frac{1}{\pi} \frac{\Gamma(Q)}{(\hbar \omega)^2 + \Gamma(Q)^2} + c(Q) \cdot (\hbar \omega) + d(Q) \quad (2.6)$$

The first term is attributed to the elastic scattering from those atoms that move too slow to be resolved in QENS [131] where  $b(Q)$  is a  $Q$  dependent constant and  $\delta(\hbar\omega)$  is a delta function. The second contribution is the quasi-elastic bordering of the elastic peak. For a translational diffusion this is approximated by a Lorentz profile with the amplitude  $a_L$  and a full width at half maximum  $\Gamma(Q)$  [132]. The remaining parameters  $c(Q)$  and  $d(Q)$  describe a linear background.

In proton conductors, the diffusion model by Chudley and Elliott is usually employed [133]. It describes the jump diffusion for a proton between oxygen sites within the lattice where the jump length  $l$  is fixed and  $\Gamma(Q)$  is expressed as:

$$\frac{\Gamma(Q)}{2} = \frac{\hbar}{\tau} \left( 1 - \frac{\sin(Ql)}{Ql} \right) \quad (2.7)$$

Here,  $\tau$  is the relaxation time or the time the proton spends at a new position before its next jump. Referring to chapter 1.5, it should be noted that there are at least two different proton motions in BZCY72. However, due to the low scattering contrast of the measurements, more elaborate models cannot be justified and, thus, not all details of the proton motion can be resolved.

The QENS experiments were performed at the IRIS indirect neutron spectrometer within target station 1 at the spallation source ISIS Rutherford Appleton Laboratory, United Kingdom, **figure 2.4**. IRIS is an inverted geometry spectrometer where neutrons scattered by the sample are energy-analyzed by means of Bragg scattering from large-area crystal-analyzer array. For data analysis, the time-of-flight technique is used. Should interactions within the sample lead to a loss/gain in neutron energy then a distribution of arrival times will result. By measuring the total time-of-flight  $t$  and knowing the distance from the moderator to the sample  $L_1$ , the distance from the sample to the detector  $L_2$  and the time it takes for the neutron to travel the latter distance  $t_2$ , the energy difference can be calculated with the neutron mass  $m_n$ :

$$\Delta E = \frac{1}{2} m_n \left[ \left( \frac{L_1}{t - t_2} \right)^2 - \left( \frac{L_2}{t_2} \right)^2 \right] \quad (2.8)$$

For the QENS experiment two BZCY72 samples were prepared by SPS ( $p \sim 76$  MPa, HR = 150 K/min,  $t = 5$  min) at 1350 °C and 1550 °C, respectively. Hydration was achieved at 680 °C for 24 h under 3% H<sub>2</sub>O/Ar atmosphere within a tube furnace. The samples with a total thickness of 8 mm and 20 mm diameter were sealed into a quartz tube and loaded into a vacuum furnace (see **appendix 8.4.2**). QENS measurements were taken at 50, 200, 300, 400, 500 and 600 °C. A graphite 002 analyzer with a wavelength of 6.7 Å and an energy resolution of 15 µeV was used to screen the reflected neutrons which was cooled with liquid helium to reduce background contributions from thermal diffuse scattering. The investigated momentum transfer range was  $0.45 \text{ \AA}^{-1} \leq Q \leq 1.85 \text{ \AA}^{-1}$ . All  $Q$ -dependent spectra were summed into 15 groups to increase the statistics. The strong Bragg reflection within the  $Q$  range from  $1.25 \text{ \AA}^{-1}$  to  $1.45 \text{ \AA}^{-1}$  (see **appendix 8.4.4**) was excluded by discarding the corresponding detector signals. The energy dependent absorption of neutrons was corrected using a vanadium standard spectrum. One 50 °C measurement was used as resolution function for the data analysis [134]. Data reduction and analysis was performed by means of the Mantid software [135, 136].

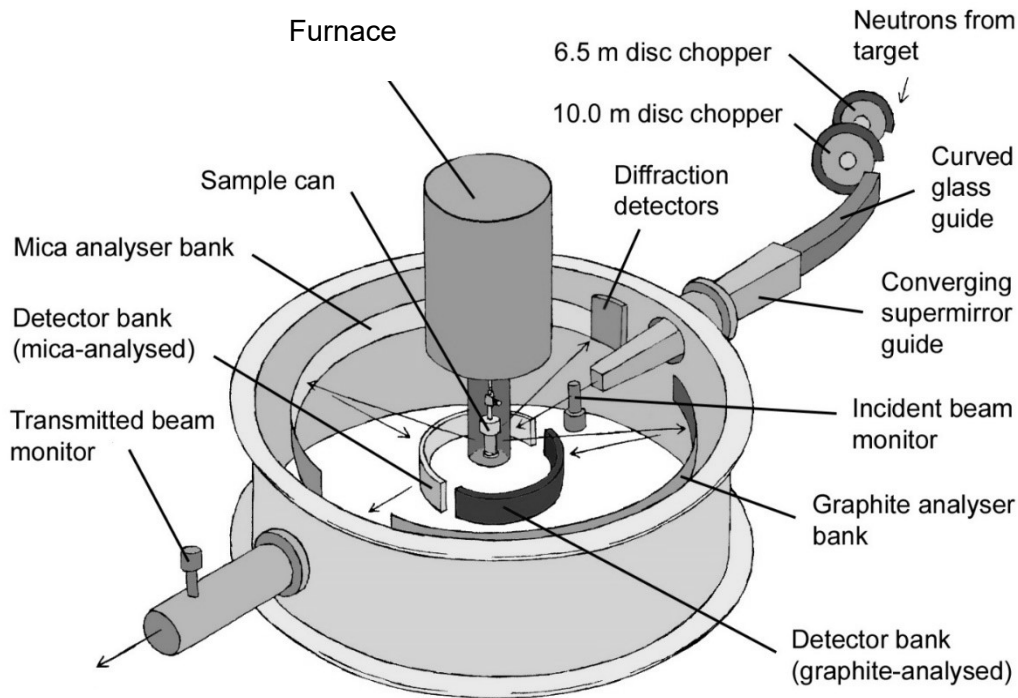


**Figure 2.4:** The IRIS setup used for QENS experiments. Neutrons are produced by the spallation process when the 160 kW proton beam from the particle accelerator hits a tungsten-tantalum target. They are then passed through a liquid hydrogen moderator (19 K) to slow the neutron down. Two choppers are employed to set a known band of wavelengths for neutron to define the energy window. A curved glass guide focuses the neutron beam and gives it a characteristic wavelength of 2.5 Å. An additional nickel-titanium super mirror scales the neutron beam area down to 32 mm × 21 mm. This is the incident beam for the QENS experiment with a neutron flux of  $5 \cdot 10^7$  neutrons · cm<sup>-2</sup> · s<sup>-1</sup>. Image recreated from [134]. The sample scatters part of the neutron beam to the Graphite analyzer, which reflects neutrons of specific energies to the ZnS scintillator detector banks and <sup>3</sup>He gas detector banks.

### 2.2.5 Neutron Compton scattering

Neutron Compton Scattering (NCS), or Deep Inelastic Neutron Scattering (DINS) is a mass-selective neutron scattering technique which employs epithermal neutrons in the eV range [137]. This method gives access to the nuclear momentum distribution for any measured isotope. Within the eV energy region, the incident neutron energy and consequently the energy transfer is well above the binding energies of atoms and other energy scales in the sample. In contrast to QENS, this method is not limited by any time window [137-141]. Another advantage is the mass-selectivity. Each atomic mass in the investigated sample contributes to the time of flight (TOF) spectrum as a Doppler-broadened recoil peak due to their individual atomic motions [142]. The external forces on the neutron-nucleus systems become negligible for high neutron energies and there is a direct relationship between energy and momentum transfer. This is called the impulse approximation (IA). Within this approximation the count intensity  $C(\theta, t)$  for every detector at a given scattering angle,  $\theta$ , and time of flight value,  $t$ , is given by the following expression [137, 138, 143-150]:

$$C(\theta, t) = \frac{E_0 I(E_0)}{Q} \sum_M M c_M J_M(x_M) \otimes R_M(x_M) \quad (2.9)$$

where  $M$  is the mass of the corresponding nuclear isotope (H, O, Y, Zr, Ba, Ce from the sample and Al from sample containers),  $E_0$  and  $I(E_0)$  are the incident neutron energy and intensity spectrum, respectively, and  $Q$  is the neutron momentum transfer. The Factor  $c_M$  contains the probability of a neutron to be detected and the number of nuclei of mass  $M$  that are illuminated by the incident beam. The convolution between the longitudinal momentum distribution  $J_M(x_M)$  and the instrument resolution function  $R_M(x_M)$  considers the effects of the finite resolution of the spectrometer when measuring  $J_M(x_M)$  [137-141]. The variable  $x_M = y_M \cdot (\sigma_M \sqrt{2})^{-1}$  represents a scaled and centered magnitude of the longitudinal momentum of a nucleus of mass  $M$  for its standard deviation  $\sigma_M$  where  $y_M$  is the West-scaling variable [151]. For the NCS measurement on BZCY72  $J_M(x_M)$  was modeled as a Gaussian function corrected for the deviations from ideal impulse approximation conditions which are denoted as the third-order Hermite polynomials  $H_3(x_M)$  [137, 138, 143-150]:

$$J_M(x_M) = \frac{1}{\sqrt{2\pi\sigma_M^2}} e^{-x_M^2} \left( 1 - \frac{\sqrt{2}\sigma_M}{12} \frac{\sigma_M}{Q} H_3(x_M) \right) \quad (2.10)$$

The sample used for the NCS experiment was sintered at 1450 °C under a pressure of 76 MPa at a heating rate of 150 K/min and 5 min holding time. The hydration procedure was the same as applied for QENS measurements. The pellet was sealed into a square-shape (90 × 90 mm<sup>2</sup>) aluminum container.

NCS was carried out at the VESUVIO time of flight (TOF) spectrometer at ISIS Rutherford Appleton Laboratory, United Kingdom [152]. The setup is detailed in **appendix 8.4.5**. Measurements were performed on the sintered BZCY72 sample at 70 K, 100K, 150 K, 200 K and 300 K. The following procedure was adjusted for BZCY72 from [137, 139, 146, 153, 154].

Since the BZCY72 sample did not cover the entire cross section area of the beam, a canonical scattering of 10 % was assumed in order to fix the initial estimate of the ratio of the single to multiple scattering from the sample. The TOF data from the backscattering detector were pre-fitted according to equation 2.9. An estimation of the momentum distribution widths of the nuclear species except hydrogen was generated by using stoichiometric fixing. Based on the obtained widths of the previous step, the forward scattering data were fitted including the hydrogen momentum distribution. For the analysis of the hydrogen recoil peak shape, the TOF region from 275 to 285 μs was masked in DINS spectra in order to exclude neutron-gamma resonances from metallic nuclear species present in BZCY72. The sample-dependent multiple scattering (MS) and gamma background (GB) was then calculated and subtracted from the backscattering data and the final estimates of the widths and relative scattering intensities for the heavy nuclei were determined. The obtained results served as input for fitting the forward scattering data again to get a more precise hydrogen peak width. MS and GB were calculated again and subtracted from the raw forward scattering data. The hydrogen recoil peak was isolated and transformed from TOF to the domain of longitudinal momentum fitting.

## 2.3 Electron microscopy

### 2.3.1 Scanning electron microscopy

Scanning Electron Microscopy (SEM) was employed to analyze the microstructure of powders, fractured surfaces and polished cross-sections of sintered specimens. Pellets were cut using a Buehler Isomet 4000 precision saw and subsequently embedded in Epoxy EpoThin2 before being polished by means of a Buehler AutoMet 250 Polisher to a 50 nm finish (MasterDep Polishing Suspension). To prevent surface charging during SEM investigation, a 3 nm Au coating was applied prior to the microscopy study by magnetron sputtering. Images were taken by a Jeol JSM 7500 F SEM, applying an acceleration voltage of 5 kV at a working distance of 6-8 mm. For a better contrast, a low-angle backscattered electron (LABE) detector was employed, allowing for surface information at fine-scale resolution. Also, in comparison to secondary-electron detectors, the higher-energy backscattered electrons are less affected by charging of the sample surface by the electron beam. Information on the grain size distribution was obtained by analyzing multiple images (400-900 grains) by the Alicona MeX software package. The true grain size  $G$  was calculated from the radius according to:  $G = \sqrt{6r^2}$  [83].

Energy-dispersive X-ray spectroscopy (EDX) was carried out to determine the nominal cation ratios and composition homogeneity, applying an acceleration voltage of 25 keV. Evaluation of the spectra was done by the Esprit software. Reference materials for the quantitative analysis were taken from external standards from the Bruker Esprit atomic database using the L series of each atom. For elemental analysis 10 different spots with areas of approximately  $5 \mu\text{m}^2$  were investigated and the average weight ratio was determined. The collection time was 2 min and 20 min for elemental analysis and EDX mapping, respectively.

### 2.3.2 Transmission electron microscopy

Grain boundaries of dense specimens were examined using Transmission Electron Microscopy (TEM) at Colorado School of Mines. The lift-out specimens were prepared on an FEI Helios 600i NanoLab SEM/FIB, using a 30 kV accelerating voltage for making the trenches and doing the initial thinning. A final surface milling step at 2 kV was used for each face. The TEM imaging was performed in an FEI Talos F200X using a 200 keV accelerating voltage. The STEM-HAADF imaging used a 70  $\mu\text{m}$  Condenser 2 aperture and a spot size of 6 at the magnifications indicated with the images. The EDX-maps were collected for durations between 30 and 45 minutes with a resolution of 25 data points per  $\text{nm}^2$ .

## 2.4 Impedance spectroscopy

### 2.4.1 Fundamentals

Impedance spectroscopy (IS) is a powerful and versatile tool to characterize electrical properties of materials and their interfaces [155, 156]. The method allows to separate different responses contributed by each phenomenon within the investigated system by resolving their ideally unique time constants in the frequency domain. IS measurements may be performed by means of a

Potentiostat based on a Wheatstone bridge, where the resistance and capacitance of a sample is balanced against variable resistors and capacitors. The samples internal representation of circuit elements (see **appendix 8.5.1**), also referred to as equivalent circuit, are unknown. Therefore, it is important to measure the resistance  $R$  and capacitance  $C$  of a sample over a wide range of frequencies. An IS experiment performs an excitation to the system based on a harmonic perturbation voltage  $v(t) = V_0 \sin(\omega t)$  for multiple frequencies and measures the phase shift  $\phi$  and amplitude of the response  $i(t) = I_0 \sin(\omega t - \phi)$  where  $\omega$  is the angular frequency and  $V_0$  and  $I_0$  are the amplitude of the voltage and current, respectively.

A low amplitude alternative current (AC) excitation signal (generally not more than 50 mV) is used to operate within a linear regime of the cell [155]. This is important, since high stimulus signals would cause harmonic distortion in the AC current response (see **appendix 8.5.2**). Assuming a linear system the impedance of the system can be expressed (analogous to resistance defined by Ohm's law) as the ratio of the AC voltage and current:

$$Z(j, \omega) = \frac{V_0 \sin(\omega t)}{I_0 \sin(\omega t - \phi)} = \frac{V_0 e^{j\omega t}}{I_0 e^{j(\omega t - \phi)}} = Z_0 e^{j\phi} \quad (2.11)$$

where  $j = \sqrt{-1}$  and  $Z^* = Z' + jZ''$  is the complex impedance consisting of real and imaginary part. For further interpretation  $-Z''$  is usually plotted as a function of  $Z'$  as a Nyquist plot. Another IS data representation is the Bode plot where  $Z''$  is plotted against the frequency  $f$ . In addition, within complex systems it is often meaningful to calculate the electric modulus  $M^* = M' + jM''$  to give emphasis to elements with small capacitances:

$$M^* = j\omega C_0 Z^* \quad (2.12)$$

where  $C_0$  is the vacuum capacitance of the cell. For a full IS analysis, each data representation must be taken into consideration [157]. Assuming a RC element, the capacitance and resistance are calculated by:

$$C = \frac{\epsilon_0}{2M''_{max}} \quad (2.13)$$

$$R = \frac{1}{\omega C} \quad (2.14)$$

where  $\epsilon_0$  is the vacuum permittivity. Within the Nyquist representation, each process contribution appears as an arc and can be modeled as a capacitor and resistance in parallel configuration with time constant  $\tau = RC = \omega_{max}^{-1}$ . Given that the time constant are sufficiently different, the corresponding phenomenon can be resolved. **Appendix 8.5.3** lists typical capacities for different phenomena. To focus on the effects contributed the electrolyte, Au or Pt electrodes are applied to both sides to prevent discharges or chemical reactions. In real systems, the ideal capacitor is often replaced by a Constant Phase Element (CPE), denoted in parallel with a resistance as RQ element [155, 156, 158]. CPE originate from non-uniform current density along inhomogeneous surfaces,

resulting in “depressed semicircles” in the Nyquist plot. [156]. The impedance of a CPE and capacity of a RQ element are given by:

$$Z(j, \omega) = \frac{1}{(j\omega)^n Q_0} \quad (2.15)$$

$$C = R^{\left(\frac{1}{n}-1\right)} Q^{\left(\frac{1}{n}\right)} \quad (2.16)$$

where  $0 \leq n \leq 1$  and  $Q$  is the numerical value of the admittance. The CPE represents a capacitor when  $n = 1$  and a resistor for  $n = 0$ . The resistivity  $\rho$  and conductivity  $\sigma$  of the sample and its compartments can be calculated by:

$$\sigma = \frac{1}{\rho} = \frac{L}{RA} \quad (2.17)$$

taking the sample thickness  $L$  and electrode area  $A$  into account. This is also known as the geometric factor, correcting the data for the samples dimensions.

As mentioned in chapter 1.5 the ionic conductivity, depends strongly on temperature. By collecting impedance spectra over a wide range of temperatures, the activation energy  $E_A$  as well as the pre-exponential factor  $A$  can be obtained from a slight variation of equation 1.11:

$$\ln(\sigma T) = \ln(A) - \frac{1}{T} \frac{E_A}{k_B} \quad (2.18)$$

Usually  $\log(\sigma T)$  is therefore plotted vs  $1000/T$  to calculate  $E_A$  and  $A$  within an Arrhenius plot.

## 2.4.2 Experimental setup

The impedance measurements were conducted in a symmetric cell configuration with identical electrodes and atmosphere at both sides of the samples (i.e., single chamber). Depending on the mechanical integrity of the pellets, the electrode area varied from 1 to 3.1 cm<sup>2</sup> with a typical thickness of  $\sim 0.18$  cm. Platinum paste (OS 2, CL 11-5349, Heraeus) was painted on both sides and fired in static air at 800 °C for 2 h. Subsequently, the samples were inserted into a measurement jig and fixed in place with a spring-loaded mechanism (see **appendix 8.5.4**).

In **figure 2.5**, a complete overview of all components for the IS experiment is shown. The jig is placed into a quartz tube which is itself inside a tube furnace. The measurements were performed in a dry or moist (3% H<sub>2</sub>O) 5% H<sub>2</sub>/Ar atmosphere with a flow rate of  $\sim 40$  sccm which was monitored via a mass flow controller and via a gas flow meter. The gas was passed through sulfuric acid for the purpose of drying. For moist atmosphere the gas was additionally passed through a water bubbler kept at 21 °C. Data was collected by means of an Autolab PGSTAT302N and analyzed by the NOVA 2.1 software connected to the sample by Pt current collectors.



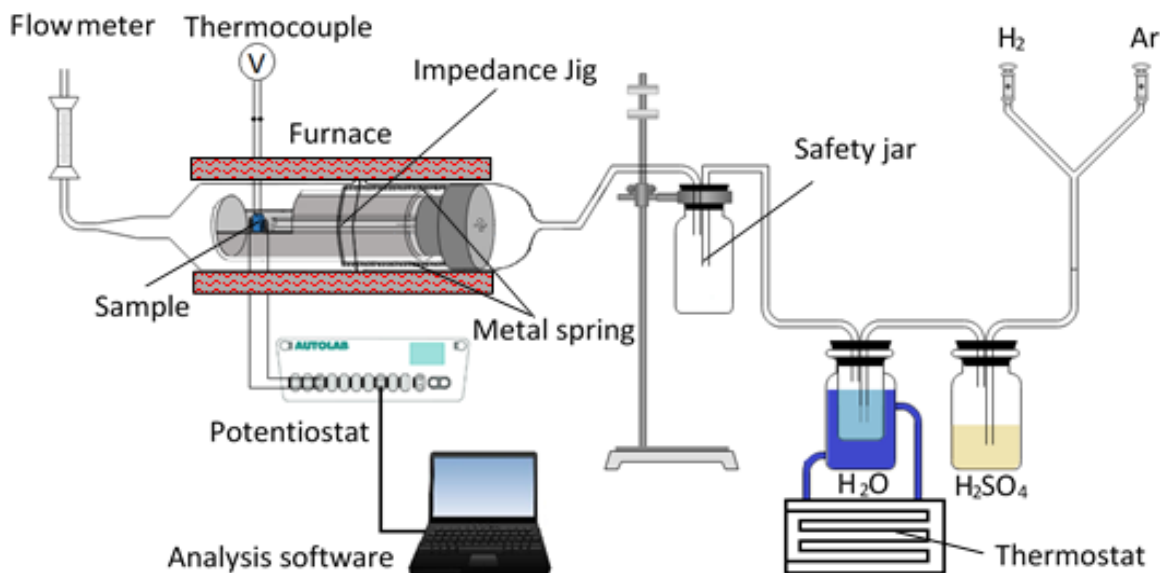


**Figure 2.5:** Experimental setup for the electrochemical impedance spectroscopy.

IS measurements were carried out over a temperature range from 200 °C to 600 °C. The excitation signal was an A.C. voltage of 50 mV and its frequency was varied from 10 MHz to 0.1 Hz. To allow the system to equilibrate, it was initially heated to 600 °C with a dwell time of 14 h. The IS measurements were performed during the cooling cycle in steps of 50 K with a cooling rate of 5 K/min and 1 h waiting time to ensure steady state conditions. All data were corrected for the geometry of pellets.

### 2.4.3 Data interpretation

Due to the nature of polycrystalline materials there are usually three arcs resolved in the Nyquist plot. Because the capacitances of each process are different (**appendix 8.5.3**), the semi-circles appear at different frequencies. The arc at the highest frequencies is attributed to the bulk material, the one at intermediate frequencies is attributed to the grain boundaries (GB) and one arc present at low frequencies is related to electrode behavior. In a first approximation the diameter of the arcs along the real axis is equal to the resistance. A simple model to determine the conductivity of polycrystalline materials is the “brick layer model” (see **figure 2.6**) [159, 160].

Polycrystalline materials consist of many irregular shaped grains of different sizes, separated by grain boundaries, **figure 2.6 a**. The “brick layer model” assumes all grains to be cubic, with a size  $D$  separated by identical grain boundaries of thickness  $\delta$ . Therefore, the resistances of every grain (also referred to as “bulk”) and grain boundary adds up to a total resistance of  $R_b$  and  $R_{gb}$ , respectively. In the case of the grain boundaries, however, the conductivity needs to be corrected for its microscopic geometry in addition to the macroscopic correction (equation 2.17). The reason for this is the unknown effective area which is related to the grain size  $D$ , and the thickness  $\delta$  of the grain boundary.

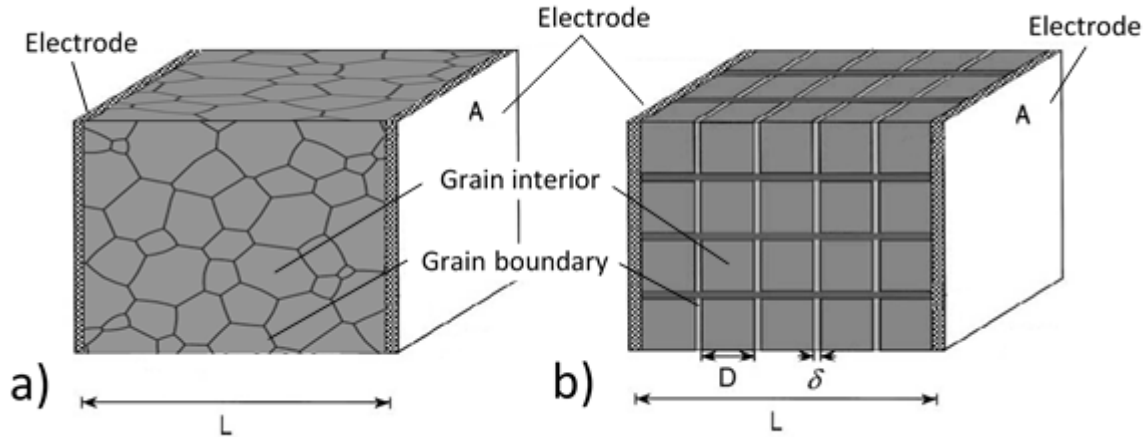


**Figure 2.6:**a) real sample microstructure b) microstructure assumed by the “brick layer model” [160].

However, a good estimation of  $D$  and  $\delta$  is given by the ratio of the capacitances of the bulk and the grain boundary, assuming the same dielectric constants for bulk and grain boundary:

$$\frac{C_{bulk}}{C_{gb}} = \frac{\frac{A}{L} \epsilon_{Bulk} \epsilon_0}{\frac{A D}{L \delta} \epsilon_{gb} \epsilon_0} = \frac{\delta}{D} \quad (2.19)$$

Then the specific (independent of microstructure) grain boundary conductivity is given by [159]:

$$\sigma_{gb,sp} = \frac{L}{A} \left( \frac{C_{bulk}}{C_{gb}} \right) \frac{1}{R_{gb}} \quad (2.20)$$

#### 2.4.4 Transport study for different oxygen partial pressures

For selected samples, impedance spectroscopy was also performed over a wide range of oxygen partial pressure under dry and wet conditions in order to characterize electronic conductivities [161]. The samples (area: 1 cm<sup>2</sup> and thickness: 1.3 mm) were coated with Pt-paste on both sides and mounted in a tube furnace sealed inside a quartz tube (see **appendix 8.5.5**). The setup was supplied with Ar/H<sub>2</sub> and Ar/O<sub>2</sub> mixtures for reducing and oxidizing conditions, respectively. Impedance spectra were recorded at 500 °C, 600 °C and 700 °C in dry and 3% moist gases over a frequency range from 10 Hz to 1 MHz by means of an Ivium CompactStat. The spectra were analyzed by the ZView software.

### 3 STRUCTURAL AND ELECTRICAL PROPERTIES OF BZCY72

#### 3.1 Investigation of precursor powders

The XRD patterns of the calcined (2 h at 1200 °C) BZCY72 precursor powders in **figure 3.1a** reveal a main perovskite phase for both powders. Fitted with  $R\bar{3}c$  symmetry, according to Mather et al. [124], the lattice parameters were observed to be  $a = 6.010(3)$  Å and  $c = 14.720(7)$  Å for the lab produced powder and  $a = 6.014(2)$  Å and  $c = 14.72(4)$  Å for the commercial powder. The crystallite size at 65(5) nm was smaller for the lab produced sample compared to 99(7) nm for the commercial sample. Small impurities of  $\text{BaCO}_3$  (PDF 00-044-1487) were found in the commercial sample (see also **appendix 8.6.1** and **8.6.2** for detailed report on the powder progression).

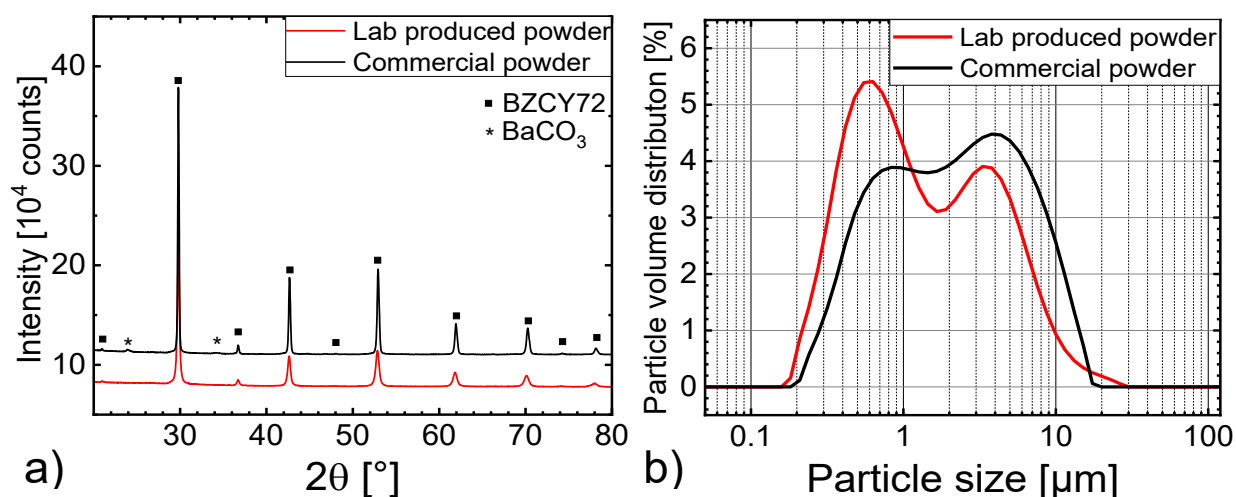


**Figure 3.1:** Comparison of commercial and lab produced BZCY72 precursor powders: a) XRD patterns of calcined powders. b) Particle size distributions of calcined powders.

The particle size distributions measured by SLS are shown in **figure 3.1 b**. Both powders are characterized by a bimodal distribution, with less distinction of the two peaks for the commercial sample. For the lab-produced powder, 90% of the particles exhibit sizes below 550 nm as opposed to 638 nm for the commercial produced powder. SEM images in **figure 3.2** confirm smaller particle sizes for the lab produced sample. The particles tend to agglomerate for both powders.

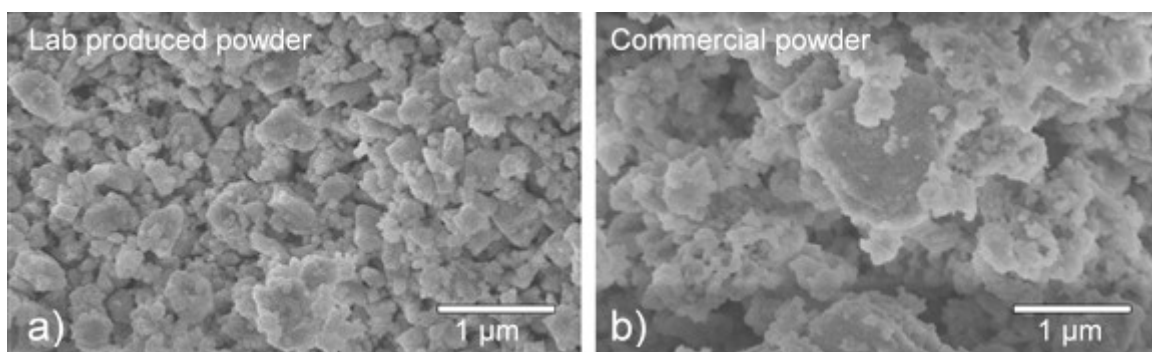


**Figure 3.2:** SEM images of the precursor powders after calcination: a) Lab produced b) Commercial.

### 3.2 Properties of sintered pellets

**Figure 3.3** shows the monitored SPS process for synthesis of the lab produced and commercial powder. As described in section 2.2, the process is divided into four stages. The relative piston position for both powders follows a similar trend during stage I as mechanical densification occurs due to particle rearrangement under increased pressure [74, 76]. Characteristic sample-related processes start to emerge in section II where thermal and electrical diffusion as well as gas evaporation leads to contraction or expansion of the powder.

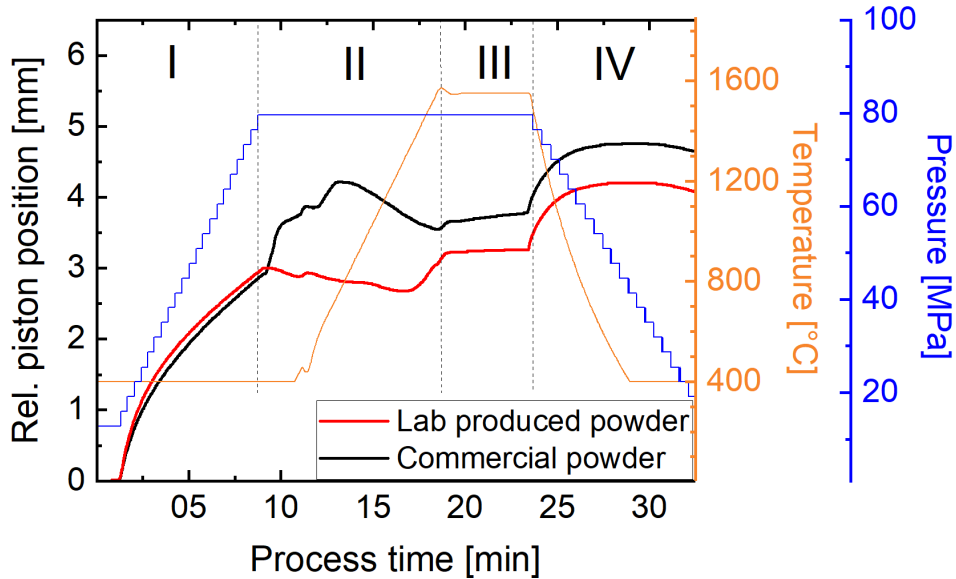


**Figure 3.3:** Pressure, temperature trace and plunger displacement as a function of process time. Vertical dotted lines separate the four distinguished phases of the sintering process.

The observed differences are most likely related to the different particle sizes of the powder, since smaller particles exhibit decreased bulk deformation [113]. On the other hand, the smaller particles, as present in the lab-produced sample, show increased mass transport phenomena, as proved by the increased piston position at higher temperatures [113]. Additionally, small particles result in higher total surface area which favors water absorption. During the heating stage, the lab produced sample seems to contract because the thermal expansion of the absorbed gases surpasses the densification by thermally activated volume diffusion until the gases eventually are vented due to the increased pressure. The commercial powder, on the other hand, rapidly densifies during the initial part of stage II, until the thermal expansion causes the piston to move backwards. The small peak visible in both graphs is due to a short stop of power supply caused by the control software and the PID controller. Further densification of both samples is achieved by lattice diffusion and grain boundary diffusion [53] during the isothermal-isobar section III. On this stage smaller grains will also evaporate and lead to grain growth [83]. During the final stage IV, both samples show a characteristic densification curve as the thermal contraction and simultaneous pressure release are the acting physical processes.

**Table 3.1:** Comparison of the BZCY72 pellets sintered by different methods.

Method	SPS lab produced	SPS commercial	SSRS	Conventional
Rel. density geometric	98.4 %	97.8 %	94 %	74 %
Rel. density Archimedes	99.7(8) %	98.6(8) %	95.5(7) %	81.2(9) %

After a surface polish the samples appear as pictured in **table 3.1**. The pellet prepared from lab-produced powder appeared black while the pellet made from commercial powder appeared beige-colored, with grey-colored graphite remaining from the die employed for the sintering process. The difference in color could be explained by a variation of oxygen nonstoichiometry as suggested by Anselmi-Tamburini et al.[162]. After a second calcination step, the sample color changed to brown. Both samples fractured into halves after their release from the graphite die by the hydraulic press. As expected for SPS prepared samples, the densification for both samples was near 100 % of the crystallographic density of  $6.2 \text{ g cm}^{-3}$  in agreement with other work [34, 100]. Small deviations between the different density determination methods suggest small amounts of open porosity.

Compared to the BZCY72 pellet prepared by the state-of-the-art SSRS method, which appears black due to the 1 wt% Ni content, the SPS method provides much higher densification. The difference to BZCY72 pellets prepared by conventional sintering to SPS prepared is significant and demonstrates a great advantage of SPS in fabrication of poorly sinterable ceramics.

As displayed in **figure 3.4**, the surfaces of the SPS pellets is inhomogeneous. Localized collected Raman spectra indicate that the mode at  $702\text{-}740 \text{ cm}^{-1}$  that represents the stretching of B-site octahedra is greatly enhanced going from the center position to the outer parts of the pellet (the analysis of Raman spectra for BZCY72 is covered in detail in chapter 4.1.2). Changing the oxidation state of a metal centre will affect the strength of metal ligand bonds and consequently the wavenumbers of the metal-ligand (M – O, M – N, M – S, M – P etc.) stretching modes [163]. Therefore, the modes with wavenumbers from  $680$  to  $800 \text{ cm}^{-1}$  are assigned to the presence of additional occurring phases exhibiting a higher  $\text{Ce}^{3+}$  oxidation state. There might also be some degree of segregation in the outer parts of the pellets for Ce, as reported before by Theunissen et al. [164]. However, the structure as shown by localized XRD is unaffected by the observed position, figure 3.4 b. The outer zone of the pellets may also exhibit larger amounts of  $\text{BaCO}_3$ , indicated by the mode at  $1060 \text{ cm}^{-1}$  arising with increasing distance from the center position. The inhomogeneous composition of the pellet is most certainly caused by the characteristics of the SPS processing. As pointed out by Guillon et al., temperature gradients within the sample alter the mass transport mechanisms [74]. For insulating samples, the temperature in the center region for cylin-

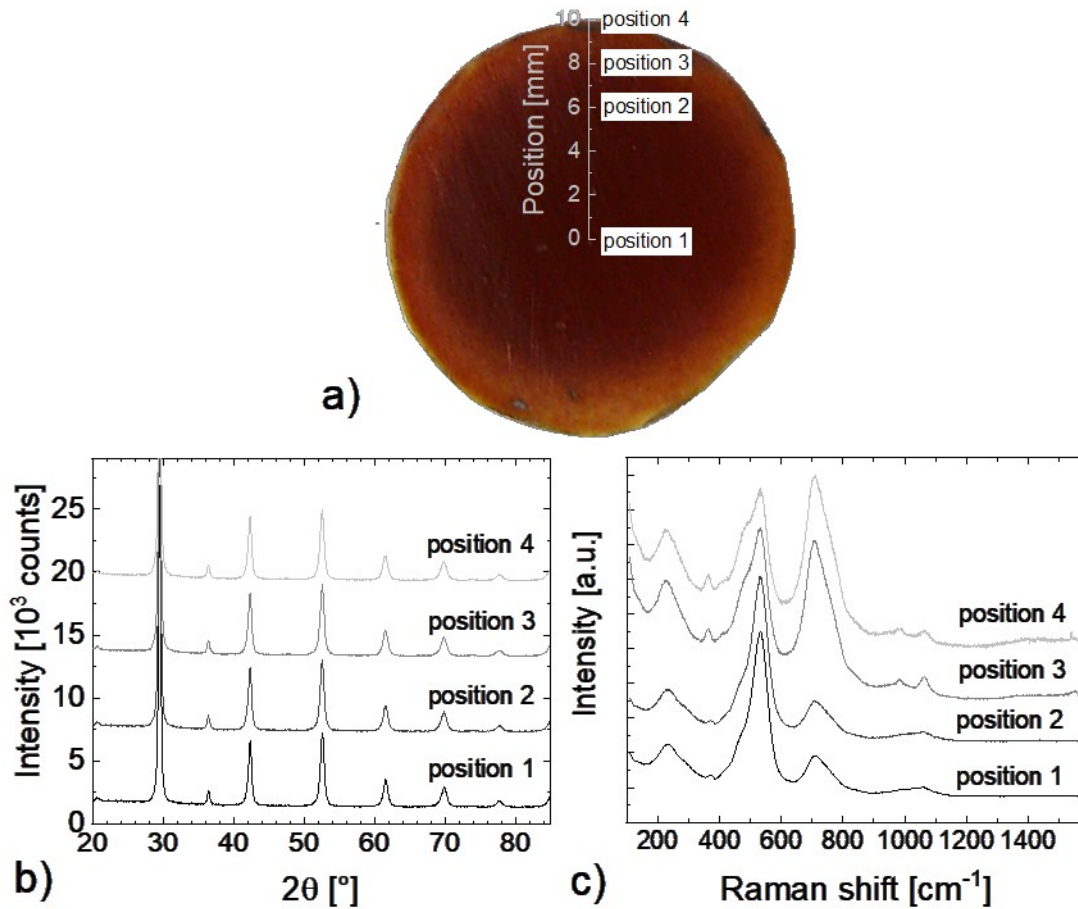


**Figure 3.4:** Investigation of the sintered pellet ( $T = 1350\text{ }^{\circ}\text{C}$ ,  $p = 76\text{ MPa}$ ) in dependence of the position. A) Picture and corresponding position; b) XRD pattern of the positions and c) their Raman spectra

drical samples is lower as compared to the outer parts. This difference is even visible to the unaided eye, as regions with presumable higher degree of reduction under given synthesis conditions and larger amounts of  $\text{Ce}^{3+}$  content appear brighter. For all further studies, the center part of the pellets ranging from position 1 to position 2 was employed for analysis since only neglectable structural variations were observed by Raman.

### 3.3 Crystallographic investigation

The X-ray diffraction patterns of the BZCY72 pellets are displayed in **figure 3.5**, with the structural details from the Rietveld refinement listed in **table 3.2** (see also **appendix 8.6.3** for the profile fittings). In all Rietveld refinements, the space group  $R\bar{3}c$  (#167) for the perovskite structure resulted in the best agreement between observed and calculated patterns. SPS samples prepared from lab-produced powder, however, contained a secondary Zr-richer perovskite phase, with an estimated content of 4 wt% (appendix 8.6.3 insert). For the pellet synthesized by SPS using commercial powder, only one main perovskite phase was obtained with good agreement between observed and calculated patterns. The  $\text{BaCO}_3$  impurity phase (PDF 00-044-1487) at  $2\theta = 24.3^{\circ}$



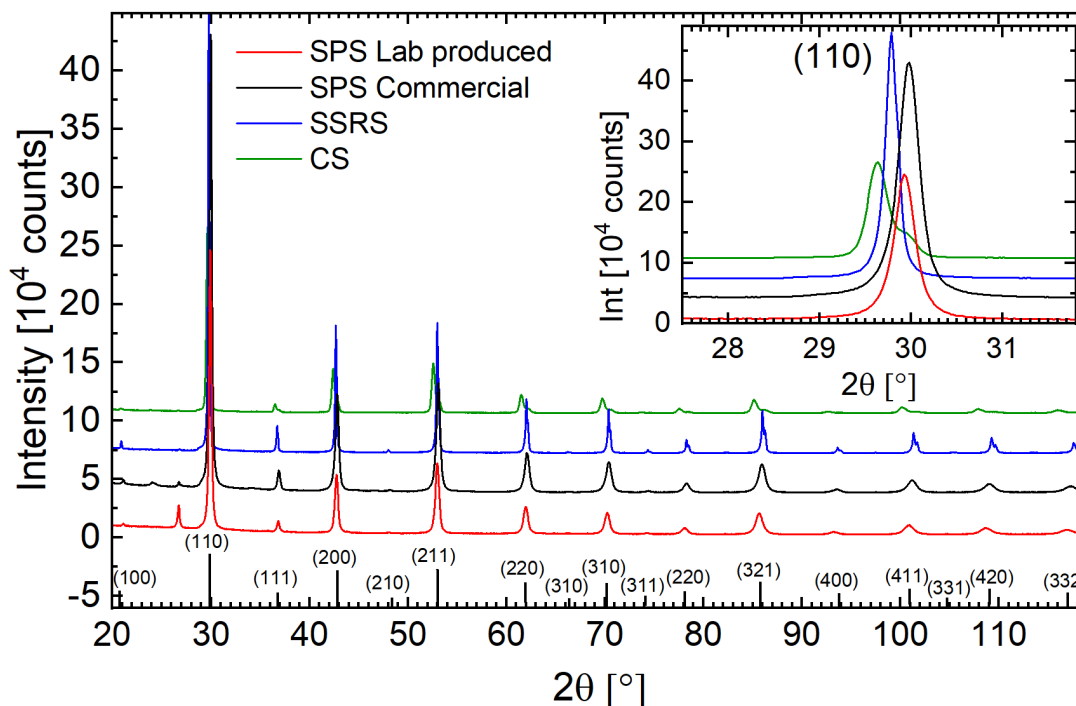


**Figure 3.5:** XRD patterns for ground up BZCY72 pellets prepared by different sintering methods. The detailed view is on the 110 reflection.

**Table 3.2:** Results of the Rietveld refinement (compare appendix 8.6.3) for BZCY72 prepared by different synthesis methods.

<b>Lab produced</b>		<b>Commercial</b>	
$\chi^2$	3.18	$\chi^2$	4.01
$R_{wp}$ [%]	4.96	$R_{wp}$ [%]	4.67
$a$ [Å]	6.010(2)	$a$ [Å]	5.994(1)
$c$ [Å]	14.716(9)	$c$ [Å]	14.715(2)
B – O bond length [Å]	2.131(1)	B – O bond length [Å]	2.127(1)
crystallite size [nm]	66(4)	crystallite size [nm]	77(4)
Occupancy $Ba^{+2}$	0.99(1)	Occupancy $Ba^{+2}$	1.00(2)
Occupancy $Zr^{+4}/Y^{+3}$	0.84(4)	Occupancy $Zr^{+4}/Y^{+3}$	0.78(4)
Occupancy $Ce^{+4}$	0.16(2)	Occupancy $Ce^{+4}$	0.22(2)
<b>Solid-State reactive sintering</b>		<b>Conventional sintering</b>	
$\chi^2$	5.18	$\chi^2$	5.20
$R_{wp}$ [%]	8.21	$R_{wp}$ [%]	8.50
$a$ [Å]	6.022(1)	$a$ [Å]	6.02712(17)
$c$ [Å]	14.718(3)	$c$ [Å]	14.715(2)
B – O bond length [Å]	2.134(1)	B – O bond length [Å]	2.136(2)
crystallite size [nm]	122(5)	crystallite size [nm]	80(9)
Occupancy $Ba^{+2}$	0.989(1)	Occupancy $Ba^{+2}$	0.984(2)
Occupancy $Zr^{+4}/Y^{+3}$	0.80(4)	Occupancy $Zr^{+4}/Y^{+3}$	0.81(5)
Occupancy $Ce^{+4}$	0.20(2)	Occupancy $Ce^{+4}$	0.19(3)

## Crystallographic investigation

was present in the commercial powder as well as in the SPS sintered pellet. The additional peak at  $2\theta = 26.8^\circ$  for both SPS prepared samples is attributable to the graphite foil used during the SPS process (PDF 00-041-1487). Peak ranges for both impurity phases,  $\text{BaCO}_3$  and graphite, were excluded from the Rietveld refinement.

For the conventionally prepared sample, however, two distinct separate perovskite phases were observed. It has been reported, that increased Ba-deficiency during conventional processing of BZY can lead to the splitting of the perovskite into two phases with the cubic perovskite structure [165, 166]. Following this finding, the same would be expected for BZCY72 due to its high Zr content.

As given in **table 3.2** and seen from the focus on the (110) reflection, the lattice parameters may depend on the fabrication route. The lattice parameters for the lab-produced sample were observed to be  $a = 6.010(2) \text{ \AA}$  and  $c = 14.716(9) \text{ \AA}$ , which is comparable to these of the precursor powder. However, the pellet fabricated from commercial powder exhibits lattice parameters of  $a = 5.994(1) \text{ \AA}$  and  $c = 14.715(2)$ , which are slightly smaller than values reported in the literature [41, 124]. Since the SPS densification process indicated different working mechanisms between the two samples, the aberration for the lattice parameters is likely caused during the heating stage. Both samples prepared by SPS show smaller lattice parameters due to the uniaxial pressure used by this technique which cause defects within the lattice [83]. Another reason for decreased lattice parameters could be oxygen losses from the reducing SPS environment, suggested by other authors [82, 167]. The lattice parameters obtained for the SSRS sintered sample are close to the values determined by Mather et al. using high resolution neutron diffraction after application of SSRS for BZCY72 sample preparation [124]. Since proton diffusion in  $\text{BaCeO}_3$  and  $\text{BaZrO}_3$  occurs by transfers between oxygen ions in the same  $\text{BO}_6$  octahedron, the O – B – O bond angle and B – O bond length were also calculated to allow for correlations between structure and electrochemical properties. According to Kreuer, higher symmetry and shorter B – O bond distances enhance the bulk protonic conductivity [66, 168]. As expected, the bond distance decreases as the lattice parameter get smaller since the position of the oxygen site does not change significantly between the fabrication routes, however, XRD only provides limited access to the O position.

Due to the shortest process times in the SPS route, there is almost no detectible Ba deficiency by XRD and no evidence of barium evaporation. On the other hand, for SSRS or conventional sintering the longer dwell times lead to barium evaporation as indicated by the Ba deficiency. During the SSRS, the Ni-BZCY72 eutectic phase can also cause repression of Ba [106]. For this reason, the latter fabrication processes are challenging and dwell times should not exceed 12 hours. Furthermore, the observed occupancies of the cations allow the calculation of the Goldschmidt tolerance factor according to equation 1.1 and the ionic radii from Shannon [29]. Values between 0.93 for the minor Ce-rich phase within the lab-produced SPS sample and 0.995 for the main lab-produced SPS sample confirms the  $R\bar{3}c$  space group for all present phases. The  $R\bar{3}c$  phase at high Ce-contents is also in agreement with Malavasi et al. [169].



### 3.4 Microstructure

SEM images confirm high microstructural densities for both SPS samples. The sample prepared from lab-produced powder appears to be close to fully densified (**figure 3.6 a**), whilst the sample prepared from the commercial powder still shows some small pores (**figure 3.6 b**). Grains are generally inhomogeneous in size and shape, indicating abnormal grain growth for both samples. Such heterogeneous microstructure is a typical consequence of the sintering mechanism that occurs in ceramics with a broad particle size distribution of the precursor powder where large seed grains consume neighboring small grains [83, 170, 171].

Presence of segregated phases are also known to cause abnormal grain growth. For the lab-produced sample, this may be caused by the presence of minor perovskite phase, whilst for the commercial sample, the presence and decomposition of  $\text{BaCO}_3$  impurities may cause further abnormalities in grain growth. From the SEM images, no evidence of neck formation is observed for samples prepared by SPS. Therefore, the dominating sintering mechanism is presumably the evaporation of small grains which is to be expected at high sintering temperatures [76, 172]. The grain sizes in the SPS samples range from 50 nm to 1.1  $\mu\text{m}$  and from 50 nm to 1.8  $\mu\text{m}$  for the lab produced and commercial sample, respectively, with the majority of grains found within the range of 300 to 600 nm. This difference in distributions is likely to arise from the different particle sizes of precursor powders. The generally small grain size range is in accordance with the literature on SPS samples [34, 173]. Due to short processing times applied in SPS ( $\sim 12$  min above 800 °C) the grain growth is limited. Diffusion effects linearly scale with process time and are therefore significantly enhanced in the SSRS and conventional process, **figure 3.6 c** and **d**. As displayed by the grain size distributions, the average grain is one order of magnitude larger for SSRS and still 3-4 times larger for conventional sintering, exhibiting average grain sizes of 5.25  $\mu\text{m}$  and 1.88  $\mu\text{m}$ , respectively. In the case of former, the sintering aid NiO enhances volume diffusion by the formed liquid phase [9, 98]. This has also a positive effect on the density compared to the conventional sintering process where large pores are present as already indicated by the relative density. **Appendix 8.6.4** shows the 3D surface representation of a fractured BZCY72 sample prepared by SPS (a) and SSRS (b) recreated by imaging under different tilting angles. Fracture always occurs at the grain boundaries. Hence, the surface of the SPS pellets is finer and offers more potential breaking points. This is also the reason why previous authors repeatedly reported on poor mechanical integrity of SPS prepared BZCY72 samples [48, 173].

Microstructure

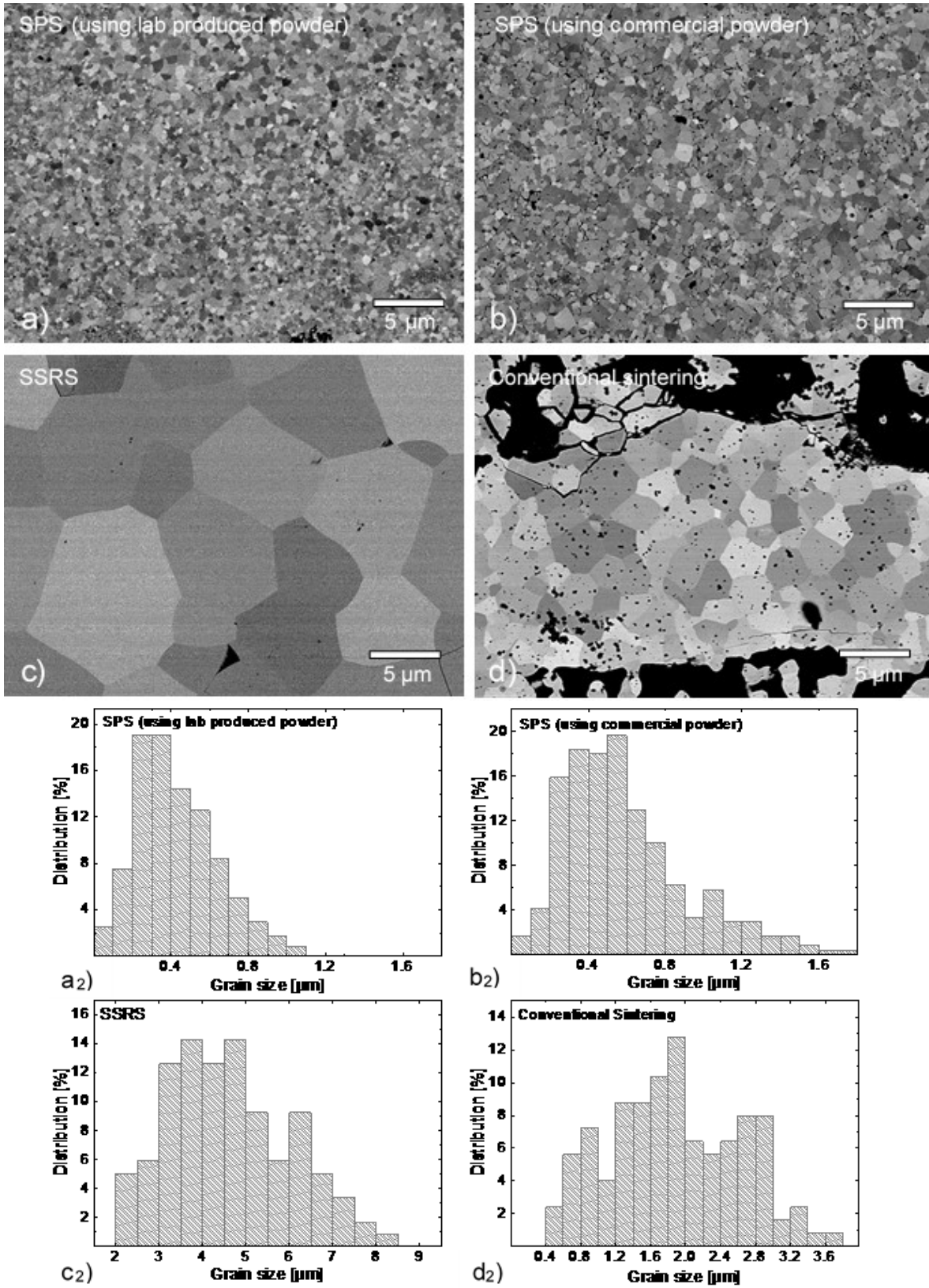


Figure 3.6: SEM images of polished cross section of pellets sintered by SPS including the corresponding grain size distributions a) SPS lab produced, b) SPS commercial, c) SSRS, d) conventional sintering

### 3.5 Electrical properties

A tabular and graphic representation of the BZCY72 sample data obtained by impedance spectroscopy at 350 °C in 3% H<sub>2</sub>O 5% H<sub>2</sub>/Ar atmosphere is presented in **table 3.3** and **figure 3.7**, respectively. For both SPS samples only two contributions are apparent, while for SSRS and conventional prepared samples the Nyquist plot is more complex. As explained in section 2.5.3, the contributions for the high and intermediate frequencies can be associated to the bulk and grain boundary regions. To confirm this hypothesis, the resistances and capacitances were calculated assuming a circuit of parallel RC elements.

The first ( $R_1C_1$ ) arc attributed to the bulk, as suggested by the calculated capacitance of  $C_1 \sim 10^{-11} \text{ F} \cdot \text{cm}^{-1}$ , is shown in more detail in **figure 3.7b**. The bulk resistance appears to be most dominant and broadest for the lab-produced sample, likely due to the poor homogeneity of the pellet (presence of the minor perovskite-like phase and associated deviation from nominal stoichiometry). Higher bulk resistance of BZCY72 prepared by SSRS and conventional sintering may be caused by Ba-deficiency as suggested by XRD data. The highest bulk conductivity was achieved by SPS using commercial powder. Therefore, SPS is fully capable of producing BZCY72 samples which exhibit high bulk conductivity, provided that homogeneous precursor powder is employed.

However, grain boundaries represented by the second ( $R_2C_2$ ) arc with  $C_2 \sim 10^{-9} \text{ F} \cdot \text{cm}^{-1}$  are significantly more distinct. As suggested by SEM, the grain size is comparably small corresponding to a high grain boundary density. For both SPS samples, grain boundary resistances were found to be around  $100 \text{ k}\Omega \cdot \text{cm}$ , with most resistive grain boundaries for the lab-produced sample. In contrast, the large-grained samples produced by SSRS and CS provide grain boundary conductivities that are about one order of magnitude higher. Space charge depletion layers have been proposed to explain the blocking behavior of grain boundaries in barium zirconates [37, 174, 175]. There is an excess of oxygen vacancies at the grain boundary core since this minimizes the energy of the mismatches between the two lattices. The core possesses a positive charge that repels any positive charge carriers creating a negative space charge layer [19, 176]. This effect can be partially reduced by Y segregation to the grain boundary core.

The third low frequency contribution ( $R_3C_3$ ) within the Nyquist plot is attributed to the electrode with typical capacities of  $C_3 \sim 10^{-6} \text{ F} \cdot \text{cm}^{-1}$  and higher [42, 159].  $R_3C_3$  is apparent for SSRS and CS samples, but dominated by the grain boundary contribution for pellets prepared by SPS. For the CS samples, the plateau shape of the plot at low frequencies is presumably caused by the porous nature of this particular pellet. Such porosities act as an additional phase, adding more overlapping contributions and rendering IS experiments impractical. At higher measurement temperatures (600 °C) there is increasing induction observed from the current collectors for all samples.

Dielectric constants of ca. 35 calculated for the grain interior are comparable for CS and SPS. The aberration for the SSRS could be caused by its deviating geometry compared to the other samples. Nevertheless, these values are in the same range as dielectric constants reported for BaZr<sub>1-x</sub>Y<sub>x</sub>O<sub>3- $\delta$</sub>  systems: 70-90 [174] and 30-90 [177].

Electrical properties

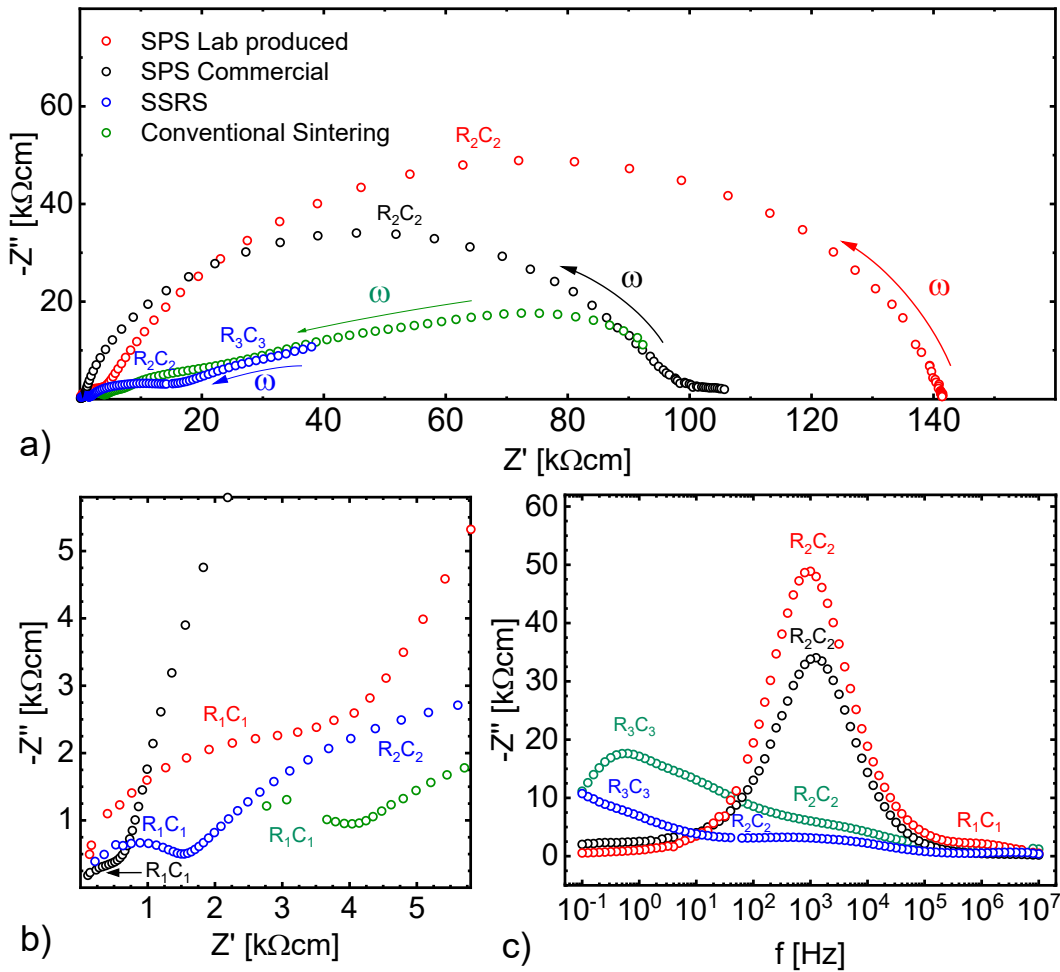


**Figure 3.7:** AC impedance spectroscopy data recorded at 350 °C in 3% H<sub>2</sub>O 5% H<sub>2</sub>/Ar atmosphere: a) Nyquist plot for all recorded frequencies, b) high frequency region, c) spectroscopic plot of  $Z''$

**Table 3.3:** Impedance data for pellets sintered at 350 °C in 3% H<sub>2</sub>O 5% H<sub>2</sub>/Ar atmosphere.

	SPS lab-produced	SPS commercial	SSRS	Conventional
$R_{Bulk}$ [kΩ · cm]	3.75	0.64	1.60	1.79
$R_{GB}$ [kΩ · cm]	137.95	97.83	7.82	7.79
$C_{Bulk}$ [F · cm <sup>-1</sup> ]	$2.93 \cdot 10^{-11}$	$8.4 \cdot 10^{-12}$	$2.88 \cdot 10^{-11}$	$1.69 \cdot 10^{-11}$
$C_{GB}$ [F · cm <sup>-1</sup> ]	$1.26 \cdot 10^{-9}$	$1.41 \cdot 10^{-9}$	$2.68 \cdot 10^{-9}$	$2.88 \cdot 10^{-9}$
$\epsilon_1$	39.7	34.5	49.3	34.4

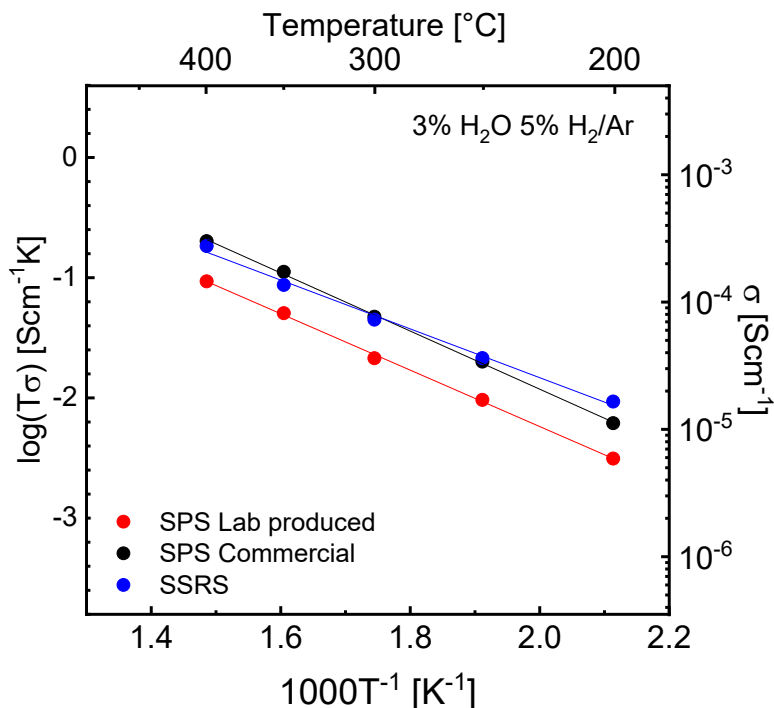


**Figure 3.8:** Arrhenius plot representation of the bulk conductivity as a function of temperature for the BZCY72 pellets prepared by SPS and SSRS in 3% moist 5% H<sub>2</sub>/Ar atmosphere.

**Figure 3.8** displays fairly linear Arrhenius plots of bulk conductivities in wet H<sub>2</sub>/Ar atmosphere, with calculated activation energies listed in **table 3.4**. For the commercial SPS sample, a higher bulk conductivity is observed as compared to the pellet using lab produced powder. The activation energies were found to be around 0.5 eV for both samples indicating that proton conduction is dominating the overall bulk conductivity [13, 42]. The small increase of bulk conductivity in the pellet that was prepared from commercial powder is in good agreement with the result of the TGA study described in detail within **appendix 8.6.5**, suggesting a higher overall concentration of oxygen vacancies and consequently protonic defects in this sample. This is further backed up by the increased pre-exponential factor  $A$  of the commercial sample, indicating the presence of a higher number of charge carriers, **table 3.4**. The lower activation energy for the sample prepared by SSRS is in agreement with previous studies by Ricote et al. where a bulk activation energy of 0.47 eV was reported [98], well within the range of protonic conductivity. Due to the larger pre-exponential factor it is also assumed that there are more charge carriers within SSRS prepared samples as a result of enhanced water uptake.

As already evident from **figure 3.7**, the specific grain boundary resistance is approximately two orders of magnitudes lower for both SPS prepared samples compared to the SSRS fabrication. For the grain boundary regions, higher activation energies around 1.0 eV were observed for both SPS pellets. Even higher values were found for SPS BZY10 samples by Wang et al. according to whom electronic conductivity contribution could cause high activation energies [33]. For the SSRS prepared sample the activation energy was observed to be 0.69 eV, which is lower compared to

values reported by Ricote et al. [98]. Possible explanations for the differences are related to the presence of additional insulating amorphous grain boundary phases, clustered defects and other non-stoichiometric impurities [176, 178, 179]. However, it should be noted that the grain boundaries are more mobile during the SPS process [85] and grain boundary heating might be preferred [88]. Both effects may therefore lead to an increase in activation energy as compared to SSRS.

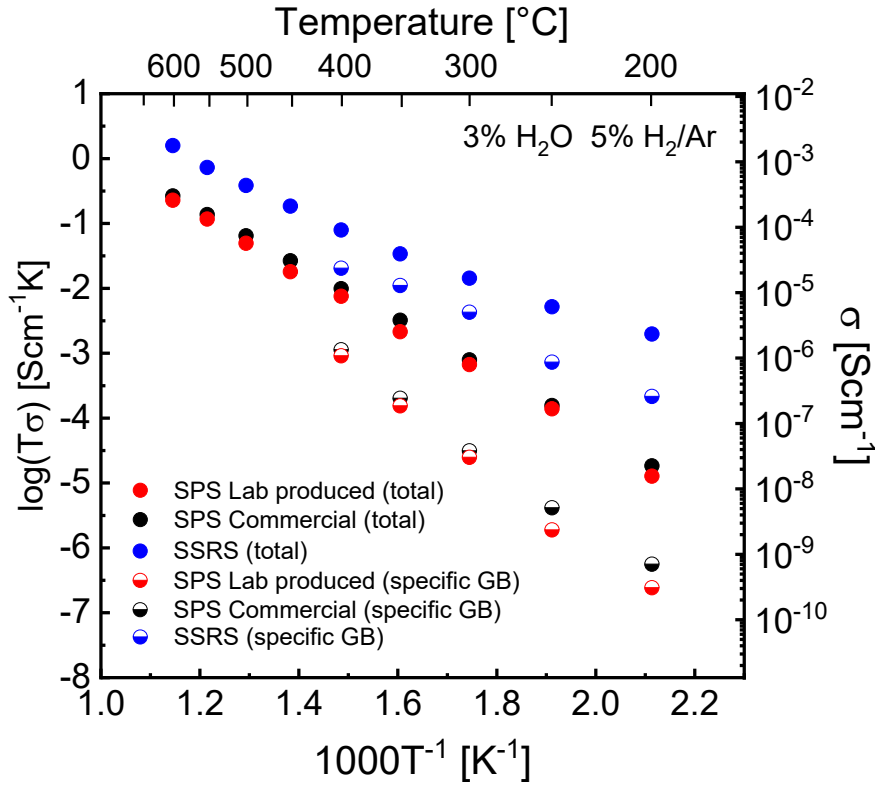


**Figure 3.9:** Total and specific grain boundary conductivity from impedance measurements on BZCY72 in 3% moist 5% H<sub>2</sub>/Ar atmosphere.

**Table 3.4:** Total conductivity, pre-exponential factor and activation energies determined from the Arrhenius plots on the BZCY72 pellets sintered by SPS and SSRS.

	SPS Lab produced	SPS commercial	SSRS
$\sigma_{total}$ at 600 °C	$2.58 \cdot 10^{-4} \text{ S} \cdot \text{cm}^{-1}$	$3.13 \cdot 10^{-4} \text{ S} \cdot \text{cm}^{-1}$	$1.82 \cdot 10^{-3} \text{ S} \cdot \text{cm}^{-1}$
pre-exponential factor, A	$1.64(5) \text{ S} \cdot \text{cm}^{-1}$	$1.97(3) \text{ S} \cdot \text{cm}^{-1}$	$3.46(8) \text{ S} \cdot \text{cm}^{-1}$
$E_A$ bulk	0.49(12) eV	0.51(1) eV	0.44(2) eV
$E_A$ specific grain boundary	1.12(6) eV	1.05(5) eV	0.69(4) eV

While the highest bulk conductivity was achieved for the SPS synthesis route using commercial powder, the total conductivity at 600 °C was observed to be seven times larger for the SSRS route. This gap increases for lower temperatures with two order of magnitude difference in conductivity at 200 °C. It must be considered that the blocking behavior of the grain boundaries is drastically reduced by the enhanced grain growth of time consuming methods [9]. To bypass this negative effect longer sintering times and a better thermal processing are mandatory.

### 3.6 Thermal expansion

The linear coefficient of thermal expansion (CTE) is usually defined as the change in lattice axis dimension assuming homogeneous expansion in all directions for polycrystalline materials [180]. For materials in high temperature fuel cell stacks the knowledge of the thermal expansion is essential since a difference between electrolyte material and electrode will cause thermal stress during operating and accelerate the ageing process of the system. The thermal expansion coefficient  $\alpha$  is expressed as contraction  $dL$  of an initial length  $L$  for a given change in temperature:

$$\alpha = \frac{1}{L} \frac{dL}{dT} \quad (3.1)$$

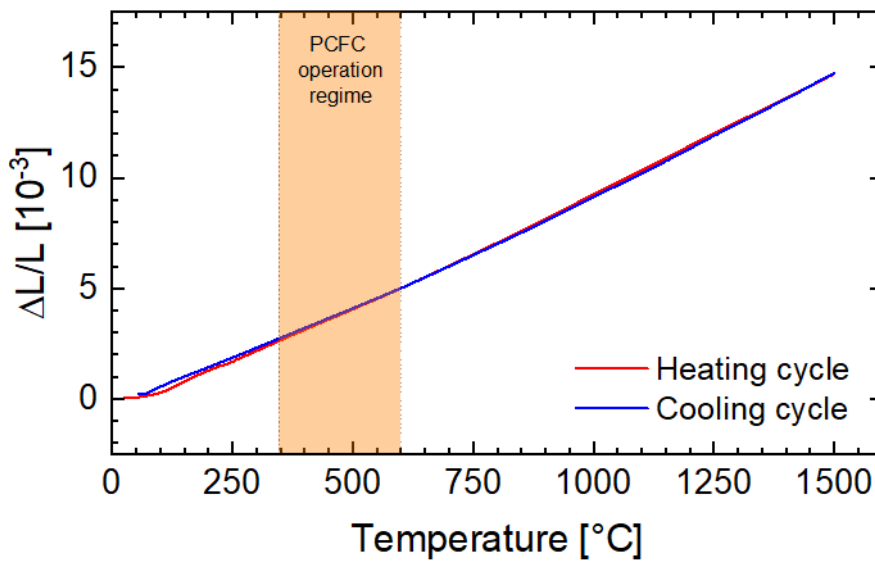


**Figure 3.10:** Dilatometry data of the BZCY72 sample prepared by SPS using commercial powder. Thermal expansion coefficients are displayed with the two temperature regimes on heating and cooling cycle. The measurement was performed on a Netzsch DIL 402C dilatometer using an  $\text{Al}_2\text{O}_3$  calibration standard.

As displayed in **figure 3.10**, the thermal expansion of BZCY72 does not follow a linear behavior. Instead, the thermal expansion coefficient varies depending on the temperature regime. From room temperature to 350 °C the CTE also differs for heating and cooling cycle, with values of  $9.10(6) \cdot 10^{-6} \text{ K}^{-1}$  and  $8.85(2) \cdot 10^{-6} \text{ K}^{-1}$ , respectively. The latter observation is caused by the additional chemical expansion on the heating cycle due to prior water uptake in laboratory air with sufficient humidity. In reality, the chemical expansion has also taken into account for the whole temperature range [180].

**Table 3.5** summarizes values for the CTE on similar systems. For the PCFC operating regime from 350 °C to 600 °C (highlighted area), a CTE of  $8.96(3) \cdot 10^{-6} \text{ K}^{-1}$  was determined, which is higher compared to the CTE reported by Hudish et al. employing in-situ high temperature XRD [180], **table 3.5**. Similarly, for the high temperature regime this aberration continues. The CTE obtained in this work are more comparable to Løken et al. who also used dilatometry [181]. To increase the accuracy on the CTE, a drying process in a vacuum chamber is therefore inevitable

## Thermal expansion

[182]. For the application, however, it should also be noted that the total expansion also includes a not neglectable chemical expansion contribution, since the material is always hydrated during operation.

**Table 3.5:** Comparison of thermal expansion coefficient for BZCY system with various literature values.

Material	Thermal expansion coefficient	Ref
BaZr <sub>0.8</sub> Y <sub>0.2</sub> O <sub>3-δ</sub>	9.65 · 10 <sup>-6</sup> K <sup>-1</sup> (100-800 °C)	[183]
BaZr <sub>0.9</sub> Y <sub>0.1</sub> O <sub>3-δ</sub>	8.80 · 10 <sup>-6</sup> K <sup>-1</sup> (100-800 °C)	[183]
BaZr <sub>0.9</sub> Y <sub>0.1</sub> O <sub>3-δ</sub>	8.78 · 10 <sup>-6</sup> K <sup>-1</sup> (30-1000 °C)	[182]
BaZr <sub>0.6</sub> Ce <sub>0.2</sub> Y <sub>0.2</sub> O <sub>3-δ</sub>	9.1 · 10 <sup>-6</sup> K <sup>-1</sup> (100-900 °C)	[184]
BaZr <sub>0.7</sub> Ce <sub>0.1</sub> Y <sub>0.2</sub> O <sub>3-δ</sub>	8.4 · 10 <sup>-6</sup> K <sup>-1</sup> (100-900 °C)	[184]
	9.64 · 10 <sup>-6</sup> K <sup>-1</sup> (25-350 °C)	
BaZr <sub>0.7</sub> Ce <sub>0.2</sub> Y <sub>0.1</sub> O <sub>3-δ</sub>	7.77 · 10 <sup>-6</sup> K <sup>-1</sup> (350-600 °C)	[180]
	8.76 · 10 <sup>-6</sup> K <sup>-1</sup> (600-1000 °C)	
	8.5(3) · 10 <sup>-6</sup> K <sup>-1</sup> (100-750 °C) Rate: 1 K/min	
BaZr <sub>0.7</sub> Ce <sub>0.2</sub> Y <sub>0.1</sub> O <sub>3-δ</sub>	8.5(2) · 10 <sup>-6</sup> K <sup>-1</sup> (170-750 °C), Rate: 10 K/min	[181]
	9.3(3) · 10 <sup>-6</sup> K <sup>-1</sup> (750-1000 °C)	
	9.10(6) · 10 <sup>-6</sup> K <sup>-1</sup> (25-350 °C)	
BaZr <sub>0.7</sub> Ce <sub>0.2</sub> Y <sub>0.1</sub> O <sub>3-δ</sub>	8.96(3) · 10 <sup>-6</sup> K <sup>-1</sup> (350-600 °C)	This work
	10.84(6) · 10 <sup>-6</sup> K <sup>-1</sup> (650-1500 °C)	



## 4 CORRELATION BETWEEN SPS PARAMETERS AND PROPERTIES OF BZCY72

### 4.1 Influence of sintering temperature and pressure

According to the literature on the SPS method, the sintering temperature as well as the applied pressure are the most influencing parameters for most materials [74, 76, 85]. Since the working pressure effects depends on the sintering temperature, the following section will cover both parameters combined. Since the IS measurements in the previous chapter provided better results for the commercial powder all following experiments are based on the commercial powder. The heating rate in this chapter was always maintained at 150 K/min and the holding time kept at 5min.

#### 4.1.1 Densification and pellet stability

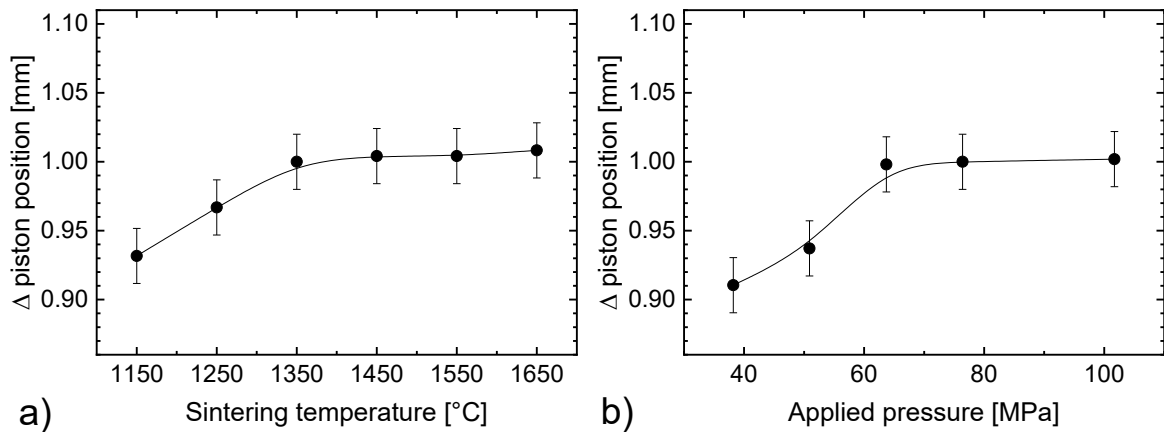


**Figure 4.1:** The normalized piston position in respective to the standard conditions ( $T = 1350$  °C,  $p = 76$  MPa): a) in relation to the sintering temperature, b) in relation to the applied pressure.

The maximal piston displacement ( $\Delta$  piston position) in **figure 4.1** provides relevant information on the densification of the sample [19]. It describes the difference between the starting position and end position of the upper punch, as described in section 2.1.3. For a better comparison,  $\Delta$  piston position was normalized to the standard parameters (section 2.1.4). The detailed trace of the piston position during the SPS process is shown in **appendix 8.7.1**. Increasing the maximal sintering temperature from 1150 °C to 1350 °C causes the maximal piston displacement to increase, meaning that the samples are likely to show a higher relative density. A similar trend can be observed for the applied pressure from 40 to 60 MPa. Only one noticeable difference can be observed upon varying the sintering temperature. It is mainly seen during stage III and stage IV, and results from the increase of thermal expansion or contraction with higher temperatures, respectively. Other minor differences in Stage II are attributed to varying particle size distributions in the precursor powder. In other words, there is no evidence for different diffusion processes during SPS when changing maximum sintering temperatures for BZCY72. Regarding the variations of the applied pressure, the differences in  $\Delta$  piston position are observed during stage I. Mechanical densification mostly occurs in this stage. Naturally by increasing the pressure, more powder agglomerates break resulting in reduced pore size [74].

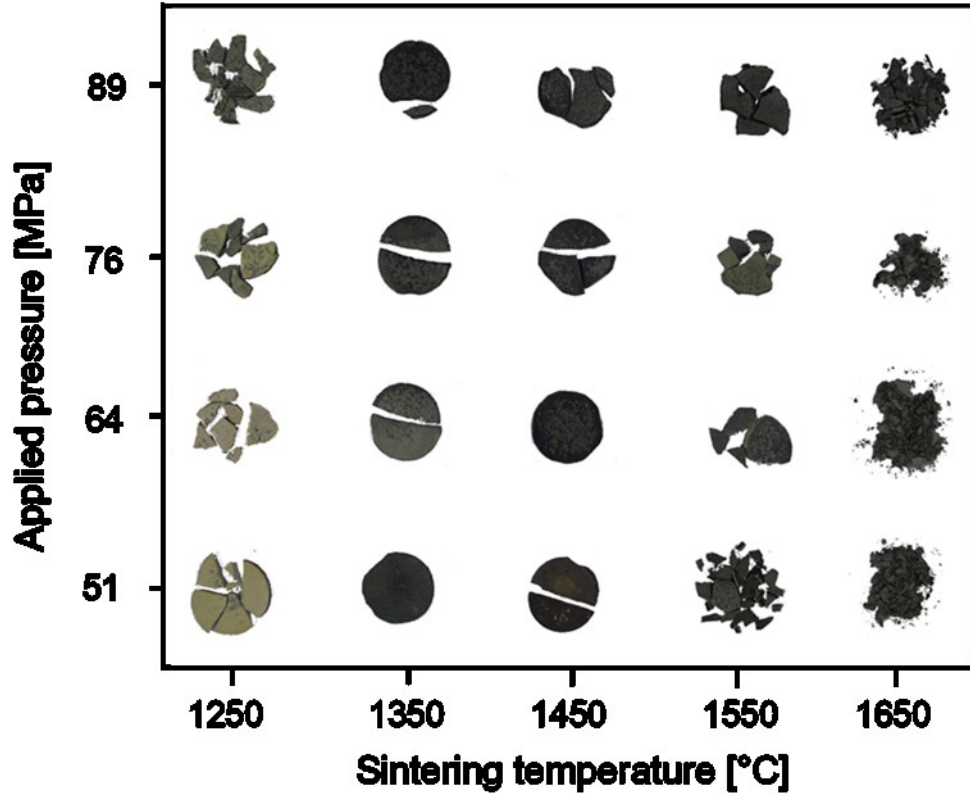
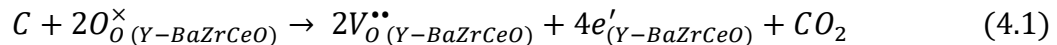


**Figure 4.2:** Photographs of the first set of BZCY72 pellets 24 h after the SPS processing. Pellets sintered at 1350 °C and 1450 °C were observed to exhibit higher stability in ambient atmosphere.

During the final stage IV and at higher applied pressures, samples mechanically expand during the release of the pressure. This is an indication of structural changes within the crystal.

From the appearance of the SPS pellets, a clear picture of the mechanical integrity depending on the SPS parameters emerges, **figure 4.2**. Pellets that were produced at 1350 °C and 1450 °C appeared to be stable in ambient laboratory environment. The difference in sample color from beige to black is related to the reduction of  $Zr^{4+}$  and  $Ce^{4+}$  at temperatures of 1350 °C and above in carbon rich environments according to the following reaction [37]:



In addition pellets disintegrated during the post sintering heat treatment directly after the pellets were released from the mold, due to the reduced internal stress during the re-oxidation of the B-site cations [164].

The long-term stability of the samples over a period of 12 months can be observed in **appendix 8.7.2**. Higher temperatures, especially i.e. 1550 °C, always resulted in complete degradation of the samples. According to Bu et al. this is a result of  $Ce^{4+}$  reduction which causes significant internal strain due to the higher ionic radius of  $Ce^{3+}$  [99, 185]. This effect is greatly emphasized within **appendix 8.7.3**, where the  $Ce^{3+}$  is visible by light microscopy as growing brighter yellowish regions at increased temperatures. The effects of internal strain become apparent for samples sintered at 1650 °C, with the presence of cracks resulting in disintegration of pellets.

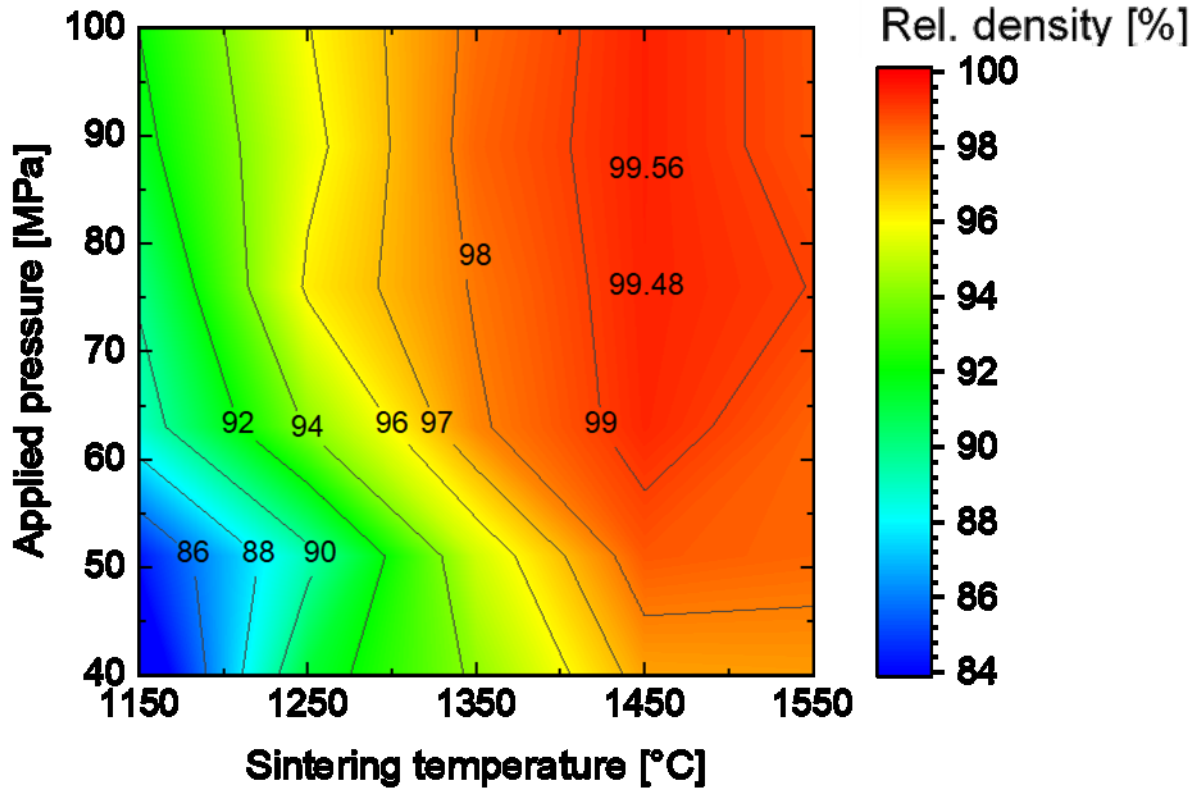


**Figure 4.3:** Relative density of SPS BZCY72 in relation to sintering temperature and applied pressure under conditions applied.

The applied pressure had no noticeable effect on the mechanical integrity of the sample, however, higher pressures lead to increased compaction of the sample within the die and consequently more force was required to release the pellet, where the latter broke apart. For temperatures around 1350 °C and 1450 °C, most samples remained intact over a period of 12 months.

Relative densities determined by Archimedes' method are shown in **figure 4.3**. There was no significant difference between densities determined by geometric method and Archimedes' method. As already indicated by **figure 4.1**, density generally increases with temperature and pressure. However, at sintering temperatures of 1550 °C and higher this trend seems to slightly reverse, most likely related to degradation. At lower temperatures the applied pressure has a distinct impact on the relative density. The highest density in this sample matrix ( $99.56 \pm 0.08$  %) was measured on samples prepared at 1450 °C and 89 MPa. Results from **figure 4.3** are in excellent agreement with the literature for SPS prepared BZCY, ranging from 92.4 % (Wang et al., 1400 °C, 4 MPa) to 99.8 % (Ricote et al., 1700 °C, 100 MPa) [33, 34, 99, 100, 174, 186].

As previously discussed, the SPS process leads to significantly higher densifications compared to other sintering techniques. For example the relative density of conventionally at 1650 °C [41] sintered samples is archived by SPS at 1150 °C under 64 MPa. Densities achieved in SSRS at 1550 °C [42] are exceeded in SPS processing at 1350 °C and 76 MPa. Conventionally sintered pellets with high densification (99.7 %) were fabricated at extremely high temperatures of 1850 °C in a vacuum furnace [187], resulting in samples with severe barium loss.

### 4.1.2 Crystallographic structure

The  $R\bar{3}c$  structure model described in section 3 was applied for the Rietveld refinement [124]. Due to rhombohedral distortion, peak splitting of fundamental reflection occurred at higher  $2\theta$ . An exemplary Rietveld refinement is shown in **appendix 8.7.4** which also holds additional information for all refined patterns. For all samples  $\chi^2$  was calculated between 2.1 and 2.8 and  $R_{wp}$  values were between 4.0 % and 5.3 %, indicating sufficient goodness of fit.

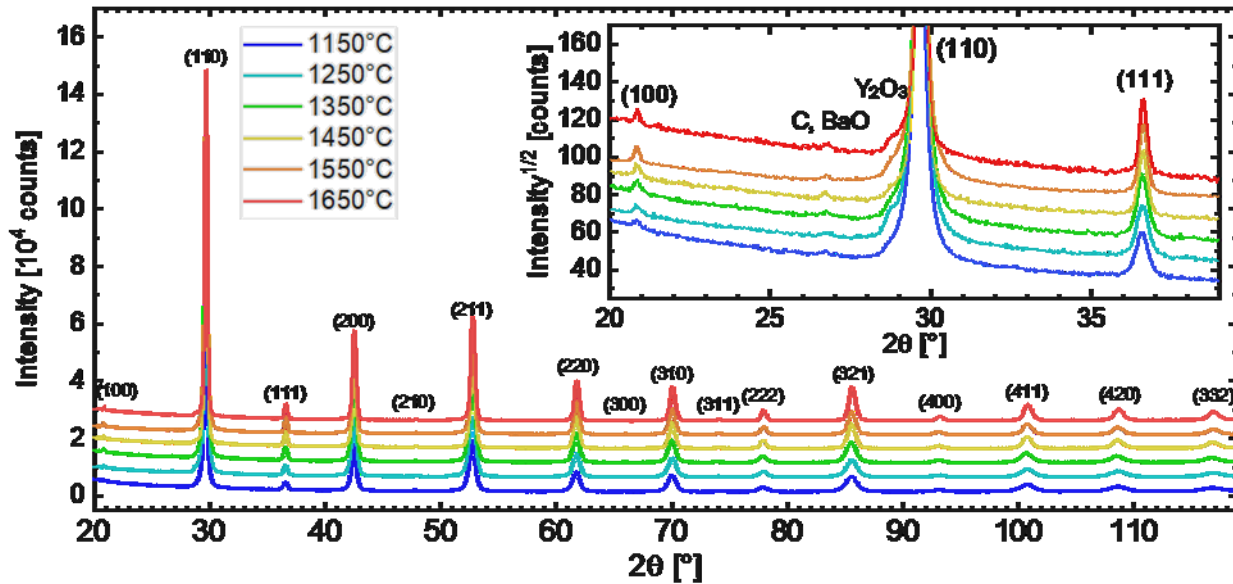


**Figure 4.4:** XRD patterns of the BZCY72 samples (vertically shifted) prepared by SPS at various sintering temperatures from 1150 °C to 1650 °C. The insert displays a close view on the impurities.

The XRD patterns for the investigation on the sintering temperatures are displayed in **figure 4.4**. Traces of carbon,  $Y_2O_3$  and BaO were found in samples independent of the sintering temperatures. Since small amounts of  $BaCO_3$  was already present in the precursor powder, the minor BaO phases (PDF 01-078-5719) can form without Ba deficiency of the perovskite. The latter was not observed even at temperatures where traditional methods show significant Ba loss at 1650 °C. The highest phase purity is observed for samples SPS processed at a temperature of 1350 °C. The small shoulder before the (110) reflex at  $2\theta \sim 29^\circ$ , as clearly shown from the insert, could be assigned to  $Y_2O_3$  (PDF 00-041-1105).

**Figure 4.5** presents crystallographic properties as a function of the sintering temperature. There is no evidence for a clear relation to the lattice parameters. This seems to be in contradiction to Wang et al. [33] who reported increasing lattice parameters for higher sintering temperatures for SPS prepared  $BaZr_{0.9}Y_{0.1}O_{3-\delta}$ . However, they used a lower calcination temperature. **Figure 4.5b** shows that the crystallite sizes increase with rising temperature, following an exponential crystallite growth. This is expected from the description of crystallite growth and the reaction rate which is an exponential function of the temperature and in agreement with the literature [188-191].

CORRELATION BETWEEN SPS PARAMETERS AND PROPERTIES OF BZCY72

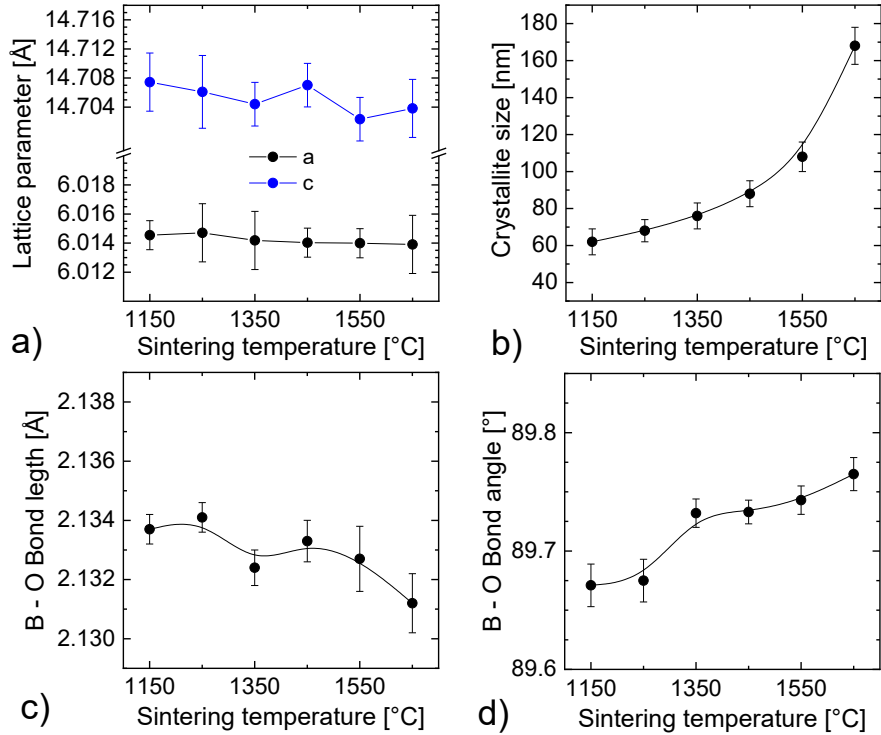


**Figure 4.5:** Results for crystallographic parameters observed from Rietveld refinement: (a) Lattice parameters, (b) crystallite size, (c) B – O distance and (d) B – O – B angle in relation to sintering temperature.

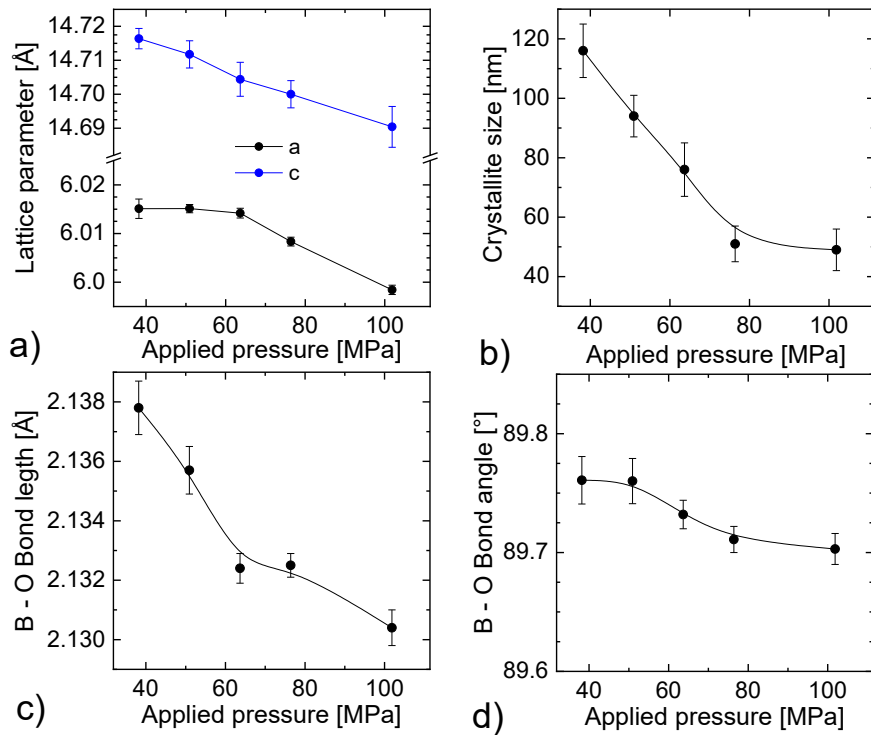


**Figure 4.6:** Results for crystallographic parameters observed from Rietveld refinement. (a) Lattice parameters (b), crystallite size, (c) B – O distance and (d) B – O – B angle as a function of applied pressure.

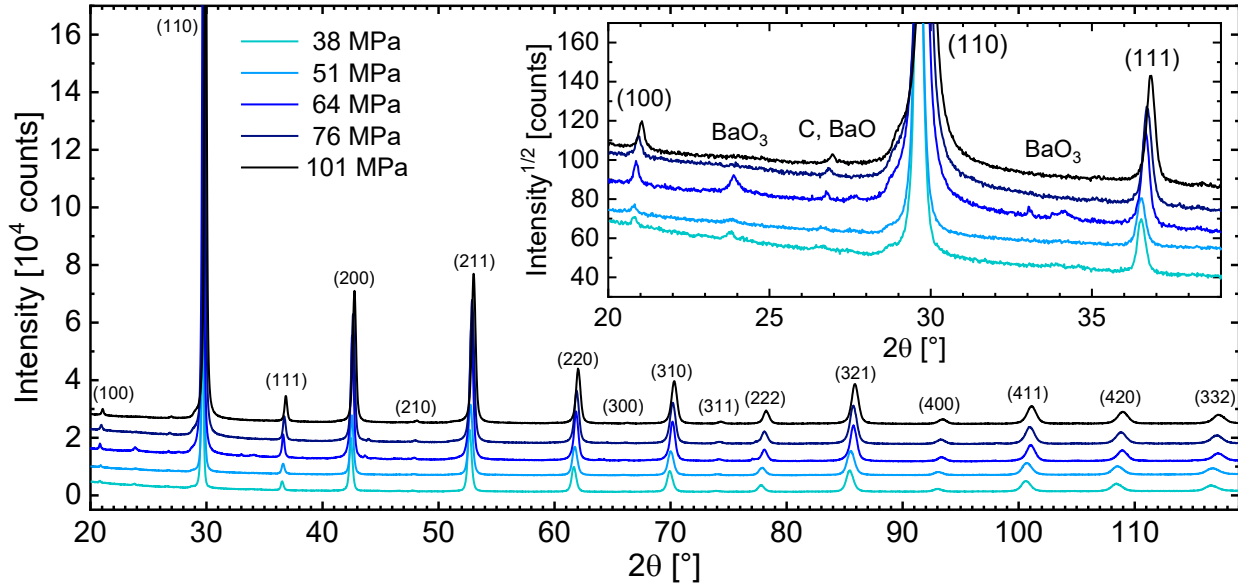


**Figure 4.7:** XRD patterns of the SPS BZCY72 (vertically shifted) prepared at different applied pressures from approximately 38 MPa to 101 MPa. The insert displays a close view on the impurities and peak shift.

The B – O bond distance slightly decreases while the B – O bond angle increases with increasing the sintering temperature, **figure 4.5c,d**. In other words, the  $\text{BO}_6$ -octahedra are slightly less tilted as the sintering temperature increases (i.e. higher symmetry).

The BZCY72 crystallographic parameters as a function of the applied pressure are displayed in **figure 4.6** and the XRD pattern in **figure 4.7**. Here, the additional  $\text{BaCO}_3$  impurity is not related to the particular pressure but result from a different batch of BZCY72 delivered by Cerpotech. Other impurities are the same as found upon the previous investigation. The lattice parameter decreases with increasing pressures as the perovskite reflexes shift towards higher  $2\theta$  values. As covered in section 3.3, the applied pressure in SPS seems to have a shrinking effect on the final unit cell volume. The same trend was found for ZrC-Mo cermet by Yung et al. [192]. An explanation is the formation of lattice defects under high pressure that cause smaller unit cells, which is also supported by increased micro strain for high pressures, as shown in **appendix 8.7.4**. During the SPS process there are situations where the unit cell is compacted under the pressure. However, this is an elastic phenomenon and is reversed as soon as the pressure gets released which is evident from **appendix 8.7.1** especially at 101 MPa. The crystallite size also decreases with the applied pressure. As the particles begin to rearrange and break down in the initial sintering stage, they also grind each other during this process which causes smaller crystallite sizes [83]. This effect is proportional to the mechanical force and has a maximum depending on the particle size which also explains why the crystallites stagnate in size at higher pressures. Both the B – O bond distance and B – O bond angle decrease for increased pressure as a direct result of the smaller unit cell (**figure 4.6c** and **d**). The compression of the unit cell therefore leads to increasing tilt angles and reduced symmetry. Within this study the space group and the tilt system  $a^-a^-$  is not affected, since the investigated pressures are nearly sufficient to induce a phase transition. According to Vogt et al. who investigated  $\text{LaCoO}_3$  (also  $R\bar{3}c$  space group) under high pressures, such transition occurs in pressure ranges in the order of several GPa [193].

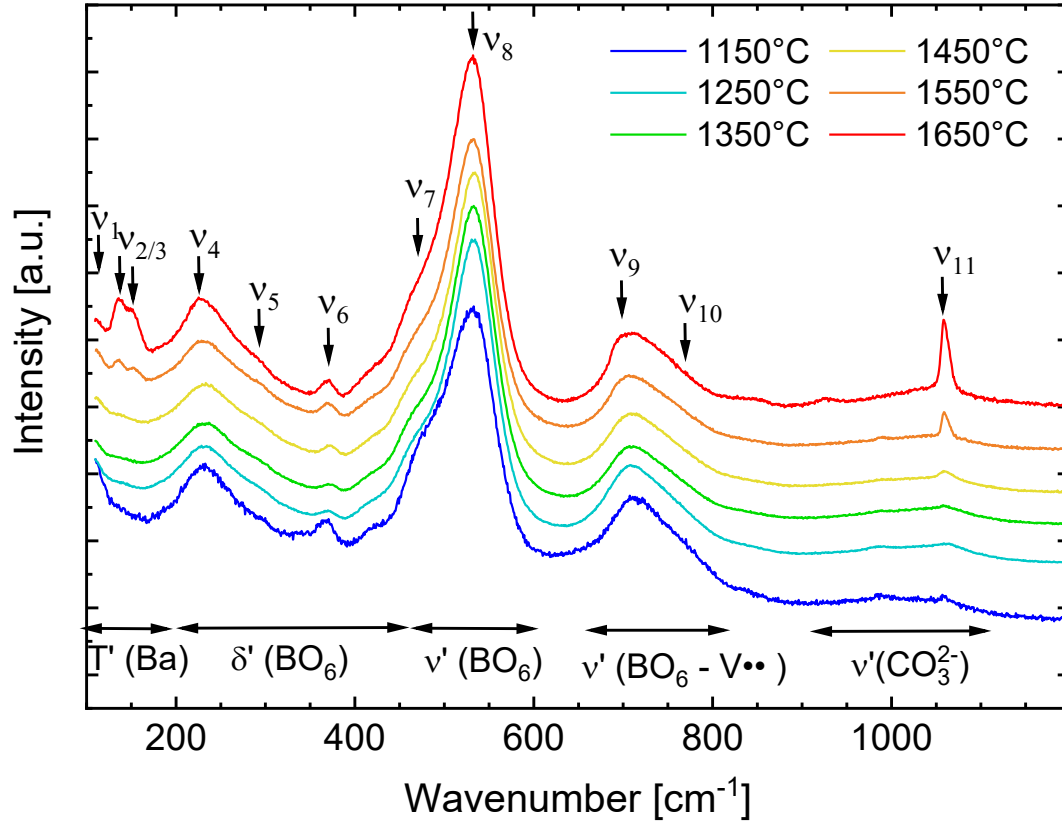


**Figure 4.8:** Raman spectra for SPS BZCY72 pellets for different maximal sintering temperatures. All major modes are indicated and described in the text.

A complementary structural Raman study is presented in **figure 4.8** for different maximum sintering temperatures: all spectra look similar showing the main phase BZCY72. Nevertheless, modes from increasing  $\text{BaCO}_3$  arise in the spectra from samples sintered at higher temperatures due to higher excess Barium ( $\nu_1$ ,  $\nu_2$ ,  $\nu_{11}$ ). A detailed analysis with corresponding peak attributes is given in **appendix 8.7.5**. Recalling from section 1.4, the structure is composed of a covalent-bonded sub-lattice formed by  $\text{BO}_6$  octahedra (where  $\text{B} = \text{Zr, Ce, Y}$ ) and a Coulomb dominated Ba cation sub-lattice. The wavenumber region below  $200 \text{ cm}^{-1}$  is dominated by the translational oscillation modes of the Ba cations, such as Ba – O stretching and O – Ba – O bending [194, 195]. Moreover, according to Charrier-Cougoulic et al. the  $R\bar{3}c$  structure is confirmed by only one band in the low wavenumber regime at  $\nu_1 = 100 \text{ cm}^{-1}$  [194], which is unfortunately out of the measurement range of the used setup. The following middle range shows characteristic symmetric stretching bands ( $200 - 400 \text{ cm}^{-1}$ ) and bending bands ( $400 - 600 \text{ cm}^{-1}$ ) for the  $\text{BO}_6$  octahedra [196]. In the BZCY72 system the structure consists of three types of different octahedra which all contribute to rather broad Raman modes, because of their interactions among each other [195]. Consequently, nanodomains with different symmetries are known to arise in perovskite materials [195]. The Raman mode at  $\nu_4 = 230 \text{ cm}^{-1}$  does not appear in pure BCY systems and is therefore assigned to the Zr – O bending mode [40]. A minor mode of  $\nu_6 = 368 \text{ cm}^{-1}$  is likely to be related to the Y – O bending mode [47]. The most intense mode  $\nu_8 = 534 \text{ cm}^{-1}$  is attributed to the  $\text{ZrO}_6$  octahedra stretching which is accompanied by a shoulder at lower wavenumber related to the  $\text{CeO}_6$



octahedra stretching mode. This is a result of the  $\text{Ce}^{4+}$  ions being heavier than the  $\text{Zr}^{4+}$  ions [40]. The Raman vibration at  $\nu_9 = 702 \text{ cm}^{-1}$  is related to the oxygen vacancies. According to Slodczyk et al. this doublet is assigned to the Zr – O bonds disturbed by a nearby vacancy [196]. Another origin of this mode might be the partial reduction of  $\text{Ce}^{4+}$  where the different oxidation state affects the strength of the metal ligand bond and thus, the stretching mode. At higher sintering temperatures, the presence of  $\text{BaCO}_3$  is indicated by mainly the lattice modes  $\nu_2 = 135 \text{ cm}^{-1}$  and  $\nu_3 = 149 \text{ cm}^{-1}$  [197]. For higher wavenumbers an additional symmetric stretching of the  $\text{CO}_3^{2-}$  anion of the  $\text{BaCO}_3$  structure can be observed at  $\nu_{11} = 1060 \text{ cm}^{-1}$  [197].  $\text{BaCO}_3$  does not show up in the XRD patterns, presumably either due to the amorphous nature of this phase or too small amounts to be detected.

The Raman spectra collected for samples prepared at different applied pressures are shown in **appendix 8.7.6**. All present modes are already discussed above. It is apparent that the applied pressure during SPS has no strong effect on the BZCY72 modes. Only minor peak shape changes are most likely the result of the changing unit cell size suggested by XRD. At high pressure  $\text{BaCO}_3$  is present, however, there is no evidence this is related to the parametrization of the SPS process.

### 4.1.3 Microstructure

From results for density and stability in chapter 4.1.1, it is apparent that the BZCY72 microstructure is strongly affected by the sintering temperature and applied pressure. **Figure 4.9** presents exemplary SEM-images for the material sintered at various maximal sintering temperatures and pressures. In addition, the grain size distributions for a set of temperatures and pressures are summarized in **figure 4.10**. Samples prepared at low sintering temperatures show intergranular pores, which shrink with increasing temperatures and pressures in agreement with observed increase of relative densities. Microscopically dense samples appearing can be obtained at  $1350 \text{ }^\circ\text{C}$ , which is in agreement with results by Bu et al. [99]. For higher temperatures, small pores appear again. Presumably, the temperature is high enough to evaporate small nanograins or gas is trapped within in the material. Furthermore, small cracks are present within the samples processed at  $1550 \text{ }^\circ\text{C}$  and  $1650 \text{ }^\circ\text{C}$ . The fractures always occur along the grain boundaries and eventually lead to premature degradation as already discussed.

As expected, the grain sizes remain comparably small due to the limited process time (chapter 3.4). Typical mean grain sizes observed for samples prepared at lower sintering temperatures are between  $190 \text{ nm}$  and  $290 \text{ nm}$ . Higher sintering temperatures lead to larger grains, averaging  $500 \text{ nm}$ , but also to wider grain size distributions. Comparable to the crystallite size, the grain growth is exponential to the sintering temperature as mass transport across the grain boundaries requires high activation energy [83, 198]. At lower temperatures, atomic diffusivity occurs along the grain boundary in form of surface diffusion, which is responsible for high relative densities at comparably low temperatures [89]. As the maximum sintering temperatures increases, the acting diffusion mechanism change in favor of volume diffusion and/or grain boundary diffusion. Those mechanisms allow for net atomic diffusivity between grains, leading to grain growth [83]. Typical for SPS ceramics, there is no distinct neck formation between particles [93], since no to little current is running through the samples.



## CORRELATION BETWEEN SPS PARAMETERS AND PROPERTIES OF BZCY72

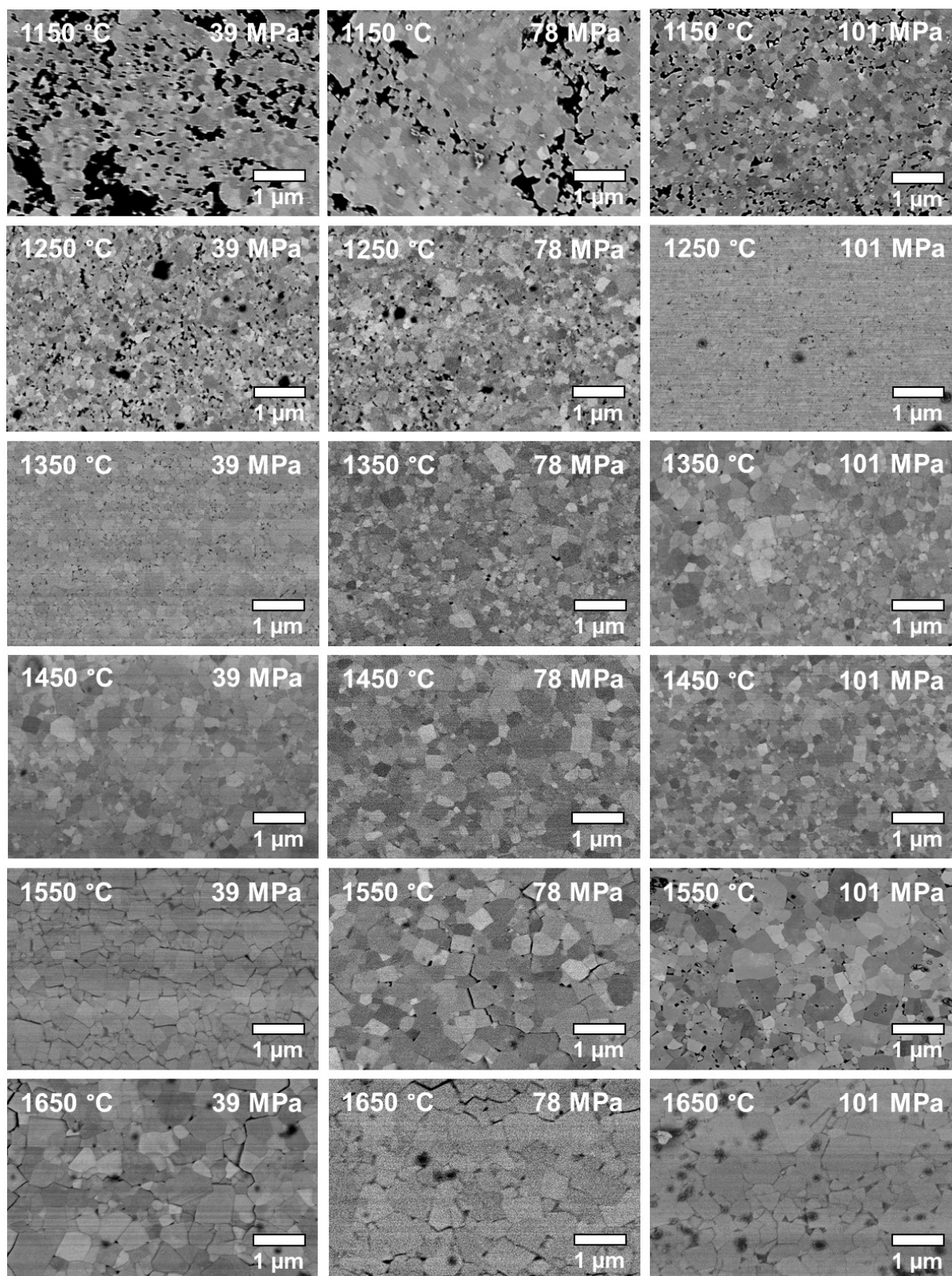


**Figure 4.9:** SEM images of polished cross section of SPS BZCY72 samples prepared at different temperatures (which increases from top to bottom) and pressures (which rises from left to right).

## Influence of sintering temperature and pressure

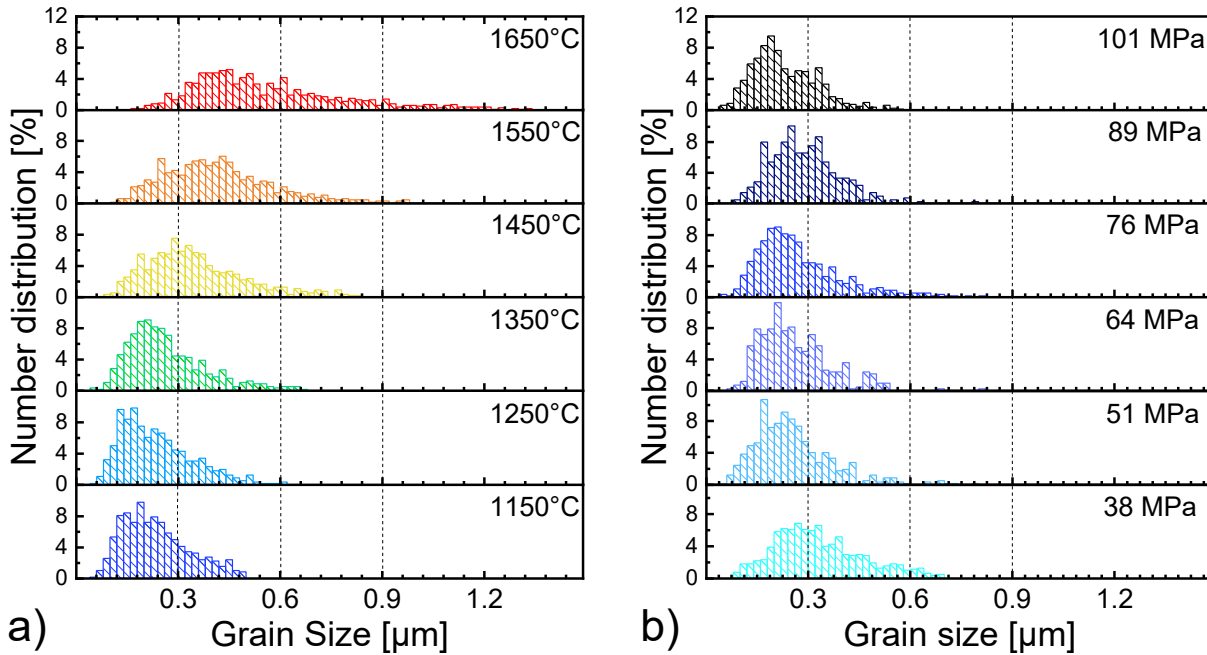


**Figure 4.10:** Histogram of grain size distribution obtained from statistical analysis of various SEM images: a) at 76 MPa; b) at 1350 °C.

At 1650 °C there are no pores sizes below 100 nm, as they are likely evaporated at this point. The difference in size and grain shapes for samples sintered at higher sintering temperature suggest abnormal grain growth during the process, which can be expected according to German et al. [83]. The applied pressure does not seem to have a noticeable effect on grain growth (**figure 4.9** and **4.10b**). Increasing the applied pressure only leads to higher densification, in agreement with the general understanding of the influence of external pressure on density [87]. SPS pressure studies on SiC and WC led to the same conclusion: the applied pressure has no influence on the material grain growth [199, 200]. However, some authors concluded that higher pressures affect the temperature gradients within the punch/die/sample assembly, which could be responsible for the observed broader grain size distribution at lower pressures [201].

Elemental EDX mapping of the BZCY72 cross-section is presented in **figure 4.11**. Homogeneous elemental distributions are observed for the samples sintered at 1350 °C, with evidence of graphite impurities. These could either arise from the sintering process or from the polishing step, since SiC sand paper was employed and Si could also be detected (see **appendix 8.7.7**). At higher temperatures, the elemental distribution appears inhomogeneous, with impurity phases (as BaCO<sub>3</sub> and Ba(OH)<sub>2</sub>) preferentially located in cracks or at grain boundaries. This could be expected considering the higher diffusion rates under those conditions and was also apparent in XRD and Raman. These impurities could also explain the instability of the BZCY72 samples prepared at high sintering temperatures.

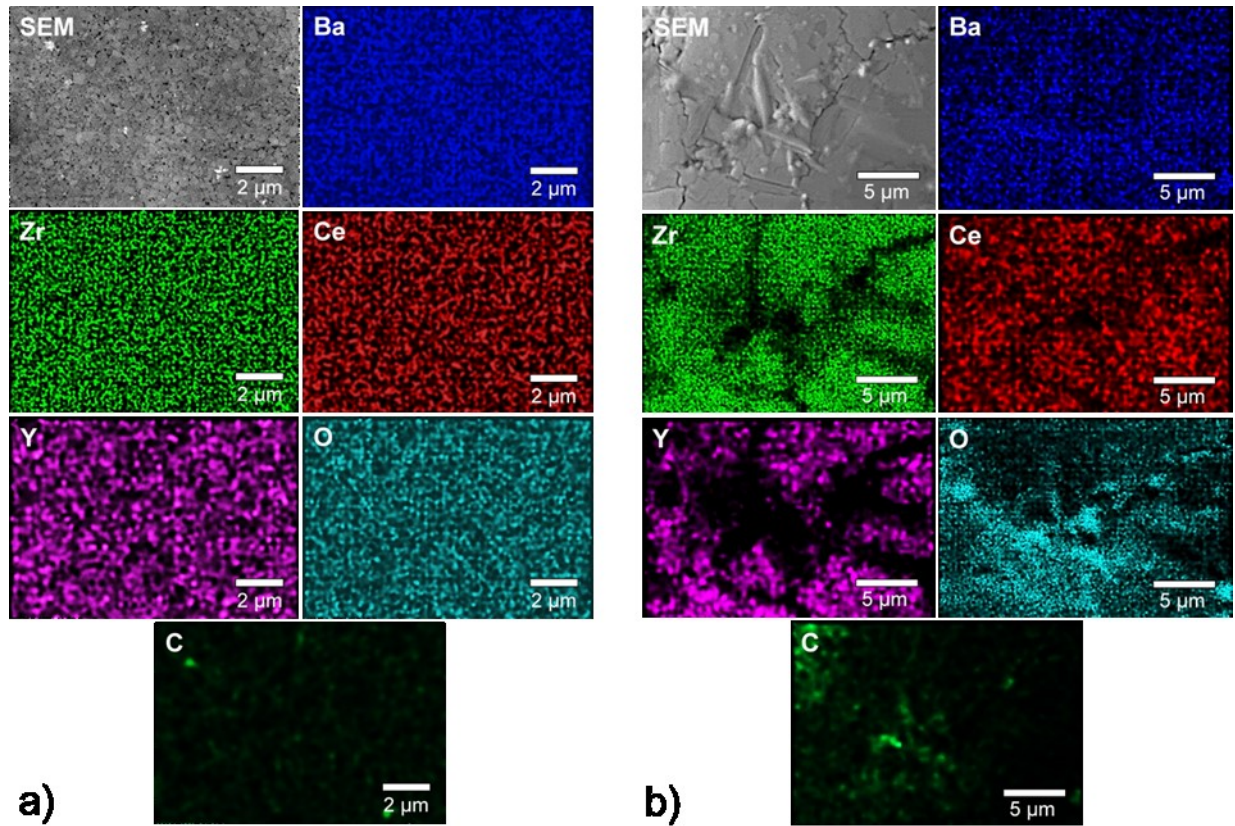


**Figure 4.11:** EDX analysis of BZCY72 samples prepared at 76 MPa and a) a sintering temperature of 1350 °C or b) a sintering temperature of 1750 °C.

#### 4.1.4 Conductivity

The effect of the sintering temperature and applied pressure on the impedance response is displayed in **figure 4.12** with detailed information given in **table 4.1**. All SPS prepared samples show a typical Nyquist plot with a low resistance  $R_1C_1$  element at high frequencies in series with a dominant  $R_2C_2$  element. Again,  $R_1C_1$  represents the bulk with a typical geometrically corrected capacity of  $C_1 \sim 10^{-12}$  to  $10^{-11} \text{ F} \cdot \text{cm}^{-1}$  and the second dominating  $R_2C_2$  semicircle is assigned to the grain boundary, with a capacity in the range of  $C_2 \sim 0.5$  to  $1.5 \times 10^{-9} \text{ F} \cdot \text{cm}^{-1}$ . At low frequencies there is a third contribution ( $R_3C_3$ ) which is attributed to the electrode with a capacity of  $C_3 \sim 10^{-5} \text{ F} \cdot \text{cm}^{-1}$ . With increasing sintering temperature, the grain boundary resistance  $R_2$  decreases, **figure 4.12a**. This trend is more significant at lower sintering temperatures. The reason for this correlation lies in the enhanced grain growth for higher sintering temperatures and thus leading to smaller grain boundary density corresponding to enhanced grain boundary conductivity [9]. Additionally, below 1350 °C samples are not fully densified (see **figure 4.3**). Therefore, porosity within the sample results in overestimating the bulk and grain boundary resistances. Despite enhanced grain growth at temperatures above 1550 °C, the conductivity could not be obtained due to the premature sample degradation. The grain boundary capacity increases with increasing sintering temperature, presumably related to changing grain boundary geometries due to enhanced grain boundary diffusion. Similar trends are known for yttrium stabilized zirconia (YSZ) [162].



Influence of sintering temperature and pressure

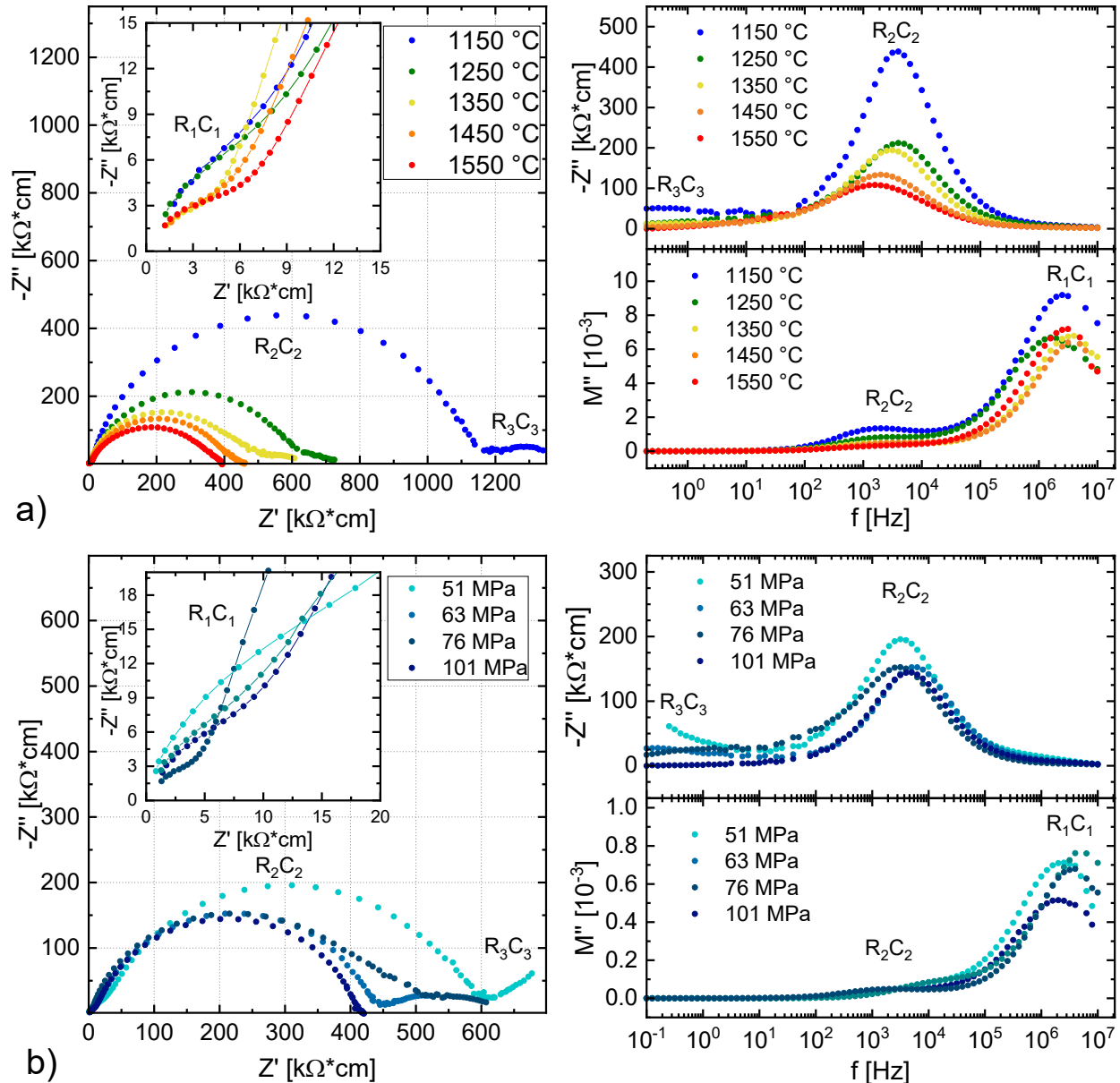


**Figure 4.12:** IS data obtained at 300 °C in 3 % H<sub>2</sub>O 5% H<sub>2</sub>/Ar atmosphere for BZCY72 samples prepared by SPS. Data is presented in Nyquist plots on the left with the insert emphasizing the  $R_1C_1$  arc. On the right the spectroscopic plot is displayed above the modulus. First set of data is related to the sintering temperature at 76 MPa (a) and second set is for the varied applied pressure at 1350 °C (b).

The bulk resistance ( $R_1$ ) was observed to show its minimum at 1350 °C. It follows the same trend as the B – O bond distance which is the lowest for this preparation temperature. It is assumed that smaller B – O distances are related to smaller hopping distance for the protons and thus, higher bulk conductivity. The bulk semicircles in the Nyquist plots become more depressed at temperatures around and above 1350 °C. This effect may originate from grain inhomogeneity, resulting from the abnormal grain growth and broader grain size distribution at higher temperatures [202].

**Table 4.1:** Results of the IS data fitting at 300 °C in 3 % H<sub>2</sub>O 5% H<sub>2</sub>/Ar atmosphere. Resistance, capacitance and bulk dielectric constant for BZCY72 are reported for different sintering temperatures at constant pressure of 76 MPa (top) and pressures at a constant sintering temperature of 1350 °C (bottom).

T [°C]	C <sub>1</sub> [F · cm <sup>-1</sup> ]	R <sub>1</sub> [kΩ · cm]	C <sub>2</sub> [F · cm <sup>-1</sup> ]	R <sub>2</sub> [kΩ · cm]	ε <sub>r</sub> Bulk
1150	8.87 · 10 <sup>-12</sup>	8.81	4.22 · 10 <sup>-10</sup>	1132	72
1250	8.77 · 10 <sup>-12</sup>	7.71	5.80 · 10 <sup>-10</sup>	626	85
1350	1.07 · 10 <sup>-11</sup>	4.06	9.96 · 10 <sup>-10</sup>	495	68
1450	8.91 · 10 <sup>-12</sup>	5.29	1.46 · 10 <sup>-9</sup>	419	92
1550	8.67 · 10 <sup>-12</sup>	6.47	3.03 · 10 <sup>-9</sup>	394	116

p [MPa]	C <sub>1</sub> [F · cm]	R <sub>1</sub> [kΩ · cm <sup>-1</sup> ]	C <sub>2</sub> [F · cm]	R <sub>2</sub> [kΩ · cm <sup>-1</sup> ]	ε <sub>r</sub> Bulk
51	1.03 · 10 <sup>-11</sup>	10.43	5.00 · 10 <sup>-10</sup>	592	76
63	1.09 · 10 <sup>-11</sup>	7.41	5.80 · 10 <sup>-10</sup>	426	69
76	1.07 · 10 <sup>-11</sup>	4.06	9.96 · 10 <sup>-10</sup>	495	68
101	1.12 · 10 <sup>-11</sup>	6.86	8.09 · 10 <sup>-10</sup>	388	80

For samples prepared at higher applied pressure, R<sub>2</sub> decreases up to a 76 MPa when full densification is achieved (compare **figure 4.3**). At temperatures around 1550 °C, a pressure of 101 MPa had a negative effect on the grain boundary conductivity. In contrast to the temperature variation, the capacity C<sub>2</sub> does not show a trend for increasing pressures suggesting a certain preservation of the grain boundary geometry. The different shapes of the R<sub>1</sub>C<sub>1</sub> arc of the bulk could be a result of small variations in the oxidation conditions for the samples [37] in combination with inhomogeneous grain sizes. Overall, the bulk conductivity increases with increasing pressure as a result of the smaller B – O bond distances.

The bulk dielectric constants were observed to increase with temperature. This may be caused by increasing impurities or inhomogeneity as suggested by EDX. The calculated values fit within the range of 30 and 90 reported in the literature [177] except for the sample prepared at 1550 °C. Furthermore, the dielectric constant appears to be independent of the applied pressure.

**Figure 4.13** shows the calculated Arrhenius plots for the bulk and grain boundary conductivity for all investigated temperatures and pressures in 3% moist 5% H<sub>2</sub>/Ar atmosphere that follow a linear behavior. The activation energies were calculated from the equations 1.11 and 2.18 and are displayed in **figure 4.14**. The activation energy for the bulk remains independent of the sintering temperature at approximately 0.57 eV, which corresponds to protonic conductivity [67, 68]. For the grain boundary region, the activation energy was found to increase from 0.79 eV to 0.94 eV with increasing sintering temperature. This is most likely caused by varying impurity segregation at the grain boundary. Another explanation could be the porosity within samples prepared below 1350 °C, there are less solid-solid interfaces where space charge layer can be formed. Thus, the charge carrier concentration differ, resulting in different activation energies. Increasing sintering temperatures also enhance diffusion processes along the grain boundaries. Impurities such as BaO or Ba(OH)<sub>2</sub> might accumulate in the grain boundary regions and could be responsible for higher activation energies.

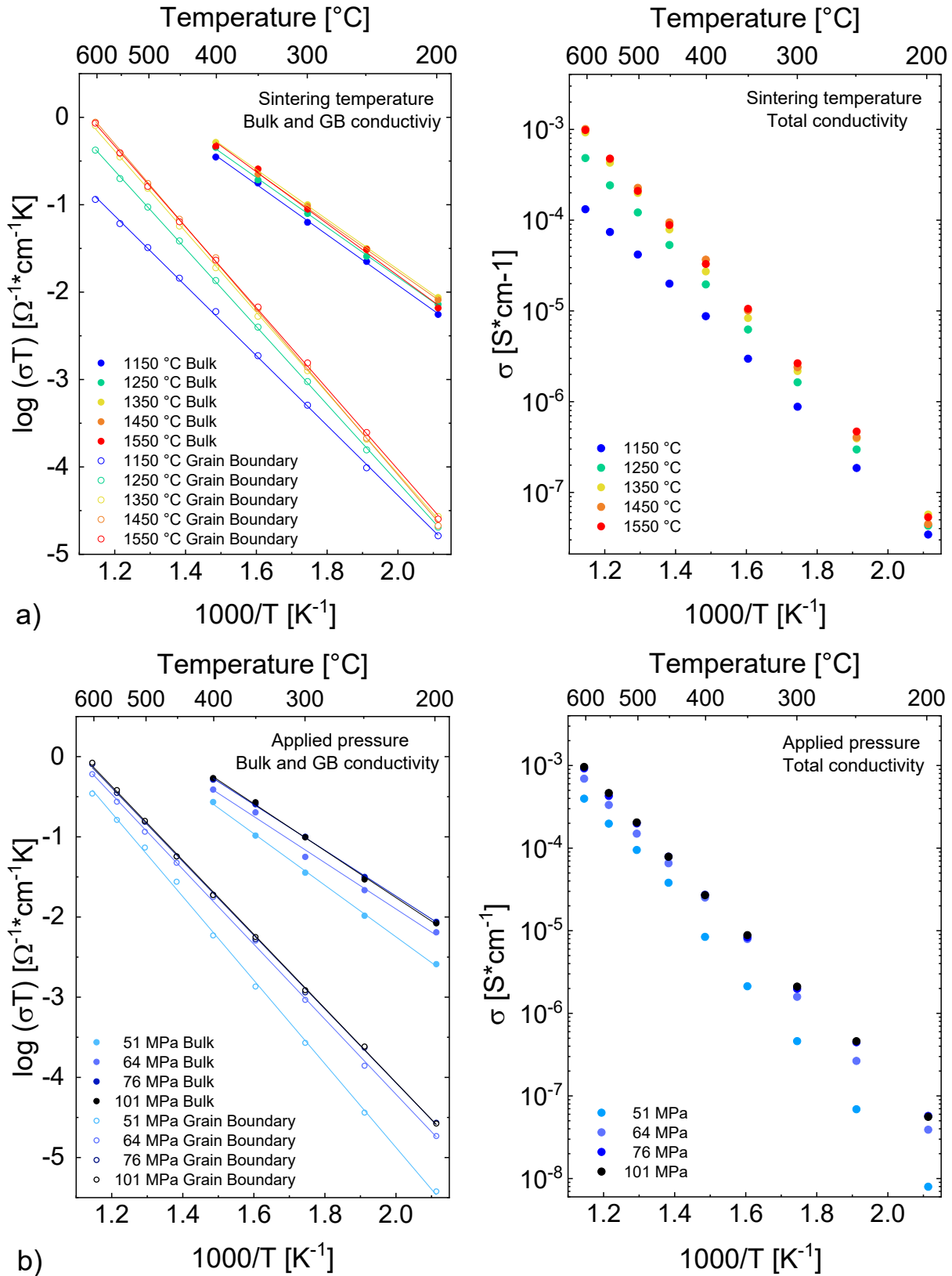


**Figure 4.13:** Arrhenius plots for bulk and grain boundary and total conductivity of BZCY72 samples in 3 % H<sub>2</sub>O 5% H<sub>2</sub>/Ar atmosphere for (a) different sintering temperatures and (b) varying applied pressures.

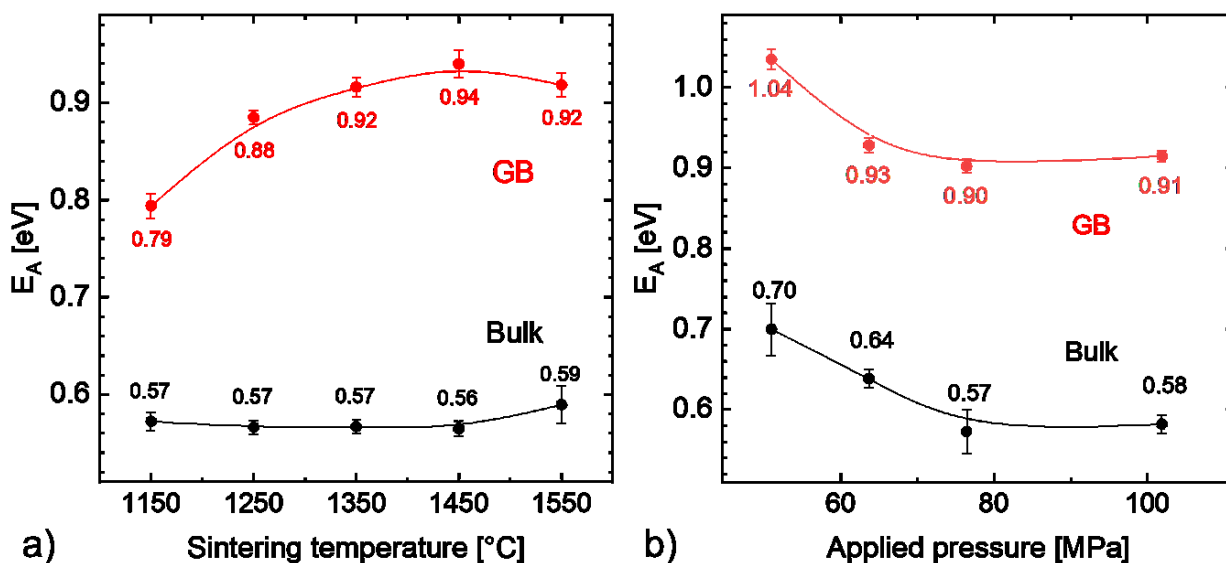


**Figure 4.14:** Relation between activation energies for bulk and grain boundaries for SPS BZCY72 samples and varying (a) sintering temperatures at 76 MPa, (b) applied pressures at 1350 °C and.

In this work, the reported activation energies are about 0.2 eV higher as compared to the SSRS prepared BZCY72 samples [42, 98, 103] but in the same range as the SPS synthesized pellets [33]. Bulk and grain boundary activation energies were observed to decrease with rising pressure during SPS. This is in accordance with the decrease of B – O distance observed by XRD. A further explanation was proposed by Irvine et al. for the BZY by suggesting the presence of two cubic phases: an  $\alpha$ -phase with lower conductivity/higher activation energy and a higher-conducting  $\beta$ -phase [165]. Higher bulk activation energies above 0.6 eV would indicate high concentration of the  $\alpha$ -phase [47]. The applied pressure might therefore have an influence on the phase polymorph distribution. There was no indication of this separation observable by XRD, likely due to poor resolution as depicted by Wang et al. [33]. Neutron powder diffraction experiments are necessary to reveal the local structure and thus, the true cause of this behavior. The pre-exponential factor increases with rising temperatures and pressures, indicating higher concentration of protonic charge carriers

The total conductivity of SPS prepared BZCY72 samples as a function of temperature and pressure is presented in **figure 4.15a**. At 76 MPa, the total conductivity at 600 °C rapidly rises from  $1.32 \cdot 10^{-4} \text{ S} \cdot \text{cm}^{-1}$  for the sample prepared at 1150 °C to  $9.24 \cdot 10^{-4} \text{ S} \cdot \text{cm}^{-1}$  for a sample prepared at 1350 °C while the highest conductivity in this set of measurements with  $\sigma = 1.015 \cdot 10^{-3} \text{ S} \cdot \text{cm}^{-1}$  was achieved for the sample prepared at 1450 °C and 76 MPa. In general, samples prepared at higher pressures showed poorer stability in moist conditions in the environment of the IS measurement. This is the reason for reduced performance under the conditions in the top right corner of **figure 4.15a**. The conductivity is also shown as a function of rel. density of the material and grain sizes, **figure 4.15b-c**. Below 1350 °C, the relative density is the determining influence for the conductivity. After full densification, the grain size is the defining factor to increase the conductivity.

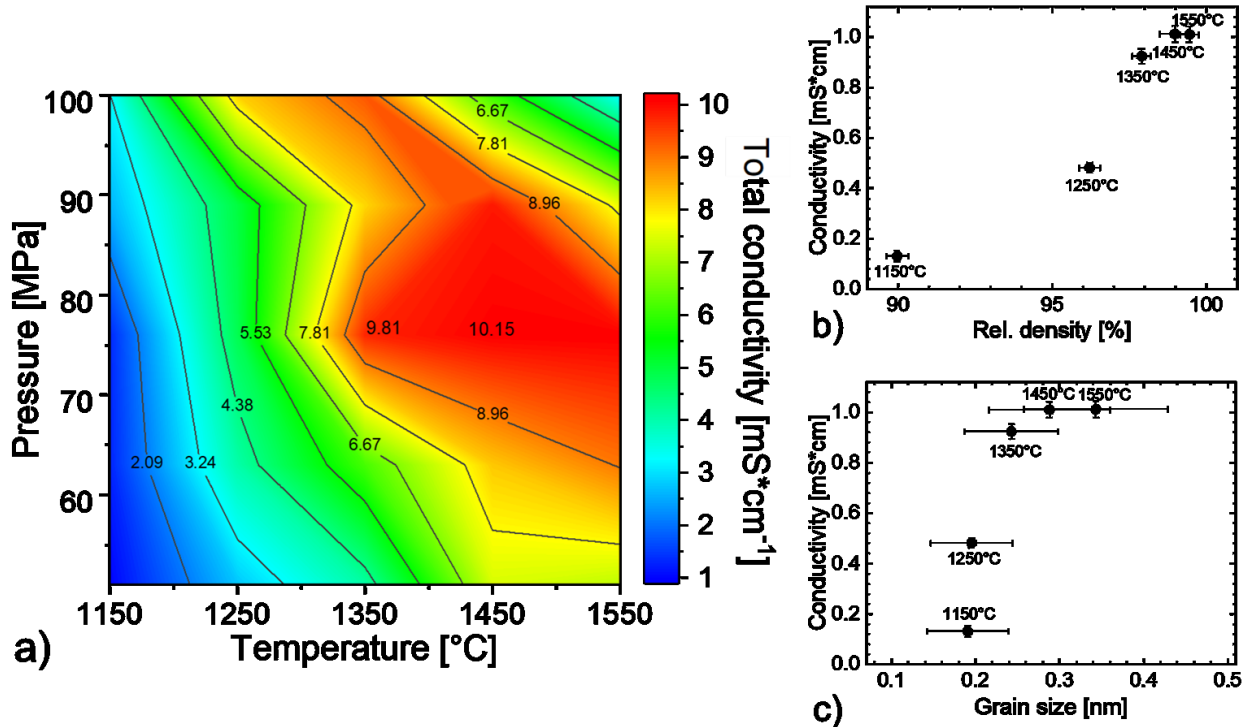


**Figure 4.15:** Summary of the total conductivity at 600 °C dependence on sintering parameters (a) , the relative density at 76 MPa (b) and grain size at 76 MPa (c).

It is however interesting to note that the conductivity remains constant when increasing the sintering temperature from 1450 °C to 1550 °C, despite the grain growth. A possible reason is the degradation of the pellets. This degradation becomes even more apparent in wet oxidizing atmosphere (setup described in chapter 2.5.4). **Appendix 8.7.8** emphasizes the effect of the Ba(OH)<sub>2</sub> formation in the form of needles according to [203]:

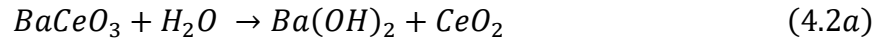


**Figure 4.16** displays the total conductivity as a function of oxygen partial pressure for BZCY72 samples prepared at different sintering temperatures at 76 MPa. Within the investigated pO<sub>2</sub> range, the electro-neutrality condition  $2[V_O^{\bullet\bullet}] = [Y'_{Zr}]$  is obtained, **appendix 8.1.5**. Protonic conductivity appears to be dominant, since no dependence on pO<sub>2</sub> is visible [54, 204]. At higher temperatures, in oxidizing atmospheres, p-type conductivity becomes arises, attributable to defect formation shifting in favor of electron holes (see equation 1.7). It is presumed that the p-type conduction occurs via O-site polarons [65, 205]. Significant p-type conductivities were reported for SPS prepared samples [41]. It was concluded that in reducing atmosphere during the SPS process holes are created. Due to the relatively fast cooling there is no time for a reoxidation step and holes become trapped in the material. The greater slope in conductivity at high pO<sub>2</sub> for the higher preparation temperature supports this theory, since more holes are generated at more extreme conditions, increasing the p-type conductivity. Unfortunately, progressive degradation renders measurements under moist conditions impractical.



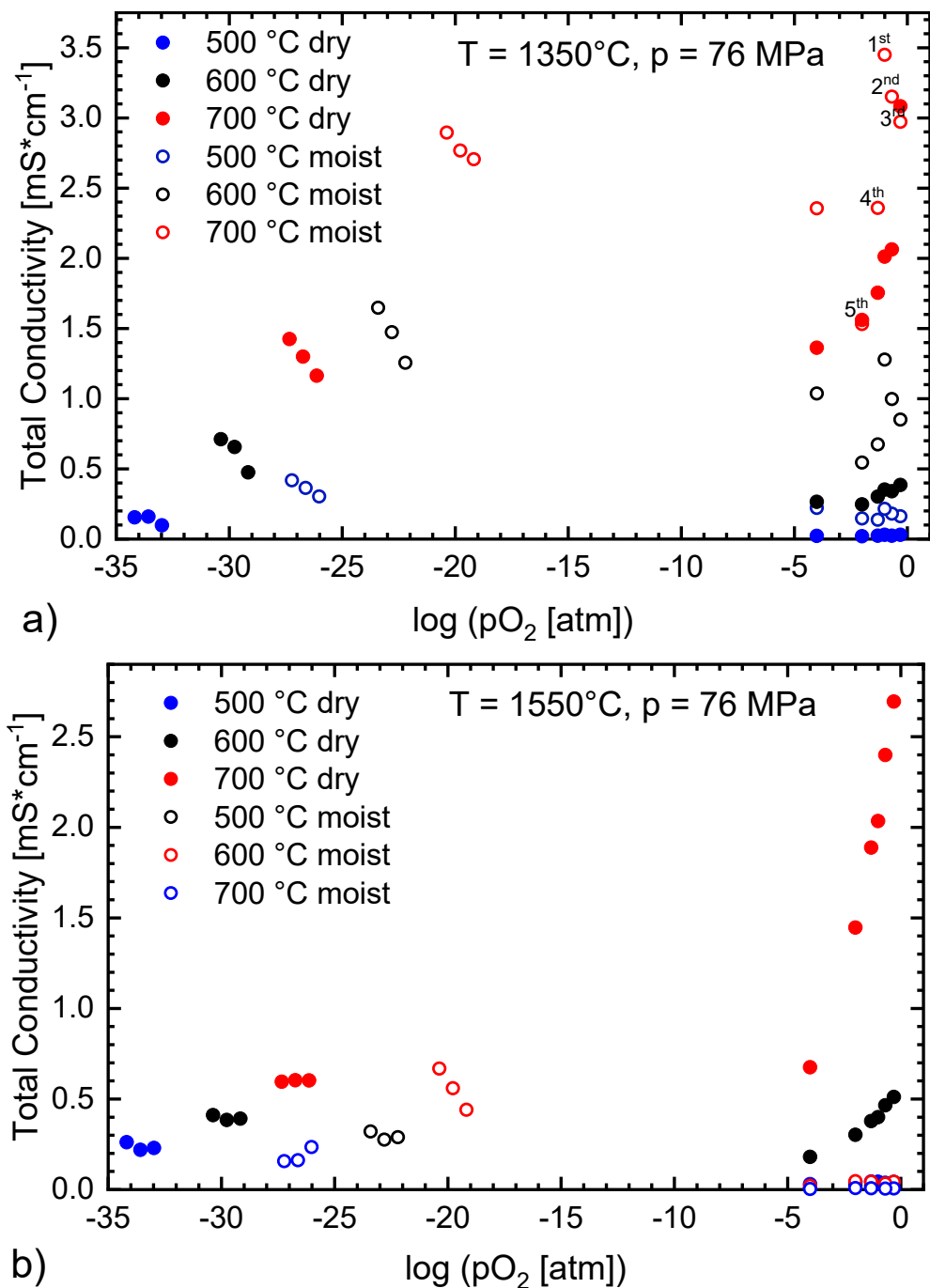


**Figure 4.16:** The  $p\text{O}_2$  dependence of the total conductivity for a SPS BZCY72 at (a)  $1350^{\circ}\text{C}$  and (b)  $1550^{\circ}\text{C}$  in moist and dry atmospheres. The numbers indicate the order of the measurements for the degrading sample under moist oxidizing conditions.

For the sample prepared at  $1350^{\circ}\text{C}$  numbering of data set indicate the order of the measurements. It was observed that the conductivity values decrease drastically as measurements are progressing due to degradation of samples. The sample prepared at  $1550^{\circ}\text{C}$  degraded much faster under oxidizing conditions, so that no reliable results could be obtained. Interestingly, under low  $p\text{O}_2$  conditions and moist conditions this effect was partially reversible, presumably due to the

depletion of Ba(OH)<sub>2</sub> and other oxide impurities. Because of the severe degradation of the sample prepared at 1550 °C, only the results obtained for the sample sintered at 1350 °C are discussed. Under reducing atmosphere, the conductivity rises when switching to moist conditions. According to the Brouwer diagram the concentration of protonic defects increases under those conditions due to hydration, see **appendix 8.1.5** [65]. Under dry reducing conditions, the conductivity increases with decreasing the oxygen partial pressure and is suggested to be n-type due to the presence of small cerium polarons [65]. Such cerium polarons have been observed on thin BZCY72 membranes [206]. Moreover, the mobility of charge carriers also differs along the grain boundaries. While they are blocking for protonic defects and still highly resistive to holes, they are fairly conductive for electronic contributions [37, 47, 207]. This might be the possible reason for observation of electronic conductivity at higher grain boundary densities present for the sample prepared at 1350 °C. In general, the conductivity follows the expression:

$$\sigma_{tot} = \sigma_i + \sigma_p(P_{O_2})^{1/4} + \sigma_n(P_{O_2})^{-1/4} \quad (4.3)$$

which is typically observed for proton conducting materials where  $\sigma_i$ ,  $\sigma_p$  and  $\sigma_n$  are the ionic, p-type and n-type conductivity, respectively [65, 161, 208]. The highest measured total conductivity in this setup was  $1.25 \cdot 10^{-3} \text{ S}\cdot\text{cm}^{-1}$  which is higher than the previous measurement most likely because of a longer equilibrium time (5 days vs 14 hours).

## 4.2 Influence of heating rate

SPS is characterized by high heating rates that are not achievable by other sintering techniques. The idea behind the variation of this parameter is that certain sintering mechanisms can be either bypassed using high heating rates or enhanced in the case of low heating rates [198]. In the following section the sintering temperature was maintained at 1350 °C and the pressure at 76 MPa since those parameters resulted in the highest conductivities.

### 4.2.1 Densification

The detailed densification progression monitored by the plunger displacement is shown in **appendix 8.7.9** and the final relative densities of BZCY72 samples are plotted in **figure 4.17**. The progression of the piston position at 25 K/min shows, that densification does not take place until a certain temperature threshold around 900 °C is reached. This observation is in agreement with the SPS models, where densification and coarsening mechanisms take place at different temperature regimes [76, 82, 83, 198, 209]. Hence, an SPS process employing high heating rates bypasses the temperature regimes where no densification of the material occurs and increased densification rates are expected, as shown in **appendix 8.7.9**. At 200 K/min the densification starts right at the beginning of stage II with a high rate. In this particular process the maximum densification is already reached before the heating has ended and the rapid thermal expansion causes the piston to move backwards at the end of this sintering stage.

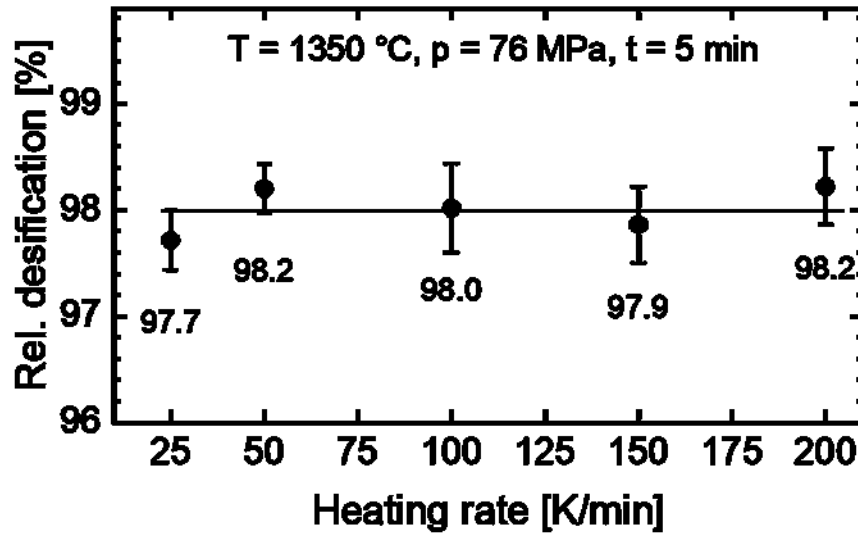


**Figure 4.17:** The relative densifications obtained at different heating rates under the given conditions.

Despite the different densification progression, from variation of the plunger position, the final density appears to be little affected by heating rate, in agreement with geometric density calculations. This is in contrast to previous experiments on SPS-prepared  $\text{Al}_2\text{O}_3$  that showed a strong correlation between heating rate, temperature and density [75, 210]. Density increased with the heating rate at 1150 °C but, not at 1300 °C. It was also observed that the densification even decreases at very high heating rates of 600 K/min. Presumably, at lower sintering temperatures around 1150 °C, the heating rate would have an effect on the densification of BZCY72 as well.

#### 4.2.2 Crystallographic structure

The XRD patterns of the BZCY72 samples prepared at different heating rates show no visual differences, **figure 4.18**. Samples synthesized within this series provided the best overall quality in terms of phase purity. This might partly explain greater mechanical integrity obtained at all heating rates which is also in agreement with earlier discussed results (referring to **appendix 8.7.2**).

**Figure 4.19** gives an overview for the calculated crystallographic parameters with detailed values presented in **appendix 8.7.10**. The heating rate does not appear to have an effect on the lattice parameters although a slightly higher unit cell volume was found at 25 K/min. Aldica et al. investigated the effect of the heating rate on the superconductor  $\text{MgB}_2$  and also reported constant lattice parameters within the range between 20 K/min and 475 K/min [211]. The crystallite size decreases with increasing heating rate since the sample is exposed longer to temperatures of which coarsening occurs via mass transport mechanisms along the grain boundaries with lower activation energies such as surface diffusion [83].

Influence of heating rate

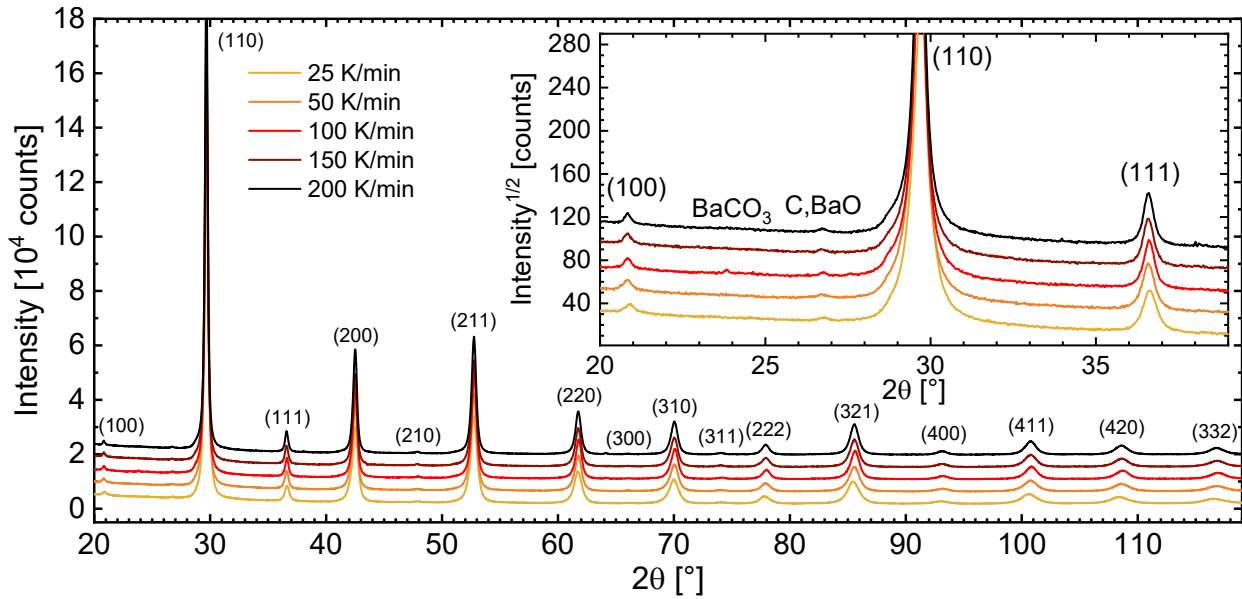


**Figure 4.18:** XRD patterns for the SPS BZCY72 samples at different heating rates from 25 K/min to 200 K/min. The insert displays the  $2\theta$  region between 20 and 40° where impurity peaks are observed.

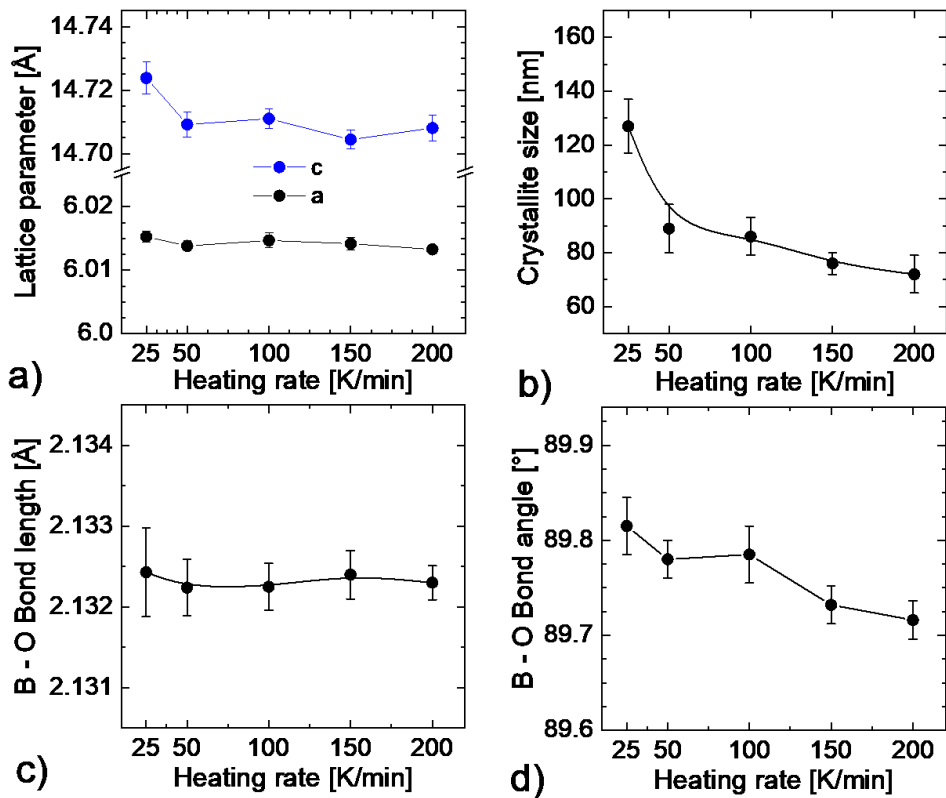


**Figure 4.19:** Results of the Rietveld refinement of XRD patterns in **figure 4.18**. Lattice parameters (a), crystallite size, (c) B – O distance and (d) B – O – B angle as a function of heating rate.

Therefore, the heating rate allows for control of the microstructure without any losses in densification or varying other crystallographic properties. Due to the high accessible range for heating rates in SPS, this method allows for more control of the material properties [76, 81, 82]. In accordance with this work, Anselmi-Tamburini et al. found the same relation between crystallite size and heating rate for yttrium stabilized zirconia (YSZ) [212]. Khalil et al. demonstrated that the crystallite size even further decreases with higher heating rates up to 1200 K/min [213].

To the best of the author's knowledge, there is no systematic study of the bond geometry in SPS prepared samples based on barium zirconate as a function of heating rate so far. In this study, in accordance to variations of the lattice parameters, the B – O bond distance remains independent of the heating rate. Nevertheless, the B – O – B angle was observed to decrease with rising heating rates. This may be a result of the thermal stress within the sample. In electronically insulating SPS materials produced at higher heating rates, thermal gradients were introduced during the heating stage [74]. Furthermore, there were also defects initially stored in the material by the powder synthesis or in the particle boundaries [82, 214]. According to those authors, high heating rates promote the formation of initial defects. This goes back to assumptions where large DC currents required for rapid heating generate high-temperature plasma on the particle surfaces [215, 216]. In perovskites, defects can cause a tilting of the BO<sub>6</sub> octahedra which is responsible for the observed deviation of the B – O – B bond angle from 180°. This might add an explanation for the higher observed lattice parameters for the sample prepared at 25 K/min.

### 4.2.3 Microstructure

An overview of the microstructure of BZCY72 samples prepared at varying heating rates is given in **figure 4.20**. No conclusive trend in grain sizes was observed, despite the decreasing crystallite sizes with rising heating rate. The smallest grain sizes were obtained at 25 K/min. It is important to note that grain growth proceeds slow below a rel. density of 70% [83]. In other words, even for a longer periods of time spent under particle coarsening conditions in the case of 25 K/min, densification and grain growth might not be expected. For rapid grain growth, a rel. density of 90 % and more is essential. Since the sintering time spent above this threshold is approximately equal for all heating rates (see **appendix 8.7.9**), the mean grain size is not significantly affected by the heating rate. However, there is a major disagreement in literature. Conflicting results for the same materials are reported where the grain size was observed to be either proportional [216, 217], inversely proportional [75, 210, 218] or invariable to the heating rate [209]. The impact of the heating rate also depends on the sintering temperature and pressure [209, 210].

The SEM images in **figure 4.20** reveal different shapes of the grain boundary regions. At 200 K/min the grains exhibited smooth boundaries while at lower heating rates the grain transitions appeared to be sharp. This is an evidence for different mass transport mechanisms. More surface diffusion occurs at lower heating rates that cannot penetrate the grain boundaries.

## Influence of heating rate

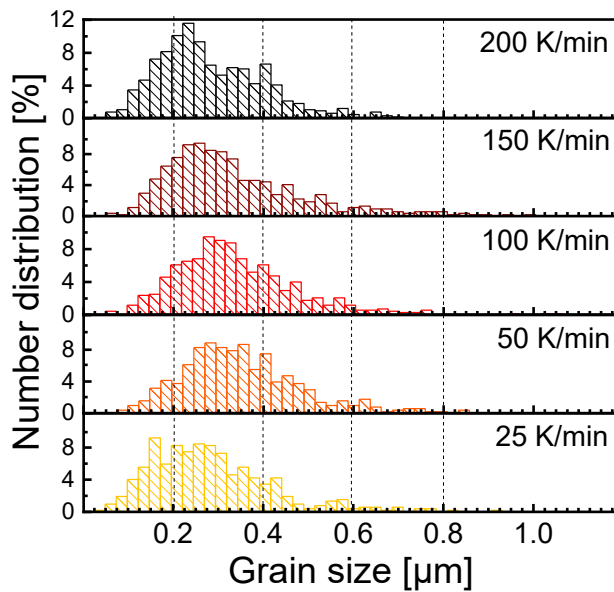
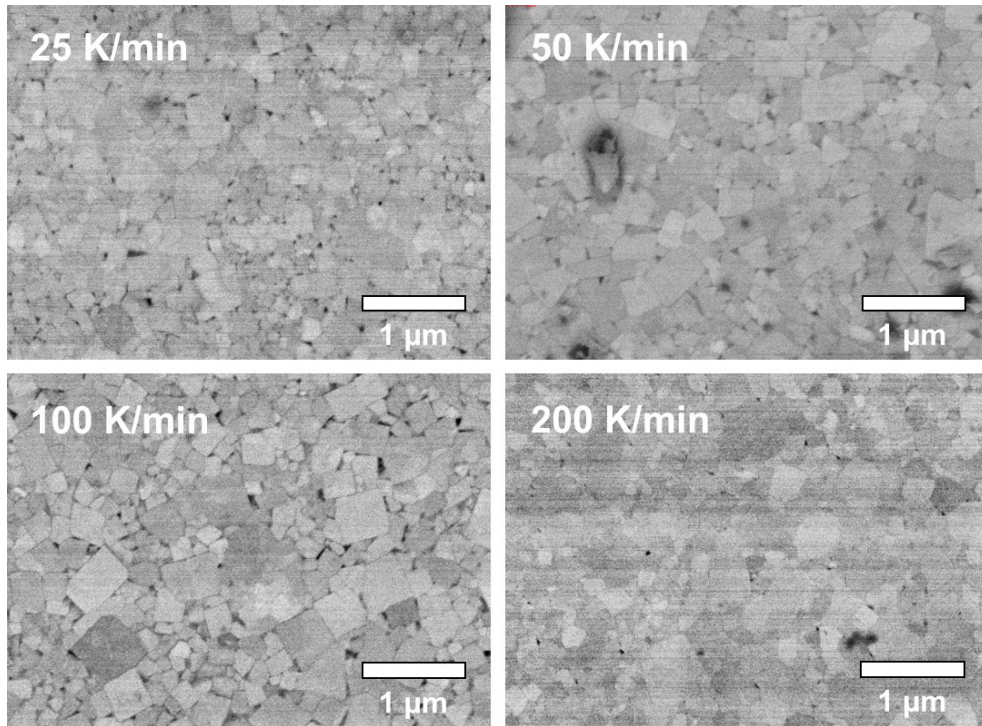


**Figure 4.20:** Top: SEM images of polished cross section of SPS BZCY72 samples prepared at different heating rates. Bottom: The corresponding grain size distribution in relation to the heating rate.

Mass transport along the grain boundaries results in sharp distinct edges of the grains, which appears to cause broader grain boundaries. At higher heating rates of 200 K/min, the above mentioned mechanisms are bypassed. The sample directly enters the temperature regime where volume diffusion is dominant and atoms start to move across the grain boundaries. This leads to less defined grain boundaries as shown in **figure 4.20** for the samples prepared at 200 K/min.



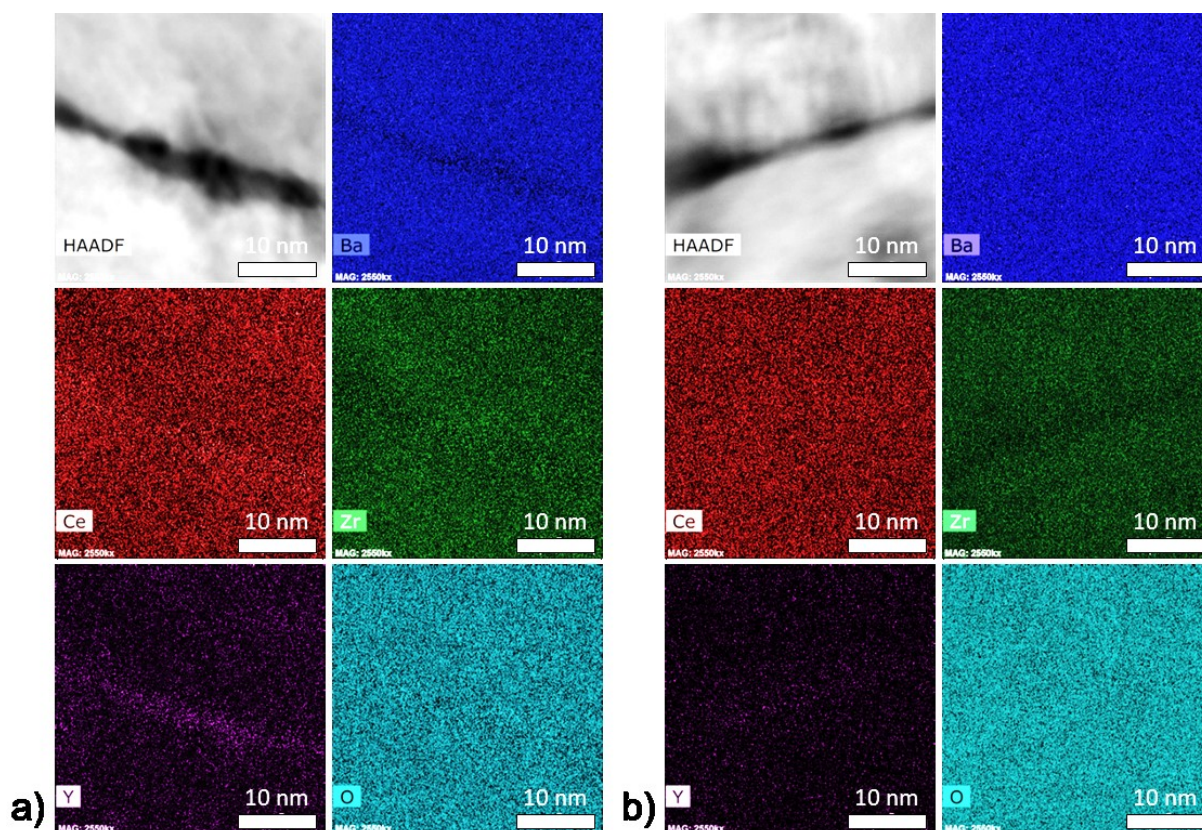


**Figure 4.21:** High-angle annular dark field (HAADF) image and TEM-EDX mapping of a grain boundary in BZCY72 samples prepared by SPS with a heating rate of (a) 25 K/min and (b) 150 K/min.

A closer inspection of local structure of the grain boundaries employing TEM in **figure 4.21** shows that grain boundaries are free of any significant accumulation of secondary phases visible on the XRD patterns. Nevertheless, major differences for the investigated heating rates were found in the elemental composition. The BZCY72 sample prepared at 25 K/min exhibits a higher concentration of Y while a Ba deficiency occurs at the grain boundaries. Excess Y was not found in the grain boundaries of the samples synthesized at 150 K/min (**figure 4.21b**) or 50 K/min (**appendix 8.7.11**). Instead, for the latter sample, Zr-deficiency is evident in the grain boundary region. The higher concentration of the acceptor dopant within the grain boundary region can be discussed in terms of the space charge layer model for proton conductors proposed by Kjølseth et al. [174]. Employing this model, the Schottky barrier height  $\Delta\phi(0)$  is expected to be higher for the sample prepared at 25 K/min. This quantity describes the potential of the intersection between grain boundary core and space charge layer relative to the grain interior and can be used to determine the width of the space charge layer (see subsection below). The width of the grain boundary can be estimated from the EDX line scans (**figure 4.22**), where the grain boundary width for the lower heating rate was observed to be double of that of the sample prepared at 150 K/min. Therefore, the mass transport mechanisms across the grain boundary for higher heating rates has likely a thinning effect on this region. Diffusion processes along the grain boundary, however, allow for dopant accumulation since the grain boundary core acts as a barrier and prevents cation mixing. Outside of the grain boundary regions, all samples appeared homogeneous in terms of the elemental composition.

## Influence of heating rate

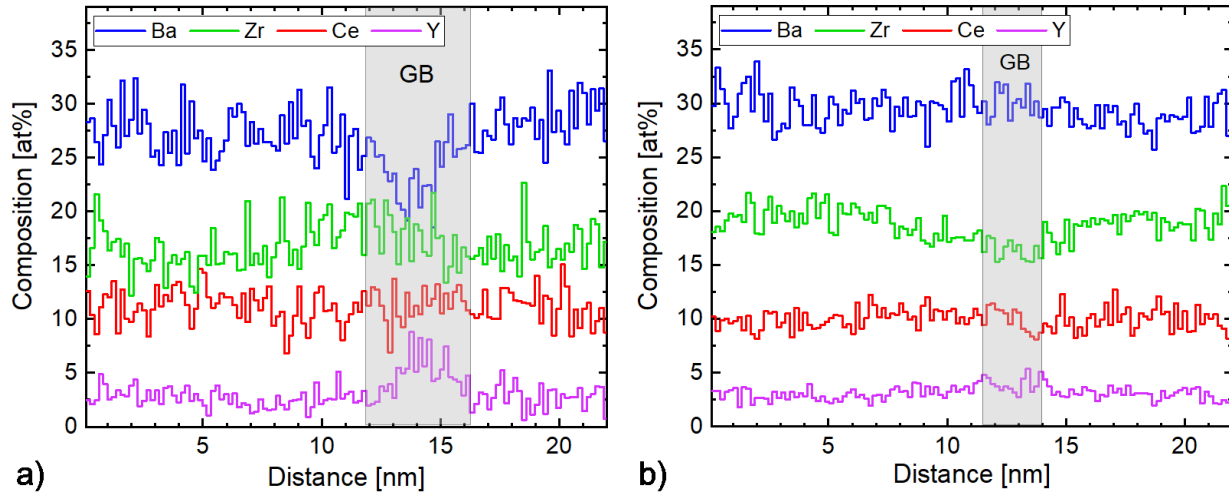


**Figure 4.22:** EDX line scan revealing the atomic composition through the grain boundaries investigated in the **figure 4.21**: (a) 25 K/min and (b) 150 K/min.

### 4.2.4 Conductivity

The results of the IS for all investigated heating rates are presented within **figure 4.23** and **table 4.2**. The Nyquist plots show bulk and grain boundary contributions expressed as  $R_1C_1$  and  $R_2C_2$ , respectively.  $R_2$  decreases with rising heating rates, which could be explained by the decreasing Y dopant concentration as suggested by TEM. Referring back to the space charge layer model, protonic defects are repelled from the positively charged grain boundary core [174]. From the EDX and TEM analysis, wider grain boundaries were observed for low heating rates, suggesting higher grain boundary resistances. On the other hand, the capacitances  $C_2$  are decreasing first and start to increase again at high heating rates. Presumably, varying the dopant concentration in combination with decreasing the space charge layer widths are responsible for this trend. Bulk resistances  $R_1$  are within the same range as for the previously investigated samples, however,  $R_1$  values are noticeably higher for lower heating rates, and higher dielectric constants were obtained. A possible explanation for this observation could be the accumulation of  $Y^{3+}$  at the grain boundary and the depletion of Y within the bulk. Therefore, according to equation 1.2 and 1.4, less protonic defects are formed, resulting in lower bulk conductivities. For heating rates of 100 K/min and above, the dielectric constants are in agreement with the literature [174, 177].

For an estimation of the dimensions of the space charge layer the eponymous model originally introduced by Kim et al. [219] which was adjusted for proton conductors [174] is used. In a first step, the Schottky barrier height  $\Delta\varphi(0)$  is calculated via the following equation:

$$\frac{\sigma_{bulk}}{\sigma_{GB}} = \frac{\exp\left(\frac{e \cdot \Delta\varphi(0)}{k_B T}\right)}{\frac{2e \cdot \Delta\varphi(0)}{k_B T}} \quad (4.4)$$



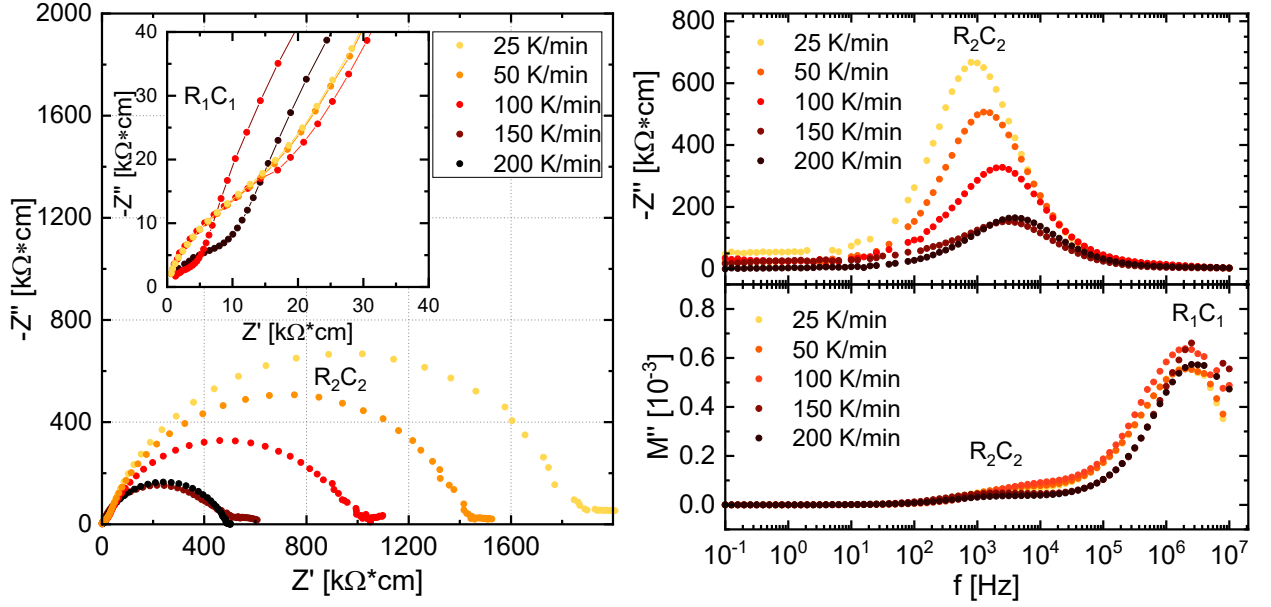


**Figure 4.23:** IS data obtained at 300 °C in 3 % moist 5% H<sub>2</sub>/Ar atmosphere for BZCY72 samples prepared by SPS at different heating rates. Left: Nyquist plot, Right: Spectroscopic plot and modulus plot.

**Table 4.2:** Results of the IS data fitting at 300 °C in 3 % moist 5% H<sub>2</sub>/Ar atmosphere. Resistance, capacitance and bulk dielectric constant for BZCY72 are presented for different heating rates (HR).

HR [K/min]	C <sub>1</sub> [F · cm <sup>-1</sup> ]	R <sub>1</sub> [kΩ · cm]	C <sub>2</sub> [F · cm <sup>-1</sup> ]	R <sub>2</sub> [kΩ · cm]	ε <sub>r</sub> Bulk
25	8.76 · 10 <sup>-12</sup>	11.47	1.31 · 10 <sup>-9</sup>	1847	147
50	7.34 · 10 <sup>-12</sup>	10.52	1.16 · 10 <sup>-9</sup>	1429	138
100	9.59 · 10 <sup>-12</sup>	9.98	5.82 · 10 <sup>-10</sup>	971	67
150	1.07 · 10 <sup>-11</sup>	4.06	9.96 · 10 <sup>-10</sup>	495	68
200	1.05 · 10 <sup>-11</sup>	7.16	1.31 · 10 <sup>-9</sup>	431	73

where  $e$ ,  $k_B$  and  $T$  have their typical meaning and conductivity values were obtained from impedance spectroscopy, **figure 4.24**. The subsequent calculation is presented in **table 4.3** and the effective space charge layer width can now be calculated using equation 4.5:

$$\lambda^* = \sqrt{\frac{2\varepsilon \cdot \Delta\varphi(0)}{e \cdot C_Y(\infty)}} \quad (4.5)$$

where  $\varepsilon$  is the dielectric constant and  $C_Y(\infty)$  is the Y-concentration in the grain interior for which the value of  $8.9 \cdot 10^{26} \text{ m}^{-3}$  was used according to Iguchi et al. [177]. All results are shown in **table 4.3**, confirming a lowering of the Schottky barrier height and the effective space charge layer width for samples prepared at higher SPS heating rates. Similar values for barrier heights were reported for BZY10 by other authors [174, 177, 220]. The effective space charge layer width is slightly higher compared to BZY10 prepared by SPS by Ricote et al. [34, 221].

## Influence of heating rate

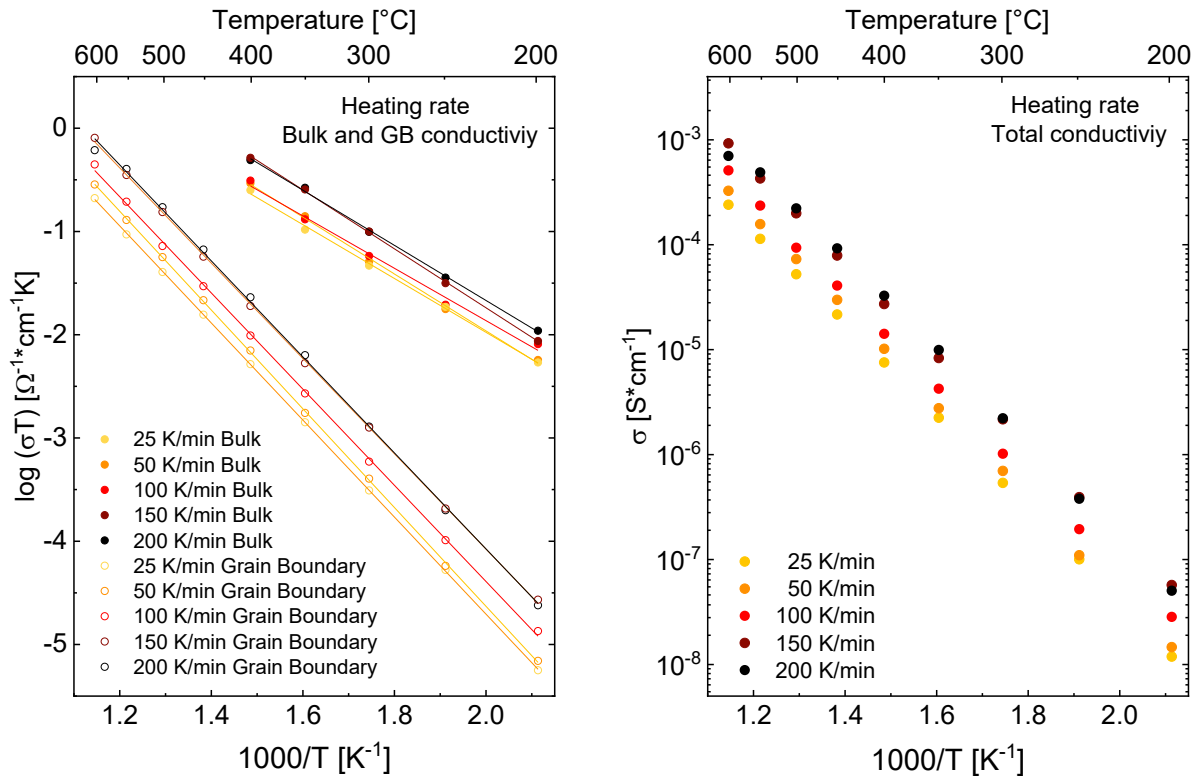


**Figure 4.24:** Arrhenius plots for bulk and grain boundary conductivity as well as total conductivity of SPS BZCY72 samples prepared at different heating rates in 3 %  $\text{H}_2\text{O}$  moist 5%  $\text{H}_2/\text{Ar}$  atmosphere.

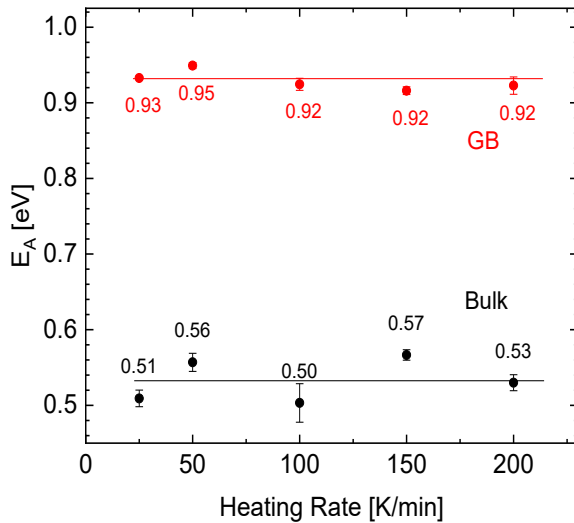


**Table 4.3:** The Schottky barrier height ( $\Delta\phi$ ) and the effective space charge layer width ( $\lambda^*$ ) calculated by equation 4.4 and 4.5

T [°C]	Sample prepared at 25 K/min		Sample prepared At 150 K/min	
	$\Delta\phi(0)$ [V]	$\lambda^*$ [nm]	$\Delta\phi(0)$ [V]	$\lambda^*$ [nm]
200	0.38	2.7	0.34	1.7
250	0.37	2.7	0.34	1.7
300	0.37	2.7	0.33	1.7
350	0.34	2.6	0.32	1.7
400	0.34	2.6	0.31	1.6

**Figure 4.25:** Bulk and grain boundary activation energies for SPS BZCY72 samples as a function of heating rate.

As displayed in **figure 4.24**, Arrhenius plots for bulk and GB follow a linear trend. The activation energies obtained from the Arrhenius plots are plotted in **figure 4.25** do not show a dependence on the SPS heating rate. They are similar to the values reported in section 4.1.4, implying protonic conductivity for the bulk and mixed conductivity for the grain boundary region.

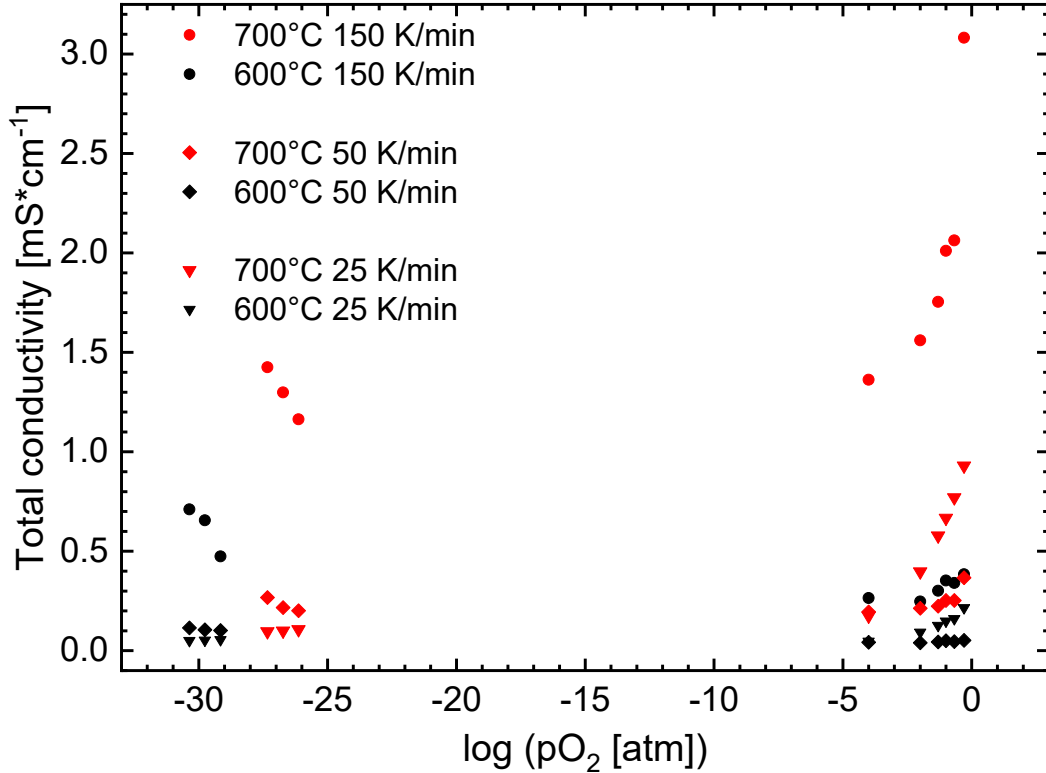


**Figure 4.26:** The  $pO_2$  dependence of the total conductivity in dry atmosphere for a BZCY72 samples prepared at different heating rates by SPS.

To further explore the conductivity mechanism, the IS experiment was performed in different atmospheres with the results shown in **figure 4.26**. Under reducing conditions, the measured conductivities show the same trend as for the sintering temperature investigation. It is, however, evident that there is an increased n-type conductivity as the heating rate rises which also contributes to the observed progression of the total conductivity. It is reasonable to assume that cerium polarons are the source of n-type conductivity as already discussed in the previous investigation (section 4.1.4). In the regime of high oxygen partial pressure, the conductivity rises for all samples due to the incorporation of the oxygen and consequent p-type conduction (equation 1.7). At 600 °C and below, most of the conductivity is ionic given the plateau shape of the graph. The sample prepared at 50 K/min turned out to be unstable under oxidizing conditions which is the reason for the lower conductivity in this regime. Generally, it can be concluded that higher heating rates result in higher conductivities.

### 4.3 Influence of holding time

Holding times over 10 min are rarely investigated in SPS fabrication routes, since long-dwell times defeat the original advantages of SPS in terms of short process times with conserved microstructure. In fact, this process parameter is not even discussed in most review papers on SPS. However, it is well known from other fabrication routes, such as SSRS and CS, that sufficient grain growth requires time [9, 103]. Therefore, it is worth to explore this relatively uncharted process region to reveal its impact on the grain growth and material performance.

#### 4.3.1 Densification

In **appendix 8.7.12** the detailed densification route is displayed where the final relative densities are shown in **figure 4.27**. Densification happens mainly during the first 5 min of dwell time. No further densification is observed when increasing the dwell time. For a holding time of 60 min, the plunger displacement during the SPS process was stagnating for the last 35 min of the dwell time before it changed again during the cooling due to thermal contraction. While all samples prepared up to 40 min did not show any signs of degradation, no stable samples could be fabricated beyond this time limit. The sintering temperature, pressure and heating rate as given in **figure 4.27** were chosen based on promising conductivity results from the previous chapters.

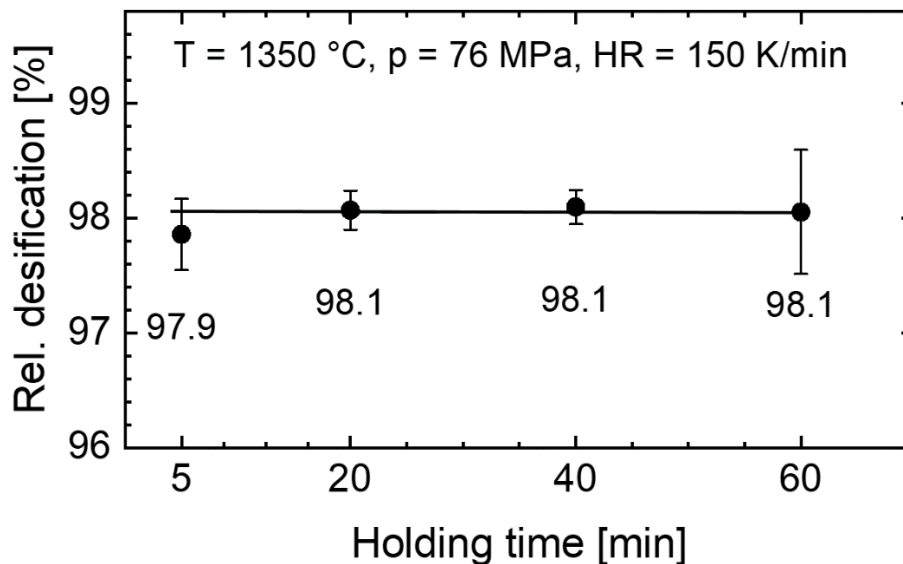


**Figure 4.27:** The relative densities of SPS BZCY72 samples at different holding times.

The results can be correlated to yttria stabilized zirconia (YSZ) investigated by Khor et al. The relative densification increased up to holding times of 3 min and remained constant [222]. Guillard et al. also reported increasing densities up to only holding times of 5 min for SiC and concluded that the dwell time is not as significant as other SPS parameters in this matter [200]. In this context, it should be mentioned that the holding time has more impact on the final sample density of BZCY72 samples when lower sintering temperatures are employed. Nevertheless, as with the heating rate, a higher sintering temperature is preferred over longer dwell times.

### 4.3.2 Crystallographic structure

The XRD patterns of the BZCY71 samples for different SPS dwell times are presented in **figure 4.28**. The obvious background aberration for 60 min comes from the sample holder, since less sample material could be used. Furthermore, it cannot be excluded that amorphous impurity phases are present as a result of extended diffusion and reaction processes. Otherwise, the XRD patterns do not show any difference in respect to the holding time. From the Rietveld refinement, no signs of Ba evaporation were observed up to 60 min holding time.

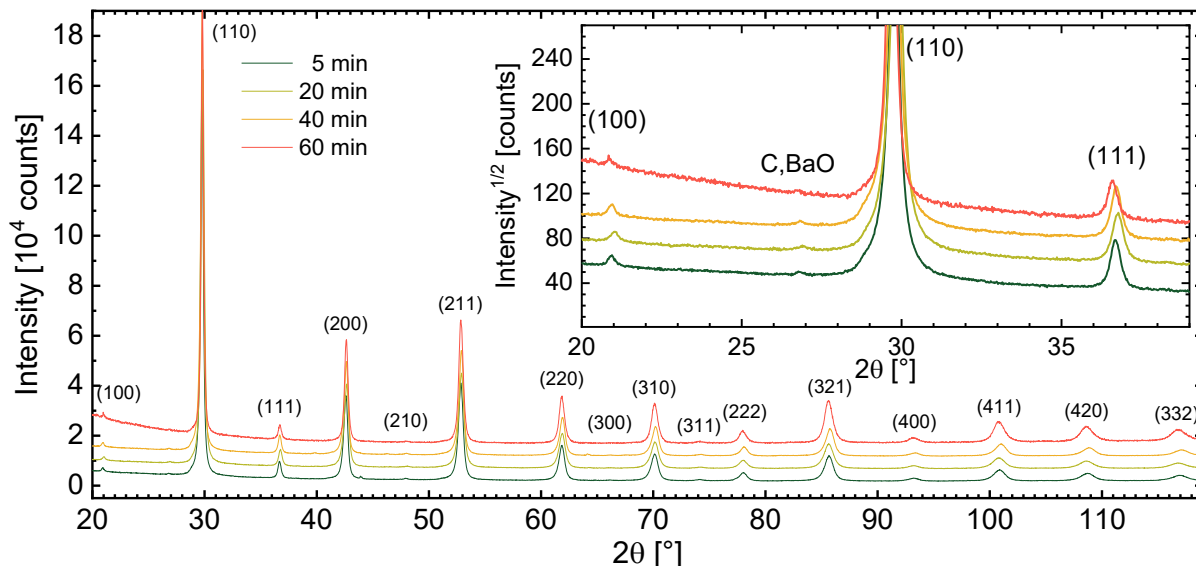


**Figure 4.28:** XRD patterns of the BZCY72 samples (vertically shifted) prepared by SPS at different holding times from 5 min to 60 min. The insert displays a close view on the impurities and peak shift.

A small peak shift in this series is observed from the inset of **figure 4.28** and from the lattice parameters in **figure 4.29a** (with additional information in **appendix 8.7.14**). A consistent trend with holding time is, however, not apparent, in agreement with the literature. Longer dwell times for the SSRS process caused Ba evaporation which led to a slight decrease in the lattice parameter of only 0.05 Å [109]. However, this phenomenon was only observed after 12 h dwell time – considerably longer than the holding times in this work. The crystallite sizes increase with longer dwell times, and so does the micro strain (**figure 4.29b**). The micro strain for the sample prepared with a 60 min dwell time is by far the highest of all investigated samples. One possible explanation are additional defects from extended carbon containing diffusion processes due to the longer dwell time.

Crystallite sizes may be expected to increase since growth processes advance with time in most materials as atoms have longer diffusion paths. From **figure 4.29c** and **4.29d** it appears that the perovskite geometry is barely changing for different times. The bond length follows the same trend as the unit cell volume and B – O bond angle, namely slightly increasing for the sample prepared at 60 min.

## Influence of holding time

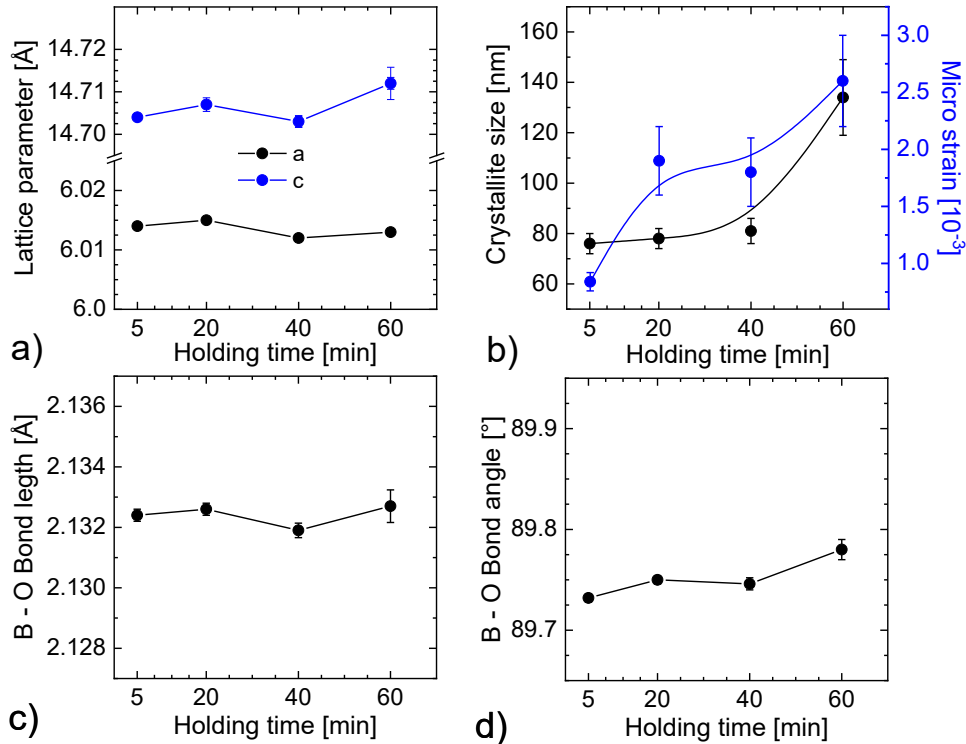


**Figure 4.29:** Results from the Rietveld refinement of the XRD pattern in figure 4.28. Lattice parameters (a), crystallite size (b), B site cation – oxygen distance (c) and angle (d) as a function of holding time.

The Raman spectra in **appendix 8.7.13** reveal major intensity differences in modes which was similarly observed for the outer regions in chapter 4.1.2 (**figure 4.8**). This can be interpreted as the result of advanced diffusion mechanisms and reduction of  $\text{Ce}^{4+}$  over longer dwell times.

### 4.3.3 Microstructure

The SEM images as well as the grain size distribution in **figure 4.30** clearly show drastically increasing grain sizes with longer holding times. After 5 – 20 min, the maximum densification is reached and grain growth is accelerated since the internal energy can only be further lowered by reduction of the total area of grain boundary [83]. As with the crystallite size, the mass transport processes (presumably grain boundary or volume diffusion) continue over the whole dwell time period. This is a well expected result and has been demonstrated by Khor et al. for SPS prepared YSZ where the grain size increased from 5  $\mu\text{m}$  for 1 min dwell time to 15  $\mu\text{m}$  at 12 min [222]. However, the discontinuous nature of the grain growth for SPS prepared BZCY72 samples as shown for preparation at 60 min dwell time leads to premature degradation due to microstrains. Some grains have sizes of 5  $\mu\text{m}$  while areas with smaller grains are still found, **figure 4.30**. The transition from 40 to 60 min dwell times appears very drastic, which was also confirmed in repetitions of sample preparation, **appendix 8.7.15**. Initially formed large particles (apparent in **figure 4.30** for a setting of 5min) may act as a nucleation for abnormal grain growth.



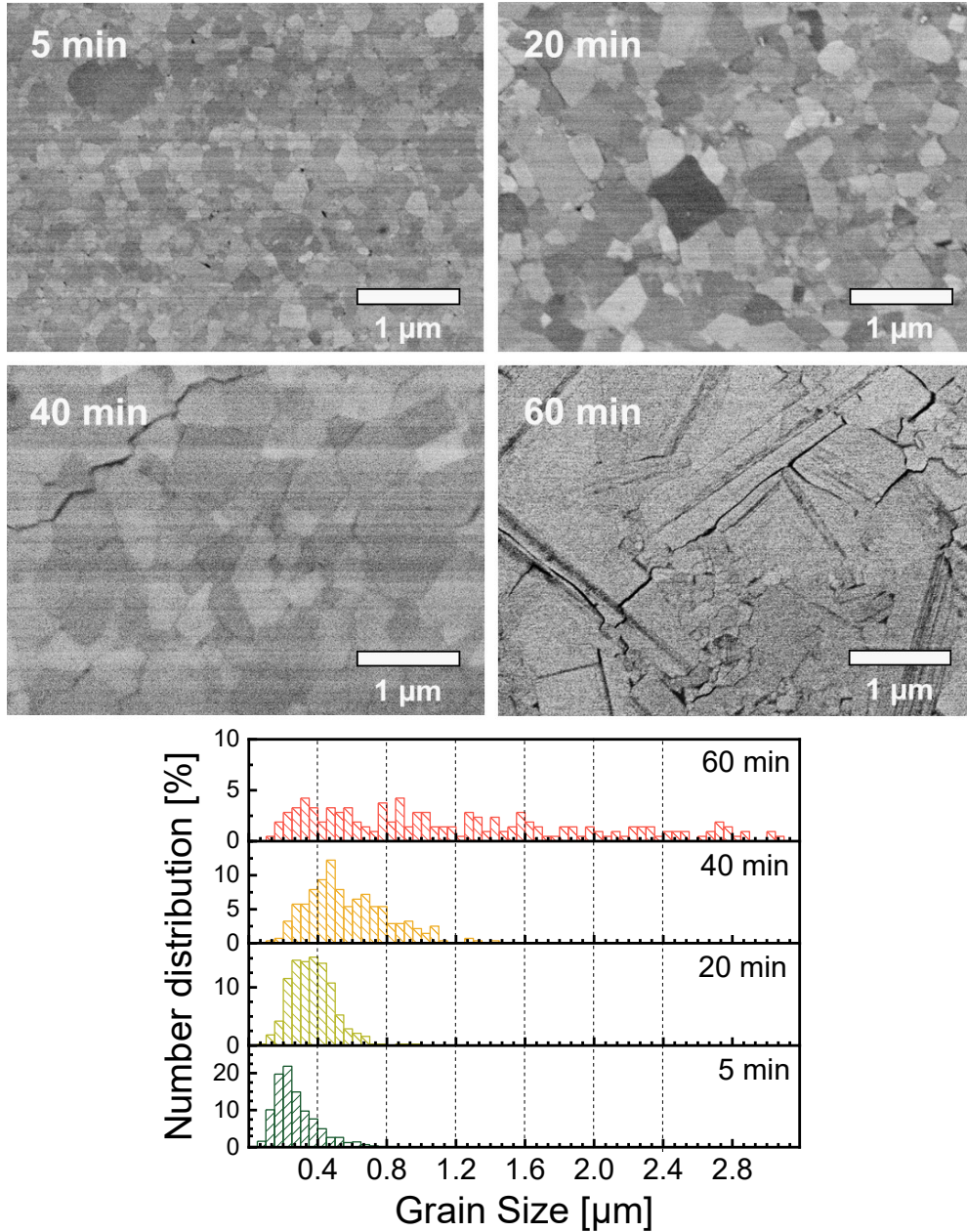


**Figure 4.30:** Top: SEM images of polished cross section of BZCY72 samples prepared by SPS at given holding times. Bottom: The corresponding grain size distribution for different holding times in SPS.

The larger grains exhibit a lower surface energy per unit volume. Accordingly, random diffusion events are more likely to happen at the expense of smaller grains. Moreover, abnormal grain growth results in increased micro-strain as suggested by XRD and can also lead to the formation of cracks where impurities could easily accumulate. Despite the discontinuous behavior of grain growth, some general trends may be observed. The grain boundary angles approaching 120 degree from 5 min to 40 min holding time. Nevertheless, inhomogeneous grain growth behavior provides a major challenge for achieving large-grained SPS BZCY72 specimens, because of stress and inhomogeneous enhanced diffusion.

### 4.3.4 Conductivity

Electrochemical data calculated and summarized in **table 4.4** as well as the corresponding Nyquist plots in **appendix 8.7.16** show results for different holding times. The grain boundary conductivity appears to be independent of the holding time across the whole measurement range. The bulk conductivity decreases with longer dwell times (**figure 4.31**). Results from spectroscopy suggest diffusion of C and reduction of  $Ce^{4+}$  as a possible explanation. Moreover, the electrical field during SPS affects all mobile charge carriers including  $Ce^{3+}$ ,  $[Y']$  and  $[V_O^{\bullet\bullet}]$  and lead to segregation of those elements. Presumably, more  $Y^{3+}$  accumulates into the space charge layers and oxygen vacancies segregate in the grain boundary core for longer dwell times. Interestingly, there was no increase in grain boundary conductivity observed, presumably due to dominance of the grain boundary resistance by other factors such as defect formation and presence of impurities

**Table 4.4:** Results of the IS data fitting at 300 °C in 3 % moist 5%  $H_2/Ar$  atmosphere. Resistance, capacitance and bulk dielectric constant for BZCY72 are presented for different holding times.

Holding time [min]	$C_1 [F \cdot cm^{-1}]$	$R_1 [k\Omega \cdot cm]$	$C_2 [F \cdot cm^{-1}]$	$R_2 [k\Omega \cdot cm]$	$\epsilon_r \text{ Bulk}$
5	$1.07 \cdot 10^{-11}$	4.06	$9.96 \cdot 10^{-10}$	495	68
20	$7.37 \cdot 10^{-12}$	17.16	$1.44 \cdot 10^{-9}$	549	135
40	$8.67 \cdot 10^{-12}$	21.15	$1.57 \cdot 10^{-9}$	581	148

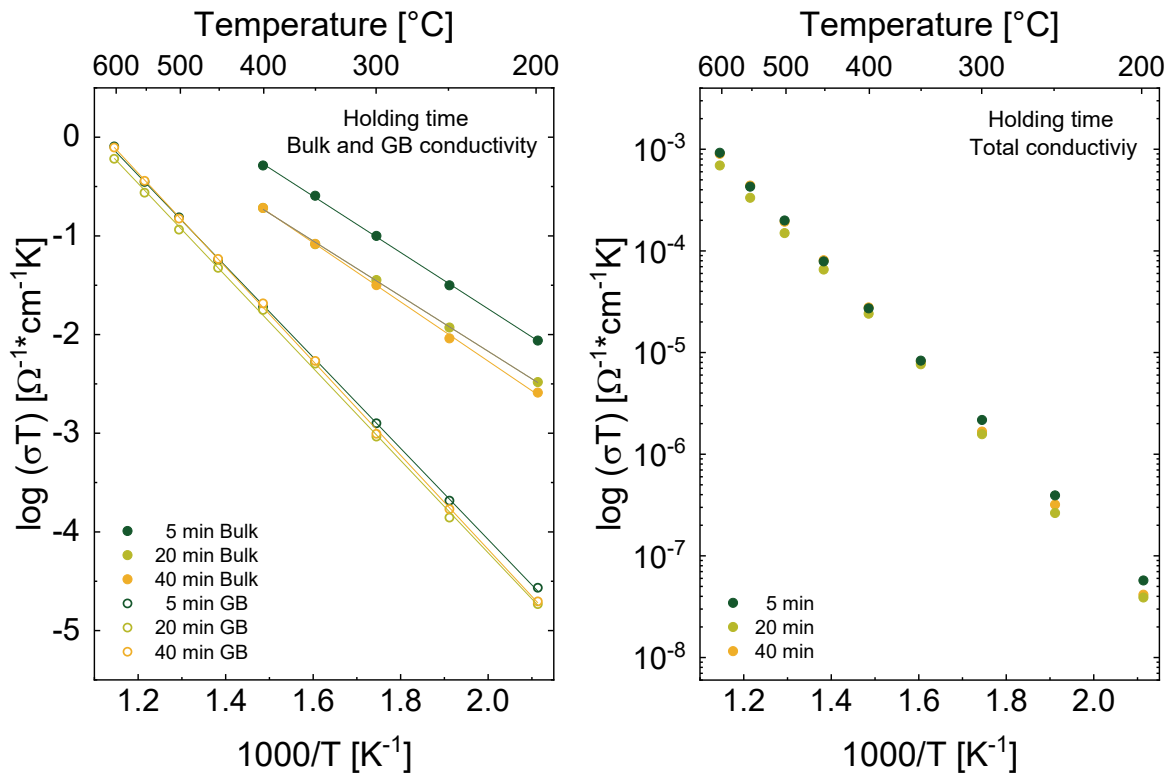


**Figure 4.31:** Arrhenius plots for bulk and grain boundaries as well as total conductivity of SPS BZCY72 samples prepared at different holding times in 3 %  $H_2O$  5%  $H_2/Ar$  atmosphere.



This suggests that longer holding times lead to an increase of the Schottky barrier height or a broader effective space charge layer width, limiting the total conductivity [174, 219]. Consequently, concentration of oxygen vacancies and, therefore, of protonic defects is reduced lowering bulk conductivity. This is confirmed by an increase of bulk dielectric constant with holding time by a factor of 2 over the investigated time range.

#### 4.4 Chapter summary

The influence of SPS process parameters on the BZCY72 sample properties is summarized in **table 4.5**. The sintering temperature had the most significant impact, because of its exponential contribution to the mass transport mechanism during the sintering process. At temperatures above 800 °C, the diffusion across the grain boundary (volume diffusion) seems to cross the activation energy for this material and becomes the dominant mass transport contribution during the heating step II. However, within the holding time (step III), a significant portion to the mass transport comes from evaporation from small grains that accumulate at larger grains. At 1650 °C and above this process is the dominant mass transport mechanism and is most likely responsible for the unstable pellets prepared at this temperature as suggested by pores within the grain boundaries in the SEM images. *With increasing temperature the samples were denser, exhibited larger crystallite and grain sizes and consequently higher grain boundary conductivities.* Other crystallographic attributes i.e. bond lengths between B-site cation and oxygen were less effected and are likely responsible for the nonlinear progression of the bulk conductivity as a function of sintering temperature. *Samples prepared by higher sintering temperatures indicated a slightly higher crystal symmetry* as suggested by the decreasing octahedra tilts with increasing temperatures. One possible explanation could be the evaporation small Ba amounts that cannot be detected by XRD. The change is only 0.1 ° for a 500 °C temperature difference. However, this could be sufficient enough to alter the arrangement to create more room for the octahedras.

The applied pressure plays a major role in densification at temperatures below 1450 °C. At 100 MPa, a relative densification of 96 % was archived at only 1250 °C. Furthermore, increased pressure lead to smaller unit cells within the BZCY72 samples, which is most likely an effect of the increasing micro strain and corresponding defects in the lattice. As a result, the B – O distance was shorter at higher applied pressures which lowered the bulk activation energy for the proton jumps and could in addition explain the increasing bulk conductivity. Grain sizes and grain boundary conductivity were not significantly affected by variation of the applied pressure. Within the investigated pressure range there were no indication of different active mass transport mechanisms. However, for pressures below 40 MPa the grain growth was enhanced. It can be assumed that further decrease in pressure will result in larger grains but at the cost of lower densification as observed from other synthesis routes.

As a result of *increasing heating rates, the BZCY72 exhibited higher grain boundary conductivities.* TEM investigation suggest that the grain boundaries are broader for lower heating rates. Presumably, mass transport processes across the grain boundaries only occur at higher temperatures due to the higher activation energy. Below 900 °C the dominant mass transport mechanism is the surface diffusion as it requires lower energies. In this context, the effective width of the space charge layer, a phenomenon responsible for the high grain boundary resistance in

## Chapter summary

BZCY72, could be determined. The space charge width is decreasing from 2.7 nm to 1.7 nm for higher heating rates. The reason behind this experimentally confirmed phenomenon is a higher Y-concentration within the grain boundaries for low heating rates. Since the Y dopant is negatively charged it presumably undergoes electro migration along the grain boundaries where it accumulates for a longer time in the case of a low heating rate. Crystallographic properties did not show variations, except for a slight decrease of the crystallite size.

An increasing holding time within the SPS process lead to larger crystallite sizes and grain sizes, since grain growth is most efficient during this sintering stage. Grain sizes of 3  $\mu\text{m}$  and more were observed at 60 min holding time. However, the grain growth was found to be inconsistent and abnormal, as small grains were still present in the microstructure. The longer holding time lead to carbon diffusion into the sample causing strain and cracking of the sample. Samples that remained intact did not show higher conductivity values presumably due to higher yttrium accumulation in the space charge layer.

The highest performance was achieved at a sintering temperature of 1350  $^{\circ}\text{C}$ , an applied pressure of 76 MPa, a heating rate of 150 K/min and a holding time of 5 min (see **appendix 8.7.18**). The Conductivity was  $\sigma = 1.25 \cdot 10^{-3} \text{ S}\cdot\text{cm}^{-1}$  and  $\sigma = 4.6 \cdot 10^{-3} \text{ S}\cdot\text{cm}^{-1}$  at 600  $^{\circ}\text{C}$  and 800  $^{\circ}\text{C}$ , respectively. A comparison with conductivities reported in the literature is given in **table 4.6**, showing promising performance of SPS sintered specimen. The higher total conductivity reported by Fish et al. was measured in a more  $\text{H}_2$  containing atmosphere which could improve the total conductivity if n-type conductivity is present [223]. Other authors archived improved conductivities only by employing SSRS due to the large grained samples produced by it and the resulting low grain boundary resistances. It should be noted, however, that due to the NiO sintering aid, there might be an n-type contribution which enhances the total conductivity but might not be suitable for an application.

## CORRELATION BETWEEN SPS PARAMETERS AND PROPERTIES OF BZCY72

**Table 4.5:** Overview off the effects on BZCY72 properties caused by SPS process parameter variation. Important property trends for applications are marked green (desirable effect) or red (adverse effect).

SPS parameter variation	Effect on BZCY72 attributes
<b>Increase of sintering temperature</b>	↑ Rel. density increases (only up to 1450 °C)
	→ Unit cell Volume remains constant
	↑ Crystallite size increases
	↑ Grain size increases
	↑ Bulk conductivity slightly increases
	↑ Grain boundary conductivity increases
<b>Increase of applied pressure</b>	↑ Activation energy increases
	↑ Rel. density increases
	↓ Unit cell Volume decreases
	↓ Crystallite size decreases
	↓ Grain size slightly decreases
	↑ Bulk conductivity increases
<b>Increase of heating rate</b>	→ Grain boundary conductivity remains constant
	↓ Activation energy decreases
	→ Rel. density remains constant
	→ Unit cell Volume remains constant
	↑ Crystallite size slightly increases
	→ Grain size slightly remains constant
<b>Increase of holding time</b>	→ Bulk conductivity remains constant
	↑ Grain boundary conductivity increases
	→ Activation energy remains constant
	→ Rel. density remains constant
	→ Unit cell Volume remains constant
	↑ Crystallite size increases
<b>Increase of holding time</b>	↑ Grain size increases
	↓ Bulk conductivity decreases
	→ Grain boundary conductivity remains constant
	→ Activation energy remains constant

**Table 4.6:** Comparison of total conductivities in this work and reported values from the literature related to BZCY72 prepared by SPS and SSRS.

Synthesis	Conditions	Total conductivity	Atmosphere	Ref
SPS	900°C, 5 min	0.1 mS · cm <sup>-1</sup> (550°C)	Air, 2.35 % H <sub>2</sub> O	[224]
SPS	1350°C	0.44 mS · cm <sup>-1</sup> (600°C)	H <sub>2</sub> , 3 % H <sub>2</sub> O	[99]
SPS	1350°C, 5 min	1.25 mS · cm <sup>-1</sup> (600°)	5% H <sub>2</sub> , 3 % H <sub>2</sub> O	This work
SPS	1350°C, 5 min	2.8 mS · cm <sup>-1</sup> (600°C)	9% H <sub>2</sub> , 3 % H <sub>2</sub> O	[223]
SSRS	1600°C, 16 h	1.3 mS · cm <sup>-1</sup> (600°C)	5% H <sub>2</sub> , 3 % H <sub>2</sub> O	[98]
SSRS	1550°C, 6 h	1.82 mS · cm <sup>-1</sup> (600 °C)	5% H <sub>2</sub> , 3 % H <sub>2</sub> O	This work
SSRS	1700°C, 6 h	1.89 mS · cm <sup>-1</sup> (600°C)	9% H <sub>2</sub> , 1.5 % H <sub>2</sub> O	[173]
SSRS	1575°C	2.08 mS · cm <sup>-1</sup> (600°C)	9% H <sub>2</sub> , 1.5 % H <sub>2</sub> O	[42]
SSRS	1600°C, 8 h	3.7 mS · cm <sup>-1</sup> (700°C)	5% H <sub>2</sub> , 3 % H <sub>2</sub> O	[225]



## 5 NEUTRON STUDIES OF THE PROTON TRANSPORT

The profound understanding of proton motions in proton conducting ceramics is important to determine material properties, such as dopant concentrations. New materials are specifically designed with the proton path in mind. Neutron scattering experiments offer the possibility to determine the proton mobility on an atomic length scale and correlate the macroscopic conductivity with the atomic level.

### 5.1 Proton diffusion by QENS

**Figure 5.1** displays the experimental data  $S_{\text{meas}}(\omega, Q)$  at various temperatures, while **appendix 8.8.1** shows the QENS spectra at different  $Q$  values. In both graphs the quasi-elastic component has a comparably small amplitude for both samples. Additionally, it decreases with increasing  $Q$  values.

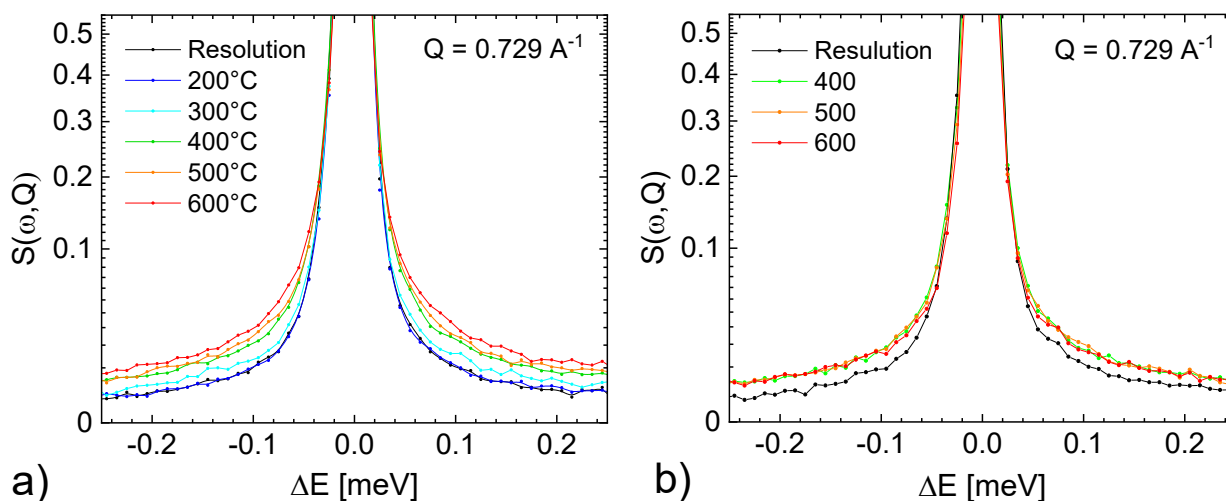


**Figure 5.1:** Corrected quasi-elastic neutron scattering spectra of hydrated BZCY72 prepared by SPS at (a) 1350 °C and (b) 1550 °C.

From **figure 5.1** it is evident that the quasi-elastic contribution appears broader with increasing temperature, which is expected for a thermally activated proton motion. Similar quasi-elastic broadenings were observed for samples sintered at 1350 and 1550 °C, suggesting the same characteristic timescale. However, the ratio between the elastic and total scattering intensity is smaller for the sample prepared at 1550 °C for all  $Q$  values. Since from XRD there is no evidence of a different structural geometry one reasonable explanation could be a different proton uptake, which is a known phenomenon from TGA measurement on similar samples (**appendix 8.6.5**). As shown in **appendix 8.8.1**, all spectra could be fitted using a Lorentzian quasi-elastic scattering function and an elastic delta function in convolution with the instrument resolution function as well as a linear background contribution, as exercised in equation 2.6. Even upon close inspection and brute force fitting, it was not possible to find a second stable Lorentzian. The dynamical window of the experiment was optimized to see translational diffusion. Localized motions of

trapped proton states near dopant sites, as suggested by Hempelmann et al. were not resolvable [226, 227]. Moreover, the rotation of the proton around the oxygen ions predicted by the Grotthuss mechanism were difficult to detect. For this reason, the proton jump behavior at temperatures of 400 °C and above manifests in one single Lorentzian.

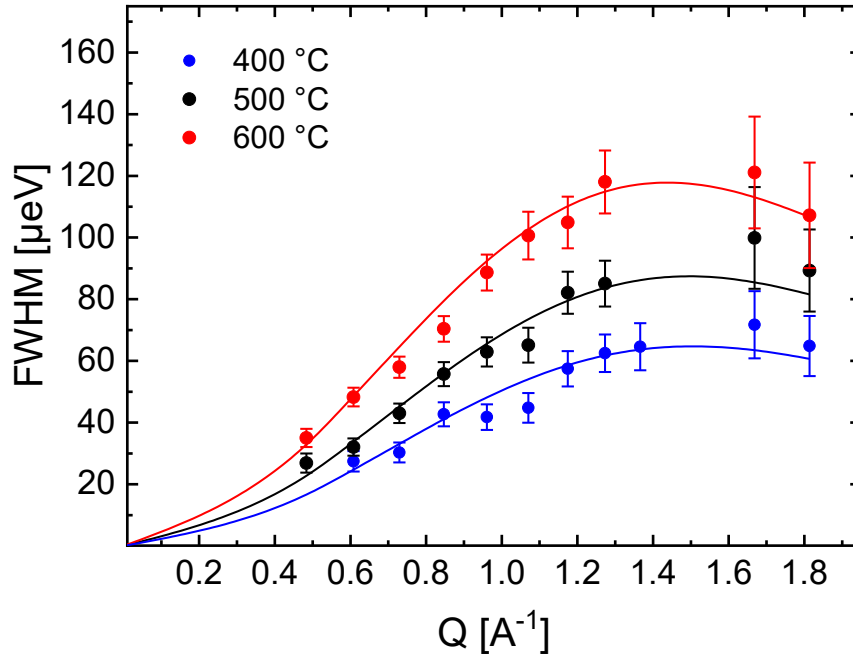


**Figure 5.2:** The quasi-elastic linewidths as a function of the scattering vector modulus  $Q$  and its accordance with the Chudley-Elliott jump model. Data points are the linewidths for the BZCY72 sample prepared at 1350 °C using the Chudley-Elliott model. The solid line represents the linewidth  $\Gamma(Q)$  calculated by eq. 2.7

The quasi-elastic linewidth as a function of  $Q$  is shown in **figure 5.2**. For small  $Q$  values, the FWHM is proportional to  $\frac{\hbar l^2}{6\tau} Q^2$  where  $l$  is the jump length and  $\tau$  the residence time, as described in chapter 2.3.4. At large  $Q$  values, the line width begins to oscillate around an average value given by  $\frac{\hbar}{\tau}$ . A similar behavior was reported for BCY20 by Chen et al. [228]. The lack of data points at  $1.25 < Q < 1.45$  is due to a Bragg reflex causing strong elastic scattering at this  $Q$  range.

**Table 5.1** summarizes the results for the fit employing equation 2.7. The diffusion constant is calculated by the expression  $D = \frac{l^2}{6\tau}$ . The jump distance coincides with the interatomic distance between two oxygen ions within the  $Pm\bar{3}m$  structure at a given temperature and confirms the interoctahedra transfer of protons as suggested by the Grotthuss diffusion [32, 62, 124]. Due to the thermal lattice expansion the jump distance increases with increasing temperature. A possible proton migration path is demonstrated in **figure 5.3**.

**Table 5.1:** Results of the Chudley-Elliott fit for both BZCY72 samples sintered at 1350 °C and 1550 °C.

T [°C]	T <sub>Sinter</sub> = 1350 °C			T <sub>Sinter</sub> = 1550 °C		
	l [Å]	τ [ps]	D [cm <sup>2</sup> /s]	l [Å]	τ [ps]	D [cm <sup>2</sup> /s]
400	2.98(5)	24.8(4)	5.97 · 10 <sup>-6</sup>	3.02(4)	22.2(2)	6.85 · 10 <sup>-6</sup>
500	3.01(7)	18.3(3)	8.25 · 10 <sup>-6</sup>	3.05(4)	15.89(9)	9.75 · 10 <sup>-6</sup>
600	3.12(5)	13.6(5)	1.19 · 10 <sup>-5</sup>	3.12(3)	12.03(7)	1.34 · 10 <sup>-5</sup>

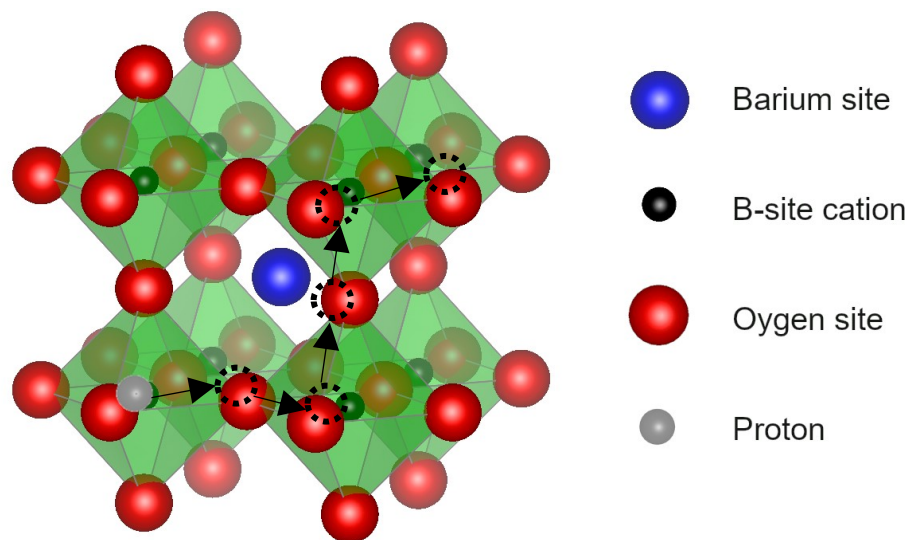


**Figure 5.3:** Schematic image of a possible migration path for the lateral proton diffusion, the mean jump distance is around 3 Å – the typical distance between oxygen atoms in  $Pm\bar{3}m$ .

Typical residence times between 10 and 25 ps were obtained which matches values reported for proton conductors [228]. As expected for diffusional behavior, higher thermal energy results in shorter residence times since the activation energy for the proton jump is easier to overcome. The observations moreover suggest slightly higher proton mobility for the sample prepared at 1550 °C which corresponds with the first conductivity measurements in chapter 4.1. The value obtained for the diffusion constant  $D \sim 0.6 - 1.3 \cdot 10^{-5} \text{ cm}^2 \text{ s}^{-1}$  is nearly two orders of magnitude higher than reported by Noferini et al. [229] but smaller than the values reported by Braun et al. [230] which both investigated BZY10. The activation energies for the proton jumps have been calculated to  $E_A = 0.16 \text{ eV}$  for BZCY72 prepared by SPS at 1350 °C and  $E_A = 0.17 \text{ eV}$  for the sample prepared at 1550 °C. The small difference is likely due to the different B – O bond distance for both samples, as suggested by XRD in **figure 4.5**. Both values are in good agreement with energies reported for the BZY10 parent compound [131, 230].

To further verify the results, an alternative calculation was employed. For low  $Q$  values the details about the jump mechanism are lost, because of the view on a large number of jumps simultaneously. In other words, the same expression to describe macroscopic diffusion can be used, known as Fick diffusion. The quasi-elastic peak broadening caused by the proton motion can therefore be simplified to [133, 230]:

$$\Gamma(Q) = 2\hbar D Q^2 \quad (5.1)$$

Here, the slope  $2\hbar D$  follows a linear trend as depicted in **figure 5.4** for both samples. Confirming the previous calculation, the diffusion constant increases with temperature and is larger for the sample prepared at 1550 °C, **appendix 8.8.2**. The activation energies were  $E_A = 0.17 \text{ eV}$  and  $E_A = 0.18 \text{ eV}$  for 1350 °C and 1550 °C preparation temperature, respectively, in good agreement with the values calculated from the Chudley-Elliot model, justifying the latter to be applicable.

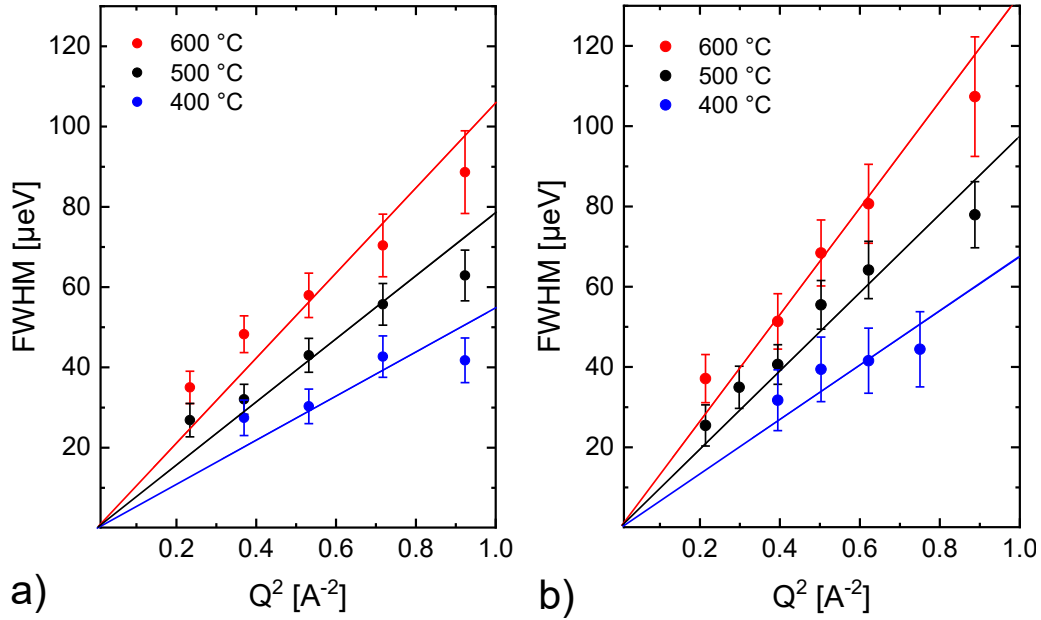


**Figure 5.4:** The Full width at half maximum (FWHM) plotted vs  $Q^2$  with a linear regression to determine to determine  $E_A$  for the proton jump diffusion: (a) BZCY72 prepared at 1350 °C and (b) prepared at 1550 °C.

An additional elastic window scan performed from 50 °C to 600 °C in the energy window  $\Delta E = 0.03$  meV (**figure 5.5**) shows an intensity anomaly at 300 °C. Since the incoherent scattering of neutrons gives information about the dynamics, this result suggests alternation within the proton movement within the BZCY72 structure. This can be interpreted as phase transition from  $R\bar{3}c$  to  $Pm\bar{3}m$  as reported by Mather et al. [124]. Presumably, the second order phase transition around this temperature to the more symmetric cubic space group enhances translational protonic diffusion at the expense of local diffusion.

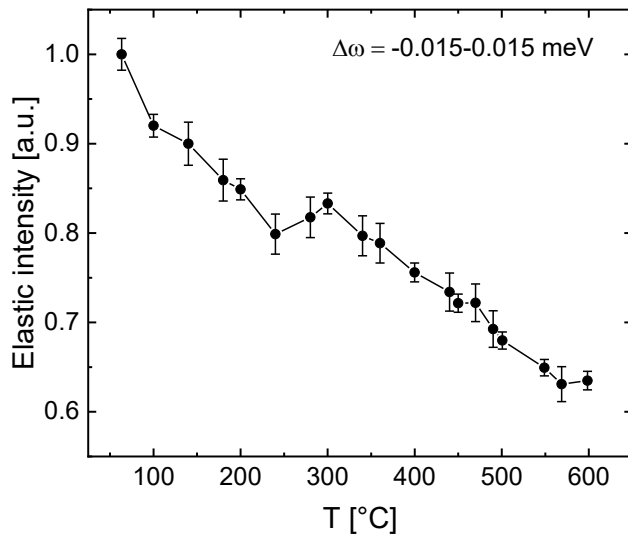


**Figure 5.5:** Elastic window scan for the BZCY72 sample prepared at 1350 °C. The peak at 300 °C can be interpreted as a proton dynamics change as a result of the phase transition from  $R\bar{3}c$  to  $Pm\bar{3}m$ .



To assess whether a further localized motion exists, a fit with a further Lorentzian line was applied in equation 2.6 instead of the background. A localized motion will contribute with a Lorentzian line, which is expected to be quite broad due to the fast localized motion and an elastic contribution. Detection of this fast motion proved to be difficult since the additional flat Lorentzian was spread out over a wide energy window that may be exceeding the energy boundaries of the measurement and hence difficult to separate unambiguously from vibrations. At a temperature of 500 °C it was possible to extract a meaningful elastic incoherent structure factor (EISF) which is the ratio of the elastic intensity and the total intensity (see **appendix 8.4.1**). The EISF is related to the motion geometry and is interpreted as the probability for a proton to be found in the same volume of space defined as  $2\pi/Q$  after a certain time  $t$  [130].

As suggested by Hempelmann et al., two models describing the localized motion were employed [231]. Firstly, a 180 degree jump around one oxygen site is considered where the FWHM for the second Lorentzian is fixed for different  $Q$  values. This is reasonable because for other perovskite proton conductors such as  $\text{SrCeO}_3$  no significant  $Q$ -dependence of the FWHM was observed for the rotational diffusion [226]. The second model represents an isotropic rotation on a sphere, which is a good approximation for the adjacent oxygen ions regularly formed around the protonic defect.

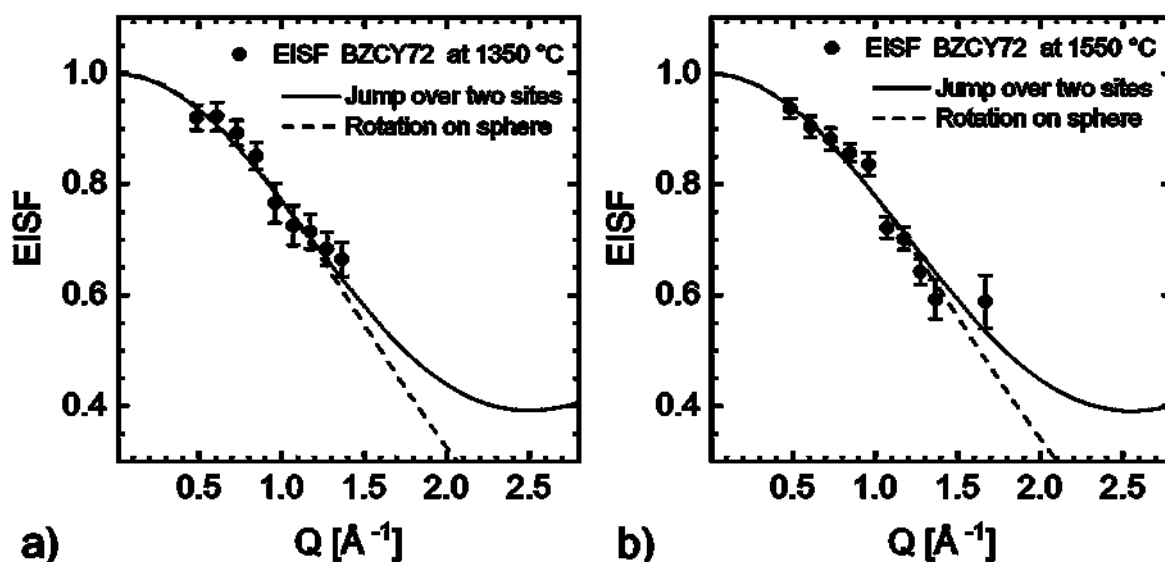


**Figure 5.6:** Elastic incoherent structure factor (EISF) at 500 °C of (a) SPS sample prepared at 1350 °C and (b) prepared at 1550 °C ( $p = 76$  MPa, HR = 150 K/min, 5 min dwell time). The measured data is marked by the symbols with error bars. The continuous line and dashed line represent the progression of the EISF modeled by a jump over two sites and spherical rotation, respectively.

**Figure 5.6** displays the elastic incoherent structure factor EISF for both BZCY72 samples prepared at 1350 °C and 1550 °C by SPS. Higher  $Q$  values could not be used due to the Bragg reflection. The calculation used for the two jump model and spherical diffusion is given in **appendix 8.4.1** and the fitted parameters are presented in **table 5.2**. The O – H distances obtained by the two-site jump model are smaller compared to the spherical diffusion with a radius of the motions of 0.90 and 1.02 Å, respectively. Matzke et al. reported a rotation radius of 1.1 Å using the model for the isotropic spherical rotation in  $\text{SrCeO}_3$  with a similar perovskite structure [226]. On the other hand, Mather et al. loaded BZCY72 with deuterium and determined an O – D distance

of 0.76 – 0.94 Å by neutron diffraction [124]. Considering the generally larger O – H distance the values from our QENS experiments are in good agreement. Furthermore, atomistic simulation techniques on BaZrO<sub>3</sub> provide additional accordance (O – H distance of 0.98 Å) [232]. For the rotational diffusion in SPS sintered BZCY72 the spherical rotation seems to be the underlying motion geometry. Both samples provide similar O – H distances within the error regime indicating no influence of the sintering temperature of this bond distance. A subsequent QENS experiment with a broader energy window (at least 2 meV [226, 231]) at a broader temperature range is required to uncover more details such as activation energy and timescales of the fast reorientation step of the Grotthuss mechanism.

**Table 5.2:** Resulting O – H distances for the two geometric models discussed in the text for SPS prepared samples at sintering temperatures of 1350 °C and 1550 °C.

	T <sub>Sinter</sub> = 1350 °C	T <sub>Sinter</sub> = 1550 °C
<b>Two-site jump model</b>	0.90(2) Å	0.88 (4) Å
<b>Spherical rotation</b>	1.02(4) Å	1.01(6) Å

## 5.2 Neutron Compton scattering and proton transports in BZCY72

In a preceding neutron diffraction experiment pellet at VESUVIO an alternative view on the crystal structure of BZCY72 was investigated. The neutron diffractograms of BZCY72 are shown in **appendix 8.8.3**. Excluding the d-space regions corresponding to peaks arising from the Al sample container, the quality of the refinement is satisfactory with an R<sub>wp</sub> value of 2.0 %. Mather et al. concluded from high resolution neutron and synchrotron X-ray diffraction experiments a phase transition from orthorhombic to rhombohedral symmetry at 85 K [124]. Within this work, a low temperature data refinement at 70 K affirmatively suggested the *Imma* space group at this temperature for BZCY72, while at 300 K the *R3c* space group resulted in the best fit. For the data recorded at 70 K, the fitted lattice are a = 5.990 Å, b = 8.508 Å, and c = 6.0193 Å. The lattice parameters for the data recorded at 300 K are a = 6.0246 Å, b = 6.0246 Å, and c = 14.724 Å. Those values are comparable to the results obtained by Marther et al., considering the different measurement temperatures. The ND refinement suggested a slightly (~ 0.5 %) larger unit cell compared to previous XRD investigations.

The localization of the hydrogen atoms within the hydrated sample turned out to be challenging, since fitting procedures had a tendency to locate hydrogen atoms pointing towards centers of the BO<sub>6</sub> octahedra, which was disproved by Kreuer et al. [32]. Previous XRD studies were carried out on pristine (free of hydrogen) BZCY72 samples, while the ND data was obtained for hydrated samples. By comparing the arrangements of the Ba, Y, Zr, Ce and O framework atoms the root-mean-square deviations (RMSDs) of both refinements were obtained and are shown within **appendix 8.8.4**. The RMSDs of oxygen atoms are ca. four (at 300K) to five (at 70 K) times bigger than the values for the other BZCY72 framework atoms, where the latter are almost identical at both temperatures. Thus, the presence of the hydrogen in the BZCY72 lattice causes a neglectable amount of lattice distortion for the cations but rather a displacement of the oxygen atoms placed at the corners of the octahedra. This effect is a direct consequence of the O – H bonding.

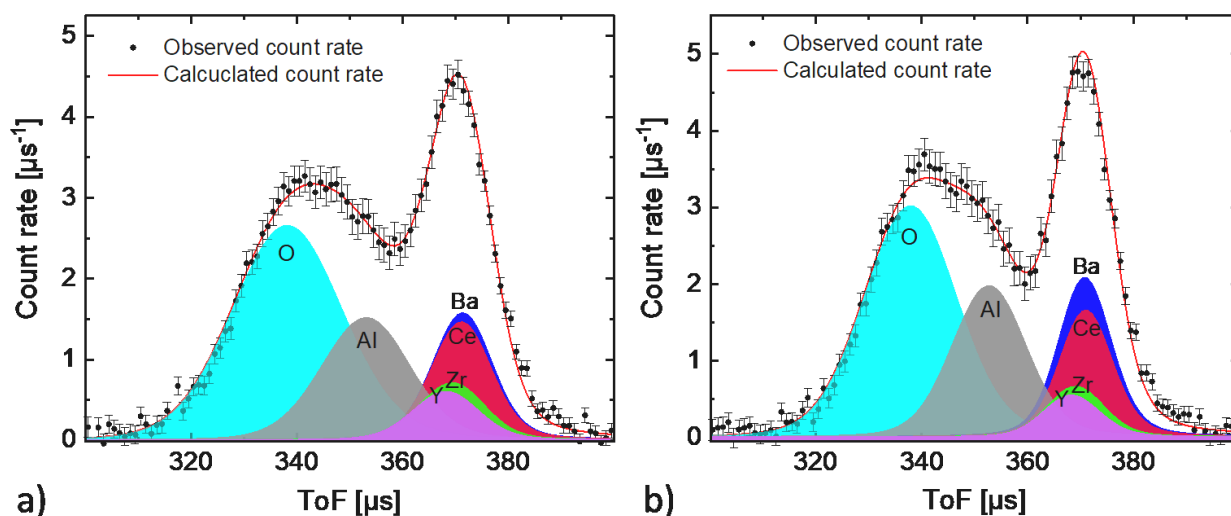


**Figure 5.7:** NCS data (black points) from BZCY72 (prepared at 1450 °C) at (a) 300 K and (b) 70 K recorded in backscattering after corrections described in section 2.3.5. The recoil peaks present in the corrected NCS data were fitted using Gaussian profile functions, shown as shaded areas with labels pertaining to respective atomic species present in the sample. The sum of the fitted recoil peaks is shown as a solid red line.

**Figure 5.7** displays the data generated from the neutron Compton scattering (NCS) experiments in backscattering after the correction as described in chapter 2.3.5. Due to kinematics of NCS, the single scattering events of protons present in the sample are not present in backscattering. The order of the recoil peaks of each element is determined by its atomic mass [137, 233-235]. Thus, oxygen appears at lower ToF values followed by Al from the sample container and the heavier nuclei (Y, Zr, Ba, Ce). Furthermore, the resolution is inversely proportional to the square of the recoiling mass [137, 233-235]. The BZCY72 cations recoil peaks are therefore closely stacked. Despite comparable cation masses, the widths of each peak could be fitted with satisfying precision as shown in **appendix 8.8.5**. As expected, the values of the widths are greater for larger nuclear masses and increase with increasing temperature in an almost monotonic manner. Thus, reflecting the Boltzmann population of partial vibrational densities of states contributing to respective peak Doppler broadening, a situation commonly occurring in the case of heavyweight nuclear species in condensed matter systems [137, 235]. Deviations from the harmonic lattice-dynamics predicted trends for the widths of nuclear momentum distributions as a function of temperature are most evident for O and Ce. The degree of binding or confinement is higher than expected and indicates strong anharmonicity for all nuclear species except for Ba, which is the only evenly distributed ion within this system. Material systems with anharmonicity also have low thermal conductivities as a consequence of enhanced phonon scattering [236-238]. While this has not been determined for BZCY72 directly, BaZrO<sub>3</sub> and BaCeO<sub>3</sub> both show low thermal conductivities [239, 240]. Additionally, the increase in the anharmonic character observed for Ce with increasing temperature seems to correlate with models and observations present in the literature suggesting that an increased level of cerium in BZCY is responsible for increased parameters, water uptake and increased conductivity (total and ionic) [41, 180, 241]. The behavior of Ce<sup>3+</sup> and O<sup>2-</sup> may therefore

be viewed as a sign for anharmonicity-driven mixed conductivity at higher temperatures as proved repeatedly in chapter 4. Observations based on NCS data recorded in backscattering therefore provide important information for the modeling and further understanding of proton conduction in BZCY72.

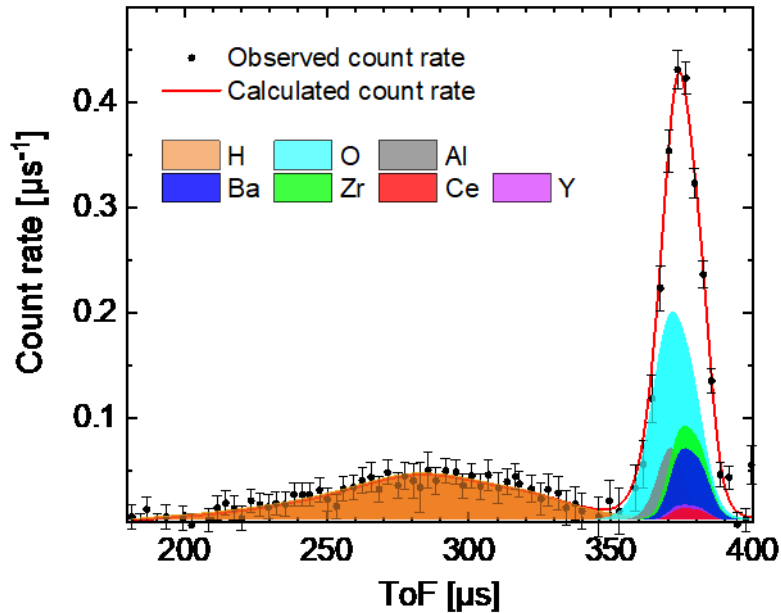


**Figure 5.8:** The mass-resolved NCS of BZCY72 (prepared at 1450 °C) in forward scattering at a temperature of 70 K. The black data points with error bars represent the corrected NCS data and the red solid line the total fit to the data. The shaded areas represent the contribution to the total count rate from individual nuclear mass species. The presented data has been corrected for multiple scattering and gamma background, according to the procedure described in section 2.3.5.

Further information is obtained from the NCS data recorded in forward scattering where the hydrogen is visible in **figure 5.8** as a broad and flat recoil peak (orange area). The heights and position of peaks arising from cations are different from the backscattering data due to different trajectories of the scattered neutrons in the  $Q, \omega$  domain during the measurement. The forward scattering data for all investigated temperatures is furthermore presented in **appendix 8.8.6**. In all graphs, a well-resolved hydrogen recoil peak is visible, enabling the quantitation of the hydrogen in BZCY72 as a function of temperature. In an NCS experiment, the peak area is proportional to the product of the total bound scattering cross-section and the number of moles per formula unit of the corresponding nuclear isotope [137, 242]. Following this correlation, the hydrogen concentration in BZCY72 is obtained as a function of temperature from the ratio of the integral scattering intensities of hydrogen and any heavier nuclear species. For the latter, Ba is chosen due to its non-statistical occupation and high integral intensity. Results of the hydrogen quantization together with the widths of the hydrogen momentum distributions are shown in **figure 5.9**.

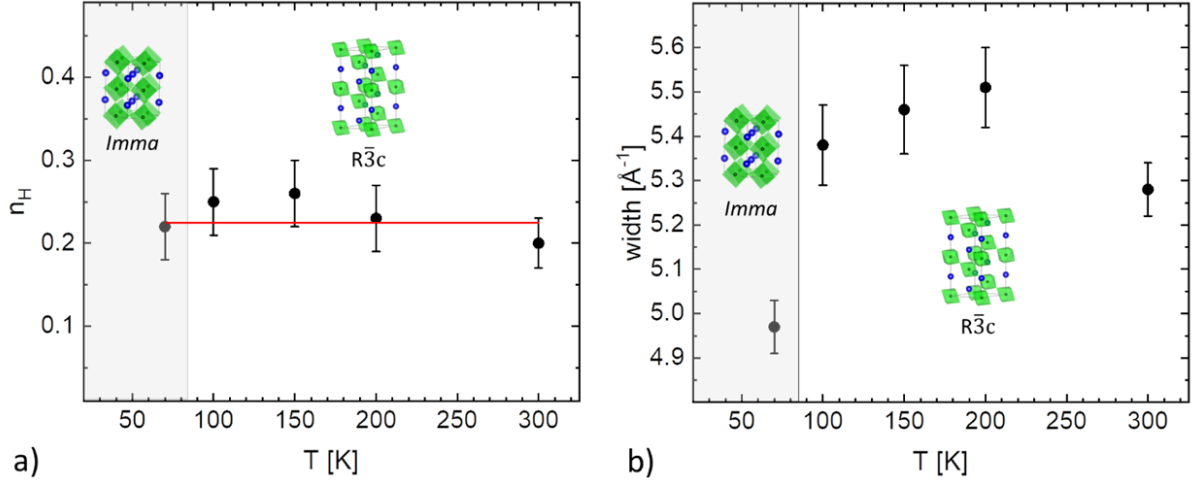


**Figure 5.9:** (a) The number of hydrogen atoms per formula unit ( $n_H$ ) of BZCY72 obtained as a function of temperature using the scattering intensities of H and Ba, fitted from mass-resolved NCS spectra recorded in forward scattering (b) Widths of the hydrogen momentum distribution in BZCY72 as function of temperature. The phase transition from orthorhombic to rhombohedral is marked as vertical line.

The number of H atoms per formula unit was found to be stable across the orthorhombic to a rhombohedral phase transition, averaging  $0.22 \pm 0.01$ . This value is in accordance with concentrations of protons in acceptor doped  $\text{BaZrO}_3$  and  $\text{BaCeO}_3$  at lower temperatures, and commensurate with the total concentration of vacancies [181]. From **figure 5.9b** there is a distinct increase of the hydrogen NMD width across the phase transition at 85 K as a consequence of the higher crystal symmetry from *Imma* to *R3c* space group and thus change in the degree of O – H bonding. Within the orthorhombic structure, there are two independent H –sites and the H NMD width results from the average between the two proton sites. On the other hand, there is only one proton site within the rhombohedral structure that should represent the NMDs of H above 85 K. Inspired by the NMD decrease at 300 K, further investigations at higher temperatures are highly desired to investigate the hydrogen bonding at operation temperatures.

### 5.3 Comparison with results from impedance spectroscopy

IS and QENS experiments are both capable to measure the mobility of the charge carriers. Complementary to QENS, in an IS measurement the conductivity  $\sigma$  can be translated into a diffusion constant  $D$  by the Nernst-Einstein equation [228, 230]:

$$D = \sigma \cdot \frac{k_B T}{e^2} \frac{V}{[OH^\bullet]} \quad (5.2)$$

where  $V$  is the unit cell volume determined by XRD,  $[OH^\bullet]$  is the protonic defect concentration which can be extracted from NCS or TGA measurements (**appendix 8.6.5**) and  $k_B, T$  and  $e$  have their usual meaning. The unit cell volume was taken from [180] for the pseudo cubic unit cell, which is implemented here because of the phase transition of BZCY72. From the NCS experiment in the previous section, the number of hydrogen atoms per formula unit was determined to 0.2

## Comparison with results from impedance spectroscopy

which is equal to the protonic defect concentration per formula unit. From TGA measurements, it is concluded that water loss and consequently charge carrier loss starts at 450 °C.

The resulting diffusion constants of all experiments are shown in **figure 5.10**. The activation energies obtained for bulk and grain boundary below 600 °C were 0.58 and 0.88 eV, respectively. Above 600 °C the activation energy for the grain boundary was 1.38 eV. Similar  $D(T)$  progressions were obtained for BCY20 by Chen et al. and resulted from other contributions and water loss at higher temperatures [228].

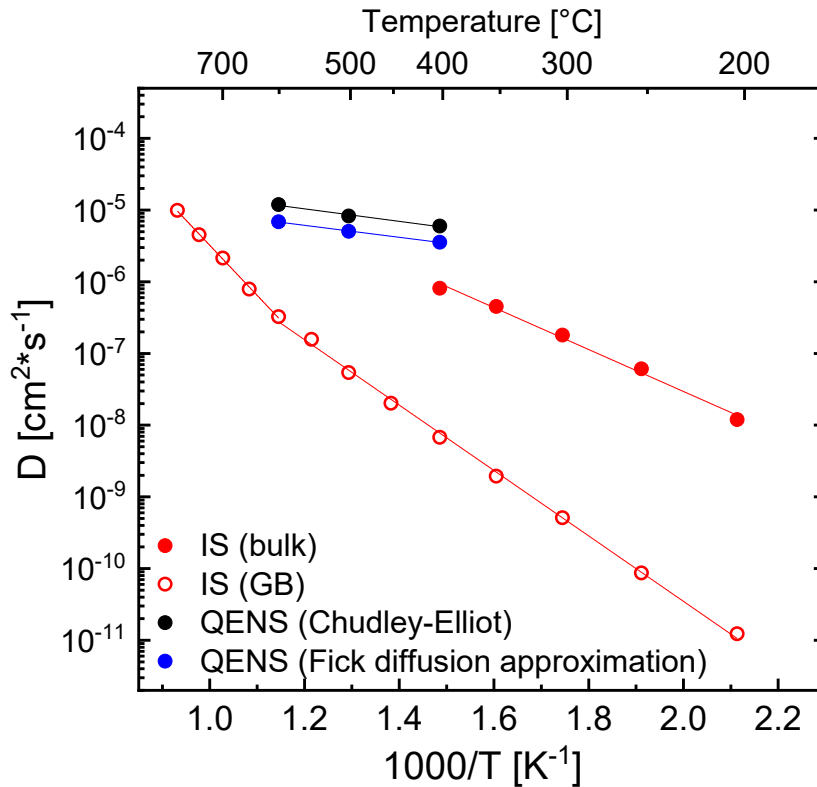


**Figure 5.10:** Diffusion constants obtained at various temperatures by QENS and IS compared for BZCY72 prepared by SPS at a sintering temperature of 1350 °C ( $p = 76$  MPa,  $HR = 150$  K/Min,  $t = 5$  min).

The diffusion coefficients measured by QENS are at least one order of magnitude higher than those extracted from the IS data. It should be noted, however, that the electric response in IS and neutrons for QENS are entirely different probes and thus, give different diffusion constants and activation energies. While the former measures the sum of proton diffusion and other diffusion (i.e. oxygen vacancies and electronic charge carriers) on a macroscopic scale, QENS investigates only the proton self-diffusion on an atomic scale [228, 230]. Thus, the protonic diffusion processes can be separated from other conductivity contributions. Diffusion constants are higher for QENS because it is also able to resolve fast local proton movements. From the progression of the diffusion constant of the bulk, it seems that it merges with the diffusion constant obtained from the QENS experiment 550 °C, as a result of the decreasing defect concentration [243]. QENS spectra for higher temperatures would be helpful together with IS to determine the ratio of protonic conductivity to total conductivity.

## 6 CO-SINTERING OF A MEMBRANE-ELECTRODE-ASSEMBLY

Electrolytes are often manufactured together with the supporting anode. Such Membrane-electrode-assemblies require carefully designed fabrication routes that consist of multiple steps. In the following chapter, a proof-of-concept for an SPS process for co-sintering of MEAs is provided.

### 6.1 Structural investigations

The electrolyte in ceramic based fuel cells is commonly co-sintered together with the composite anode. NiO is the most common used compound employed in anodes, applied as a BZCY7/NiO Cermet [26]. Synthesis is usually a two-step process, where the electrolyte is co-sintered with BZCY72/NiO first and subsequently, NiO is reduced to Ni in a second tempering, leaving a porous BZCY7/Ni composite electrode. Ni provides a good electronic conductivity and catalytic activity at PCFC operating temperatures of 500-600 °C. BZCY72 exhibits protonic conductivity and matches the thermal expansion coefficient of the cermet for the electrode [244]. Combined with the porosity of the electrode this provides a larger triple-phase boundary, where gas phase, electron and proton conductor coexist. Since SPS is used for synthesis of bulk materials, there are no studies investigating BZCY72 thin electrolytes. **Figure 6.1** shows the first thin-film-synthesis of an SPS BZCY72 on the minimum layer thickness for BZCY72 of < 200  $\mu\text{m}$ . Although, the layer remains intact at 200  $\mu\text{m}$  thickness, thinner layers are likely to break during SPS and contaminated with the electrode composite, as displayed in **figure 6.1b**. Reduction of the NiO to Ni in SPS BZCY72/NiO is shown in **figure 6.2** introducing porosity into the electrode layer. The reduction is not complete in all samples regions, i.e. the outer layers. Nevertheless, the results for this one-step process are encouraging. Samples with thickness below 200  $\mu\text{m}$  are challenging for preparation by SPS for the following reasons. First and foremost, depending on the tool diameter, the precursor powder is required to be evenly distributed inside the die. This is difficult to achieve for thinner layers. The second reason is percolation of the electric current through the thin electrically insulating layer, i.e. the electrolyte [245]. There are small channels through which the current is able to penetrate the BZCY72. If the layer is thin enough, mass transport along these channels occurs and leads to the impurities observed in **figure 6.1b**. Additionally, ceramic layers with thicknesses below 200  $\mu\text{m}$  are more fragile to mechanical stress during the sintering process, increasing the chances of crack formation.

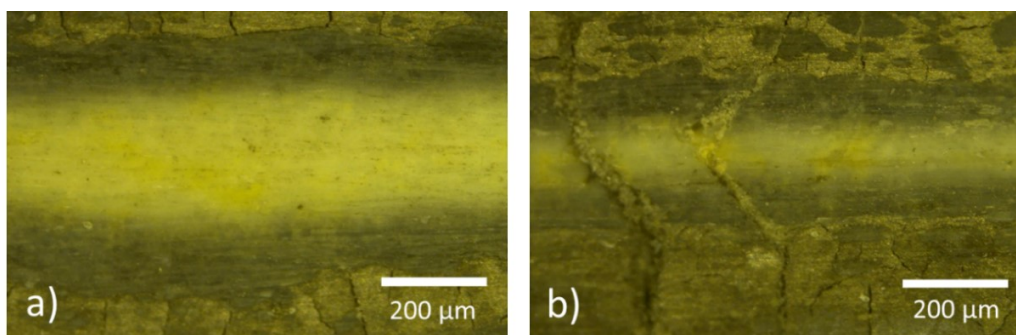


**Figure 6.1:** Microscopic images of the NiO-BZCY72 MEA co-sintered at 1350 °C, 76 MPa and 150 K/min heating rate: a) electrolyte thickness of 250  $\mu\text{m}$ , b) electrolyte thickness of 100  $\mu\text{m}$ .



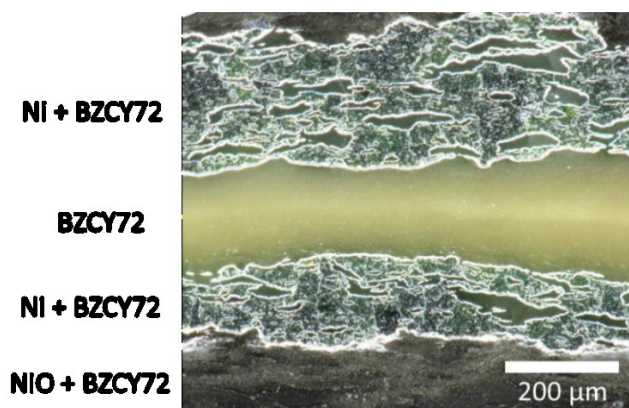


**Figure 6.2:** Microscopic images of the polished symmetrical cell with 200  $\mu\text{m}$  electrolyte layer thickness. The reduction of NiO only occurs close to the electrolyte layer and asymmetrical.

Unevenly distributed degree of NiO reduction may be attributed to the electric field in SPS. While NiO is fully reducing to Ni in air at 1000  $^{\circ}\text{C}$  [246], it is assumed that the BZCY72 electrolyte acts as a dielectric layer between two conductive electrodes during the process comparable to a capacitor. Consequently, the electric field varies within the sample which might affect the reduction processes. An alternative explanation might be oxidation of the sample when handled in atmospheric air after the sintering.

The **figure 6.3** displays the XRD patterns of the electrode regions with details given in **appendix 8.9.1**. The outer face of the MEA reveals the main phases of NiO and BZCY72 but also impurity phases such as  $\text{BaNiO}_3$  (PDF 00-029-0196) and  $\text{BaY}_2\text{NiO}_5$  (PDF 00-047-0090) in **figure 6.3a**. Both phases are known to form during co-sintering of NiO – BZY mixtures in solid-state synthesis from  $\text{BaCO}_3$  precursors [247-249]. Following this literature,  $\text{BaY}_2\text{NiO}_5$  forms at around 900  $^{\circ}\text{C}$  at only 2 wt% NiO addition and  $\text{BaNiO}_3$  forms at around 800  $^{\circ}\text{C}$ . In **figure 6.3b**, it appears that all NiO has been reduced to Ni. From calculated results, 82.1 wt% Ni which are present, much more than the nominal value of 60 wt% NiO. A possible reason is poor percolation of the BZCY72 phase. No impurity phases were observed in this part of the MEA. According to Tong et al.,  $\text{BaNiO}_3$  disappears at temperatures above 900  $^{\circ}\text{C}$ . Possibly, it was formed during the stage IV of the SPS process at the outer layers. Additionally, partial melting of the BaO-NiO mixed phase should be taken into consideration, referring to **appendix 8.2.1**, where the eutectic phase lowers the melting point down to 1400  $^{\circ}\text{C}$  which could locally be reached. During the cool-down and the solidification,  $\text{BaNiO}_3$  might emerge as a result. Further phases are C from the SPS environment and  $\text{BaCO}_3$  from the precursor powder.

The lattice parameters for Ni and NiO ( $Fm\bar{3}m$  space group for both) were refined to  $a_{\text{Ni}} = 3.524(1)$   $\text{\AA}$  and  $a_{\text{NiO}} = 4.178(1)$   $\text{\AA}$ , respectively. This is in good agreement with the literature [250, 251]. However, the BZCY72 unit cell observed for the electrode region is about 1.3 % smaller compared to the BZCY72 unit cell in the electrolyte. The lattice parameters are  $a = 5.980(3)$   $\text{\AA}$  and  $c = 14.714(14)$   $\text{\AA}$  as a result of the coexisting Ni phase where the atoms are more closely arranged. Similar trends were observed for functionally graded materials, where the unit cells of each material slightly adjust to each other [73, 252]. Even smaller lattice parameters were found for the NiO-rich part of the electrode with  $a = 5.968(4)$   $\text{\AA}$  and  $c = 14.686(13)$   $\text{\AA}$ . Ba-deficiency was observed by Rietveld refinement. This is most likely linked to the formation of  $\text{BaNiO}_3$  and



$\text{BaY}_2\text{NiO}_5$ . As a result of Ba deficiency, the unit cell volume is decreased down in accordance with reports by Yamazaki et al. [253]. The crystallite size for the BZCY72 within the electrode is in the same range as purely sintered BZCY72 under the same conditions at around 63 nm.

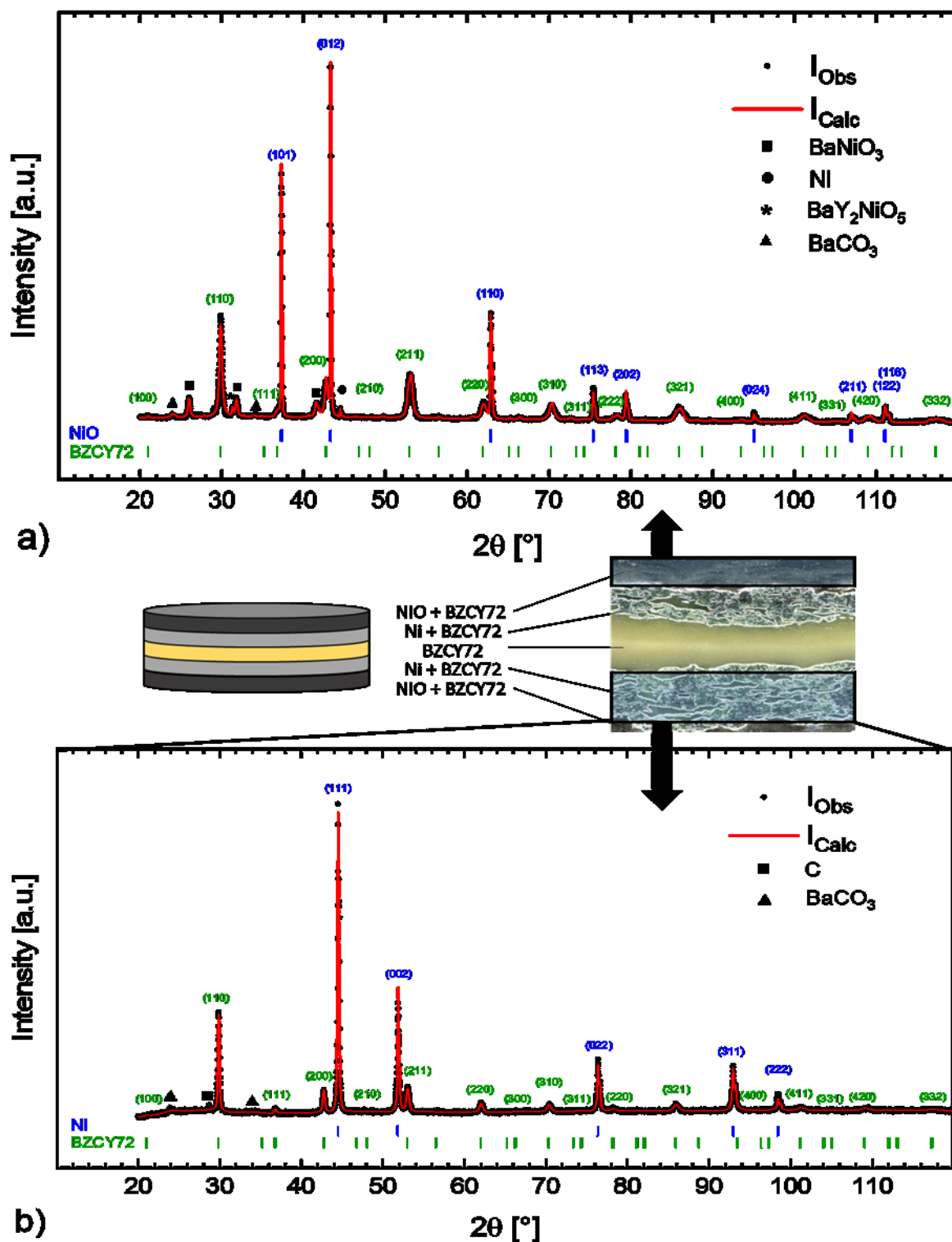


**Figure 6.3:** XRD patterns of the two different regions in the electrode of the NiO-BZCY72 MEA prepared at 1350 °C, 76 MPa, 150 K/min and 5 min holding time: a) non-reduced area, b) reduced area.

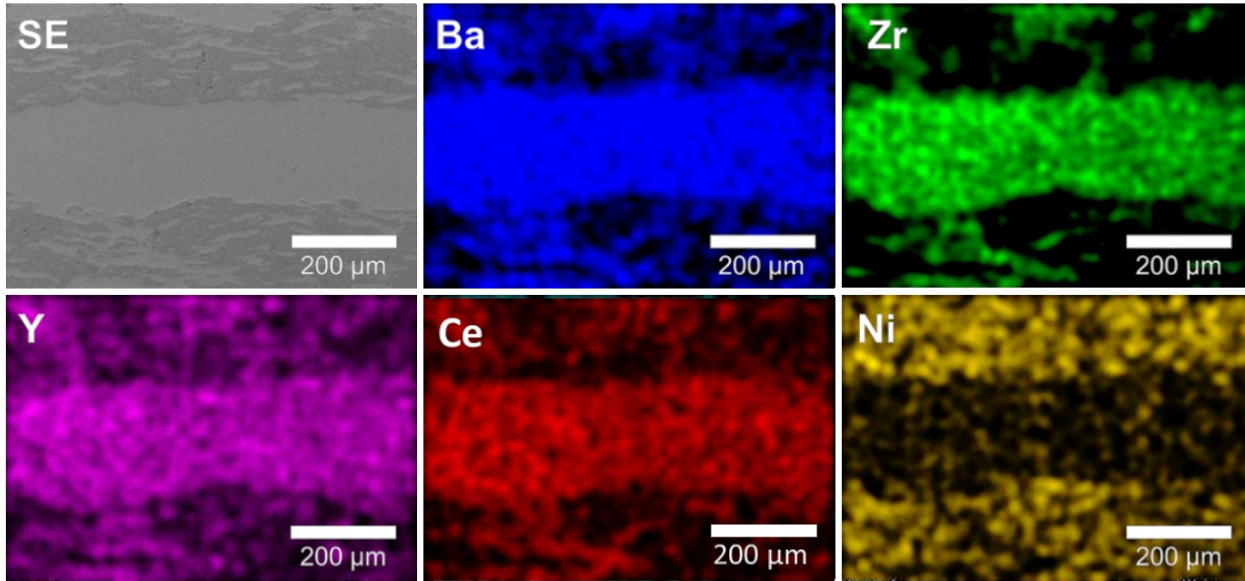


**Figure 6.4:** EDX analysis of the symmetric NiO-BZCY72 cell prepared at 1350°C, 150 K/min and 76 MPa.

**Figure 6.4** shows the elemental distribution of the symmetrical NiO-BZCY72 cell. The layers are well separated. As already evident from the previous images, BZCY72 and NiO are not homogeneously distributed within the electrode. Instead, BZCY72 is present within the elongated hotspots that form under the pressure during the SPS process. Nevertheless, within the BZCY72 electrolyte layer, all corresponding elements are uniformly distributed. Furthermore, there are also small quantities of Ni present in the BZCY72 electrolyte as a result of diffusion.

Upon closer inspection in **figure 6.5**, the grains are significantly larger compared to previous pure BZCY72 samples by SPS under similar conditions. An average grain size of  $(910 \pm 120)$  nm was determined by SEM which corresponds to an increase of 200 %. The grain boundaries are smooth compared to the sharp grain edges observed for BZCY72 (**figure 4.9**). The positive effect of small amounts of NiO (as suggested by EDX) on the grain growth in barium zirconates is well established within the literature and utilized in SSRS [9, 42, 98, 103, 248] which was covered in section 2.1.2.

The interface between electrode and electrolyte remains a challenge due to the different expansion coefficients combined with the high heating and cooling rate in SPS which causes fissures along the boundaries as shown in **appendix 8.9.2**.

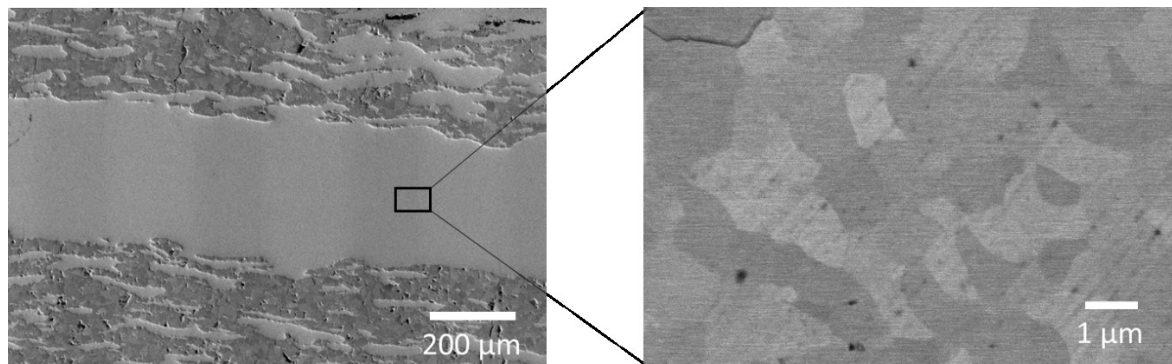


**Figure 6.5:** SEM image of the BZCY72 layer and its microstructure prepared at 1350 °C and 76 MPa.

## 6.2 Electrical investigations

In order to carry out conductivity measurements, the outer layer of the MEA-faces containing NiO was polished to provide evaluable data as shown in **figure 6.6**. There are four contributions. The  $R_1C_1$  arc (enlarged) could be from the bulk of the electrolyte layer with a capacity of  $C_1 \sim 10^{-11}$  F. The  $R_2C_2$  arc may be the bulk contribution of the BZCY72 inside the electrode region since it has a similar capacity but a much higher resistance due to the poor percolation of the BZCY72 as suggested by XRD. The  $R_3C_3$  arc could be attributed to the grain boundary resistance of the cell with a capacity of  $C_3 \sim 10^{-9}$  F. The  $R_4C_4$  contribution with a capacity of  $C_4 \sim 10^{-6}$  F may be related to the electrode. The calculated data for each RC element are given in **table 6.1**. The bulk conductivity obtained for the electrolyte is  $2.29 \cdot 10^{-3} \text{ S} \cdot \text{cm}^{-1}$  at  $400 \text{ }^\circ\text{C}$  which is considerably higher compared to the bulk conductivities of other samples covered in this work and not far from the highest reported bulk conductivities of  $1.2 \cdot 10^{-2} \text{ S} \cdot \text{cm}^{-1}$  at  $450 \text{ }^\circ\text{C}$  by Haile et al. for this material class [9]. Presumably, due to the larger grains, the GB resistance was observed to be lower compared to electrolytes investigated in chapter 3 and 4. Nevertheless, the poor percolation of BZCY72 in the electrode might limit the ionic pathways and results in high  $R_4$  values.

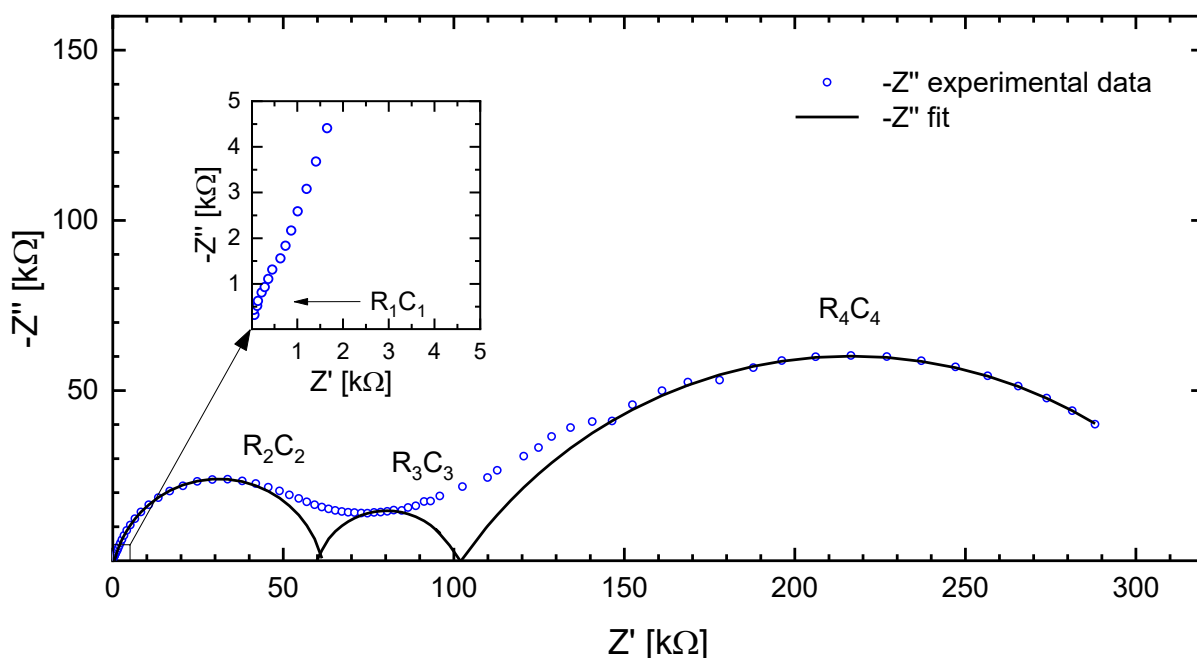


**Figure 6.6:** IS data obtained at  $300 \text{ }^\circ\text{C}$  in  $3 \text{ } \%$   $\text{H}_2\text{O}$   $5 \%$   $\text{H}_2/\text{Ar}$  atmosphere for the MEAs prepared by SPS. The high frequency region of the Nyquist plot is magnified to emphasize the show the  $R_1C_1$  contribution.

**Table 6.1:** Details of the IS experiment on the symmetrical NiO-BZCY72 cell. All values were obtained in  $3 \text{ } \%$   $\text{H}_2\text{O}$   $5 \%$   $\text{H}_2/\text{Ar}$  atmosphere at the given temperatures.

	Bulk electrolyte	BZCY72 electrode	GB	Electrode
<b>R (300 °C)</b>	411 $\Omega$	60.97 k $\Omega$	41.15 k $\Omega$	228.7 k $\Omega$
<b>C (300 °C)</b>	$5.34 \cdot 10^{-11}$ F	$7.13 \cdot 10^{-11}$ F	$9.46 \cdot 10^{-9}$ F	$1.10 \cdot 10^{-6}$ F
<b><math>\sigma</math> (400 °C)</b>	$2.29 \cdot 10^{-3} \text{ S} \cdot \text{cm}^{-1}$	$5.71 \cdot 10^{-5} \text{ S} \cdot \text{cm}^{-1}$	$2.61 \cdot 10^{-5} \text{ S} \cdot \text{cm}^{-1}$	$1.69 \cdot 10^{-5} \text{ S} \cdot \text{cm}^{-1}$
<b><math>\sigma</math> (600 °C)</b>	-	$6.34 \cdot 10^{-4} \text{ S} \cdot \text{cm}^{-1}$	$9.65 \cdot 10^{-4} \text{ S} \cdot \text{cm}^{-1}$	$3.16 \cdot 10^{-4} \text{ S} \cdot \text{cm}^{-1}$



## 7 CONCLUSIONS

### 7.1 Summary

Sintered specimen of the state-of-the-art ceramic proton conductor  $\text{BaZr}_{0.7}\text{Ce}_{0.2}\text{Y}_{0.1}\text{O}_{3-\delta}$  were successfully prepared by spark plasma sintering. This work demonstrates the possibilities but also the challenges for the preparation of BZCY72 ceramic proton conductors by SPS.

The first part was to investigate to what extent the SPS route is viable to synthesize barium zirconate based proton conductors suitable for applications. An important aspect is the relative density where SPS provides an attractive approach to produce BZCY72 pellets with densities near 100% and high phase purity in a rapid process. Bulk proton conductivities were exceeding state-of-the-art solid state reactive sintering since Ba-evaporation is avoided and no impurities diffuse into the grain interior. However, the grain boundaries exhibited high resistivity due to the space charge layer formed around the grain boundary core. Determined by the SPS process, sintered specimens were characterized by small grain sizes. This translates to high grain boundary densities in the case of BZCY72 which is a severe drawback for applications as electrolyte materials.

The objective was to investigate the effect of the SPS process parameters on the properties of the resulting BZCY72 samples to study the most favorable conditions for enhanced grain growth and conductivity. One approach to improve the grain growth is to enhance diffusion processes across the grain boundaries by increasing the sintering temperature. Within a wide range of investigated sintering temperatures, it was shown that the total conductivity of the samples decreases above 1450 °C despite larger grains. Raman studies suggested a significant increase in  $\text{BaCO}_3$  impurities which arises due to the enhanced diffusion of C from the surrounding die during the process and negatively affects the mechanical integrity of BZCY72. A second and more effective way to enhance the grain boundary conductivity is to reduce the space charge layer width. The Schottky barrier height, as well as the space charge layer width were calculated for various heating rates. The results suggested that higher heating rates lead to decreased space charge layer widths. This could be verified by TEM measurements which indicated smaller grain boundary widths for increasing heating rates. The third approach for increasing grain growth is application of longer holding times. However, this was shown to be limited by the abnormal grain growth behavior and resulting microstrain suggested by SEM and XRD, respectively.

The best conditions for BZCY72 in terms of its desirable properties are a sintering temperature of 1350 °C, an applied pressure of 76 MPa, a heating rate of 150 K/min and a holding time of 5 min. The best achieved total conductivity at 600 °C in wet 5 %  $\text{H}_2/\text{Ar}$  atmosphere was  $1.25 \cdot 10^{-3} \text{ S} \cdot \text{cm}^{-1}$ . Even though descent conductivity level can be reached by SPS, the SSRS synthesis route provides overall better conductivity for BZCY72 samples. For a broad commercialization the conductivity needs to be around  $10^{-2} \text{ S} \cdot \text{cm}^{-1}$  at 600 °C.

The purpose second part of this thesis was to improve the understanding of the proton conduction mechanism. For the first time quasi-elastic neutron scattering was employed to access the two underlying local motions within one energy window. The results confirm that protons move through the lattice by successive jumps along the oxygen ions as suggested by the Grotthuss mechanism. The data could be fitted according to the Chudley-Elliott model. QENS studies have shown that the typical residence time of the proton at an oxygen site is around  $2 \cdot 10^{-11} \text{ s}$  with a

## Summary

jump activation energy of 0.17 eV which gets smaller for decreasing B – O distances. Additionally, rotational motions of the proton around the oxygen sites could be implemented with a reasonable O – H distance of 0.9 - 1.01. The EISF of this local motion could be modeled as either a 180 degree jump over two sites or a rotation around a sphere. Diffusion constants obtained by QENS and impedance data could be compared and suggested that there are significant other than proton conductivity contributions especially within the grain boundaries, which are mostly electron-holes and possibly cerium polarons according to obtained progressions of the conductivity as a function of oxygen partial pressure.

The phase transition of BZCY72 from  $R\bar{3}c$  to  $Pm\bar{3}m$  suggested a decrease in local protonic motion, indicating an enhanced translational protonic diffusion for the cubic symmetry. Likewise, the transition from  $Imma$  to  $R\bar{3}c$  could be observed by the change of the nuclear momentum distribution of the incorporated hydrogen due to reorientation of the O – H bonds.

For the first time, a mass selective view of the combined thermal and nuclear quantum effect on the local, effective binding of atomic species present in hydrated BZCY72 was given. The NCS analysis of the proton momentum distribution reveals that the concentration of the hydrogen in the BZCY72 lattice is constant across the orthorhombic to rhombohedral phase transition and further down to the room temperature. Moreover, the average hydrogen concentration obtained from the NCS analysis seems to be commensurate with the total vacancy concentration in BZCY72 framework.

A co-sintered BZCY72/NiO symmetrical cell (MEA) was synthesized by SPS for the first time. It was shown that the state-of-the-art two-step process of co-sintering and NiO reduction could be achieved in one SPS process. The minimum thickness of a BZCY72 electrolyte layer that remained stable was 200  $\mu\text{m}$ . Nevertheless, both outer layers of the electrodes still had significant amounts of NiO and Ni diffused into the electrolyte layer. The latter effect increased the grain size. Bulk conductivities were higher compared to pure BZCY72 samples, although this might be an effect of additional non-protonic conductivity contributions.

Without significant grain growth in SPS, further increase of the conductivity cannot be expected. Moreover, the fabrication of thin electrolyte layers below 10  $\mu\text{m}$  with large electrode areas by this technique is unrealistic. Therefore, the preparation of electrolyte layers for fuel cells by SPS in a direct approach is not recommended. Other synthesis routes i.e. SSRS or tape casting and additional tempering provide solutions to the challenges mentioned above and are commonly used today. In electrolyzers, however, thicker electrolytes that are producible by SPS could be employed when used in high pressure environment. Due to the cost efficiency and large scale capability of SPS, MEAs produced by this technique might be able to find such niche applications and is most certainly a worthy route to follow in the future.

## 7.2 Outlook and future work

The development of proton conducting electrolytes for energy conversion devices remains a wide open field and interest of the research and industry. Up to this day BZCY72 is still considered the most promising electrolyte candidate for PCFCs or PCECs. Lowering the high grain boundary resistivity would give electrochemical cells a remarkable field for applications. Fabrication of BZCY72 self-supported electrolytes by SPS is unlikely to lead to further improvement. For this reason, the best alternative for SPS is the preparation of BZCY72 or other ceramic targets for sputtering deposition if thin layers are required. This synthesis route is highly suited for this approach due to the high densities, mechanical stability and reasonable purities. Material deposition by magnetron sputtering using ceramic targets prepared by SPS provides thin electrolyte layers under 10  $\mu\text{m}$  thickness that could pave the way for future applications for PCFC such as ammonia synthesis and processing.

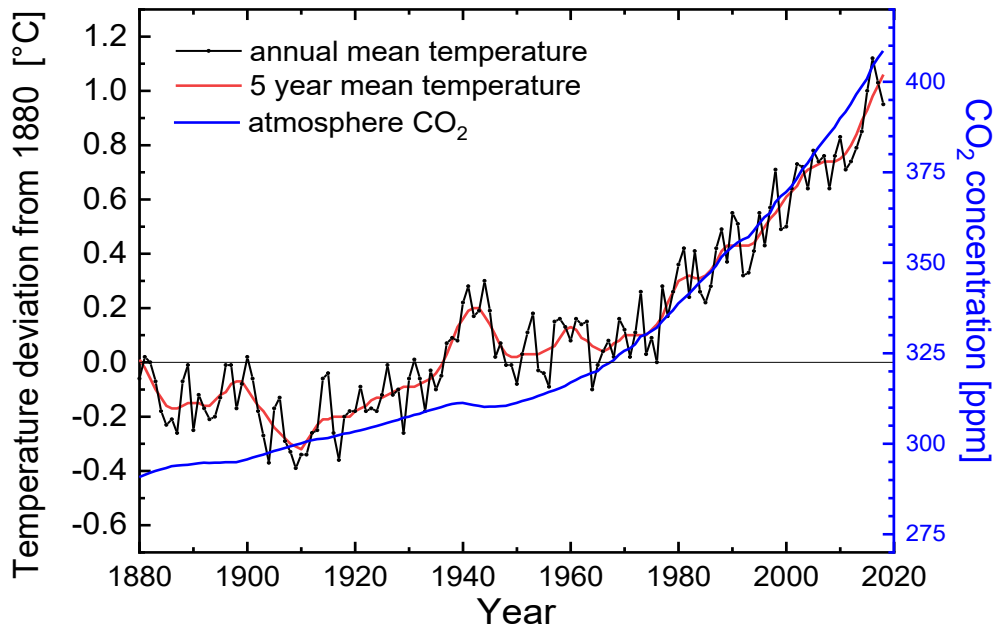
However, independently of this alternative path, there are still other open questions regarding the properties of BZCY72 prepared by SPS. So far, the mechanical properties were only superficially covered by the samples extrinsic integrity. The Vickers hardness and fracture toughness of BZCY72 would be of great interest from an applications' perspective. Higher pressures during the SPS process could lower the sintering temperature even more, although this would mean using SiC composite dies in the setup. Such a high pressure experiment would give more insight into the crystallographic attributes as a function of applied pressure, since the defect formation that causes the decreasing lattice parameters remains unclear at this moment. More TEM experiments are also desirable due to the importance of the grain boundaries in this material. Especially the effect of the temperature and holding time on the space charge layer could be revealed to further understand the conductivity behavior. More and recurring experiments on the holding time should be carried out to observe the grain growth more thoroughly.

From the experimental physics perspective, a subsequent QENS experiments at higher temperatures up to 900  $^{\circ}\text{C}$  gives more precise results of the translational proton diffusion and jump activation energies. More importantly, the energy window could be varied to further investigate on other proton dynamics. While a broader window would give more insights into the rotational diffusion, a narrower window would be used to reveal the proton trapping at the Y sites. As for the Neutron Compton scattering, more spectroscopic work above room temperature is highly desired in order to fully understand the structure-properties relationship in hydrated BZCY72 with the ultimate goal of being able to engineer the conductivity of this technologically important system. Ideally, those findings should be augmented by *ab initio* density functional theory modelling.

This context leaves also room for sintering aids. As demonstrated in chapter 6, the diffused NiO had a positive effect on the conductivity in the BZCY72 electrolyte layer. Small amounts under 0.5 wt% of commonly used sintering aids such as NiO, CoO or ZnO could significantly improve the grain growth and are worth investigating. The co-sintering of NiO-BZCY72/BZCY72/NiO-BZCY72 MEAs by SPS provides a very cost-efficient method, although a better understanding is required. Sinter parameters should be varied more and further conductivity measurements of such a system are of high interest. As the transition from bulk materials to thinner layers and the influence of the electrodes changes the material properties of SPS BZCY72, further synthesis experiments should reveal the potential of this novel approach.

## 8 APPENDIX

### 8.1 Introduction



**Appendix 8.1.1:** The world-wide temperature anomaly since the beginning area of the industrial revolution and the atmospheric CO<sub>2</sub> concentration increased due to burning fossil fuels. With the known greenhouse effect of CO<sub>2</sub> the recent temperature rise has most probably an anthropogenic origin. Source data from [254-256].

**Appendix 8.1.2:** Electrochemical reactions for the applications given in chapter 1.2. The Methanisation is more complex and has at least 7 different reactions for both electrodes [7] [8, 26, 244].

Application	Reactions
Fuel cell	$\text{Anode: } H_2 \rightarrow 2H^+ + 2e^-$ $\text{Cathode: } \frac{1}{2}O_2 + 2H^+ + 2e^- \rightarrow H_2O$ $\text{Overall: } H_2O \rightarrow H_2 + \frac{1}{2}O_2$
Electrolyser	$\text{Anode: } H_2O \rightarrow \frac{1}{2}O_2 + 2H^+ + 2e^-$ $\text{Cathode: } 2H^+ + 2e^- \rightarrow H_2$ $\text{Overall: } H_2O \rightarrow H_2 + \frac{1}{2}O_2$
Methanisation	$\text{Overall: } 4H_2 + CO_2 \rightarrow CH_4 + 2H_2O$
SSAS	$\text{Anode: } 3H_2O \rightarrow \frac{3}{2}O_2 + 6H^+ + 6e^-$ $\text{Cathode: } N_2 + 6H^+ + 6e^- \rightarrow 2NH_3$ $\text{Overall: } 3H_2O + N_2 \rightarrow 2NH_3 + \frac{3}{2}O_2$

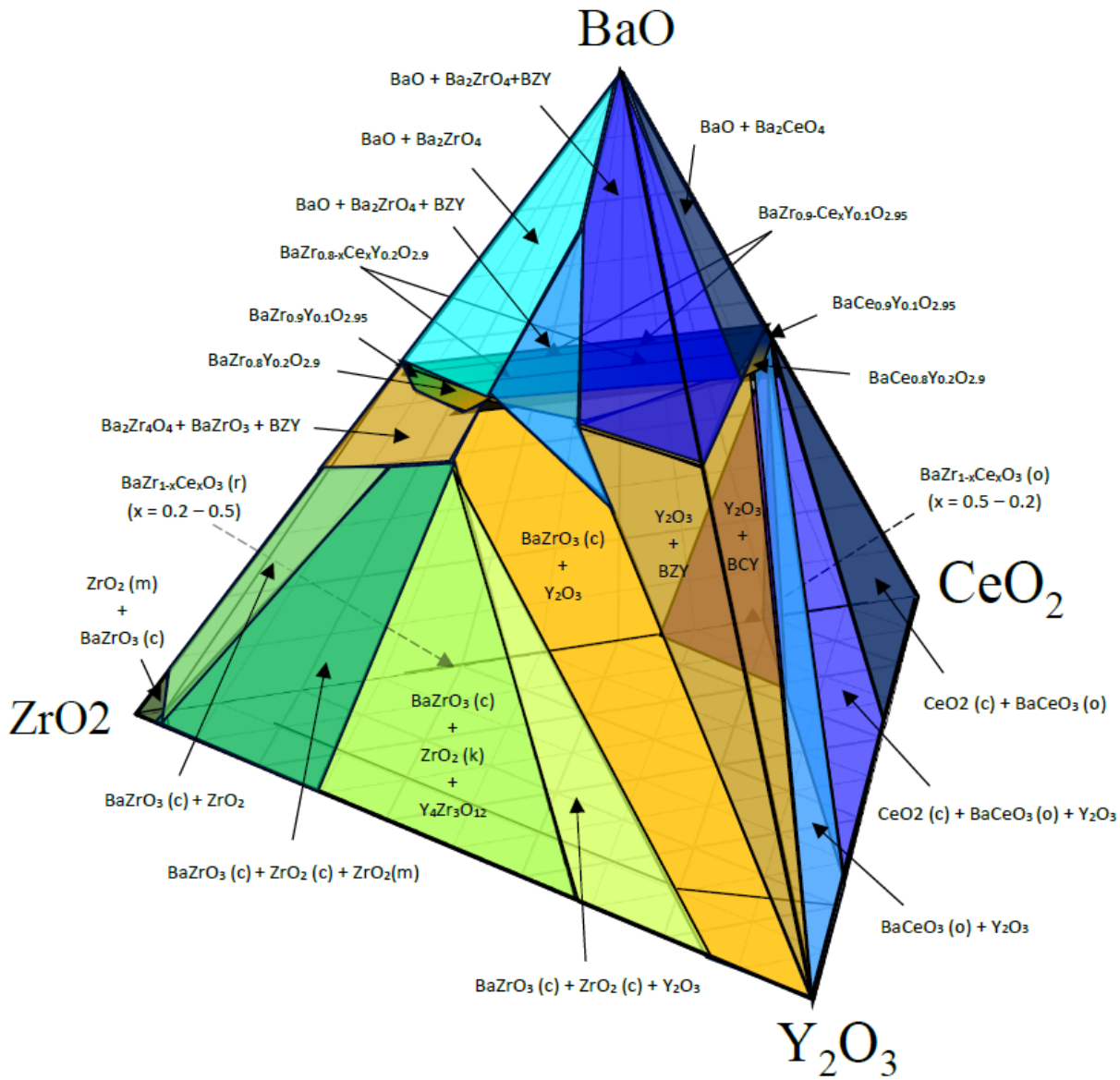


**Appendix 8.1.3:** The versatility of perovskite materials leads to their description as chemical chameleon. Properties and applications of perovskites taken from [13].

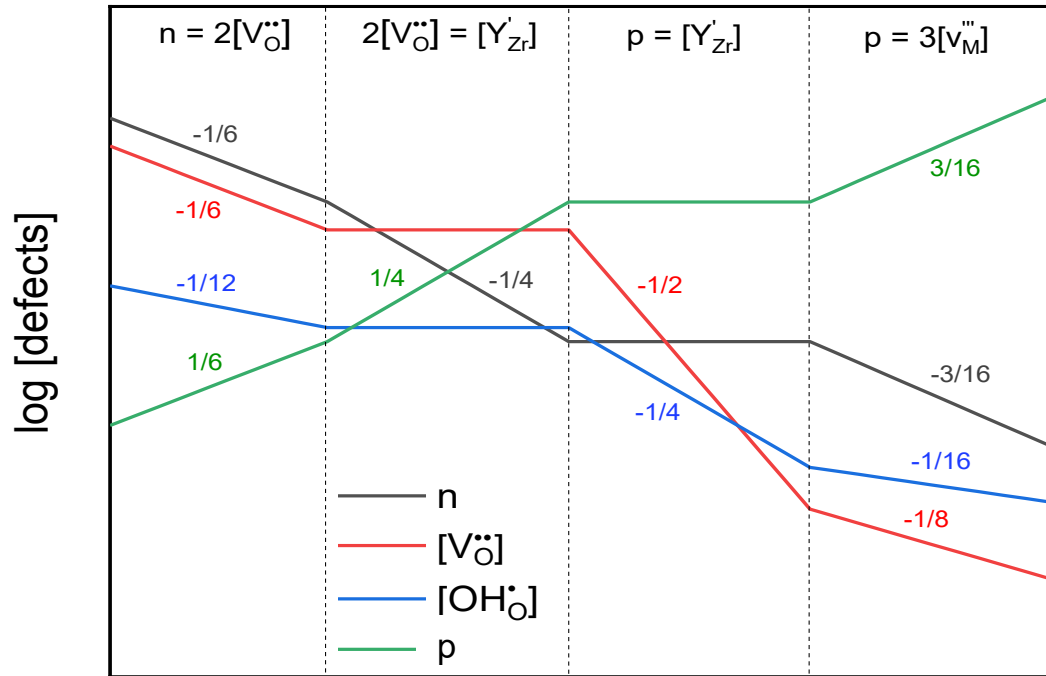
Property	Application	Material	Ref.
Proton conductivity	SOFC electrolyte, H <sub>2</sub> sensor, H <sub>2</sub> production	BaCeO <sub>3</sub> , SrCeO <sub>3</sub> , BaZrO <sub>3</sub>	[27, 108, 257]
Mixed conductivity	SOFC electrode	La(Sr,Ca)MnO <sub>3-δ</sub> , LaCoO <sub>3</sub>	[258, 259]
Ferromagnetic	Magnetic memory	GdFeO <sub>3</sub> , LaMnO <sub>3</sub>	[260]
Electric	Multilayer capacitor, Thin film resistor	BaTiO <sub>3</sub> , BaZrO <sub>3</sub>	[261]
piezoelectric	Piezoelectric transducer	BaTiO <sub>3</sub> , Pb(Zr,Ti)O <sub>3</sub>	[262]
Superconductivity	Superconductor	Ba(Pb,Bi)O <sub>3</sub> , BaKBiO <sub>3</sub>	[263, 264]
Catalytic	Catalyst	LaFeO <sub>3</sub> , La(Ce,Co)O <sub>3</sub>	[265, 266]
Optical	Laser	YAlO <sub>3</sub>	[267]
Photoelectric	Solar cell	MH <sub>3</sub> NH <sub>3</sub> PbI <sub>3</sub>	[268]

**Appendix 8.1.4:** The classification of the octahedral tilting and their relation to the space group in the perovskite structure according to Glazer [21, 22].

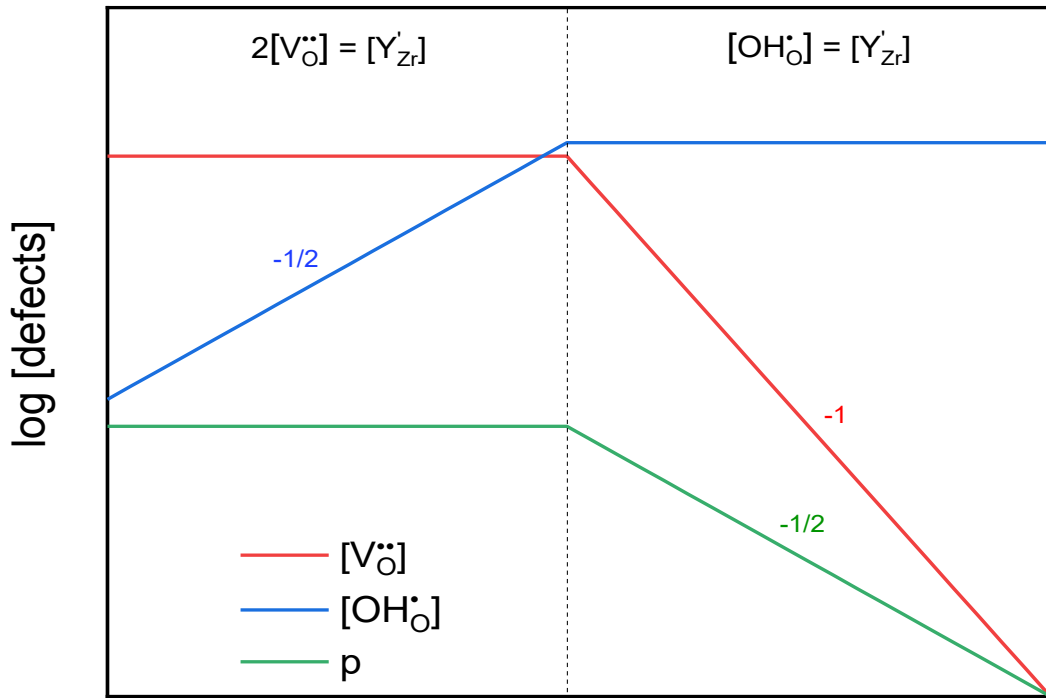
	Lattice centering	Relative pseudo cubic subcell parameters	space group
<i>Zero-tilt systems</i>			
$a^0a^0a^0$	P	$a = b = c$	Pm3m (#221)
<i>One-tilt systems</i>			
$a^0a^0c^+$	C	$a = b < c$	C4/mmb (#127)
$a^0a^0c^-$	F	$a = b < c$	F4/mmc (#140)
<i>Two-tilt systems</i>			
$a^0b^+c^+$	I	$a < b \neq c$	Immm (#71)
$a^0b^+b^+$	I	$a < b = c$	I4/mmm (#139)
$a^0b^+c^-$	B	$a < b \neq c$	Bmmb (#63)
$a^0b^+b^-$	B	$a < b = c$	Bmmb (#63)
$a^0b^-c^-$	F	$a < b \neq c \quad \alpha \neq 90^\circ$	F2/m11 (#12)
$a^0b^-b^-$	F	$a < b = c \quad \alpha \neq 90^\circ$	Imcm (#74)
<i>Three-tilt systems</i>			
$a^+b^+c^+$	I	$a \neq b \neq c$	Immm (#71)
$a^+b^+b^+$	I	$a \neq b = c$	Immm (#71)
$a^+a^+a^+$	I	$a = b = c$	Im3 (#204)
$a^+b^+c^-$	P	$a \neq b \neq c$	Pmmn (#59)
$a^+a^+c^-$	P	$a = b \neq c$	Pmmn (#59)
$a^+b^+b^-$	P	$a \neq b = c$	Pmmn (#59)
$a^+a^+a^-$	P	$a = b = c$	Pmmn (#59)
$a^+a^-c^-$	A	$a \neq b \neq c \quad \alpha \neq 90^\circ$	A2 <sub>1</sub> /m11 (#11)
$a^+a^-c^-$	A	$a = b \neq c \quad \alpha \neq 90^\circ$	A2 <sub>1</sub> /m11 (#11)
$a^+b^-b^-$	A	$a \neq b = c \quad \alpha \neq 90^\circ$	Pmnb (#62)
$a^+a^-a^-$	A	$a = b = c \quad \alpha \neq 90^\circ$	Pmnb (#62)
$a^-b^-c^-$	F	$a \neq b \neq c \quad \alpha \neq \beta \neq \gamma \neq 90^\circ$	F $\bar{1}$ (#12)
$1a^-b^-b^-$	F	$a \neq b = c \quad \alpha \neq \beta \neq \gamma \neq 90^\circ$	I2/a (#15)
$a^-a^-a^-$	F	$a = b = c \quad \alpha = \beta = \gamma \neq 90^\circ$	R $\bar{3}c$ (#167)



**Appendix 8.1.5:** The estimated and over simplified four dimensional phase diagram of the BZCY system. The abbreviations r,m and c stand for rhombohedral, monoclinic and cubic space symmetries, respectively. Data was combined from [17, 43, 194, 253, 269].



a)

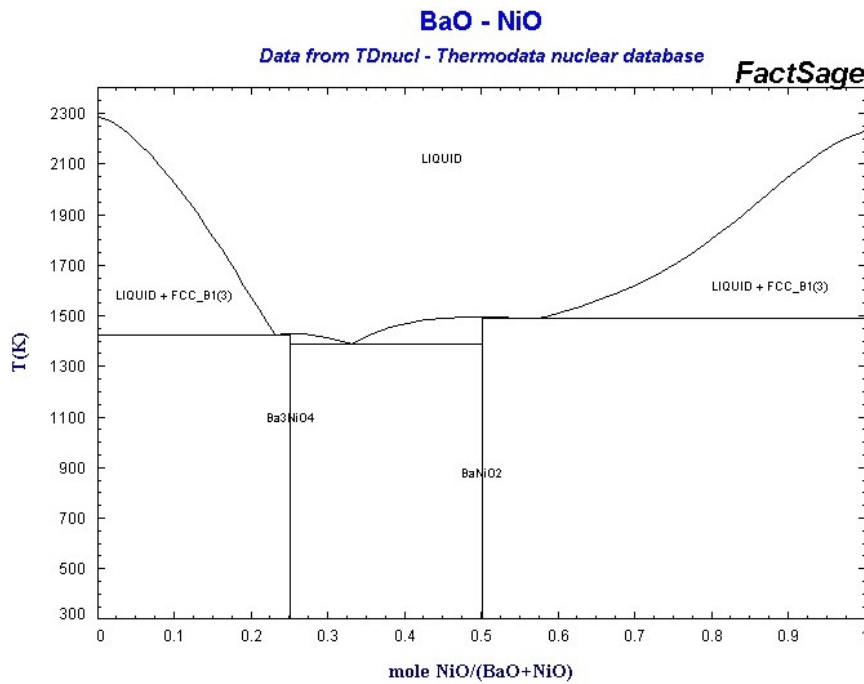


b)

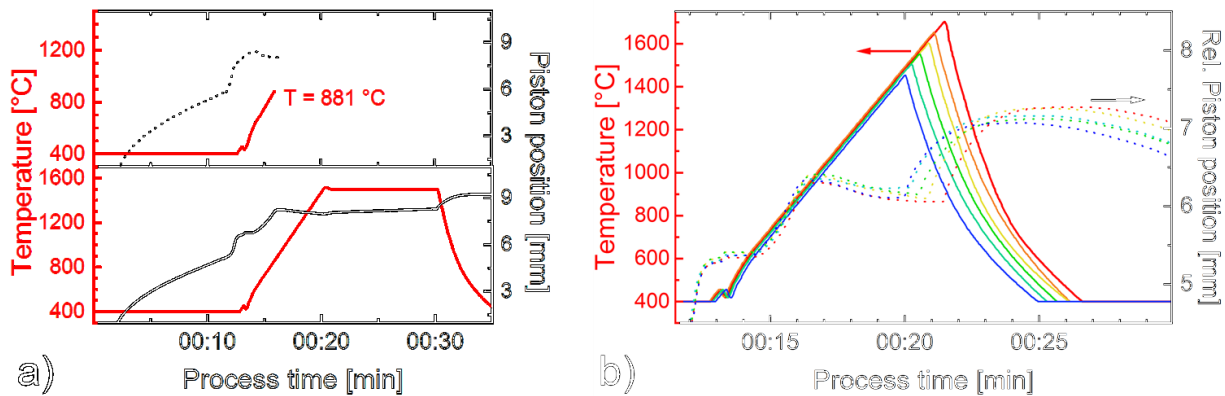
**Appendix 8.1.6:** The Brouwer diagram for BZCY systems shows the defect concentration in dependence of (a) oxygen partial pressure and (b) water vapor partial pressure. The Brouwer-type charge neutrality conditions are displayed on the top and determine the different regions where there are varying effects on the charge carrier concentration. Figure redrawn from [58].

## Sample preparation

### 8.2 Sample preparation



Appendix 8.2.1: Binary phase diagram from BaO-NiO [270].



Appendix 8.2.2: (a) First experiments on BZCY72 fabricated by SPS. Top: The Die was destroyed at 881 °C during the heating cycle. Bottom: First successful run including the densification progress. (b) A starting point for the maximum sintering temperature was based on a series of experiments varying the peak sintering temperature from 1450°C (Wang et al.) [33] to 1700°C (Ricote et al.) [41]. While higher densification could be reached for higher temperatures the most stable samples were fabricated below 1600°C. Thus, the temperature range from 1150 °C to 1650 °C was chosen.

**Appendix 8.2.3:** Overview of all relevant samples produced and used in the current work. The sintering details, sample quality, relative density and use are given. The quality refers to the mechanical integrity of the sample: (\*) means full disintegration into small pieces (\*\*\*\*\*) means the sample remained in one piece. Impedance measurements required at least \*\*\* quality.

Sample Name	T <sub>Max</sub> ; p <sub>Max</sub> ; heating rate; holding time	Quality	Density[%]	Remarks/Use
161026_SPS1	1500 °C ; ~100 MPa; 150 K·min <sup>-1</sup> ; 5 min	-	-	Die broke
161026_SPS2	1500 °C ; ~100 MPa; 150 K·min <sup>-1</sup> ; 5 min	-	-	Die broke
161026_SPS3	1500 °C ; ~100 MPa; 150 K·min <sup>-1</sup> ; 5 min	-	-	Die broke
170227_SPS1	1500 °C ; ~80 MPa 150 K·min <sup>-1</sup> ; 5 min	**	96.4%	First successful sample
170227_SPS2	1500 °C ; ~100 MPa 150 K·min <sup>-1</sup> ; 5 min	**	-	Test series
170227_SPS3	1500 °C ; ~100 MPa 150 K·min <sup>-1</sup> ; 10 min	**	-	Test series
170227_SPS4	1600 °C ; ~100 MPa 150 K·min <sup>-1</sup> ; 10 min	*	-	Test series
170227_SPS5	1700 °C ; ~100 MPa 150 K·min <sup>-1</sup> ; 10 min	*	83.5%	Test series
170306_1450	1450 °C ; ~100 MPa; 150 K·min <sup>-1</sup> ; 0 min	***	94.61%	Temperature test
170306_1500	1500 °C ; ~100 MPa; 150 K·min <sup>-1</sup> ; 0 min	***	95.60%	Temperature test
170307_1550	1550 °C ; ~100 MPa; 150 K·min <sup>-1</sup> ; 0 min	***	97.48%	Temperature test
170307_1600	1600 °C ; ~100 MPa; 150 K·min <sup>-1</sup> ; 0 min	**	99.03%	Temperature test
170307_1650	1650 °C ; ~100 MPa; 150 K·min <sup>-1</sup> ; 0 min	*	96.26%	Temperature test
170307_1700	1700 °C ; ~100 MPa; 150 K·min <sup>-1</sup> ; 0 min	*	92.94%	Temperature test
170328_QENS1	1550 °C ; ~100 MPa; 150 K·min <sup>-1</sup> ; 5 min	***	99.3%	QENS sample
170328_QENS2	1550 °C ; ~100 MPa; 150 K·min <sup>-1</sup> ; 5 min	***	-	QENS sample
170328_QENS3	1550 °C ; ~100 MPa; 150 K·min <sup>-1</sup> ; 5 min	****	98.9%	QENS sample
161221_SSR1	1650 °C ; 600 min	****	54%	Conventional sintering
161221_SSR1	1550 °C ; 600 min	*****	94%	SSRS Benchmark
170117_SSR2	1550 °C ; 600 min	*****	94%	SSRS Benchmark
170117_SSR2	1675 °C ; 600 min	*****	76%	CS Benchmark
170620_C0	1550 °C ; ~100 MPa; 150 K·min <sup>-1</sup> ; 5 min	**	99.4%	Cerpotech powder
170620_M0	1550 °C ; ~100 MPa; 150 K·min <sup>-1</sup> ; 5 min	***	98.7%	Marion powder
170620_C1	1550 °C ; ~100 MPa 150 K·min <sup>-1</sup> ; 10 min	***	99.7%	Cerpotech powder
170620_M1	1550 °C ; ~100 MPa 150 K·min <sup>-1</sup> ; 10 min	**	99.2	Marion...XRD, SEM
170620_C2	1650 °C ; ~100 MPa; 150 K·min <sup>-1</sup> ; 5 min	***	-	Cerpotech powder
170620_M2	1650 °C ; ~100 MPa; 150 K·min <sup>-1</sup> ; 5 min	**	-	Marion powder
170719_NiO_C	1550 °C ; ~100 MPa; 150 K·min <sup>-1</sup> ; 5 min	***	99.0%	1 wt% NiO Cerpotech
170719_NiO_M	1550 °C ; ~100 MPa; 150 K·min <sup>-1</sup> ; 5 min	***	99.1%	1 wt% NiO Marion
170720_NiO_C	1550 °C ; ~80 MPa; 150 K·min <sup>-1</sup> ; 5 min	***	-	1 wt% NiO Cerpotech
170720_NiO_M	1550 °C ; ~80 MPa; 150 K·min <sup>-1</sup> ; 5 min	**	-	1 wt% NiO Marion
170720_LP1	1550 °C ; ~80 MPa; 150 K·min <sup>-1</sup> ; 5 min	****	98.4%	Lab produced sample
170720_LP2	1550 °C ; ~80 MPa; 150 K·min <sup>-1</sup> ; 5 min	****	99.7%	(L) XRD,SEM and IS
170808_Com1	1550 °C ; ~80 MPa; 150 K·min <sup>-1</sup> ; 5 min	***	98.9%	Commercial sample
170808_Com2	1550 °C ; ~100 MPa; 150 K·min <sup>-1</sup> ; 5 min	****	98.6%	(C) XRD,SEM and IS
170808_Com3	1500 °C ; ~100 MPa; 150 K·min <sup>-1</sup> ; 5 min	***	-	Commercial sample
170808_Com4	1600 °C ; ~100 MPa; 150 K·min <sup>-1</sup> ; 5 min	**	-	-
170808_Com5	1650 °C ; ~100 MPa; 150 K·min <sup>-1</sup> ; 5 min	*	-	-
170808_Com6	1700 °C ; ~100 MPa; 150 K·min <sup>-1</sup> ; 5 min	*	-	-
170809_Com7	1550 °C ; ~80 MPa; 150 K·min <sup>-1</sup> ; 10 min	***	-	(C) IS
170809_Com8	1550 °C ; ~100 MPa 150 K·min <sup>-1</sup> ; 10 min	***	-	(C) SEM, EDX
170809_Com9	1550 °C ; ~80 MPa; 150 K·min <sup>-1</sup> ; 5 min	**	-	(C) XRD
171116_f16_13	1350 °C ; ~51 MPa; 150 K·min <sup>-1</sup> ; 5 min	****	95.22 %	SEM, EDX, IS
171116_f20_13	1350 °C ; ~64 MPa; 150 K·min <sup>-1</sup> ; 5 min	***	97.86 %	SEM, EDX, IS
171116_f24_13	1350 °C ; ~76 MPa; 150 K·min <sup>-1</sup> ; 5 min	****	97.9 %	SEM, EDX, IS
171116_f28_13	1350 °C ; ~89 MPa; 150 K·min <sup>-1</sup> ; 5 min	*****	98.4 %	SEM, IS

## Sample preparation

171116_f16_14	1450 °C ; ~51 MPa; 150 K·min <sup>-1</sup> ; 5 min	****	97.41 %	SEM, IS
171116_f20_14	1450 °C ; ~64 MPa; 150 K·min <sup>-1</sup> ; 5 min	****	98.60 %	XRD, SEM
171116_f24_14	1450 °C ; ~76 MPa; 150 K·min <sup>-1</sup> ; 5 min	****	99.39 %	XRD, SEM, IS
171116_f28_14	1450 °C ; ~89 MPa; 150 K·min <sup>-1</sup> ; 5 min	****	99.45 %	XRD, SEM, IS
180221_10min	1450 °C ; ~62 MPa; 150 K·min <sup>-1</sup> ; 10 min	****	97.9 %	SEM
180221_20min	1450 °C ; ~62 MPa; 150 K·min <sup>-1</sup> ; 20 min	****	98.1 %	XRD, SEM, IS
180221_40min	1450 °C ; ~62 MPa; 150 K·min <sup>-1</sup> ; 40 min	***	98.1 %	XRD, SEM
180221_60min	1450 °C ; ~62 MPa; 150 K·min <sup>-1</sup> ; 60 min	*	-	
180221_QENSx	1550 °C ; ~76 MPa; 150 K·min <sup>-1</sup> ; 5 min	***	-	Test sample for QENS
180424_QENS5	1550 °C ; ~51 MPa; 150 K·min <sup>-1</sup> ; 5 min	*****	-	QENS
180424_QENS4	1450 °C ; ~51 MPa; 150 K·min <sup>-1</sup> ; 5 min	*****	-	NCS
180424_QENS3	1350 °C ; ~51 MPa; 150 K·min <sup>-1</sup> ; 5 min	*****	-	QENS
180620_T1250	1250 °C ; ~38 MPa; 150 K·min <sup>-1</sup> ; 5 min	***	91.2 %	XRD, SEM
180620_T1350	1350 °C ; ~38 MPa; 150 K·min <sup>-1</sup> ; 5 min	***	94.2 %	XRD,SEM,IS
180620_T1450	1450 °C ; ~38 MPa; 150 K·min <sup>-1</sup> ; 5 min	****	97.40 %	XRD,SEM,IS
180620_T1550	1550 °C ; ~38 MPa; 150 K·min <sup>-1</sup> ; 5 min	***	97.5 %	XRD,SEM,IS
180620_T1650	1650 °C ; ~38 MPa; 150 K·min <sup>-1</sup> ; 5 min	*	-	XRD,SEM
180620_T1750	1750 °C ; ~38 MPa; 150 K·min <sup>-1</sup> ; 5 min	*	-	XRD,SEM,EDX
180621_f22	1450 °C ; ~70 MPa; 150 K·min <sup>-1</sup> ; 5 min	***		
180621_f32	1450 °C ; ~100 MPa; 150 K·min <sup>-1</sup> ; 5 min	***		
180621_HR25	1450 °C ; ~64 MPa; 25 K·min <sup>-1</sup> ; 5 min	***	97.5 %	XRD,SEM
180621_HR50	1450 °C ; ~64 MPa; 50 K·min <sup>-1</sup> ; 5 min	****	98.1 %	XRD,SEM,IS
180621_HR75	1450 °C ; ~64 MPa; 75 K·min <sup>-1</sup> ; 5 min	***	98.0 %	XRD,SEM
180622_HR100	1450 °C ; ~64 MPa; 100 K·min <sup>-1</sup> ; 5 min	***	98.2 %	XRD,SEM
180622_30min	1450 °C ; ~76 MPa; 150 K·min <sup>-1</sup> ; 30 min	*	-	-
180622_1150	1150 °C ; ~100 MPa; 150 K·min <sup>-1</sup> ; 5 min	***	92.02 %	XRD,SEM,IS
180622_1250	1250 °C ; ~100 MPa; 150 K·min <sup>-1</sup> ; 5 min	***	95.96 %	XRD,SEM,IS
181116_T1150	1150 °C ; ~64 MPa; 150 K·min <sup>-1</sup> ; 5 min	***	88.9 %	XRD,SEM,IS
181116_T1250	1250 °C ; ~64 MPa; 150 K·min <sup>-1</sup> ; 5 min	****	94.14 %	XRD,SEM,IS
181116_T1350	1350 °C ; ~64 MPa; 150 K·min <sup>-1</sup> ; 5 min	*****	97.86 %	XRD,SEM,IS
181116_T1450	1450 °C ; ~64 MPa; 150 K·min <sup>-1</sup> ; 5 min	*****	99.39 %	XRD,SEM,IS
181116_T1550	1550 °C ; ~64 MPa; 150 K·min <sup>-1</sup> ; 5 min	****	98.42 %	XRD,SEM,IS
181116_T1650	1650 °C ; ~64 MPa; 150 K·min <sup>-1</sup> ; 5 min	**	-	XRD,SEM
181117_HR25	1350 °C ; ~64 MPa; 25 K·min <sup>-1</sup> ; 5 min	*****	98.35 %	XRD,SEM,IS
181117_HR50	1350 °C ; ~64 MPa; 50 K·min <sup>-1</sup> ; 5 min	*****	97.99 %	XRD,SEM,IS
181117_HR100	1350 °C ; ~64 MPa; 100 K·min <sup>-1</sup> ; 5 min	****	98.03 %	XRD,SEM,IS
181117_HR200	1350 °C ; ~64 MPa; 200 K·min <sup>-1</sup> ; 5 min	****	98.74 %	XRD,SEM,IS
181117_20min	1350 °C ; ~64 MPa; 150 K·min <sup>-1</sup> ; 20 min	*****	98.12 %	XRD,SEM,IS
181118_40min	1350 °C ; ~64 MPa; 150 K·min <sup>-1</sup> ; 40 min	*****	98.19 %	XRD,SEM,IS
181118_60min	1350 °C ; ~64 MPa; 150 K·min <sup>-1</sup> ; 60 min	**	-	XRD,SEM,IS
181119_T1150	1350 °C ; ~51 MPa; 150 K·min <sup>-1</sup> ; 5 min	**	84.3 %	XRD,SEM,IS
181119_T1250	1350 °C ; ~51 MPa; 150 K·min <sup>-1</sup> ; 5 min	**	89.3 %	XRD,SEM,IS
181119_T1450	1350 °C ; ~51 MPa; 150 K·min <sup>-1</sup> ; 5 min	***	98.6 %	XRD,SEM,IS
181119_T1550	1350 °C ; ~51 MPa; 150 K·min <sup>-1</sup> ; 5 min	****	98.36 %	XRD,SEM,IS
190304_pt10ms	1350 °C ; ~64 MPa; 150 K·min <sup>-1</sup> ; 5 min	**	-	XRD,SEM,IS
190304_pt70ms	1350 °C ; ~64 MPa; 150 K·min <sup>-1</sup> ; 5 min	***	-	XRD,SEM,IS
190304_pt100ms	1350 °C ; ~64 MPa; 150 K·min <sup>-1</sup> ; 5 min	***	-	XRD,SEM,IS
190304_pt150ms	1350 °C ; ~64 MPa; 150 K·min <sup>-1</sup> ; 5 min	**	-	XRD,SEM,IS
190304_pt200ms	1350 °C ; ~64 MPa; 150 K·min <sup>-1</sup> ; 5 min	**	-	XRD,SEM,IS
190304_pt250ms	1350 °C ; ~64 MPa; 150 K·min <sup>-1</sup> ; 5 min	**	-	XRD,SEM,IS

### 8.3 Rietveld refinement

**Appendix 8.3.1:** Details and Formulas used for the Rietveld Refinement from the TOPAS technical reference.

#### Structure factor

$$F_K = \sum_j N_j f_j \exp(2\pi i(hx_j + ky_j + lz_j)) \exp(-8\pi^2 u_s^2 \sin^2 \theta / \lambda^2)$$

Where  $N_j$  is the site occupancy multiplier;  $h, k, l$  are the Miller indices;  $x_j, y_j, z_j$  are the atomic positions;  $u_s^2$  is the root-mean-square thermal displacement of the atoms

#### Gaussian (G) and Lorentzian (L) profile shape function

$$G = \frac{\sqrt{\ln(2)}}{H_K \sqrt{\pi}} \exp\left(\frac{-4 \ln(2)(2\theta_i - 2\theta_K)^2}{H_K^2}\right)$$

$$L = \frac{2}{H_K \pi} \left(\frac{1 + 4(2\theta_i - 2\theta_K)^2}{H_K^2}\right)$$

Where  $H^2 = U \tan^2 \theta + V \tan \theta + W$  is the full width at half maximum with U, V and W being refinable parameters [271].

#### Modified Thompson-Cox-Hastings pseudo Voigt “TCHZ” profile function

$$TCHZ = \eta L + (1 - \eta)G$$

$$\eta = 1.36603 q - 0.47719 q^2 + 0.116 q^3$$

$$q = \Gamma_L / \Gamma$$

$$\Gamma = (\Gamma_G^5 + A\Gamma_G^4 \Gamma_L + B\Gamma_G^3 \Gamma_L^2 + C\Gamma_G^2 \Gamma_L^3 + D\Gamma_G \Gamma_L^4 + \Gamma_L^5)^{0.2}$$

$$A = 2.69269, B = 2.42843, C = 4.47163, D = 0.07842$$

$$\Gamma_G = \sqrt{U \tan^2 \theta + V \tan \theta + W + Z / \cos^2 \theta}$$

$$\Gamma_L = X \tan \theta + Y / \cos \theta$$

With U, V, W, X, Y, Z as refinable parameters

#### Weighted profile R-factor ( $R_{wp}$ ) and expected R factor ( $R_{exp}$ ) [125, 272]

$$R_{wp} = \sqrt{\frac{\sum_i^N w_i (I_{i,calc} - I_{i,obs})^2}{\sum_i^N w_i (I_{i,obs})^2}} \quad R_{exp} = \sqrt{\frac{(N - P)}{\sum_i^N w_i (I_{i,obs})^2}}$$

#### Goodness of fit G

$$G^2 = \chi^2 = \left(\frac{R_{wp}}{R_{exp}}\right)^2$$

## 8.4 Neutron scattering experiments

**Appendix 8.4.1:** Important formulas used in the QENS experiments.  $Q$  and  $\omega$  are the momentum and energy transfer, respectively.

### Dynamic structure factor for protonic motion in proton conductors [273]

$$S(Q, \omega) = e^{-Q^2 \langle u \rangle^2} \left\{ \begin{array}{l} \text{Elastic contribution} \\ \text{Rotations} \end{array} \right. \\ \left. \begin{array}{l} \text{motion geometry (EISF)} \\ \text{translation diffusion} \end{array} \right\} \\ S(Q, \omega) = e^{-Q^2 \langle u \rangle^2} \left\{ F(Q) \delta(\omega) + \frac{1}{\pi} \frac{\Gamma(Q)}{\omega^2 + \Gamma(Q)^2} + [1 - F(Q)] \frac{1}{\pi} \frac{\Gamma_R(Q)}{\omega^2 + \Gamma_R(Q)^2} \right\}$$

### Elastic incoherent structure factor (EISF)

$$F(Q) = \frac{S^{el}(Q, \omega)}{S^{el}(Q, \omega) + S^{qel}(Q, \omega)}$$

Where  $S^{el}(Q, \omega)$  is the elastic intensity and  $S^{qel}(Q, \omega)$  the quasi-elastic intensity.

### Jump model between two equivalent sites [130, 273, 274]

$$F(Q) = \frac{1}{2} \left[ 1 + \frac{\sin(Qd)}{Qd} \right]$$

Where  $d$  is the distance between the two sites.  $Q$  is the momentum transfer.

### Spherical diffusion

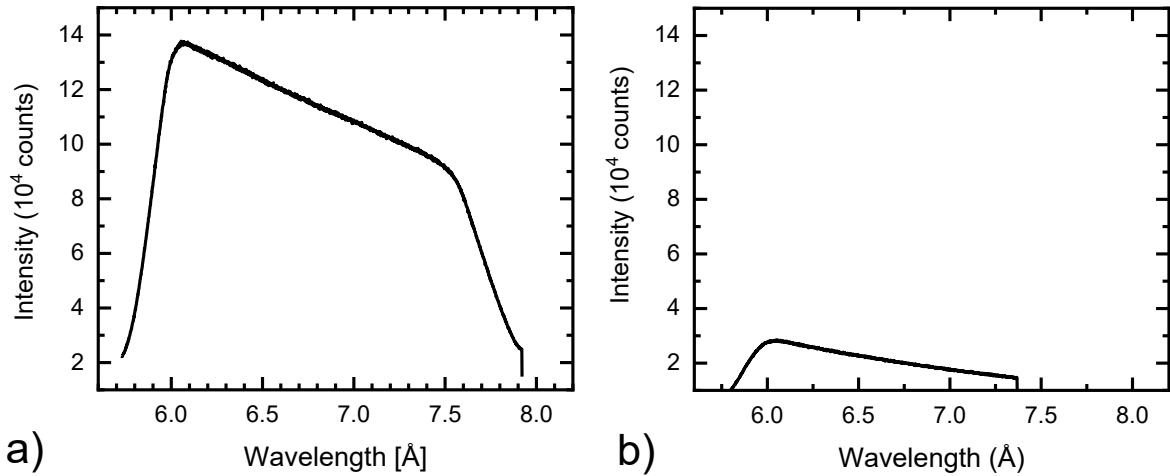
$$F(Q) = A \left( \frac{3j_1(Qd)}{Qd} \right)^2$$

Where  $d$  is the radius of the sphere,  $A$  the scale factor and  $j_1$  is the first order spherical Bessel function.

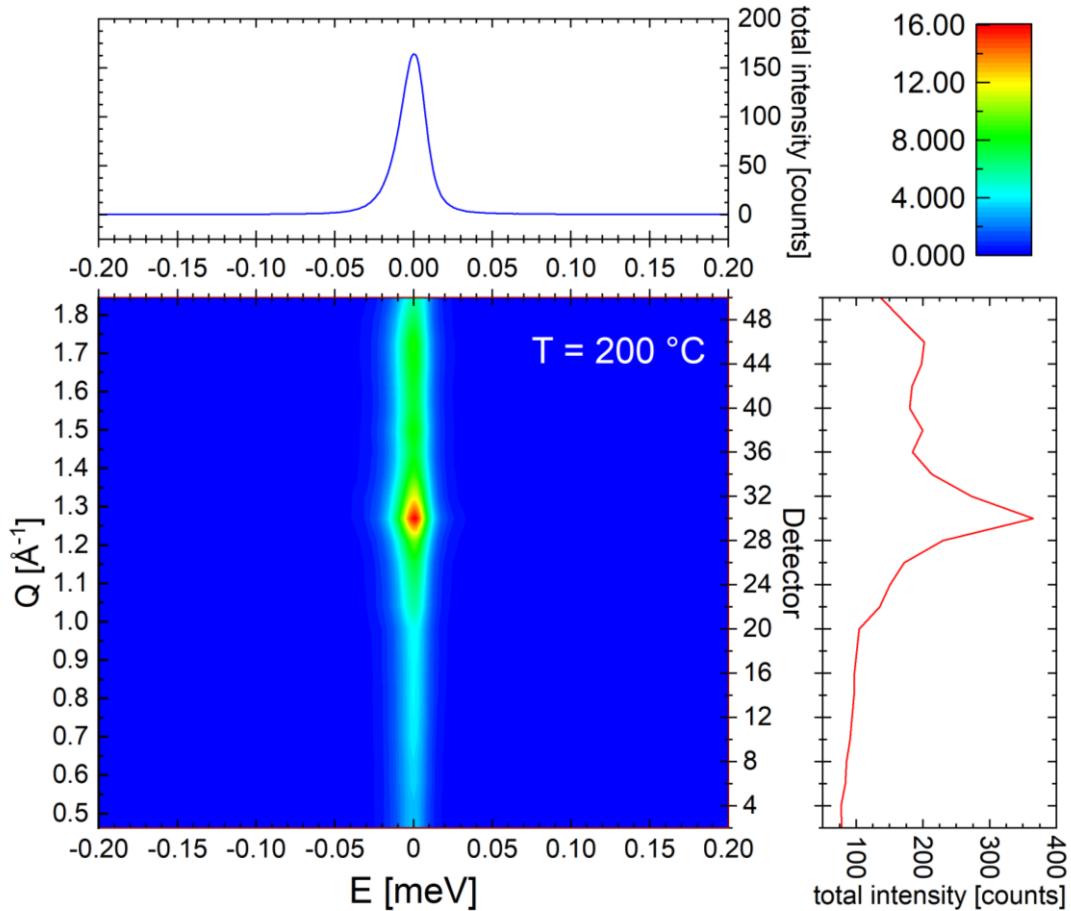


**Appendix 8.4.2:** The quartz container used for the QENS experiments. The neutron beam has an area of  $3\text{cm} \cdot 2\text{cm}$  and went through the bottom part of the containment where the sample is located. On the top side there was a stainless steel Swagelok interface to connect the sample with the system. Saturated argon was transferred through the container.

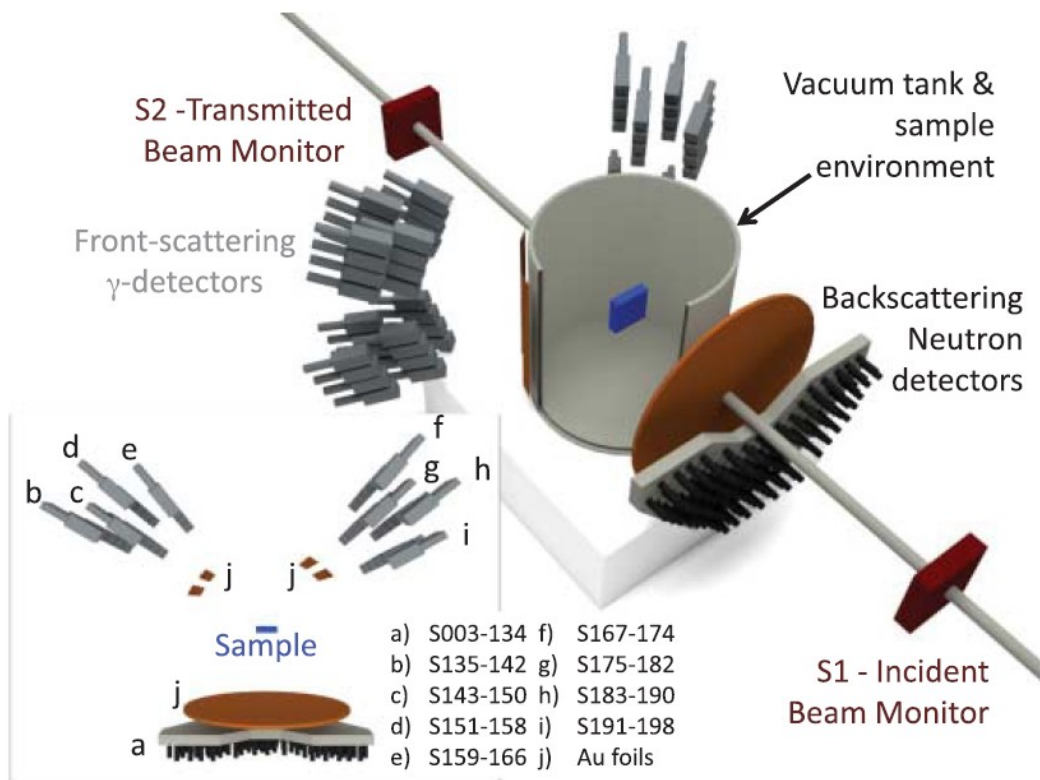




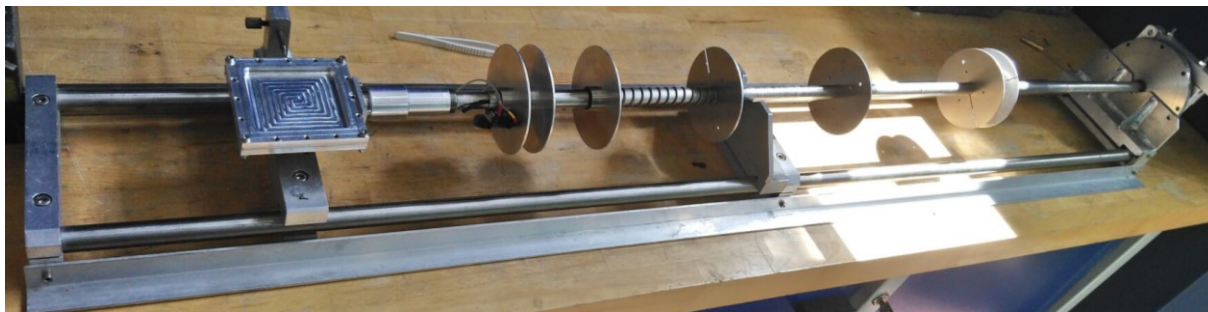
**Appendix 8.4.3:** (a) Spectrum of incident white neutron beam and (b) Spectrum of transmitted neutrons.



**Appendix 8.4.4:** The contour plot of a typical QENS signal from BZCY72. The intensity as a function of energy transfer integrated over all  $Q$ -ranges is shown on the top where the resulting peak is from the elastic and quasi elastic scattering. On the right side the intensity is summed over all  $\Delta E$  as a function of momentum transfer. The visible peak is a Bragg reflection of the system.



**Appendix 8.4.5:** Schematic of the VESUVIO TOF spectrometer. The sample sits in the middle inside of an Al container. Neutrons from the target are slowed down by a water moderator and guided to the setup. VESUVIO provides routine access to energy transfers from 0.5 eV to 150 eV and momentum transfers from  $20 \text{ \AA}^{-1}$  to  $300 \text{ \AA}^{-1}$ . 64 forward and 132 backward scattering detectors record the TOF spectra. Energy selection is done by using an Au foil as resonance filter after scattering. Image is taken from [137].

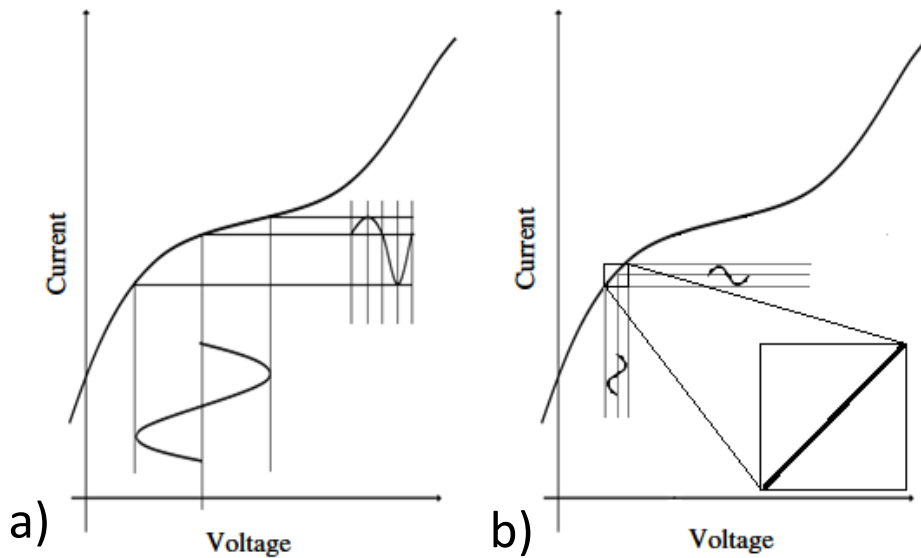


**Appendix 8.4.6:** Photograph of the VESUVIO *ab initio* sample setup. The sample is located within the square shaped aluminum can. The setup is mounted to a rod that includes different seals.

## 8.5 Impedance spectroscopy

**Appendix 8.5.1:** Overview over circuit elements relevant for this thesis and their impedance.

Circuit element	Current voltage relation	Frequency dependent relationship
Resistor	$\Delta v(t) = R\Delta i(t)$	$Z(j, \omega) = R$
Capacitor	$\Delta i(t) = C \frac{d(\Delta v(t))}{dt}$	$Z(j, \omega) = \frac{1}{j\omega C}$
Inductor	$\Delta v(t) = L \frac{d(\Delta i(t))}{dt}$	$Z(j, \omega) = j\omega L$
Constant phase element		$Z(j, \omega) = \frac{1}{(j\omega)^n Q_0}$

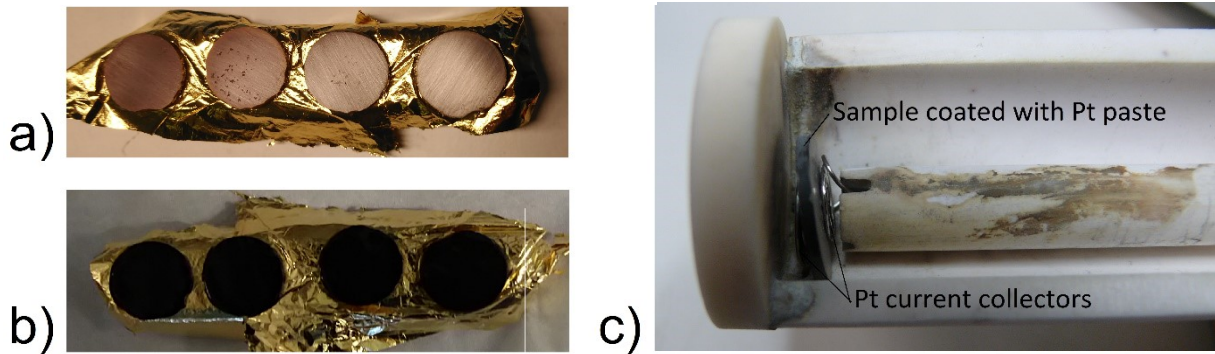


**Appendix 8.5.2:** The typical electrochemical cell as a nonlinear system: (a) Applying a high ac voltage results in a distorted response, (b) in the case of a small perturbation voltage the system responds pseudo linear. Image recreated from [155].

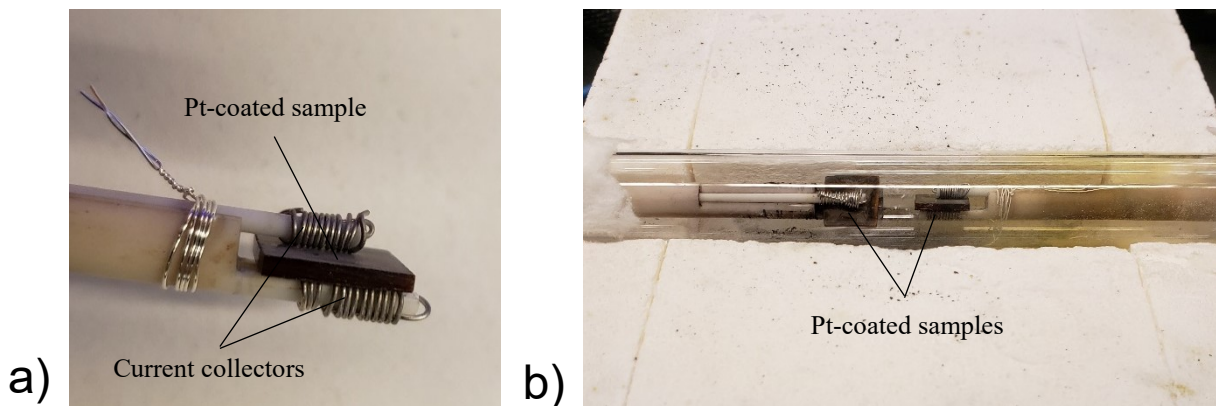
**Appendix 8.5.1:** Summary of encounterable phenomena in IS and their corresponding capacitance. [155, 158]

Capacitance [F]	Phenomenon responsible
$10^{-12}$ - $10^{-11}$	Bulk
$10^{-11}$	Minor second phase
$10^{-10}$ - $10^{-9}$	Bulk ferromagnetic
$10^{-10}$ - $10^{-8}$	Grain boundary
$10^{-9}$ - $10^{-7}$	Surface layer
$10^{-7}$ - $10^{-5}$	Space charge layer/ sample electrode interface
$10^{-6}$	Charge transfer
$10^{-4}$	Electrochemical reaction
$10^{-3}$ - $10^{-1}$	Mass transfer

## Impedance spectroscopy

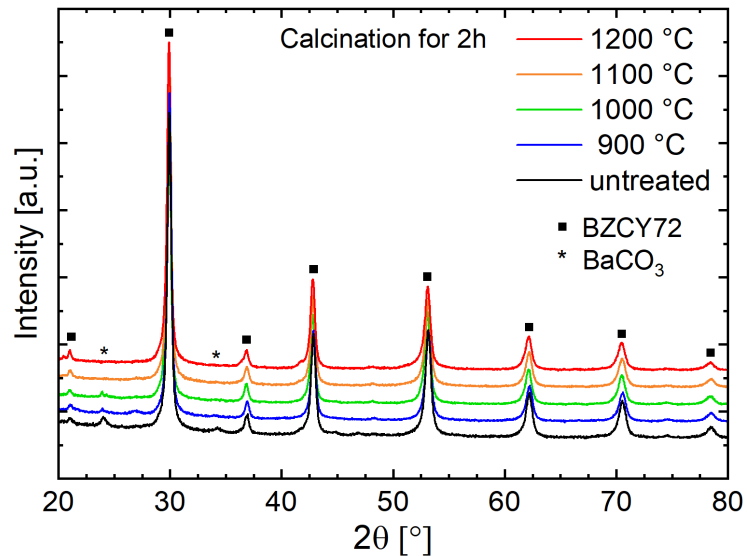


**Appendix 8.5.2:** Preparation of BZCY72 samples for impedance spectroscopy: (a) sintered Pellets on gold foil (b) pellets after coating with Heraeus platinum paste (c) samples inside the  $\text{Al}_2\text{O}_3$  impedance jig with Pt current collectors. The thermocouple and Pt current collectors run inside the small capillary tube.

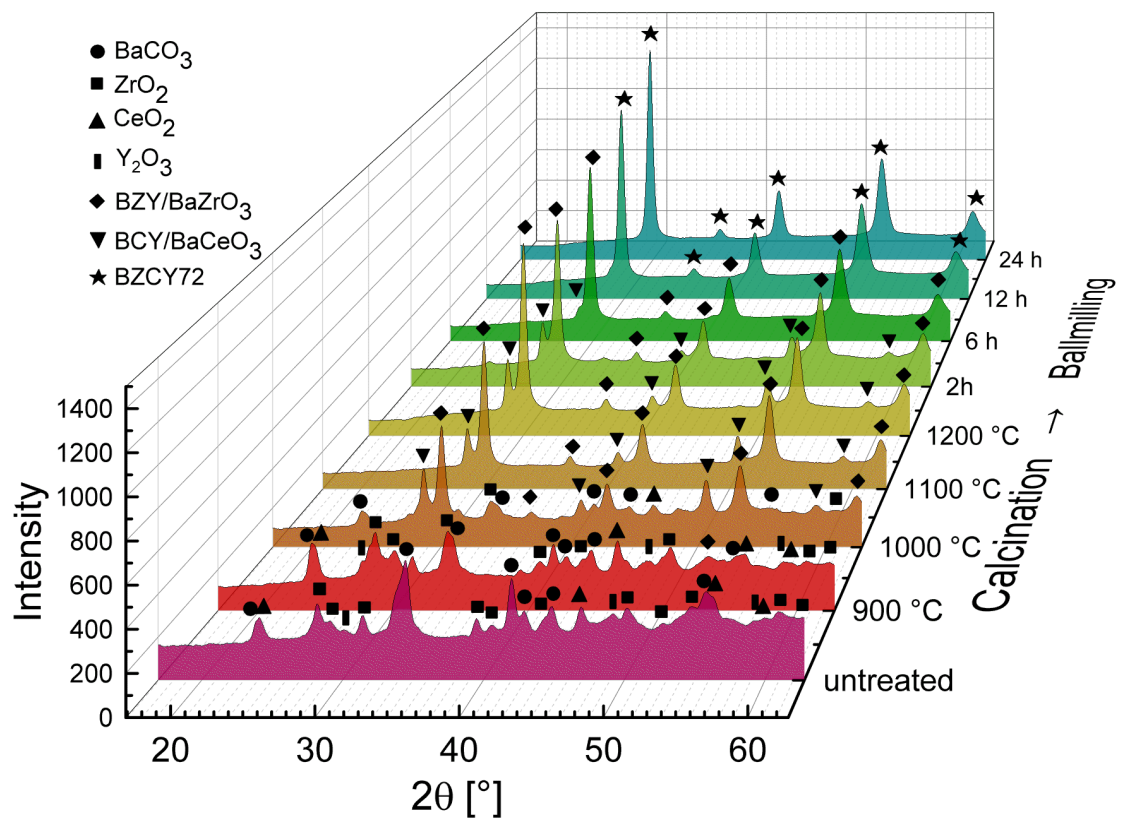


**Appendix 8.5.3:** Conductivity measurements at varying  $p\text{O}_2$ : (a) Close up on the sample fixation and Pt current collectors (b) Setup for measurements of two samples.

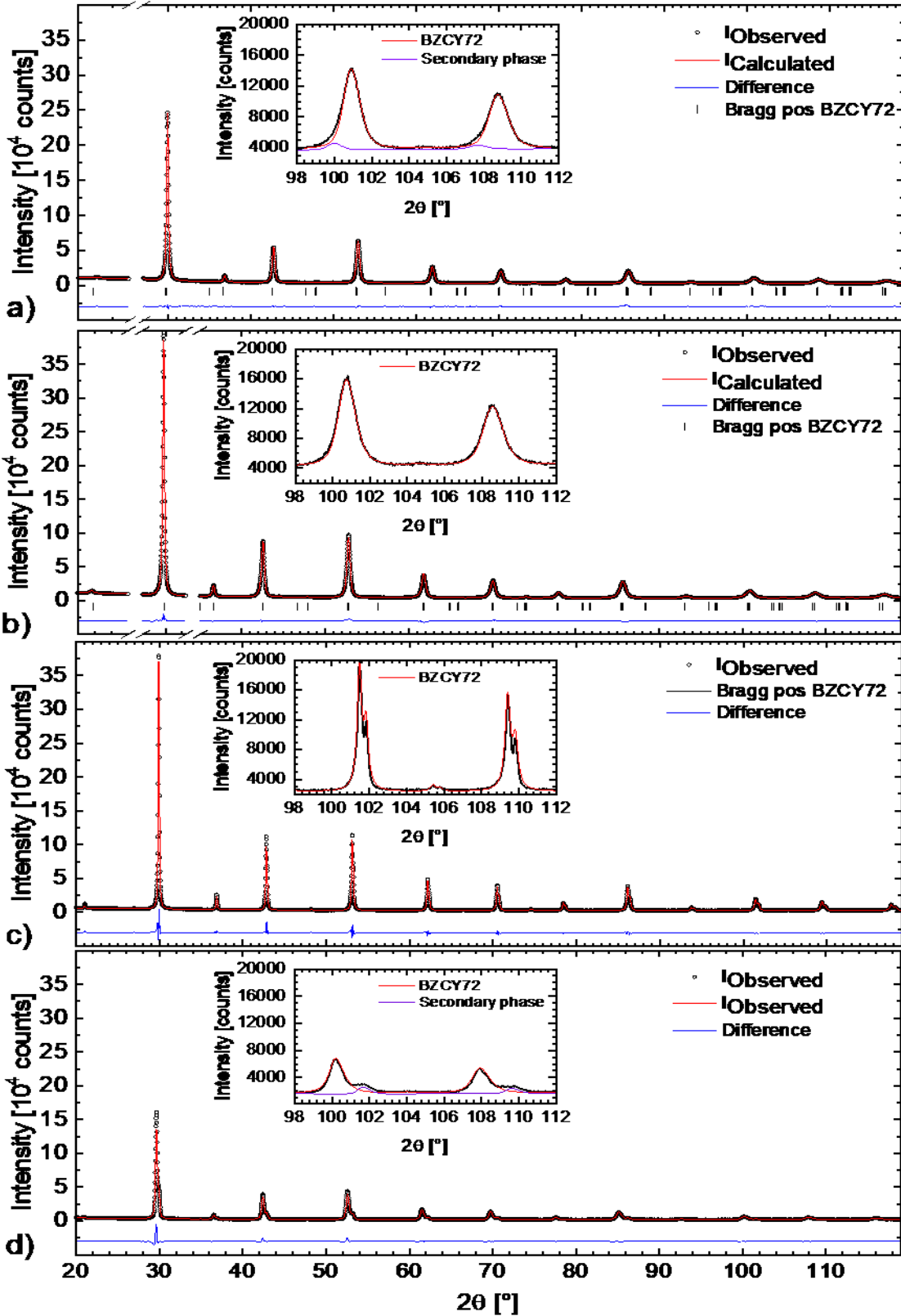
## 8.6 Properties of BZCY72



**Appendix 8.6.1:** XRD patterns of the precursor Cerpotech commercial powder after different heat treatments.

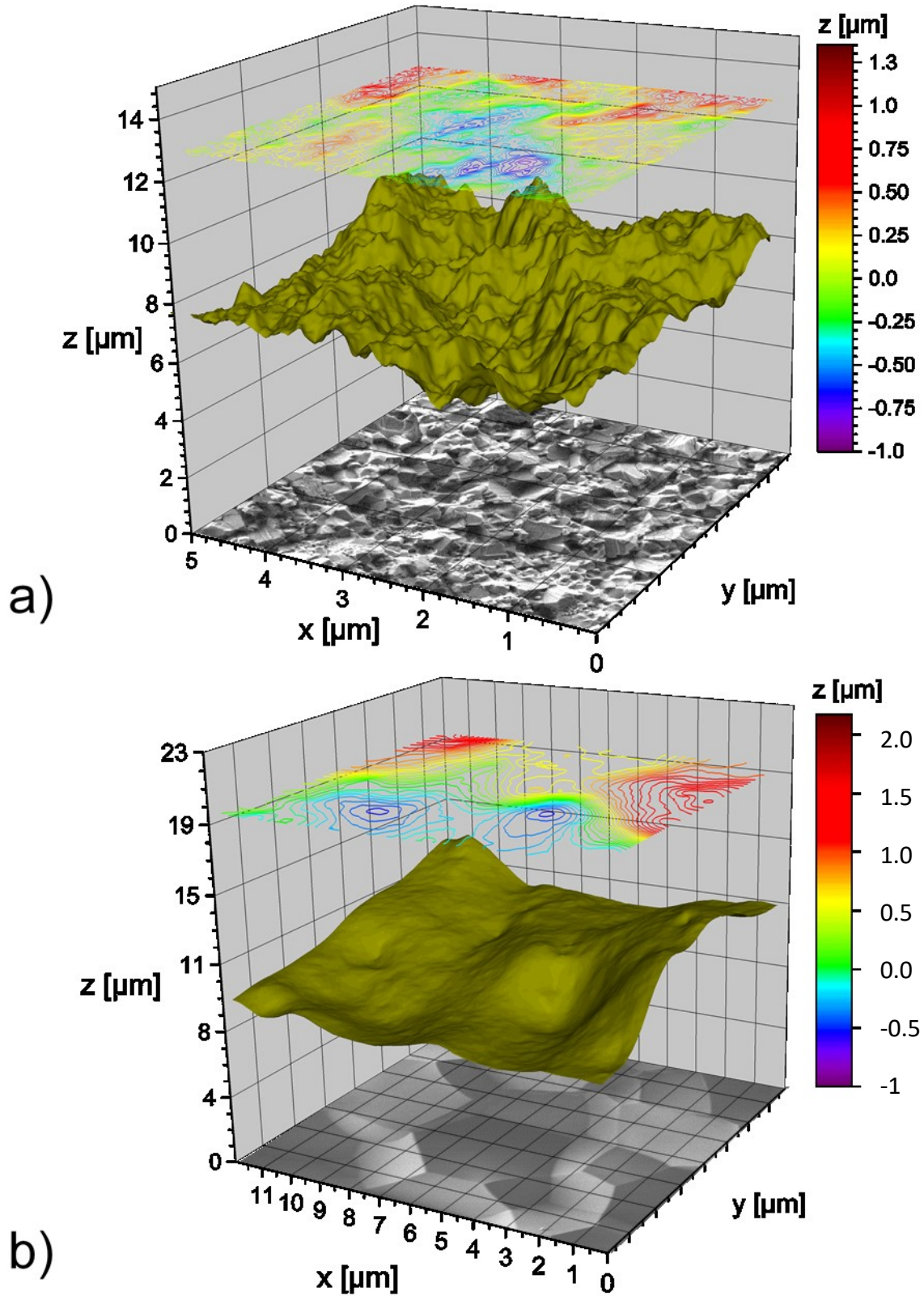


**Appendix 8.6.2:** Progress of phase formation for the lab produced powder starting from the precursor powders. Calcination temperatures of at least 1200°C are necessary to form barium cerate and zirconate. After ball milling, the final perovskite phase BZCY72 is formed from BZY and BCY.



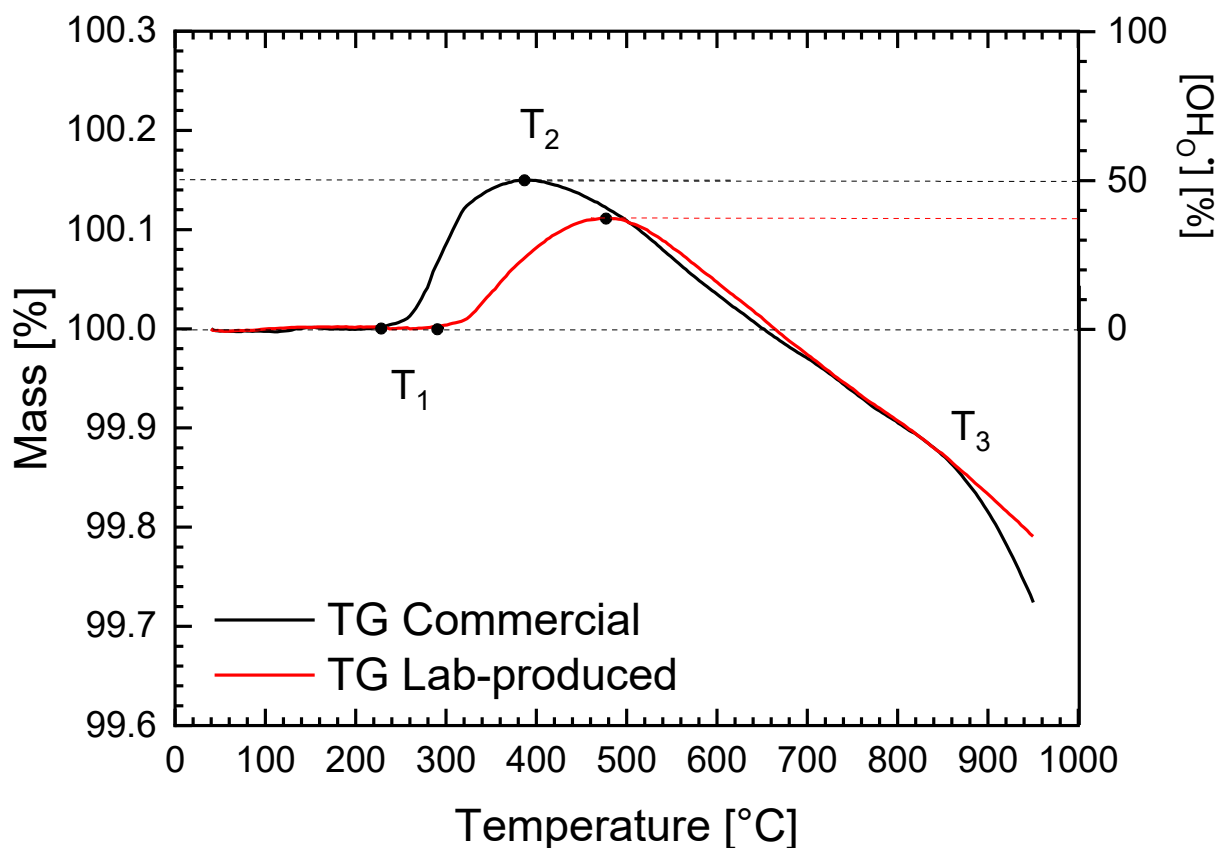
Appendix 8.6.3: Rietveld refinements of BZCY72 pellets sintered by different methods. (a) SPS lab produced, (b) SPS commercial, (c) solid-state reactive sintering (d) conventional sintering.





**Appendix 8.6.4:** 3D imaging and profiling of fractured cross-section of BZCY72 samples: (a) Sample prepared by SPS using commercial powder, (b) Sample prepared by SSRS. Images were created using the MeX software from Bruker Alicona.

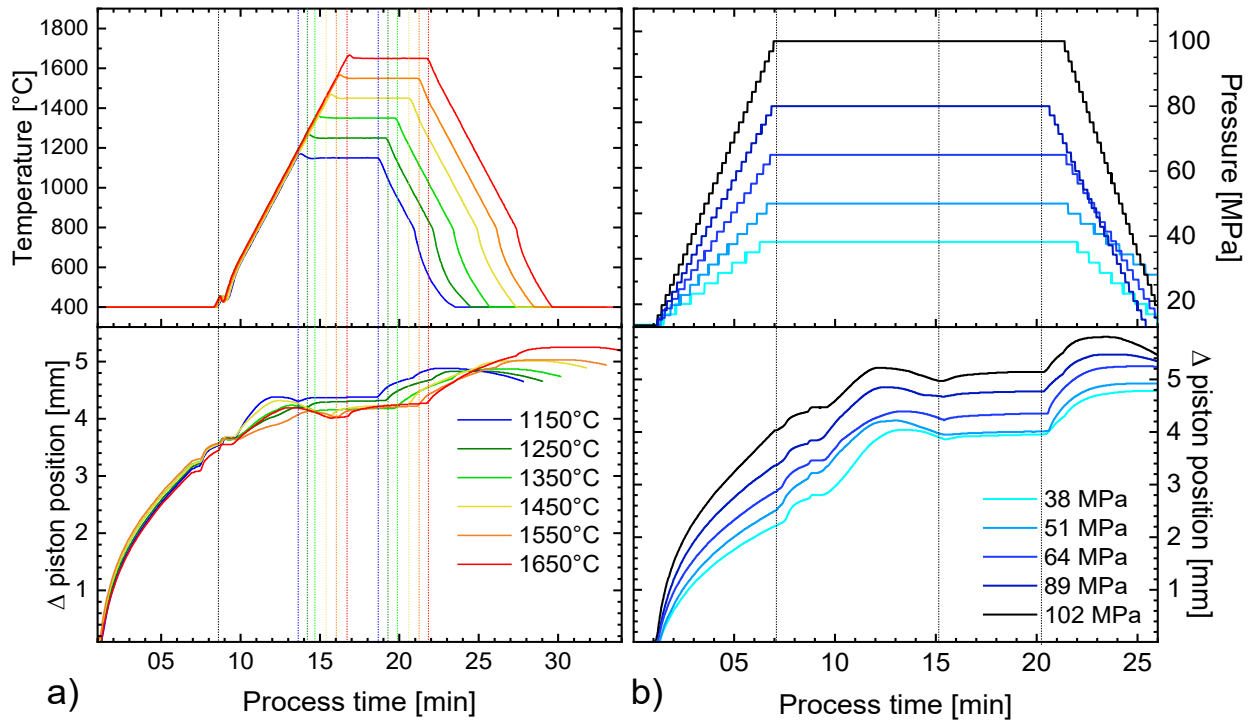
**Appendix 8.6.5:** TGA Measurements were carried out by a STA instrument (STA7200RV, Hitachi) for 170-200 mg of powder using a Pt pan. The samples were heated at 5 °C/min from 40 °C to 950 °C under Ar atmosphere with a gas flow of 100 ml/min, while the weight change was recorded simultaneously. After reaching 950 °C the temperature was held for 20 min and then subsequently cooled at 5 °C/min to 40 °C, which was held again for 20 min.



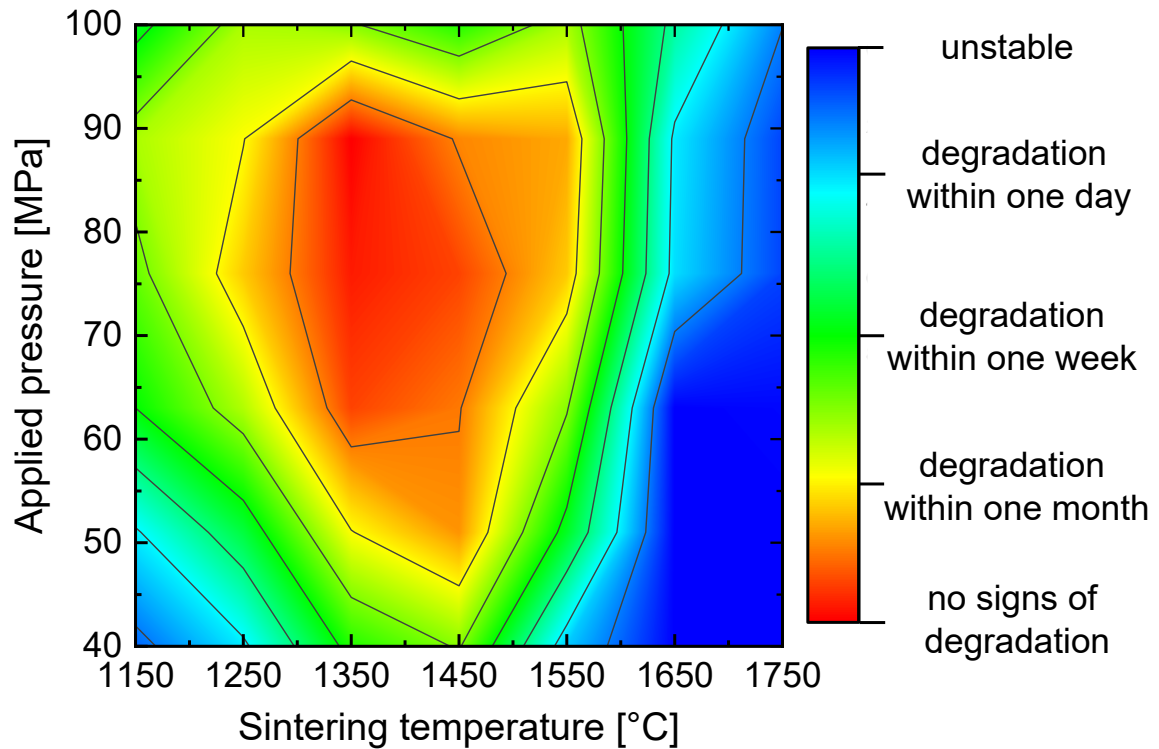
Weight traces and protonic defect concentration of the commercial and lab-produced sample in 3 % H<sub>2</sub>O Argon atmosphere. For both samples similar weight traces are observed. The weight uptake during heating can be correlated to water incorporation (hydration) whilst the weight loss maybe attributable to water loss (dehydration), although other species such as carbon dioxide may also be lost during heating [275]. For the lab-produced sample, the weight uptake happens between temperatures T<sub>1</sub> = 300 °C and T<sub>2</sub> = 480 °C, with a weight gain of 0.11 % corresponding to an estimated content of 38 % vacancies being filled by protonic defects. For the commercial sample, a larger weight gain of 0.15 mass% occurred at significant lower temperatures T<sub>1</sub> = 230 °C and T<sub>2</sub> = 380 °C, with 52% of the vacancy being hydrated at its maximum value. This may be caused by the higher Ce<sup>4+</sup> content calculated by Rietveld refinement of XRD data. Also, equilibration of the lab-produced sample during heating in moist atmosphere might be poor due to its high density as compared to the commercial sample that was observed to contain some porosity. At T<sub>3</sub> = 860 °C there is an inflection point apparent which is more distinct in the trace for the commercial sample. Above this temperature, weight loss occurs probably due to commencement of oxygen loss from the perovskite or marking commencement of decomposition of barium carbonate that is present as a minor phase.



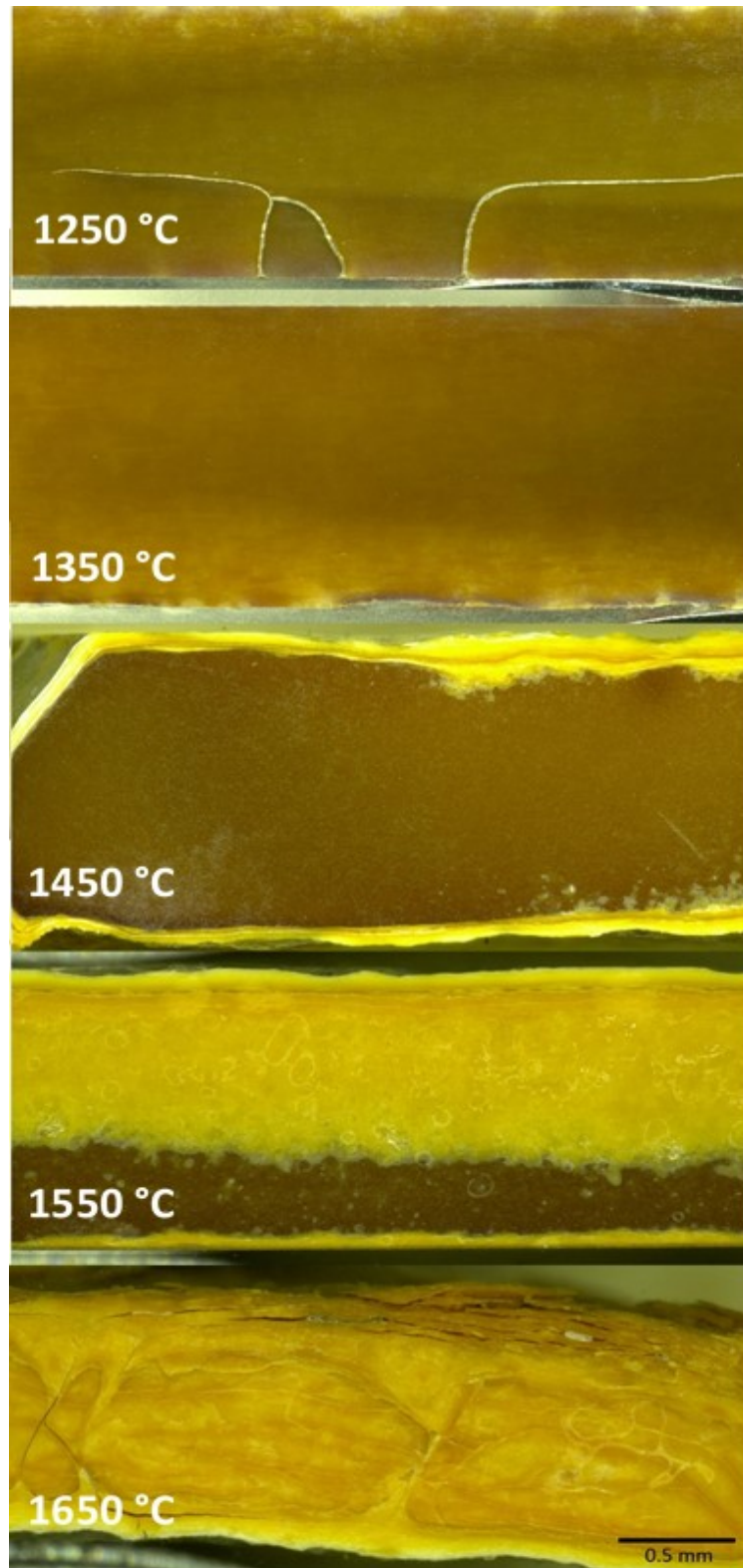
## 8.7 Influence of SPS parameters on BZCY72



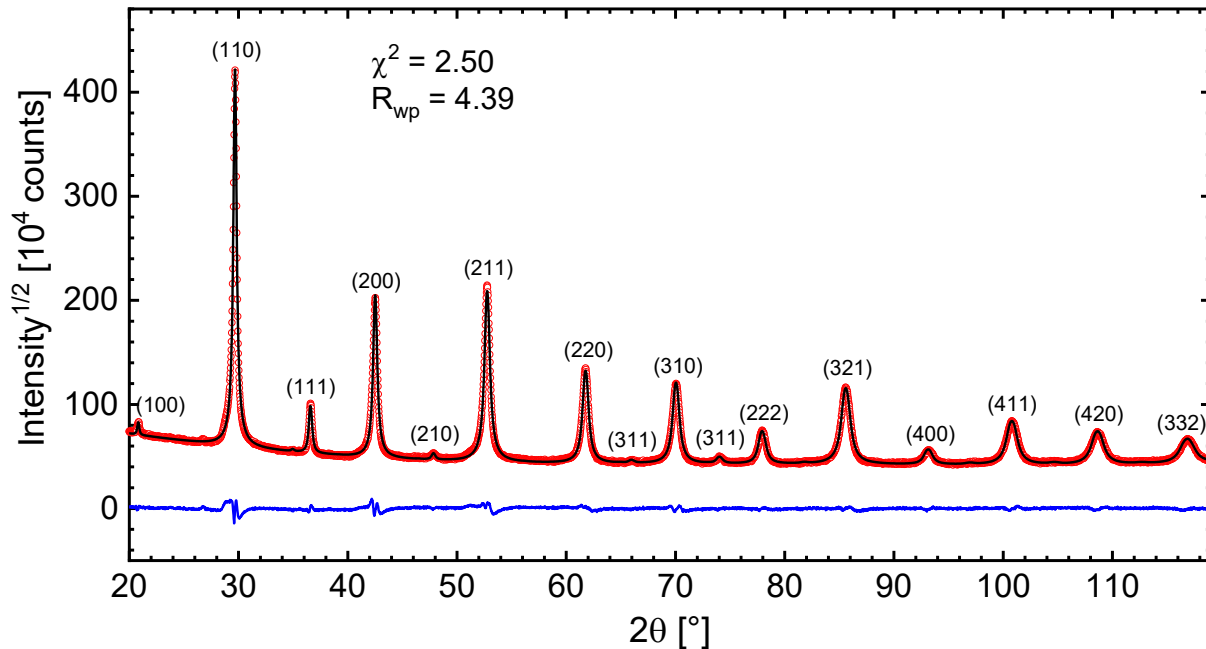
**Appendix 8.7.1:** The detailed progression of the relative piston position in dependence of the (a) maximum sintering temperature at  $p = 76$  MPa and (b) the applied pressure at  $T = 1350^\circ\text{C}$ .



**Appendix 8.7.2:** Approximate degradation time for BZCY72 as a function of the sintering temperature and the applied pressure. Observation was carried out over one year.



**Appendix 8.7.3:** Images of the polished cross section of BZCY72 samples prepared at different sintering temperatures taken by light microscopy. The difference in color is related to the increasing reduction of mainly Ce and enhanced diffusion of C into the sample at higher sintering temperatures. Interestingly, this process starts from the top site of the sample likely due to the direction of the DC current.

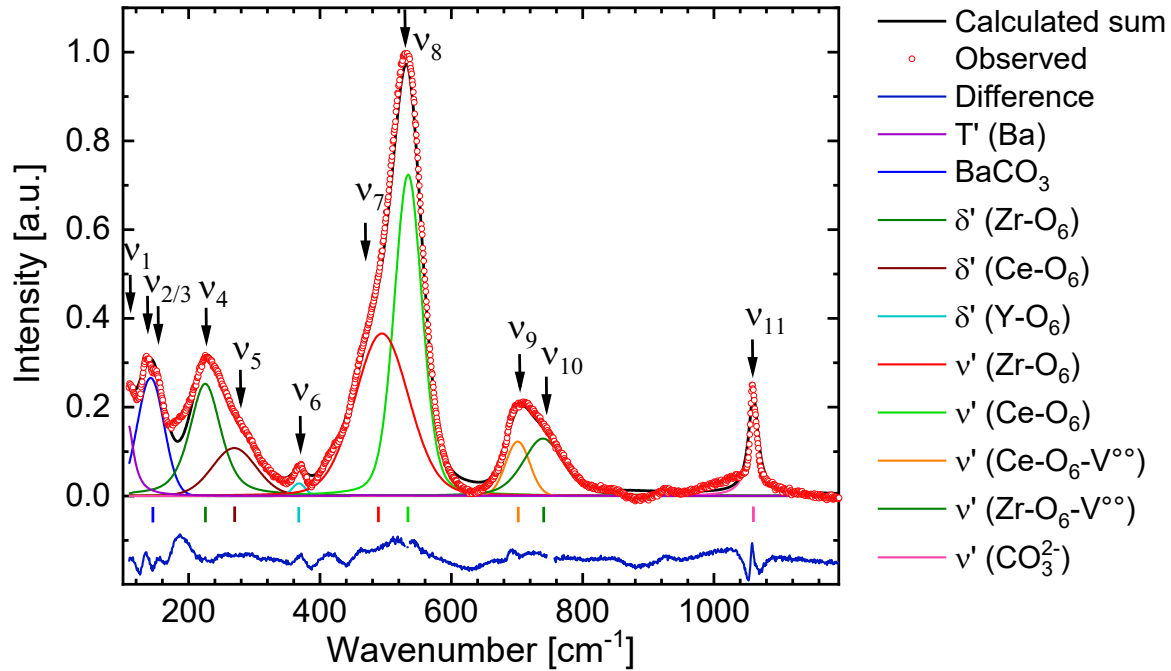


**Appendix 8.7.4:** Top: Exemplary Rietveld refinement of the BZCY72 sample sintered at 1350 °C, 76 MPa, 150 K/min and 5 min dwell time. The observed XRD pattern is represented by red dots while the calculated pattern is shown as black line and the difference as blue line.

Bottom: Structural parameters and selected B – O bond characteristics obtained from Rietveld refinement for different sintering temperatures (76 MPa) and applied pressures (1350 °C). The heating rates and holding times were kept at 150 K/min and 5 min, respectively.

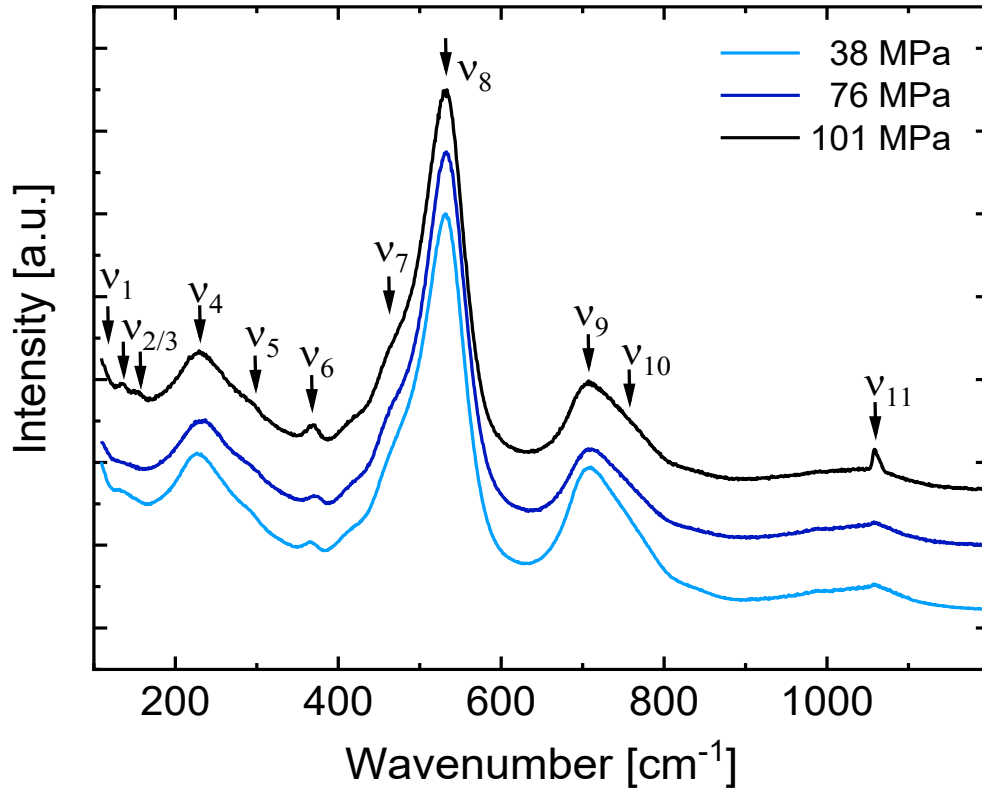
T <sub>Max</sub> [°C]	a [Å]	c [Å]	crystallites [nm]	strain [10 <sup>-3</sup> ]	Bond length [Å]	Angle [°]	R <sub>wp</sub> [%]
1150	6.014(2)	14.701(5)	62(7)	1.1(1)	2.1337(6)	89.681(15)	4.45
1250	6.015(2)	14.700(5)	68(6)	1.01(9)	2.1341(7)	89.675(18)	4.86
1350	6.014(1)	14.704(3)	76(7)	0.84(6)	2.1324(5)	89.732(13)	4.39
1450	6.014(1)	14.707(3)	88(7)	0.86(7)	2.1333(5)	89.733(13)	3.93
1550	6.014(1)	14.702(3)	108(9)	0.91(8)	2.1327(6)	89.743(14)	4.28
1650	6.014(1)	14.705(4)	170(12)	0.90(9)	2.1312(5)	89.765(14)	4.48

p [MPa]	a [Å]	c [Å]	crystallites [nm]	strain [10 <sup>-3</sup> ]	Bond length [Å]	Angle [°]	R <sub>wp</sub> [%]
39	6.018(3)	14.761(6)	116(9)	1.1(2)	2.1378(9)	89.808(2)	4.15
51	6.015(2)	14.711(5)	94(7)	0.93(9)	2.1357(8)	89.680(19)	5.21
64	6.014(2)	14.704(3)	76(7)	0.84(8)	2.1324(5)	89.732(12)	4.39
76	6.010(3)	14.700(4)	51(5)	1.0(1)	2.1325(4)	89.711(11)	3.05
101	5.998(3)	14.690(7)	54(6)	1.8(3)	2.1304(6)	89.733(13)	5.25

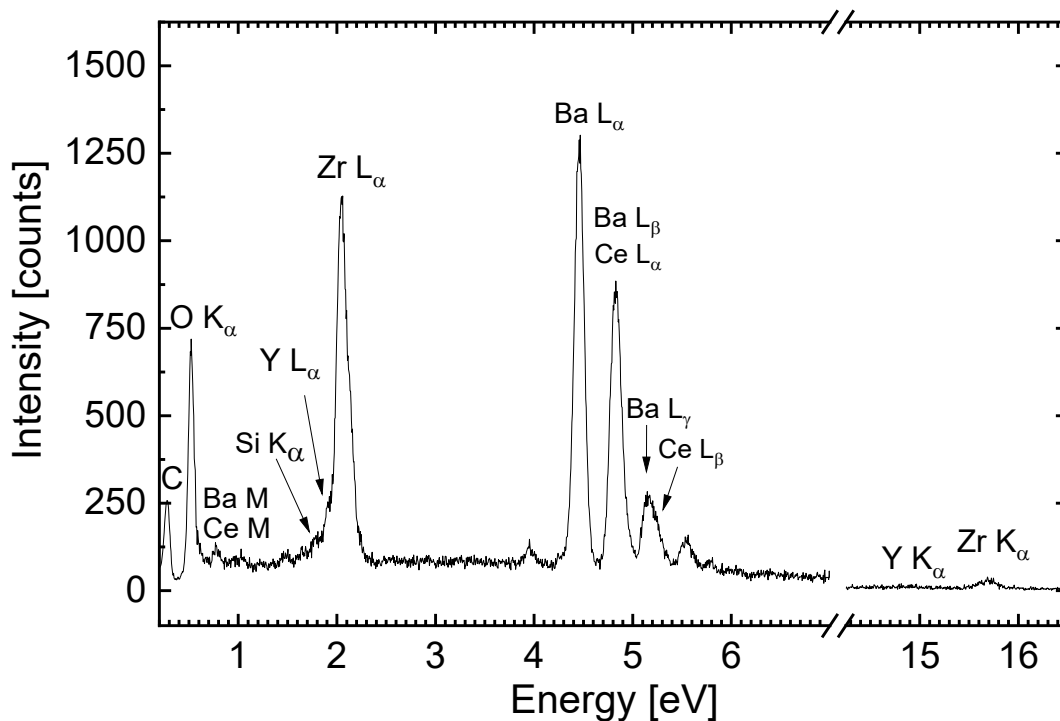


Mode	Wavenumber	FWHM	Area	Assignment
$\nu_1$	108 $\text{cm}^{-1}$	-	-	Translational oscillation of Ba
$\nu_2$	134 $\text{cm}^{-1}$	52.74	19.6	Lattice mode $\text{BaCO}_3$
$\nu_3$	148 $\text{cm}^{-1}$	-	-	Lattice mode $\text{BaCO}_3$
$\nu_4$	230 $\text{cm}^{-1}$	55.85	19.8	Zr-O bending mode
$\nu_5$	290 $\text{cm}^{-1}$	78.99	9.4	Ce-O bending mode
$\nu_6$	368 $\text{cm}^{-1}$	23.7	0.7	Y-O bending mode
$\nu_7$	490 $\text{cm}^{-1}$	50.2	43.0	$\text{CeO}_6$ octahedra stretching
$\nu_8$	534 $\text{cm}^{-1}$	96.9	40.3	$\text{ZrO}_6$ octahedra stretching
$\nu_9$	701 $\text{cm}^{-1}$	43.1	5.6	Zr-O stretching mode disturbed by near $V^{\bullet\bullet}$
$\nu_{10}$	740 $\text{cm}^{-1}$	71.4	11.51	Ce-O stretching mode disturbed by near $V^{\bullet\bullet}$
$\nu_{11}$	1059 $\text{cm}^{-1}$	18.0	5.4	Symmetric stretch of $\text{CO}_3^{2-}$

**Appendix 8.7.5:** Analysis, Fitting process (WiRE software) and additional data for the Raman spectroscopy. The 11 Modes are described by Pseudo Voigt Profile functions for the analysis part. All modes were assigned according to various sources [194-196, 276].

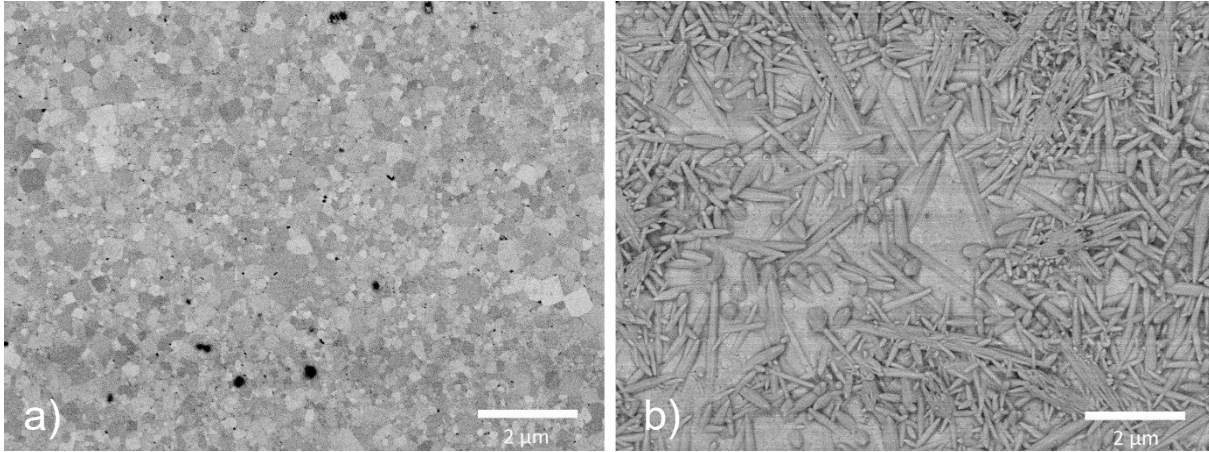


**Appendix 8.7.6:** Raman spectra of BZCY72 pellets for different applied pressures at 1350 °C, 150 K/min and 5 min dwell time with all major modes explained in section 4.1.3.

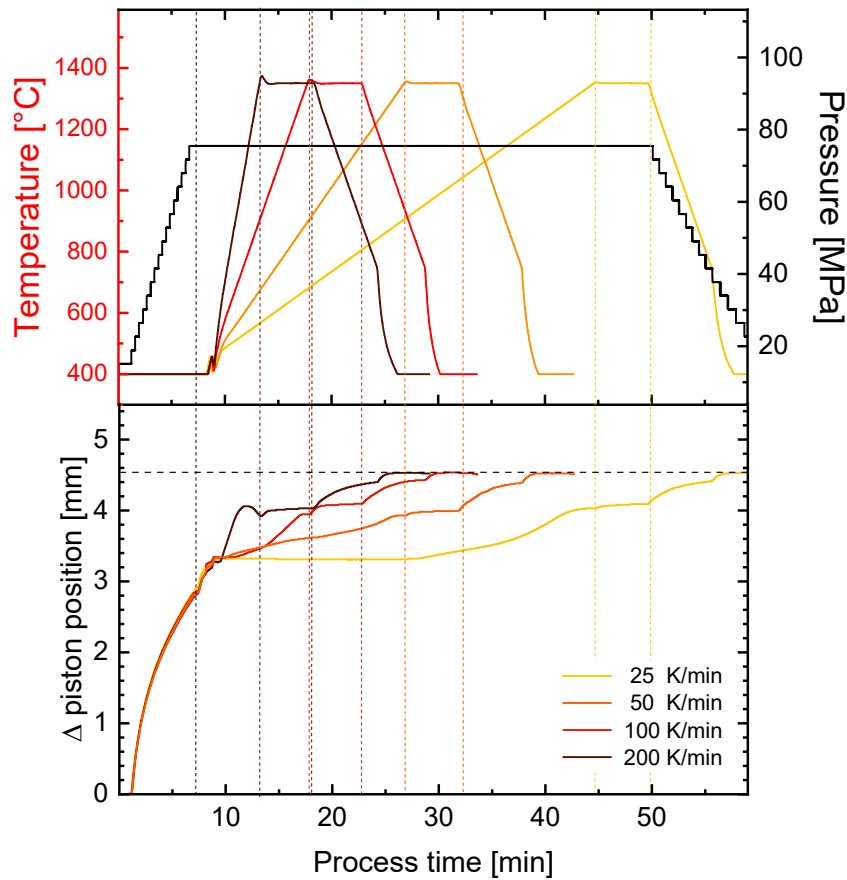


**Appendix 8.7.7:** EDX spectra of BZCY72 prepared at 1550 °C and 76 MPa using commercial powder with all elements and their characteristic energies shown in the graph.

## Influence of SPS parameters on BZCY72



**Appendix 8.7.8:** SEM micrographs of the BZCY72 sample measured in different oxygen partial pressure atmospheres. (a) Before IS measurement in wet oxygen atmosphere (b) after the measurement. The needles are Ba(OH)<sub>2</sub> crystals forming in humid oxidizing atmosphere from BaO impurities [203].

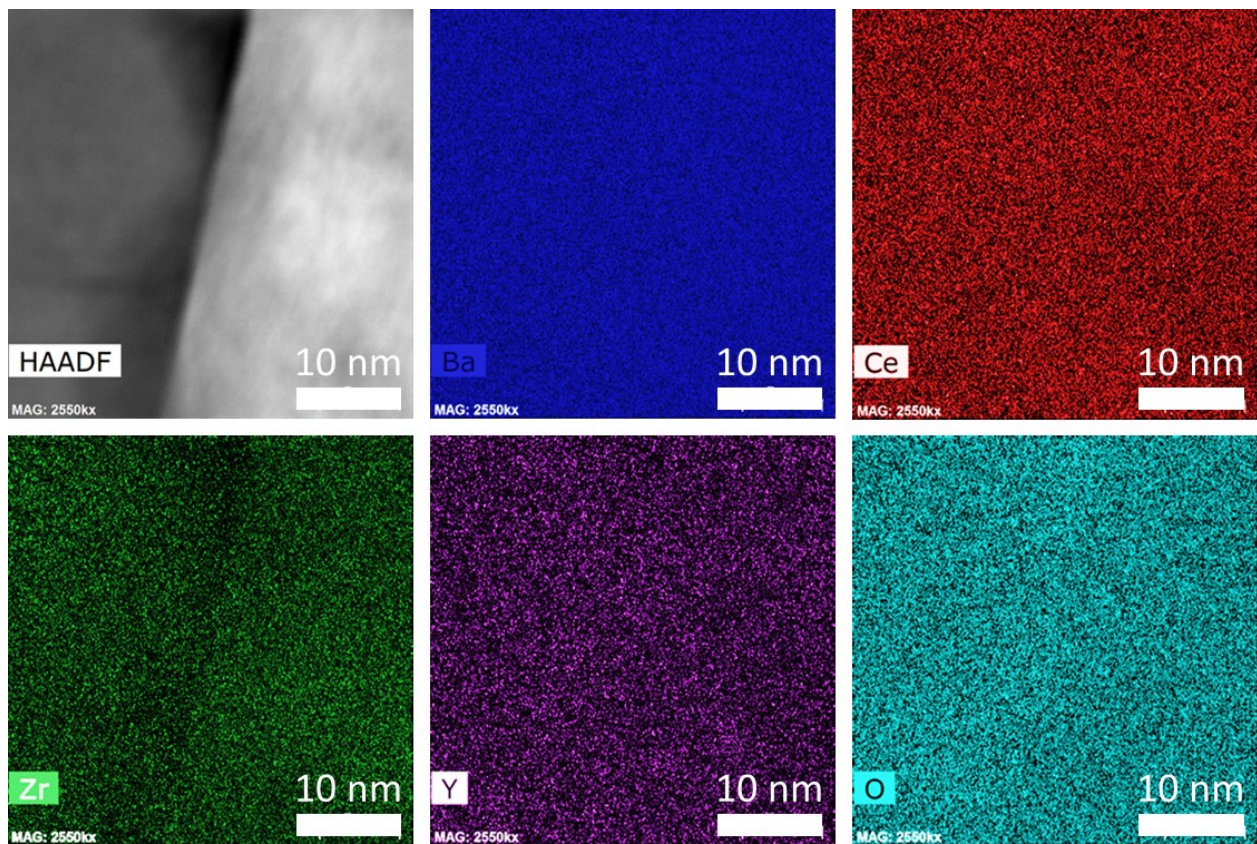


**Appendix 8.7.9:** Detailed progression of the plunger displacement during the SPS process on BZCY72 sample using varying heating rates.

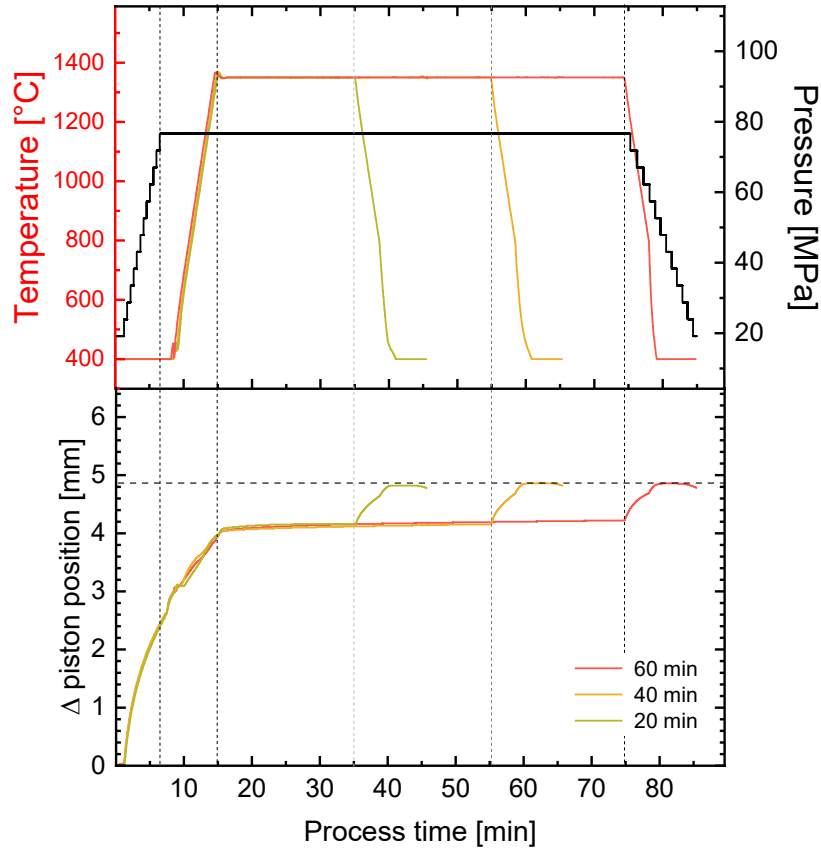


**Appendix 8.7.10:** Results from the Rietveld refinement of BZCY72 samples prepared by SPS applying various heating rates. Sintering temperature and applied pressure where 1350 °C and 76 MPa, respectively.

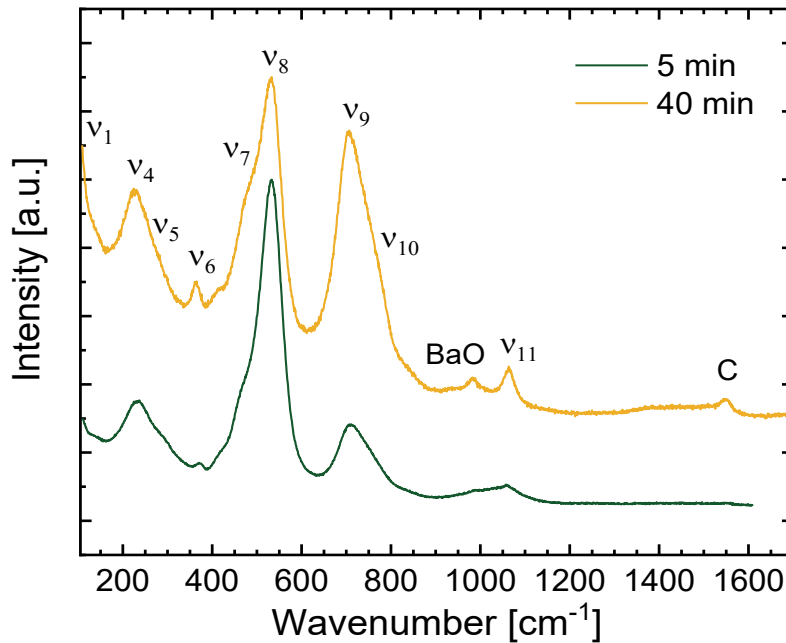
HR [K/min]	a [Å]	c [Å]	Crystallites [nm]	Strain [ $10^{-3}$ ]	Bond length [Å]	Angle [°]	R <sub>wp</sub>
25	6.015(7)	14.724(8)	127(10)	0.54(4)	2.132(2)	89.815(3)	5.69
50	6.013(5)	14.703(7)	89(16)	0.75(6)	2.1320(9)	89.780(2)	5.47
100	6.0147(3)	14.71(1)	86(7)	1.12(9)	2.132(1)	89.785(3)	5.15
150	6.014(1)	14.704(3)	76(4)	0.84(6)	2.1324(5)	89.732(2)	4.39
200	6.013(2)	14.708(8)	72(7)	1.9(2)	2.132(1)	89.716(2)	4.12



**Appendix 8.7.11:** TEM-EDX mapping of the grain boundary for a BZCY72 sample prepared at 1350 °C, 76 MPa and a heating rate of 50 K/min.



**Appendix 8.7.12:** Detailed progression of the plunger displacement during the SPS process on BZCY72 sample using varying dwell times.

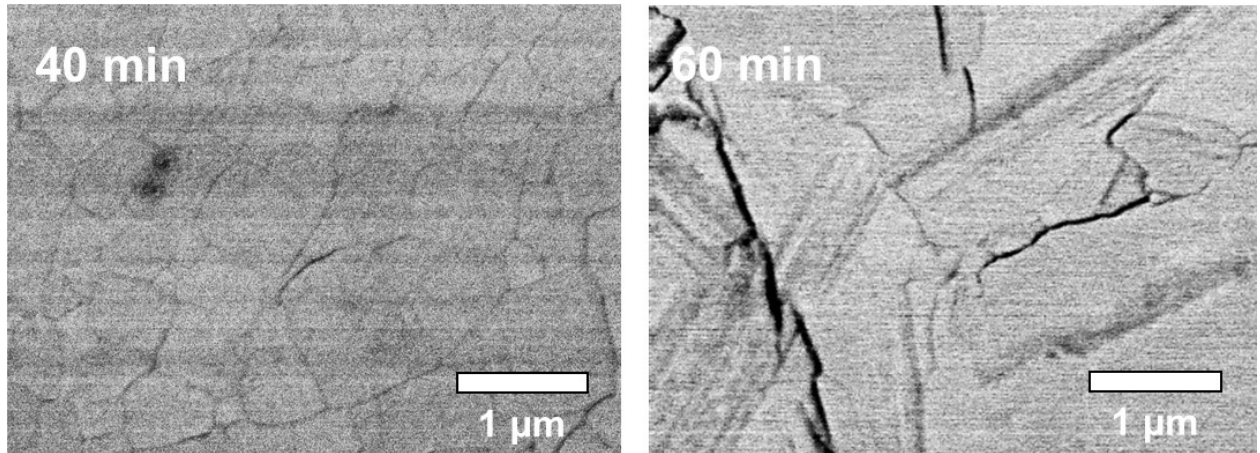


**Appendix 8.7.13:** Raman spectra of BZCY72 pellets for different holding times with all modes explained in section 4.1.2 and additional C diffusion impurities ( $T = 1350\text{ }^{\circ}\text{C}$ ,  $p = 76\text{ MPa}$ ,  $HR = 150\text{ K/min}$ ).

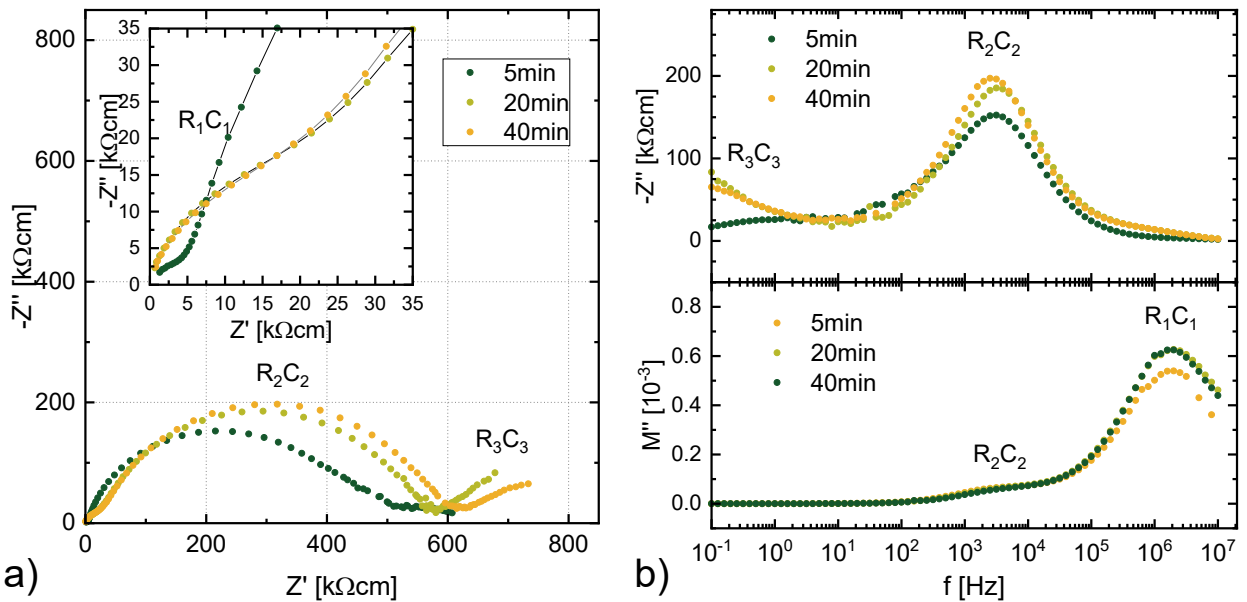


**Appendix 8.7.14:** Results from the Rietveld refinement of BZCY72 samples prepared by SPS applying various holding times. Sintering temperature and applied pressure were 1350 °C and 76 MPa, respectively.

Time [min]	a [Å]	c [Å]	Crystallites [nm]	Strain [ $10^{-3}$ ]	Bond length [Å]	Angle [°]	$R_{wp}$
5	6.014(1)	14.704(3)	76(4)	0.84(6)	2.1324(5)	89.732(2)	4.39
20	6.015(2)	14.707(8)	78(4)	1.9(3)	2.1326(9)	89.750(2)	4.98
40	6.012(3)	14.703(6)	81(5)	1.8(3)	2.132(12)	89.746(3)	4.82
60	6.013(3)	14.71(17)	134(15)	2.6(4)	2.133(3)	89.780(5)	5.15

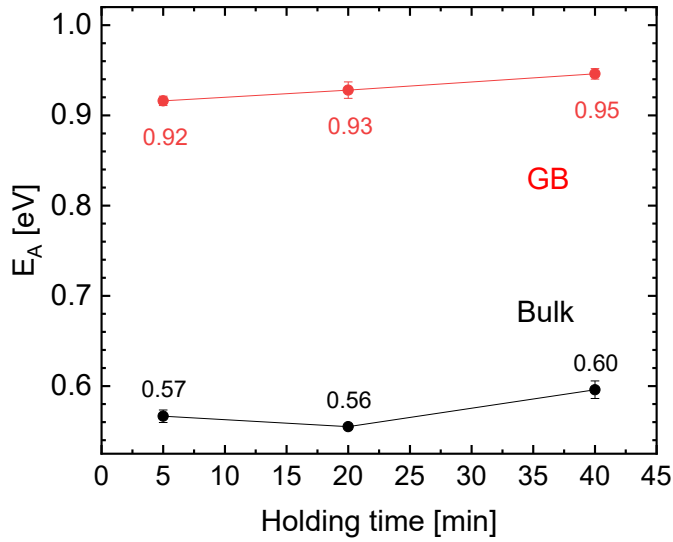


**Appendix 8.7.15:** Additional SEM imaging provided for different BZCY72 samples prepared by SPS at the same conditions as in figure 4.30 ( $T = 1350$  °C,  $p = 76$  MPa,  $HR = 150$  K/min).

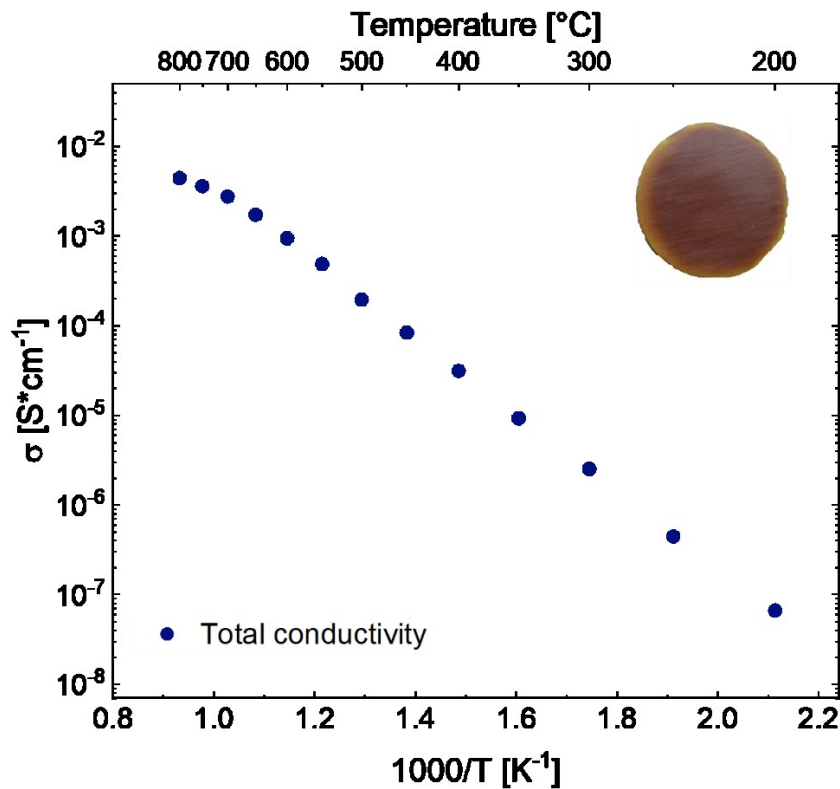


**Appendix 8.7.16:** IS data obtained at 300 °C in 3 % moist 5%  $H_2/Ar$  atmosphere for BZCY72 samples prepared by SPS at different holding times ( $T = 1350$  °C,  $p = 76$  MPa,  $HR = 150$  K/min). Left: Nyquist plot, Right: Spectroscopic plot and modulus plot.

Influence of SPS parameters on BZCY72

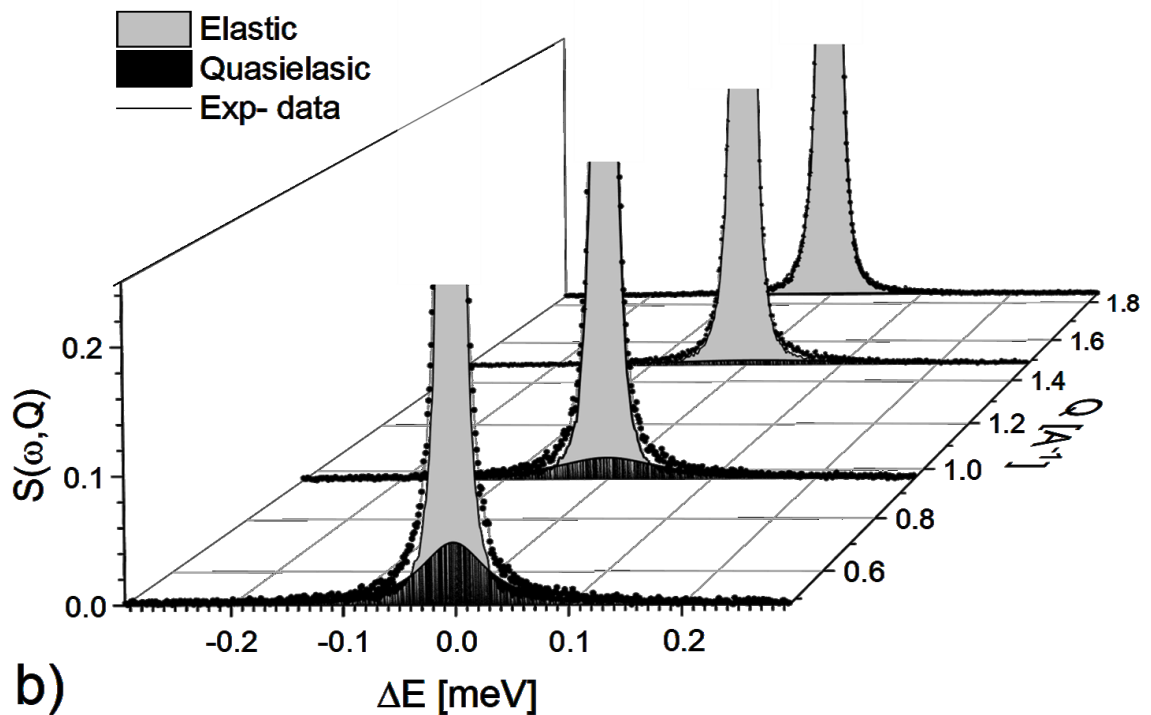
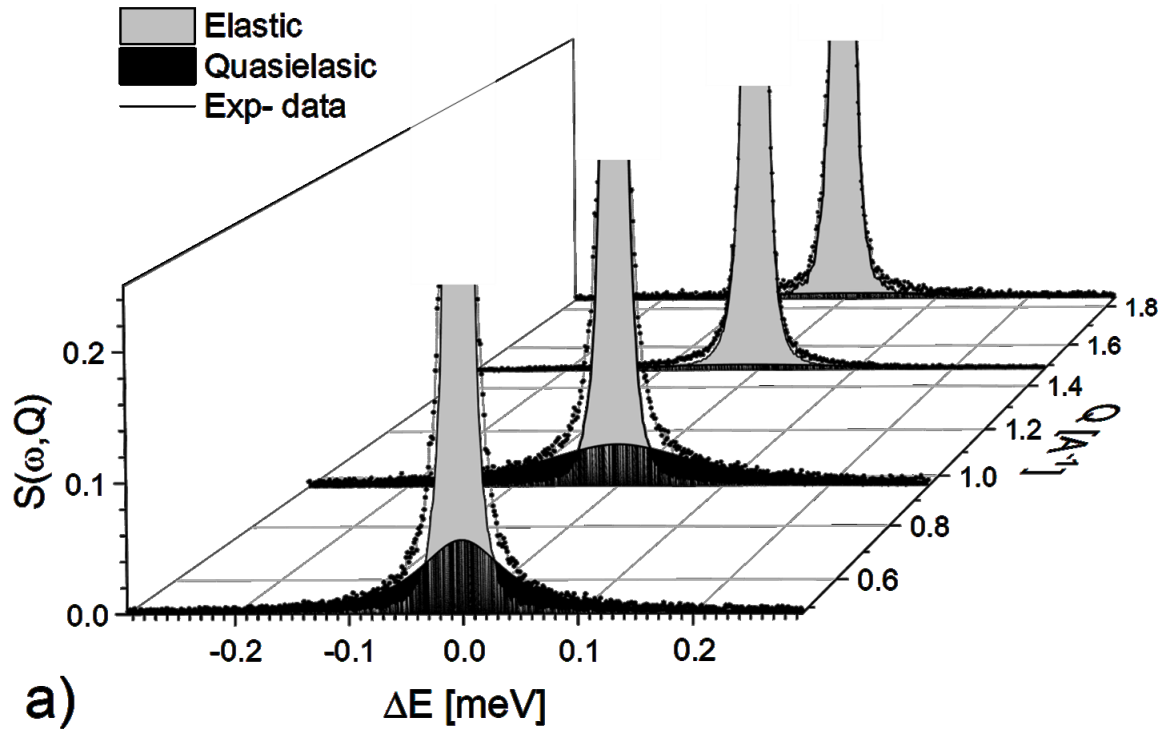


**Appendix 8.7.17:** Bulk and GB activation energies for different holding times extracted from figure 4.31. (T = 1350 °C, p= 76 MPa, HR = 150 K/min).



**Appendix 8.7.18:** According to chapter 4, the best set of conditions for SPS is T = 1350 °C, p = 76 MPa, HR = 150 K/min and t = 5 min. To confirm reproducibility, a second sample following those parameters was prepared. The resulting sample was stable as shown as picture in the graph. The total conductivity was measured up to 800 °C and is in accordance with former results. Due to water loss the Arrhenius plots starts bending above 650 °C. Conductivity:  $\sigma = 1.06 \cdot 10^{-3}$  S·cm<sup>-1</sup> at 600 °C and  $\sigma = 4.6 \cdot 10^{-3}$  S·cm<sup>-1</sup> at 800 °C.

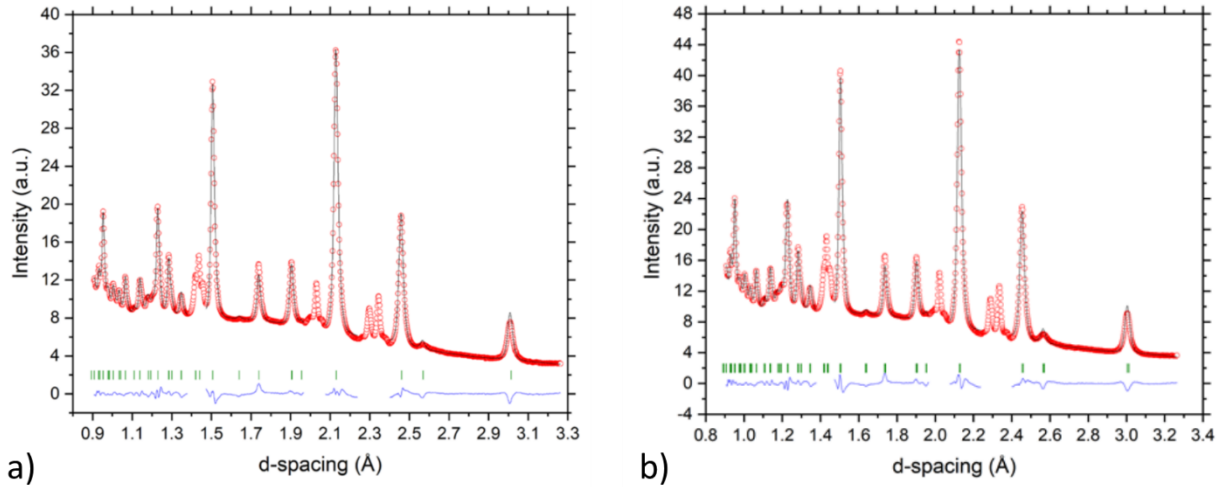
## 8.8 Neutron studies of BZCY72



**Appendix 8.8.1:** QENS spectra of BZCY72 at various  $Q$ -values at  $T = 600\text{ }^{\circ}\text{C}$ . The points represent the energy binned experimental data, grey areas are the elastic scattering part (resolution function) and black the quasi-elastic contribution. (a) SPS sample prepared at  $1350\text{ }^{\circ}\text{C}$ , (b) SPS sample prepared at  $1550\text{ }^{\circ}\text{C}$ . The elastic contribution is truncated to emphasize the quasi-elastic peak ( $p = 76\text{ MPa}$ ,  $HR = 150\text{ K/min}$ ).

**Appendix 8.8.2:** Diffusion constants of mobile species obtained by the Fick diffusion approximation through equation 5.1 ( $p=76$  MPa,  $HR=150$  K/min).

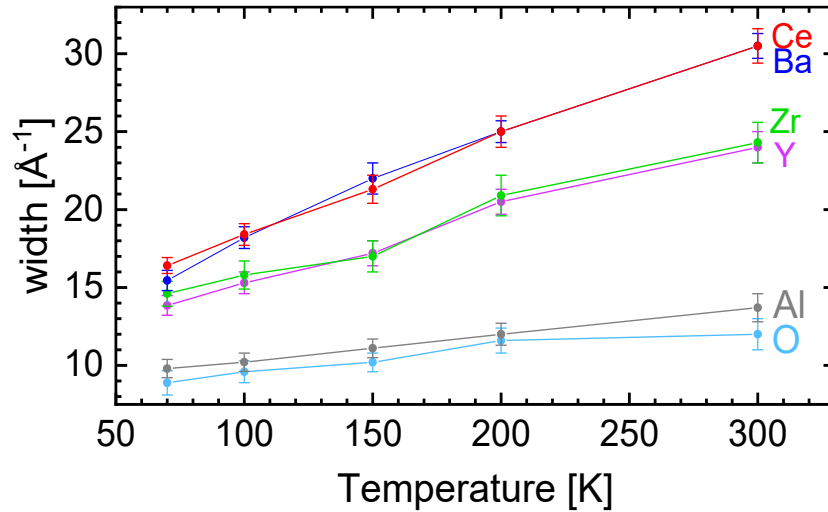
Temperature	$T_{\text{Sinter}} = 1350$ °C	$T_{\text{Sinter}} = 1550$ °C
400 °C	$D = 3.56 \cdot 10^{-6}$ cm <sup>2</sup> /s	$D = 4.61 \cdot 10^{-6}$ cm <sup>2</sup> /s
500 °C	$D = 5.05 \cdot 10^{-5}$ cm <sup>2</sup> /s	$D = 6.26 \cdot 10^{-6}$ cm <sup>2</sup> /s
600 °C	$D = 6.86 \cdot 10^{-6}$ cm <sup>2</sup> /s	$D = 9.17 \cdot 10^{-6}$ cm <sup>2</sup> /s



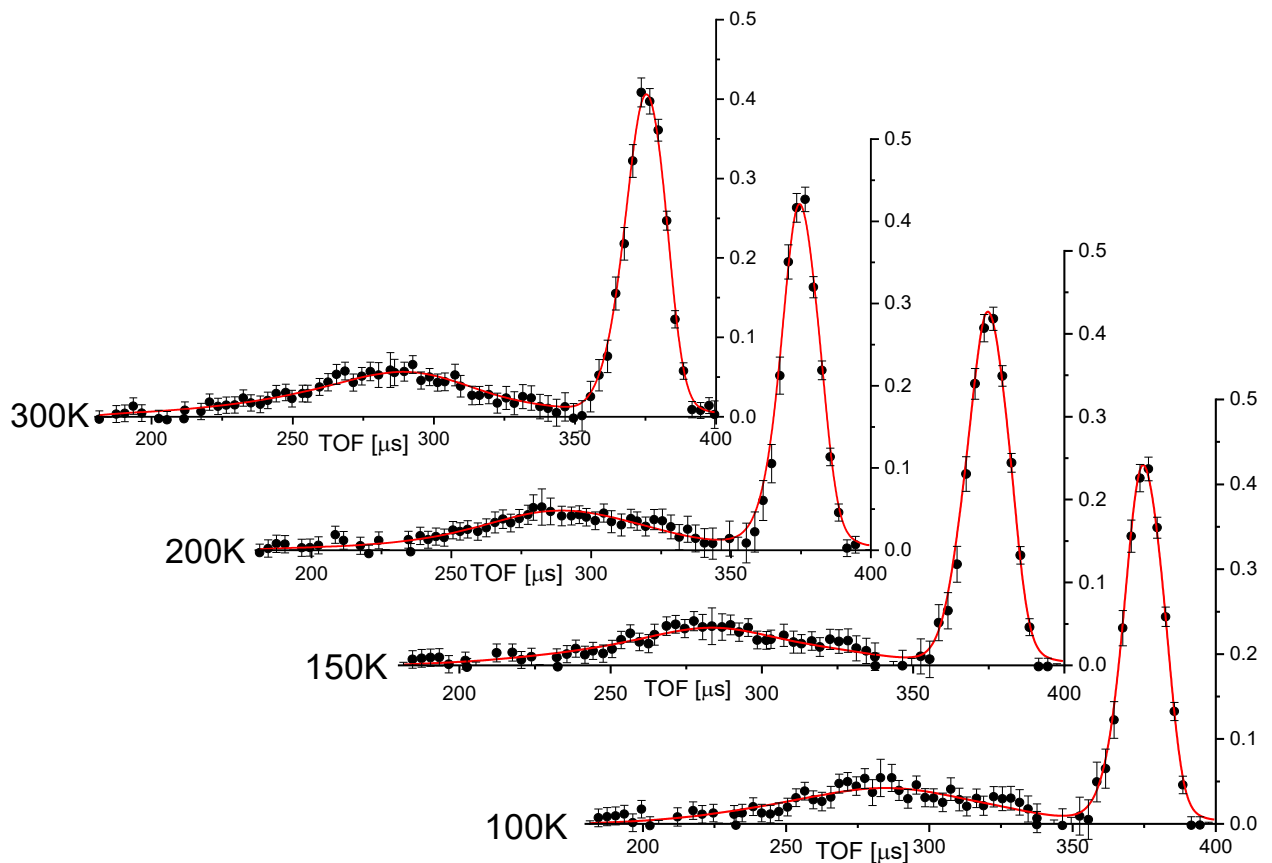
**Appendix 8.8.3:** Neutron diffraction (ND) data recorded at VESUVIO for SPS prepared ( $1450$  °C,  $76$  MPa,  $150$  K/min and  $5$  min) BZCY72 at (a)  $300$  K and (b)  $70$  K. Open red symbols – experimental data, thin black solid line – the Rietveld fit to the data, thin blue solid line – residual, thin vertical green lines – refined and indexed positions of the Bragg reflexes. The raw ND data were reduced using Mantid software and exported as ASCII for further treatment and Rietveld refinement using the TOPAS 5.0 software ( $R_{\text{wp}} = 2\%$ ). The d-spacing regions between  $1.38$  and  $1.48$  and between  $2.23$  and  $2.40$  corresponding to the scattering of the aluminium sample container have been excluded from the refinement.

**Appendix 8.8.4:** Root-mean-square deviations (RMSD) of atomic positions in the unit cell of BZCY72 obtained from XRD (untreated pellet) and ND (hydrated sample) refinement. The higher numbers for oxygen indicate the effect of the O – H bonding from the incorporated protonic defects.

Atom type	RMSD [Å] at 300 K	RMSD [Å] at 70 K
Ba	0.0022	0.0082
Zr	0.0022	0.0076
Ce	0.0022	0.0076
Y	0.0022	0.0076
O	0.0783	0.0405



**Appendix 8.8.5:** Values of the widths of Gaussian recoil peaks fitted to BZCY72 data recorded in backscattering. Widths are given by the Boltzmann population of partial vibrational densities of states causing Doppler broadening. The sample was prepared by SPS at 1450 °C, 76 MPa and 150 K/min.

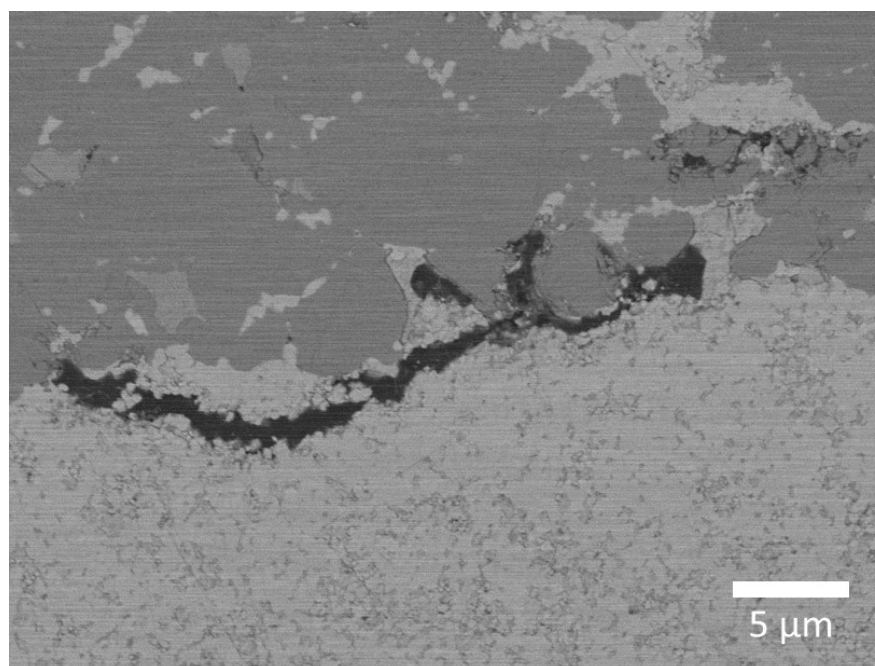


**Appendix 8.8.6:** Neutron Compton Scattering (NCS) of BZCY72 in forward scattering for all measured temperatures minus 70 K measured at VESUVIO. The black data points with error bars represent the corrected NCS data and the red solid line the total fit to the data. The presented data has been corrected for multiple scattering and gamma background, according to the procedure described in section 2.3.5.

## 8.9 Co-sintering of a membrane-electrode-assembly

**Appendix 8.9.1:** Results of the Rietveld refinement for the reduced and non-reduced part of the electrode.

Non-reduced layer	Reduced layer
$R_{exp} = 0.97$ $R_{wp} = 3.20$	$R_{exp} = 1.85$ $R_{wp} = 2.82$
$R_p = 2.27$ $\chi^2 = 3.30$	$R_p = 2.00$ $\chi^2 = 1.52$
<b>Quantitative Analysis</b>	<b>Quantitative Analysis</b>
NiO: 57.2(2) %	Ni: 82.1(11) %
BZCY72: 37.8(3) %	BZCY72: 16.2(3) %
BaNiO <sub>3</sub> : 1.5(2) %	BaCO <sub>3</sub> : 1.7(2) %
BaY <sub>2</sub> NiO <sub>5</sub> : 2.4(5) %	
BaCO <sub>3</sub> : 1.5(2) %	
<b>Nickel oxide</b>	<b>Nickel</b>
Space group: $Fm\bar{3}m$	Space group: $Fm\bar{3}m$
Lattice parameter: $a = 4.178(1)$ Å	Lattice parameter: $a = 3.524(1)$ Å
Crystallite size: 330(16) nm	Crystallite size: 174(9) nm
<b>BaZr<sub>0.7</sub>Ce<sub>0.2</sub>Y<sub>0.1</sub>O<sub>3-δ</sub></b>	<b>BaZr<sub>0.7</sub>Ce<sub>0.2</sub>Y<sub>0.1</sub>O<sub>3-δ</sub></b>
Space group: $R\bar{3}c$	Space group: $R\bar{3}c$
Lattice parameter: $a = 5.968(4)$ Å	Lattice parameter: $a = 5.980(3)$ Å
$c = 14.686(13)$ Å	$c = 14.714(14)$ Å
Crystallite size: 57(9) nm	Crystallite size: 69(15) nm
Ba Occupancy: 0.92(2)	Ba Occupancy: 0.98(3)
Zr/Y Occupancy: 0.79 (18)	Zr/Y Occupancy: 0.82 (2)



**Appendix 8.9.2:** SEM image of the interface between electrode and electrolyte for SPS prepared symmetrical NiO-BZCY72 cell prepared at 1350 °C, 76 MPa and 150 K/min.

## 9 References

1. IEA, *World Energy Balances*. Allrights reserved. 2018.
2. Urban, M.C., *Accelerating extinction risk from climate change*. *Science*, 2015. **348**(6234): p. 571-573.
3. Zemp, M., et al., *Global glacier mass changes and their contributions to sea-level rise from 1961 to 2016*. *Nature*, 2019. **568**(7752): p. 382.
4. Le Hou  rou, H.N., *Climate change, drought and desertification*. *Journal of arid Environments*, 1996. **34**(2): p. 133-185.
5. Rosenzweig, C., et al., *Climate change and extreme weather events; implications for food production, plant diseases, and pests*. *Global change & human health*, 2001. **2**(2): p. 90-104.
6. *Hydrogen Production: Natural Gas Reforming*. Department of Energy, Retrieved 6 April 2017.
7. Duan, C., et al., *Proton-conducting oxides for energy conversion and storage*. *Applied Physics Reviews*, 2020. **7**(1): p. 011314.
8. Haile, S.M., *Fuel cell materials and components*. *Acta Materialia*, 2003. **51**(19): p. 5981-6000.
9. Yamazaki, Y., R. Hernandez-Sanchez, and S.M. Haile, *High Total Proton Conductivity in Large-Grained Yttrium-Doped Barium Zirconate*. *Chemistry of Materials*, 2009. **21**(13): p. 2755-2762.
10. Fabbri, E., A. Magras  , and D. Pergolesi, *Low-temperature solid-oxide fuel cells based on proton-conducting electrolytes*. *MRS Bulletin*, 2014. **39**(9): p. 792-797.
11. Dai, H., et al., *Electrochemical performance of protonic ceramic fuel cells with stable BaZrO<sub>3</sub>-based electrolyte: A mini-review*. *Electrochemistry Communications*, 2018.
12. Tong, J., et al., *Proton-conducting yttrium-doped barium cerate ceramics synthesized by a cost-effective solid-state reactive sintering method*. *Solid State Ionics*, 2010. **181**(33-34): p. 1486-1498.
13. Souza, E.C.C.d. and R. Muccillo, *Properties and applications of perovskite proton conductors*. *Materials Research*, 2010. **13**(3): p. 385-394.
14. Babilo, P., *Processing and characterization of proton conducting yttrium doped barium zirconate for solid oxide fuel cell applications*. 2007, California Institute of Technology.
15. Halperin, B. and R. Englman, *Cooperative dynamic Jahn-Teller Effect. II. crystal distortion in perovskites*. *Physical Review B*, 1971. **3**(5): p. 1698.
16. Howard, C.J. and H.T. Stokes, *Group-theoretical analysis of octahedral tilting in perovskites*. *Acta Crystallographica Section B: Structural Science*, 1998. **54**(6): p. 782-789.
17. Knight, K., *Structural phase transitions, oxygen vacancy ordering and protonation in doped BaCeO<sub>3</sub>: results from time-of-flight neutron powder diffraction investigations*. *Solid State Ionics*, 2001. **145**(1-4): p. 275-294.
18. Goldschmidt, V.M., *Die gesetze der krystallochemie*. *Naturwissenschaften*, 1926. **14**(21): p. 477-485.
19. Ishihara, T., *Perovskite oxide for solid oxide fuel cells*. 2009: Springer Science & Business Media.
20. Hossain, S., et al., *A review on proton conducting electrolytes for clean energy and intermediate temperature-solid oxide fuel cells*. *Renewable and Sustainable Energy Reviews*, 2017. **79**: p. 750-764.
21. Glazer, A., *The classification of tilted octahedra in perovskites*. *Acta Crystallographica Section B: Structural Crystallography and Crystal Chemistry*, 1972. **28**(11): p. 3384-3392.
22. Glazer, A., *Simple ways of determining perovskite structures*. *Acta Crystallographica Section A: Crystal Physics, Diffraction, Theoretical and General Crystallography*, 1975. **31**(6): p. 756-762.
23. Thomas, D. and J. Lander, *Hydrogen as a donor in zinc oxide*. *The Journal of Chemical Physics*, 1956. **25**(6): p. 1136-1142.
24. Haugrud, R., *High Temperature Proton Conductors - Fundamentals and Functionalities*. *Diffusion Foundations*, 2016. **8**: p. 31-79.
25. Nguyen, Q.M., *Ceramic fuel cells*. *J. Am. Ceram. Soc*, 1993. **76**(3): p. 563-588.

26. Stambouli, A.B. and E. Traversa, *Solid oxide fuel cells (SOFCs): a review of an environmentally clean and efficient source of energy*. Renewable and sustainable energy reviews, 2002. **6**(5): p. 433-455.
27. Iwahara, H., et al., *Proton conduction in sintered oxides and its application to steam electrolysis for hydrogen production*. Solid State Ionics, 1981. **3**: p. 359-363.
28. Murugaraj, P., et al., *High proton conductivity in barium yttrium stannate Ba<sub>2</sub>YSnO<sub>5</sub>*. Solid State Ionics, 1997. **98**(1-2): p. 1-6.
29. Shannon, R.D., *Revised effective ionic radii and systematic studies of interatomic distances in halides and chalcogenides*. Acta crystallographica section A: crystal physics, diffraction, theoretical and general crystallography, 1976. **32**(5): p. 751-767.
30. Carneim, R.D. and T. Armstrong, *Decomposition of Yttrium-Doped Barium Cerate in Carbon Dioxide*. J. Am. Chem. Soc, 2003.
31. Carneim, R. and T. Armstrong. *Chemical stability of Barium cerates-based high temperature proton conductors*. in 225th American Chemical Society National Meeting—Fuel Division Preprint, New Orleans, LA. 2003.
32. Kreuer, K.D., *Proton-Conducting Oxides*. Annual Review of Materials Research, 2003. **33**(1): p. 333-359.
33. Wang, S., et al., *Spark-plasma-sintered barium zirconate based proton conductors for solid oxide fuel cell and hydrogen separation applications*. international journal of hydrogen energy, 2015. **40**(16): p. 5707-5714.
34. Ricote, S., et al., *Conductivity study of dense BaZr<sub>0.9</sub>Y<sub>0.1</sub>O<sub>(3-δ)</sub> obtained by spark plasma sintering*. Solid State Ionics, 2012. **213**: p. 36-41.
35. Tao, S. and J.T.S. Irvine, *Conductivity studies of dense yttrium-doped BaZrO<sub>3</sub> sintered at 1325°C*. Journal of Solid State Chemistry, 2007. **180**(12): p. 3493-3503.
36. Coors, W.G. and D.W. Readey, *Proton conductivity measurements in yttrium barium cerate by impedance spectroscopy*. Journal of the American Ceramic Society, 2002. **85**(11): p. 2637-2640.
37. Shirpour, M., R. Merkle, and J. Maier, *Evidence for space charge effects in Y-doped BaZrO<sub>3</sub> from reduction experiments*. Solid State Ionics, 2012. **216**: p. 1-5.
38. Simonenko, T.L., et al., *Synthesis of BaCe<sub>0.9-x</sub>Zr<sub>x</sub>Y<sub>0.1</sub>O<sub>3-δ</sub> nanopowders and the study of proton conductors fabricated on their basis by low-temperature spark plasma sintering*. International Journal of Hydrogen Energy, 2019.
39. Zhong, Z., *Stability and conductivity study of the BaCe<sub>0.9-x</sub>Zr<sub>x</sub>Y<sub>0.1</sub>O<sub>2.95</sub> systems*. Solid State Ionics, 2007. **178**(3-4): p. 213-220.
40. Tu, C.S., et al., *Temperature-dependent structures of proton-conducting Ba<sub>(Zr(0.8-x)Ce<sub>(x)</sub>Y<sub>(0.2)</sub>)O<sub>(2.9)</sub> ceramics by Raman scattering and x-ray diffraction</sub>*. J Phys Condens Matter, 2012. **24**(15): p. 155403.
41. Ricote, S., et al., *Synthesis, Sintering, and Electrical Properties of BaCe<sub>0.9-x</sub>Zr<sub>x</sub>Y<sub>0.1</sub>O<sub>3-δ</sub>*. Journal of Nanomaterials, 2008. **2008**: p. 1-5.
42. Ricote, S., et al., *Conductivity study of dense BaCe<sub>x</sub>Zr<sub>(0.9-x)</sub>Y<sub>0.1</sub>O<sub>(3-δ)</sub> prepared by solid state reactive sintering at 1500 °C*. International Journal of Hydrogen Energy, 2012. **37**(9): p. 7954-7961.
43. Pagnier, T., et al., *A neutron diffraction study of BaCe<sub>x</sub>Zr<sub>1-x</sub>O<sub>3</sub>*. The European Physical Journal-Applied Physics, 2000. **9**(1): p. 1-9.
44. Kröger, F. and H. Vink, *Relations between the concentrations of imperfections in solids*. Journal of Physics and Chemistry of Solids, 1958. **5**(3): p. 208-223.
45. Yushi, D., et al., *Variation of optimum yttrium doping concentrations of perovskite type proton conductors BaZr<sub>1-x</sub>Y<sub>x</sub>O<sub>3-α</sub> (0 ≤ x ≤ 0.3) with temperature*. Journal of Rare Earths, 2013. **31**(10): p. 1017-1022.
46. Malikova, N., et al., *Proton-containing yttrium-doped barium cerate: A simultaneous structural and dynamic study by neutron scattering*. The Journal of Physical Chemistry C, 2007. **111**(17): p. 6574-6580.
47. Duval, S., *Y-substituted barium zirconate, a proton conducting electrolyte for applications at intermediate temperatures*. 2008, Technische Universität München.
48. Fish, J.S., *Investigation of a novel protonic/electronic ceramic composite material as a candidate for hydrogen separation membranes*. 2014, Colorado School of Mines. Arthur Lakes Library.



49. CoorsTek, <https://www.coorstek.com/>, 2019.
50. Cerpotech, <https://www.cerpotech.com>, 2019.
51. Norby, T., *Solid-state protonic conductors: principles, properties, progress and prospects*. Solid State Ionics, 1999. **125**(1-4): p. 1-11.
52. Bonanos, N., *Transport properties and conduction mechanism in high-temperature protonic conductors*. Solid State Ionics, 1992. **53**: p. 967-974.
53. Davies, R., M. Islam, and J. Gale, *Dopant and proton incorporation in perovskite-type zirconates*. Solid State Ionics, 1999. **126**(3-4): p. 323-335.
54. Bonanos, N. and F.W. Poulsen, *Considerations of defect equilibria in high temperature proton-conducting cerates*. Journal of Materials Chemistry, 1999. **9**(2): p. 431-434.
55. Coors, W.G., H. Hélix, and F. Villefranche-sur-Mer, *On the Nature of Electronic Defects in Y-doped Barium Zirconate/Cerate*. 2018.
56. Zhu, H., et al., *Defect incorporation and transport within dense BaZr<sub>0.8</sub>Y<sub>0.2</sub>O<sub>3-δ</sub> (BZY20) proton-conducting membranes*. Journal of The Electrochemical Society, 2018. **165**(9): p. F581-F588.
57. Poulsen, F.W., *Method for calculating ionic and electronic defect concentrations in proton containing perovskites*. Journal of Solid State Chemistry, 1999. **143**(1): p. 115-121.
58. Sass, T., *Yttrium Doped Barium Zirconate: Electrical Properties and Electrodes*, in *Department of Chemistry*. 2013, University of Oslo: Oslo.
59. Münch, W., et al., *A quantum molecular dynamics study of proton conduction phenomena in BaCeO<sub>3</sub>*. Solid State Ionics, 1996. **86**: p. 647-652.
60. Pionke, M., et al., *Investigation of the hydrogen mobility in a mixed perovskite: Ba [Ca<sub>(1-x)/3</sub>Nb<sub>(2-x)/3</sub>] O<sub>3-x/2</sub> by quasielastic neutron scattering*. Solid State Ionics, 1997. **97**(1-4): p. 497-504.
61. Hempelmann, R., et al., *Muon diffusion and trapping in proton conducting oxides*. Solid State Ionics, 1998. **107**(3-4): p. 269-280.
62. Agmon, N., *The grotthuss mechanism*. Chemical Physics Letters, 1995. **244**(5-6): p. 456-462.
63. Norby, T. and R. Haugsrud, *Dense ceramic membranes for hydrogen separation*. 2006, Wiley Online Library. p. 1-48.
64. Nowick, A. and A. Vaysleyb, *Isotope effect and proton hopping in high-temperature protonic conductors*. Solid State Ionics, 1997. **97**(1-4): p. 17-26.
65. Bonanos, N., *Oxide-based protonic conductors: point defects and transport properties*. Solid State Ionics, 2001. **145**(1-4): p. 265-274.
66. Kreuer, K., *On the complexity of proton conduction phenomena*. Solid state ionics, 2000. **136**: p. 149-160.
67. Nowick, A. and Y. Du, *High-temperature protonic conductors with perovskite-related structures*. Solid State Ionics, 1995. **77**: p. 137-146.
68. Iwahara, H., et al., *Protonic conduction in calcium, strontium and barium zirconates*. Solid State Ionics, 1993. **61**(1-3): p. 65-69.
69. Etsell, T. and S.N. Flengas, *Electrical properties of solid oxide electrolytes*. Chemical Reviews, 1970. **70**(3): p. 339-376.
70. Kessel, H., et al., *Rapid sintering of novel materials by FAST/SPS—Further development to the point of an industrial production process with high cost efficiency*. FCT Systeme GmbH, 2010. **96528**.
71. Sairam, K., et al., *Influence of spark plasma sintering parameters on densification and mechanical properties of boron carbide*. International Journal of Refractory Metals and Hard Materials, 2014. **42**: p. 185-192.
72. Hulbert, D.M., et al., *The absence of plasma in “spark plasma sintering”*. Journal of Applied Physics, 2008. **104**(3): p. 033305.
73. Witte, K., et al., *High energy X-ray diffraction study of a dental ceramics—titanium functional gradient material prepared by field assisted sintering technique*. Materials Characterization, 2014. **95**: p. 266-271.
74. Guillon, O., et al., *Field-Assisted Sintering Technology/Spark Plasma Sintering: Mechanisms, Materials, and Technology Developments*. Advanced Engineering Materials, 2014. **16**(7): p. 830-849.

75. Zhou, Y., et al., *Densification and grain growth in pulse electric current sintering of alumina*. Journal of the European Ceramic Society, 2004. **24**(12): p. 3465-3470.
76. Garay, J.E., *Current-Activated, Pressure-Assisted Densification of Materials*. Annual Review of Materials Research, 2010. **40**(1): p. 445-468.
77. Bloxam, A.G., GB Patent No. 27, 002., **1906**.
78. Weintraub, G., *Process and apparatus for sintering refractory materials*. US Patent No. 1,071,488, 1913.
79. Kiyoshi, I., *Method of electrically sintering discrete bodies* US Patent No. 3,250,892., 1966.
80. Ibrahim, A., et al., *Processing of porous Ti and Ti5Mn foams by spark plasma sintering*. Materials & Design, 2011. **32**(1): p. 146-153.
81. Becker, M.Z.e., N. Shomrat, and Y. Tsur, *Recent advances in mechanism research and methods for electric-field-assisted sintering of ceramics*. Advanced Materials, 2018. **30**(41): p. 1706369.
82. Olevsky, E. and D. Dudina, *Field-Assisted Sintering*. 2018: Springer.
83. German, R.M., *Coarsening in Sintering: Grain Shape Distribution, Grain Size Distribution, and Grain Growth Kinetics in Solid-Pore Systems*. Critical Reviews in Solid State and Materials Sciences, 2010. **35**(4): p. 263-305.
84. Patterson, B. and Y. Liu, *Relationship between grain*. Metallurgical Transactions A, 1992. **23**(9): p. 2481-2482.
85. Chaim, R., *Densification mechanisms in spark plasma sintering of nanocrystalline ceramics*. Materials Science and Engineering: A, 2007. **443**(1-2): p. 25-32.
86. Rahaman, M.N., *Ceramic processing and sintering*. 2017: CRC press.
87. Kang, S.-J.L., *Sintering: densification, grain growth and microstructure*. 2004: Elsevier.
88. Chaim, R., et al., *Grain growth during spark plasma and flash sintering of ceramic nanoparticles: a review*. Journal of Materials Science, 2017. **53**(5): p. 3087-3105.
89. Brook, R., *Pore-grain boundary interactions and grain growth*. Journal of the American Ceramic Society, 1969. **52**(1): p. 56-57.
90. Munir, Z.A., D.V. Quach, and M. Ohyanagi, *Electric current activation of sintering: a review of the pulsed electric current sintering process*. Journal of the American Ceramic Society, 2011. **94**(1): p. 1-19.
91. Ghosh, S., et al., *A huge effect of weak dc electrical fields on grain growth in zirconia*. Journal of the American Ceramic Society, 2009. **92**(8): p. 1856-1859.
92. Starnes, S. and H. Conrad, *Grain size distribution in ultrafine-grained yttria-stabilized zirconia deformed without and with an electric field*. Scripta Materialia, 2008. **59**(10): p. 1115-1118.
93. Munir, Z.A., U. Anselmi-Tamburini, and M. Ohyanagi, *The effect of electric field and pressure on the synthesis and consolidation of materials: A review of the spark plasma sintering method*. Journal of Materials Science, 2006. **41**(3): p. 763-777.
94. Xie, G., et al., *Frequency effect on pulse electric current sintering process of pure aluminum powder*. Materials Science and Engineering: A, 2003. **359**(1-2): p. 384-390.
95. Chen, W., et al., *Fundamental investigations on the spark plasma sintering/synthesis process: I. Effect of dc pulsing on reactivity*. Materials Science and Engineering: A, 2005. **394**(1-2): p. 132-138.
96. Manthiram, A., J. Kuo, and J.B. Goodenough, *Characterization of oxygen-deficient perovskites as oxide-ion electrolytes*. Solid State Ionics, 1993. **62**(3-4): p. 225-234.
97. Slade, R.C., S.D. Flint, and N. Singh, *Investigation of protonic conduction in Yb- and Y-doped barium zirconates*. Solid State Ionics, 1995. **82**(3-4): p. 135-141.
98. Coors, W.G., et al., *Fabrication of Yttrium-Doped Barium Zirconate for High Performance Protonic Ceramic Membranes*, in *Perovskite Materials - Synthesis, Characterisation, Properties, and Applications*. 2016.
99. Bu, J., P.G. Jönsson, and Z. Zhao, *Dense and translucent BaZr<sub>x</sub>Ce<sub>0.8-x</sub>Y<sub>0.2</sub>O<sub>3-δ</sub> (x= 0.5, 0.6, 0.7) proton conductors prepared by spark plasma sintering*. Scripta Materialia, 2015. **107**: p. 145-148.
100. Fish, J.S., et al., *Synthesis by spark plasma sintering of a novel protonic/electronic conductor composite: BaCe<sub>0.2</sub>Zr<sub>0.7</sub>Y<sub>0.1</sub>O<sub>3-δ</sub>/Sr<sub>0.95</sub>Ti<sub>0.9</sub>Nb<sub>0.1</sub>O<sub>3-δ</sub> (BCZY27/STN95)*. Journal of Materials Science, 2013. **48**(18): p. 6177-6185.

101. Messing, G.L., S.C. Zhang, and G.V. Jayanthi, *Ceramic powder synthesis by spray pyrolysis*. Journal of the American Ceramic Society, 1993. **76**(11): p. 2707-2726.
102. Syvertsen-Wiig, G., *Impact of Raw Material Quality on Performance in Energy Applications*. Hannover Messe, 2014.
103. Babilo, P., T. Uda, and S.M. Haile, *Processing of yttrium-doped barium zirconate for high proton conductivity*. Journal of materials research, 2007. **22**(5): p. 1322-1330.
104. Babilo, P. and S.M. Haile, *Enhanced sintering of yttrium-doped barium zirconate by addition of ZnO*. Journal of the American Ceramic Society, 2005. **88**(9): p. 2362-2368.
105. Coors, W.G., *Co-ionic Conduction in Protonic Ceramics of the Solid Solution, BaCe<sub>x</sub>Zr<sub>(yx)</sub>Y<sub>(1-y)</sub>O<sub>3-d</sub>; Part I: Fabrication and Microstructure*. Ce-ramic Materials Book, 2011. **3**: p. 479-500.
106. Tong, J., et al., *Cost-effective solid-state reactive sintering method for high conductivity proton conducting yttrium-doped barium zirconium ceramics*. Solid State Ionics, 2010. **181**(11-12): p. 496-503.
107. Duan, C., et al., *Highly efficient reversible protonic ceramic electrochemical cells for power generation and fuel production*. Nature Energy, 2019. **4**(3): p. 230.
108. Sun, W., M. Liu, and W. Liu, *Chemically Stable Yttrium and Tin Co-Doped Barium Zirconate Electrolyte for Next Generation High Performance Proton-Conducting Solid Oxide Fuel Cells*. Advanced Energy Materials, 2013. **3**(8): p. 1041-1050.
109. Yun, D., et al., *Structural and electrochemical properties of dense yttria-doped barium zirconate prepared by solid-state reactive sintering*. Energies, 2018. **11**(11): p. 3083.
110. Huang, J., et al., *Fabrication of integrated BZY electrolyte matrices for protonic ceramic membrane fuel cells by tape-casting and solid-state reactive sintering*. International Journal of Hydrogen Energy, 2018. **43**(28): p. 12835-12846.
111. Tomino, H., H. Watanabe, and Y. Kondo, *Electric current path and temperature distribution for spark sintering*. Journal of the Japan Society of Powder and Powder Metallurgy, 1997. **44**(10): p. 974-979.
112. Wang, X., et al., *Finite element modeling of electric current-activated sintering: The effect of coupled electrical potential, temperature and stress*. Acta Materialia, 2007. **55**(10): p. 3611-3622.
113. Diouf, S. and A. Molinari, *Densification mechanisms in spark plasma sintering: Effect of particle size and pressure*. Powder Technology, 2012. **221**: p. 220-227.
114. Guillaume, B., et al., *Optimization of BaZrO<sub>3</sub> sintering by control of the initial powder size distribution; a factorial design statistical analysis*. Journal of the European Ceramic Society, 2005. **25**(16): p. 3593-3604.
115. Mie, G., *Beiträge zur Optik trüber Medien, speziell kolloidaler Metallösungen*. Annalen der physik, 1908. **330**(3): p. 377-445.
116. Keck, C.M. and R.H. Müller, *Size analysis of submicron particles by laser diffractometry—90% of the published measurements are false*. International journal of pharmaceutics, 2008. **355**(1-2): p. 150-163.
117. Hahn, D.W., *Light scattering theory*. Department of Mechanical and Aerospace Engineering, University of Florida, 2009.
118. Øgndal, L., *Light Scattering*. 2013.
119. Ye, Z., X. Jiang, and Z. Wang, *Measurements of Particle Size Distribution Based on Mie Scattering Theory and Markov Chain Inversion Algorithm*. JSW, 2012. **7**(10): p. 2309-2316.
120. Vortisch, H., *Beobachtung von Phasenübergängen in einzeln levitierten Schwefelsäuretröpfchen mittels Raman-Spektroskopie und elastischer Lichtstreuung*. 2002.
121. Wood, D.L. and K. Nassau, *Refractive index of cubic zirconia stabilized with yttria*. Applied Optics, 1982. **21**(16): p. 2978-2981.
122. Spieß, L., et al., *Moderne röntgenbeugung*. Vieweg+ Teubner, Wiesbaden, 2009. **2**: p. 276.
123. Rietveld, H., *A profile refinement method for nuclear and magnetic structures*. Journal of applied Crystallography, 1969. **2**(2): p. 65-71.
124. Mather, G.C., et al., *Phase Transitions, Chemical Expansion, and Deuteron Sites in the BaZr<sub>0.7</sub>Ce<sub>0.2</sub>Y<sub>0.1</sub>O<sub>3-δ</sub> Proton Conductor*. Chemistry of Materials, 2016. **28**(12): p. 4292-4299.

125. Young, R.A., *The rietveld method*. Vol. 5. 1993: International union of crystallography.
126. Edinburgh\_Instruments, *Blog What is Raman Spectroscopy*. <https://www.edinst.com/blog/what-is-raman-spectroscopy/>, 2020.
127. Carlile, C. and M.A. Adams, *The design of the IRIS inelastic neutron spectrometer and improvements to its analysers*. Physica B Condensed Matter, 1992. **182**: p. 431-440.
128. Squires, G.L., *Introduction to the theory of thermal neutron scattering*. 2012: Cambridge university press.
129. Springer, T. and R. Lechner, *Diffusion in condensed matter*. Vol. 1. 2005: Springer New York.
130. Bée, M., *Quasielastic neutron scattering*. 1988.
131. Karlsson, M., et al., *Quasielastic neutron scattering of hydrated BaZr<sub>0.90</sub>A<sub>0.10</sub>O<sub>2.95</sub> (A=Y and Sc)*. Solid State Ionics, 2009. **180**(1): p. 22-28.
132. Embs, J.P., F. Juranyi, and R. Hempelmann, *Introduction to quasielastic neutron scattering*. Zeitschrift für Physikalische Chemie, 2010. **224**(1-2): p. 5-32.
133. Chudley, C. and R. Elliott, *Neutron scattering from a liquid on a jump diffusion model*. Proceedings of the Physical Society, 1961. **77**(2): p. 353.
134. Mukhopadhyay, S., *How to use Mantid for low energy inelastic neutron scattering data analysis on indirect geometry instruments*. Rutherford Appleton Laboratory Technical Report RAL-TR-2014, 2014. **5**.
135. Arnold, O., et al., *Mantid—Data analysis and visualization package for neutron scattering and  $\mu$  SR experiments*. Nuclear Instruments and Methods in Physics Research Section A: Accelerators, Spectrometers, Detectors and Associated Equipment, 2014. **764**: p. 156-166.
136. Mantid, M., *Analysis Toolkit for Instrument Data*. Mantid Project, 2013.
137. Andreani, C., et al., *Electron-volt neutron spectroscopy: beyond fundamental systems*. Advances in Physics, 2017. **66**(1): p. 1-73.
138. Andreani, C., et al., *Chapter 7 - Atomic Quantum Dynamics in Materials Research*, in *Experimental Methods in the Physical Sciences*, F. Fernandez-Alonso and D.L. Price, Editors. 2017, Academic Press. p. 403-457.
139. Andreani, C., et al., *Experimental studies of nuclear quantum effects in condensed matter: the case of water*. Rivista Del Nuovo Cimento, 2018. **41**(5): p. 291-340.
140. Krzystyniak, M., et al., *Probing the binding and spatial arrangement of molecular hydrogen in porous hosts via neutron Compton scattering*. Faraday Discussions, 2011. **151**: p. 171-197.
141. Seel, A.G., et al., *Over the Horizon: Future Roles of Electron Volt Neutron Spectroscopy*. Vi Workshop in Electron Volt Neutron Spectroscopy: Frontiers and Horizons, 2014. **571**.
142. Andreani, C., et al., *Measurement of momentum distribution of lightatoms and molecules in condensed matter systems using inelastic neutron scattering*. Advances in Physics, 2005. **54**(5): p. 377-469.
143. Andreani, C., et al., *Discussion: Measurement and Instrumentation*. Vi Workshop in Electron Volt Neutron Spectroscopy: Frontiers and Horizons, 2014. **571**.
144. Krzystyniak, M. and T. Abdul-Redah, *Proton momentum distribution in solid and liquid HF*. Physical Review B, 2010. **82**(6): p. 064301.
145. Krzystyniak, M., et al., *VESUVIO plus : The Current Testbed for a Next-generation Epithermal Neutron Spectrometer*. 22nd Meeting of the International Collaboration on Advanced Neutron Sources (Icans Xxii), 2018. **1021**.
146. Krzystyniak, M., et al., *Mass-selective Neutron Spectroscopy Beyond the Proton*. Vi Workshop in Electron Volt Neutron Spectroscopy: Frontiers and Horizons, 2014. **571**.
147. Mayers, J. and G. Reiter, *The VESUVIO electron volt neutron spectrometer*. Measurement Science and Technology, 2012. **23**(4).
148. Romanelli, G., et al., *Data analysis of neutron Compton scattering experiments using MANTID*. Journal of Physics: Conference Series, 2018. **1055**: p. 012016.
149. Seel, A.G., M. Krzystyniak, and F. Fernandez-Alonso, *The VESUVIO Spectrometer Now and When?* Vi Workshop in Electron Volt Neutron Spectroscopy: Frontiers and Horizons, 2014. **571**.

150. Senesi, R., et al., *VESUVIO: a novel instrument for performing spectroscopic studies in condensed matter with eV neutrons at the ISIS facility*. Physica B, 2000. **276**: p. 200-201.
151. West, G.B., *Electron scattering from atoms, nuclei and nucleons*. Physics Reports, 1975. **18**(5): p. 263-323.
152. Parreira, N., N. Carvalho, and A. Cavaleiro, *Synthesis, structural and mechanical characterization of sputtered tungsten oxide coatings*. Thin Solid Films, 2006. **510**(1-2): p. 191-196.
153. Krzystyniak, M., et al., *Mass-selective neutron spectroscopy of lithium hydride and deuteride: Experimental assessment of the harmonic and impulse approximations*. Physical Review B, 2013. **88**(18).
154. Krzystyniak, M., et al., *Mass-selective neutron spectroscopy of glassy versus polycrystalline structures in binary mixtures of beryllium and zirconium*. Journal of Physics: Conference Series, 2018. **1055**: p. 012004.
155. Barsoukov, E. and J.R. Macdonald, *Impedance spectroscopy: theory, experiment, and applications*. 2018: John Wiley & Sons.
156. Niya, S.M.R. and M. Hoorfar, *Study of proton exchange membrane fuel cells using electrochemical impedance spectroscopy technique—A review*. Journal of Power Sources, 2013. **240**: p. 281-293.
157. West, A.R., *Solid state chemistry and its applications*. 2014: John Wiley & Sons.
158. Lasia, A., *Electrochemical impedance spectroscopy and its applications*, in *Modern aspects of electrochemistry*. 2002, Springer. p. 143-248.
159. Haile, S., G. Staneff, and K. Ryu, *Non-stoichiometry, grain boundary transport and chemical stability of proton conducting perovskites*. Journal of Materials Science, 2001. **36**(5): p. 1149-1160.
160. Haile, S.M., D.L. West, and J. Campbell, *The role of microstructure and processing on the proton conducting properties of gadolinium-doped barium cerate*. Journal of Materials Research, 1998. **13**(6): p. 1576-1595.
161. Bonanos, N., *Transport study of the solid electrolyte BaCe<sub>0.9</sub>Gd<sub>0.1</sub>O<sub>2.95</sub> at high temperatures*. Journal of Physics and Chemistry of Solids, 1993. **54**(7): p. 867-870.
162. Anselmi-Tamburini, U., et al., *Spark plasma sintering and characterization of bulk nanostructured fully stabilized zirconia: Part II. Characterization studies*. Journal of materials research, 2004. **19**(11): p. 3263-3269.
163. Ferraro, J.R., *Introductory raman spectroscopy*. 2003: Elsevier.
164. Theunissen, G., A.J. Winnubst, and A. Burggraaf, *Surface and grain boundary analysis of doped zirconia ceramics studied by AES and XPS*. Journal of materials science, 1992. **27**(18): p. 5057-5066.
165. Azad, A.K., et al., *Structural origins of the differing grain conductivity values in BaZr<sub>0.9</sub>Y<sub>0.1</sub>O<sub>2.95</sub> and indication of novel approach to counter defect association*. Journal of Materials Chemistry, 2008. **18**(29): p. 3414-3418.
166. Loureiro, F.J., et al., *A review on sintering technology of proton conducting BaCeO<sub>3</sub>-BaZrO<sub>3</sub> perovskite oxide materials for Protonic Ceramic Fuel Cells*. Journal of Power Sources, 2019. **438**: p. 226991.
167. Jiang, D. and A.K. Mukherjee, *The influence of oxygen vacancy on the optical transmission of an yttria-magnesia nanocomposite*. Scripta Materialia, 2011. **64**(12): p. 1095-1097.
168. Münch, W., et al., *Proton diffusion in perovskites: comparison between BaCeO<sub>3</sub>, BaZrO<sub>3</sub>, SrTiO<sub>3</sub>, and CaTiO<sub>3</sub> using quantum molecular dynamics*. Solid State Ionics, 2000. **136**: p. 183-189.
169. Malavasi, L., et al., *Combined Neutron and Synchrotron X-ray Diffraction Investigation of the BaCe<sub>0.85-x</sub>Zr<sub>x</sub>Y<sub>0.15</sub>O<sub>3-δ</sub> (0.1 ≤ x ≤ 0.4) Proton Conductors*. Chemistry of Materials, 2011. **23**(5): p. 1323-1330.
170. Omori, M., *Sintering, consolidation, reaction and crystal growth by the spark plasma system (SPS)*. Materials Science and Engineering: A, 2000. **287**(2): p. 183-188.
171. Hillert, M., *On the theory of normal and abnormal grain growth*. Acta metallurgica, 1965. **13**(3): p. 227-238.
172. German, R.M. and E.A. Olevsky, *Modeling grain growth dependence on the liquid content in liquid-phase-sintered materials*. Metallurgical and Materials Transactions A, 1998. **29**(12): p. 3057-3067.
173. Ricote, S., N. Bonanos, and G. Caboche, *Water vapour solubility and conductivity study of the proton conductor BaCe<sub>(0.9-x)</sub>Zr<sub>x</sub>Y<sub>0.1</sub>O<sub>(3-δ)</sub>*. Solid State Ionics, 2009. **180**(14-16): p. 990-997.
174. Kjølseth, C., et al., *Space-charge theory applied to the grain boundary impedance of proton conducting BaZr<sub>0.9</sub>Y<sub>0.1</sub>O<sub>3-δ</sub>*. Solid State Ionics, 2010. **181**(5-7): p. 268-275.
175. Chen, C.-T., C.E. Danel, and S. Kim, *On the origin of the blocking effect of grain-boundaries on proton transport in yttrium-doped barium zirconates*. Journal of Materials Chemistry, 2011. **21**(14): p. 5435-5442.

176. Lindman, A., et al., *Oxygen vacancy segregation in grain boundaries of BaZrO<sub>3</sub> using interatomic potentials*. Solid State Ionics, 2013. **230**: p. 27-31.
177. Iguchi, F., N. Sata, and H. Yugami, *Proton transport properties at the grain boundary of barium zirconate based proton conductors for intermediate temperature operating SOFC*. Journal of Materials Chemistry, 2010. **20**(30): p. 6265-6270.
178. Guo, X. and J. Maier, *Grain boundary blocking effect in zirconia: a Schottky barrier analysis*. Journal of the Electrochemical Society, 2001. **148**(3): p. E121-E126.
179. Babilo, P. and S.M. Haile, *Enhanced Sintering of Yttrium-Doped Barium Zirconate by Addition of ZnO*. Journal of the American Ceramic Society, 2005. **88**(9): p. 2362-2368.
180. Hudish, G., et al., *Chemical expansion in BaZr<sub>0.9-x</sub>Ce<sub>x</sub>Y<sub>0.1</sub>O<sub>3-δ</sub> (x= 0 and 0.2) upon hydration determined by high-temperature X-ray diffraction*. Journal of the American Ceramic Society, 2018. **101**(3): p. 1298-1309.
181. Løken, A., S. Ricote, and S. Wachowski, *Thermal and chemical expansion in proton ceramic electrolytes and compatible electrodes*. Crystals, 2018. **8**(9): p. 365.
182. Han, D., N. Hatada, and T. Uda, *Chemical expansion of yttrium-doped barium zirconate and correlation with proton concentration and conductivity*. Journal of the American Ceramic Society, 2016. **99**(11): p. 3745-3753.
183. Andersson, A.K., et al., *Chemical expansion due to hydration of proton-conducting perovskite oxide ceramics*. Journal of the American Ceramic Society, 2014. **97**(8): p. 2654-2661.
184. Lyagaeva, Y.G., et al., *Thermal expansion of materials in the barium cerate-zirconate system*. Physics of the Solid State, 2015. **57**(2): p. 285-289.
185. Bu, J., P.G. Jönsson, and Z. Zhao, *Transport properties of BaZr<sub>0.5</sub>Ce<sub>0.3</sub>Y<sub>0.2</sub>O<sub>3-d</sub> proton conductor prepared by spark plasma sintering*. Ceramics International, 2016. **42**(3): p. 4393-4399.
186. Anselmi-Tamburini, U., et al., *Solid-state synthesis and spark plasma sintering of submicron BaY<sub>x</sub>Zr<sub>1-x</sub>O<sub>3-x/2</sub> (x= 0, 0.08 and 0.16) ceramics*. Journal of the European Ceramic Society, 2006. **26**(12): p. 2313-2318.
187. Gorelov, V. and V. Balakireva, *Synthesis and properties of high-density protonic solid electrolyte BaZr<sub>0.9</sub>Y<sub>0.1</sub>O<sub>3-α</sub>*. Russian Journal of Electrochemistry, 2009. **45**(4): p. 476-482.
188. Gubicza, J., et al., *Influence of sintering temperature and pressure on crystallite size and lattice defect structure in nanocrystalline SiC*. Journal of materials research, 2007. **22**(5): p. 1314-1321.
189. Li, J.-G., T. Ikegami, and T. Mori, *Low temperature processing of dense samarium-doped CeO<sub>2</sub> ceramics: sintering and grain growth behaviors*. Acta Materialia, 2004. **52**(8): p. 2221-2228.
190. Witte, K., et al., *Phase transformations of stoichiometric mixtures of hematite and iron under FAST conditions*. Journal of Alloys and Compounds, 2017. **724**: p. 728-734.
191. Castro, R. and K. Van Benthem, *Sintering: mechanisms of convention nanodensification and field assisted processes*. Vol. 35. 2012: Springer Science & Business Media.
192. Yung, D.-L., M. Antonov, and I. Hussainova, *Spark plasma sintered ZrC-Mo cermets: influence of temperature and compaction pressure*. Ceramics International, 2016. **42**(11): p. 12907-12913.
193. Vogt, T., et al., *Pressure-induced intermediate-to-low spin state transition in LaCoO<sub>3</sub>*. Physical Review B, 2003. **67**(14): p. 140401.
194. Charrier-Cougoulic, I., T. Pagnier, and G. Lucazeau, *Raman spectroscopy of perovskite-type BaCe<sub>x</sub>Zr<sub>1-x</sub>O<sub>3</sub> (0 ≤ x ≤ 1)*. Journal of Solid State Chemistry, 1999. **142**(1): p. 220-227.
195. Slodczyk, A., et al., *Combined bulk and surface analysis of the BaCe<sub>0.5</sub>Zr<sub>0.3</sub>Y<sub>0.16</sub>Zn<sub>0.04</sub>O<sub>3-δ</sub> (BCZYZ) ceramic proton-conducting electrolyte*. Solid State Ionics, 2014. **262**: p. 870-874.
196. Slodczyk, A., et al., *Substitution and proton doping effect on SrZrO<sub>3</sub> behaviour: high-pressure Raman study*. Journal of Raman Spectroscopy, 2011. **42**(12): p. 2089-2099.
197. Chaney, J., et al., *A high-pressure infrared and Raman spectroscopic study of BaCO<sub>3</sub>: the aragonite, trigonal and Pmmn structures*. Physics and Chemistry of Minerals, 2014. **42**(1): p. 83-93.
198. German, R.M., *Sintering theory and practice*. Solar-Terrestrial Physics, 1996: p. 568.
199. Rumman, M.R., et al., *Effect of spark plasma sintering pressure on mechanical properties of WC-7.5 wt% Nano Co*. Materials & Design, 2015. **68**: p. 221-227.

200. Guillard, F., et al., *Densification of SiC by SPS-effects of time, temperature and pressure*. Journal of the European ceramic Society, 2007. **27**(7): p. 2725-2728.
201. Grasso, S., Y. Sakka, and G. Maizza, *Pressure effects on temperature distribution during spark plasma sintering with graphite sample*. Materials transactions, 2009. **50**(8): p. 2111-2114.
202. Brug, G., et al., *The analysis of electrode impedances complicated by the presence of a constant phase element*. Journal of electroanalytical chemistry and interfacial electrochemistry, 1984. **176**(1-2): p. 275-295.
203. Babu, A. and R. Bauri, *Synthesis, phase stability and conduction behavior of rare earth and transition elements doped barium cerates*. International Journal of Hydrogen Energy, 2014. **39**(26): p. 14487-14495.
204. Iwahara, H., *Technological challenges in the application of proton conducting ceramics*. Solid State Ionics, 1995. **77**: p. 289-298.
205. He, T., et al., *Impedance spectroscopic study of thermodynamics and kinetics of a Gd-doped BaCeO<sub>3</sub> single crystal*. Solid State Ionics, 1997. **95**(3-4): p. 301-308.
206. Babiniec, S.M., S. Ricote, and N.P. Sullivan, *Characterization of ionic transport through BaCe<sub>0.2</sub>Zr<sub>0.7</sub>Y<sub>0.1</sub>O<sub>3-δ</sub> membranes in galvanic and electrolytic operation*. international journal of hydrogen energy, 2015. **40**(30): p. 9278-9286.
207. Shirpour, M., et al., *Nonlinear electrical grain boundary properties in proton conducting Y-BaZrO<sub>3</sub> supporting the space charge depletion model*. Phys Chem Chem Phys, 2012. **14**(2): p. 730-40.
208. Kosacki, I. and H. Tuller, *Mixed conductivity in SrCe<sub>0.95</sub>Yb<sub>0.05</sub>O<sub>3</sub> protonic conductors*. Solid State Ionics, 1995. **80**(3-4): p. 223-229.
209. Hu, K., et al., *Effect of Heating Rate on Densification and Grain Growth During Spark Plasma Sintering of 93W-5.6Ni-1.4Fe Heavy Alloys*. Metallurgical and Materials Transactions A, 2013. **44**(9): p. 4323-4336.
210. Shen, Z., et al., *Spark plasma sintering of alumina*. Journal of the American Ceramic Society, 2002. **85**(8): p. 1921-1927.
211. Aldica, G., et al., *The influence of heating rate on superconducting characteristics of MgB<sub>2</sub> obtained by spark plasma sintering technique*. Physica C: Superconductivity and its Applications, 2015. **519**: p. 184-189.
212. Anselmi-Tamburini, U., et al., *Spark plasma sintering and characterization of bulk nanostructured fully stabilized zirconia: Part I. Densification studies*. Journal of materials research, 2004. **19**(11): p. 3255-3262.
213. Khalil, K.A. and A.A. Almajid, *Effect of high-frequency induction heat sintering conditions on the microstructure and mechanical properties of nanostructured magnesium/hydroxyapatite nanocomposites*. Materials & Design (1980-2015), 2012. **36**: p. 58-68.
214. Dabhade, V., T.R. Mohan, and P. Ramakrishnan, *Dilatometric sintering study of titanium–titanium nitride nano/nanocomposite powders*. Powder metallurgy, 2007. **50**(1): p. 33-39.
215. Clark, M.A. and T. Alden, *Deformation enhanced grain growth in a superplastic Sn-1% Bi alloy*. Acta Metallurgica, 1973. **21**(9): p. 1195-1206.
216. Kim, B.-N., et al., *Effects of heating rate on microstructure and transparency of spark-plasma-sintered alumina*. Journal of the European Ceramic Society, 2009. **29**(2): p. 323-327.
217. MURAYAMA, N. and W. SHIN, *Effect of rapid heating on densification and grain growth in hot pressed alumina*. Journal of the Ceramic Society of Japan, 2000. **108**(1261): p. 799-802.
218. Stanciu, L., V. Kodash, and J. Groza, *Effects of heating rate on densification and grain growth during field-assisted sintering of α-Al<sub>2</sub>O<sub>3</sub> and MoSi<sub>2</sub> powders*. Metallurgical and Materials Transactions A, 2001. **32**(10): p. 2633-2638.
219. Kim, S., J. Fleig, and J. Maier, *Space charge conduction: Simple analytical solutions for ionic and mixed conductors and application to nanocrystalline ceria*. Physical Chemistry Chemical Physics, 2003. **5**(11): p. 2268-2273.
220. Duval, S., et al., *Electrical conductivity of the proton conductor BaZr<sub>0.9</sub>Y<sub>0.1</sub>O<sub>3-δ</sub> obtained by high temperature annealing*. Solid State Ionics, 2007. **178**(25-26): p. 1437-1441.
221. Ricote, S., et al., *Effects of the fabrication process on the grain-boundary resistance in BaZr<sub>0.9</sub>Y<sub>0.1</sub>O<sub>3-δ</sub>*. Journal of Materials Chemistry A, 2014. **2**(38): p. 16107-16115.

222. Khor, K., et al., *Microstructure-property modifications in plasma sprayed 20 wt.% yttria stabilized zirconia electrolyte by spark plasma sintering (SPS) technique*. Materials Science and Engineering: A, 2004. **366**(1): p. 120-126.
223. Fish, J., et al., *Electrical properties and flux performance of composite ceramic hydrogen separation membranes*. Journal of Materials Chemistry A, 2015. **3**(10): p. 5392-5401.
224. Simonenko, T.L., et al., *Synthesis of  $BaCe_{0.9-x}Zr_xY_{0.1}O_{3-\delta}$  nanopowders and the study of proton conductors fabricated on their basis by low-temperature spark plasma sintering*. International Journal of Hydrogen Energy, 2019. **44**(36): p. 20345-20354.
225. Babiniec, S.M., S. Ricote, and N.P. Sullivan, *Characterization of ionic transport through  $BaCe_{0.2}Zr_{0.7}Y_{0.1}O_{3-\delta}$  membranes in galvanic and electrolytic operation*. International Journal of Hydrogen Energy, 2015. **40**(30): p. 9278-9286.
226. Matzke, T., et al., *Quasielastic thermal neutron scattering experiment on the proton conductor  $SrCe_{0.95}Yb_{0.05}Ho_{0.02}O_{2.985}$* . Solid State Ionics, 1996. **86**: p. 621-628.
227. Hempelmann, R., *Quasielastic neutron scattering and solid state diffusion*. 2000: Clarendon Press Oxford.
228. Chen, Q., et al., *Proton diffusivity in spark plasma sintered  $BaCe_{0.8}Y_{0.2}O_{3-\delta}$ : In-situ combination of quasi-elastic neutron scattering and impedance spectroscopy*. Solid State Ionics, 2013. **252**: p. 2-6.
229. Noferini, D., et al., *Proton jump diffusion dynamics in hydrated barium zirconates studied by high-resolution neutron backscattering spectroscopy*. Journal of Materials Chemistry A, 2018. **6**(17): p. 7538-7546.
230. Braun, A., et al., *Proton diffusivity in the  $BaZr_{0.9}Y_{0.1}O_{3-\delta}$  proton conductor*. Journal of Applied Electrochemistry, 2008. **39**(4): p. 471-475.
231. Hempelmann, R., *Hydrogen diffusion mechanism in proton conducting oxides*. Physica B: Condensed Matter, 1996. **226**(1-3): p. 72-77.
232. Stokes, S.J. and M.S. Islam, *Defect chemistry and proton-dopant association in  $BaZrO_3$  and  $BaPrO_3$* . Journal of Materials Chemistry, 2010. **20**(30): p. 6258-6264.
233. Seel, A., R. Senesi, and F. Fernandez-Alonso. *VI workshop in electron volt neutron spectroscopy: frontiers and horizons*. in *Journal of Physics: Conference Series*. 2014. IOP Publishing.
234. Krzystyniak, M., et al. *Mass-selective neutron spectroscopy beyond the proton*. in *Journal of Physics: Conference Series*. 2014. IOP Publishing.
235. Andreani, C., et al. *Discussion: Nuclear quantum dynamics-Protons and beyond*. in *Journal of Physics: Conference Series*. 2014. IOP Publishing.
236. Lin, J., et al., *Anharmonic phonon effects in Raman spectra of unsupported vertical graphene sheets*. Physical Review B, 2011. **83**(12): p. 125430.
237. Lowndes, R., *Anharmonicity in the silver and thallium halides: low-frequency dielectric response*. Physical Review B, 1972. **6**(12): p. 4667.
238. Tian, Y., et al., *Understanding the evolution of anomalous anharmonicity in  $Bi_2Te_{3-x}Se_x$* . Physical Review B, 2017. **95**(9): p. 094104.
239. Murti, P.S. and C. Mathews, *Thermal diffusivity and thermal conductivity studies on thorium-lanthanum mixed oxide solid solutions*. Journal of Physics D: Applied Physics, 1991. **24**(12): p. 2202.
240. Sreekumar, R., et al., *Elastic and thermal properties of yttrium barium zirconate*. physica status solidi (a), 1992. **133**(2): p. 341-347.
241. Lagaeva, J., et al., *Insights on thermal and transport features of  $BaCe_{0.8-x}Zr_xY_{0.2}O_{3-\delta}$  proton-conducting materials*. Journal of Power Sources, 2015. **278**: p. 436-444.
242. Andreani, C., et al., *Experimental studies of nuclear quantum effects in condensed matter: the case of water*. Rivista del Nuovo Cimento della Societa Italiana di Fisica, 2018. **41**(5): p. 291-340.
243. Knauth, P. and M.L. Di Vona, *Solid state proton conductors: properties and applications in fuel cells*. 2012: John Wiley & Sons.
244. O'Hayre, R., et al., *Fuel cell fundamentals*. 2016: John Wiley & Sons.



245. Chaim, R.J.J.o.M.S., *Electric field effects during spark plasma sintering of ceramic nanoparticles*. 2013. **48**(1): p. 502-510.
246. Kyriakou, V., et al., *An Electrochemical Haber-Bosch Process*. 2020. **4**(1): p. 142-158.
247. Narendar, N., et al., *The importance of phase purity in Ni–BaZr<sub>0.85</sub>Y<sub>0.15</sub>O<sub>3-δ</sub> cermet anodes—novel nitrate-free combustion route and electrochemical study*. 2013. **3**(3): p. 859-869.
248. Tong, J., et al., *Solid-state reactive sintering mechanism for large-grained yttrium-doped barium zirconate proton conducting ceramics*. 2010. **20**(30): p. 6333-6341.
249. Lencka, M.M. and R.E.J.C.o.m. Riman, *Thermodynamic modeling of hydrothermal synthesis of ceramic powders*. 1993. **5**(1): p. 61-70.
250. Roquette, P., et al., *Combining NMR of dynamic and paramagnetic molecules: fluxional high-spin nickel (II) complexes bearing bisguanidine ligands*. 2011. **50**(5): p. 1942-1955.
251. SASAKI, S., K. FUJINO, and Y.J.P.o.t.J.A. TAKÉUCHI, Series B, *X-ray determination of electron-density distributions in oxides, MgO, MnO, CoO, and NiO, and atomic scattering factors of their constituent atoms*. 1979. **55**(2): p. 43-48.
252. Miyamoto, Y., et al., *Functionally graded materials: design, processing and applications*. Vol. 5. 2013: Springer Science & Business Media.
253. Yamazaki, Y., R. Hernandez-Sanchez, and S.M. Haile, *Cation non-stoichiometry in yttrium-doped barium zirconate: phase behavior, microstructure, and proton conductivity*. Journal of Materials Chemistry, 2010. **20**(37): p. 8158-8166.
254. Etheridge, D.M., et al., *Natural and anthropogenic changes in atmospheric CO<sub>2</sub> over the last 1000 years from air in Antarctic ice and firn*. Journal of Geophysical Research: Atmospheres, 1996. **101**(D2): p. 4115-4128.
255. Team, G., *GISS Surface Temperature Analysis (GISTEMP), version 4*. NASA Goddard Institute for Space Studies. ataset accessed 2019-08-23 at <https://data.giss.nasa.gov/gistemp/>, 2019.
256. Lenssen, N., G. Schmidt, J. Hansen, M. Menne, A. Persin, R. Ruedy, and D. Zyss, *Improvements in the GISTEMP uncertainty model*. J. Geophys. Res. Atmos., 2019. **124**(12): p. 6307-6326.
257. Uchida, H., N. Maeda, and H. Iwahara, *Relation between proton and hole conduction in SrCeO<sub>3</sub>-based solid electrolytes under water-containing atmospheres at high temperatures*. Solid State Ionics, 1983. **11**(2): p. 117-124.
258. Teraoka, Y., et al., *Mixed ionic-electronic conductivity of La<sub>1-x</sub>Sr<sub>x</sub>Co<sub>1-y</sub>Fe<sub>y</sub>O<sub>3-δ</sub> perovskite-type oxides*. Materials research bulletin, 1988. **23**(1): p. 51-58.
259. Carter, S., et al., *Oxygen transport in selected nonstoichiometric perovskite-structure oxides*. Solid State Ionics, 1992. **53**: p. 597-605.
260. De Teresa, J., et al., *Evidence for magnetic polarons in the magnetoresistive perovskites*. Nature, 1997. **386**(6622): p. 256.
261. Kishi, H., Y. Mizuno, and H. Chazono, *Base-metal electrode-multilayer ceramic capacitors: past, present and future perspectives*. Japanese journal of applied physics, 2003. **42**(1R): p. 1.
262. Shaw, T., S. Trolier-McKinstry, and P. McIntyre, *The properties of ferroelectric films at small dimensions*. Annual Review of Materials Science, 2000. **30**(1): p. 263-298.
263. Cava, R.J., et al., *Superconductivity near 30 K without copper: the Ba<sub>0.6</sub>K<sub>0.4</sub>BiO<sub>3</sub> perovskite*. Nature, 1988. **332**(6167): p. 814.
264. Sampathkumar, T., et al., *Properties of YBa<sub>2</sub>Cu<sub>3</sub>O<sub>7-δ</sub>-BaBiO<sub>3</sub> composite superconductors*. Applied superconductivity, 1994. **2**(1): p. 29-34.
265. Spinicci, R., et al., *Catalytic properties of stoichiometric and non-stoichiometric LaFeO<sub>3</sub> perovskite for total oxidation of methane*. Materials Chemistry and Physics, 2002. **76**(1): p. 20-25.
266. Forni, L. and I. Rossetti, *Catalytic combustion of hydrocarbons over perovskites*. Applied Catalysis B: Environmental, 2002. **38**(1): p. 29-37.
267. Weber, M., M. Bass, and G. DeMars, *Laser action and spectroscopic properties of Er<sup>3+</sup> in YAlO<sub>3</sub>*. Journal of Applied Physics, 1971. **42**(1): p. 301-305.

268. Boix, P.P., et al., *Current progress and future perspectives for organic/inorganic perovskite solar cells*. Materials today, 2014. **17**(1): p. 16-23.
269. Pascual, C. and P. Duran, *Subsolidus Phase Equilibria and Ordering in the System  $ZrO_2$ - $Y_2O_3$* . Journal of the American Ceramic Society, 1983. **66**(1): p. 23-27.
270. Factsage, *Summary of Databases*. [http://www.crct.polymtl.ca/fact/phase\\_diagram.php?file=BaO-NiO.jpg&dir=TDnucl](http://www.crct.polymtl.ca/fact/phase_diagram.php?file=BaO-NiO.jpg&dir=TDnucl), 26. 07. 2019.
271. Caglioti, G., A.t. Paoletti, and F. Ricci, *Choice of collimators for a crystal spectrometer for neutron diffraction*. Nuclear Instruments, 1958. **3**(4): p. 223-228.
272. Toby, B.H., *R factors in Rietveld analysis: how good is good enough?* Powder diffraction, 2006. **21**(1): p. 67-70.
273. Tasso Springer, R.E.L., *Diffusion Studies of Solids by Quasielastic Neutron Scattering*. 2005.
274. Bee, M., *Quasielastic neutron scattering study of large amplitude motions in molecular systems*. 1996.
275. Kruth, A., *Water incorporation studies on doped barium cerate perovskites*. Solid State Ionics, 2003. **162-163**: p. 83-91.
276. Scherban, T., et al., *Raman scattering study of acceptor-doped  $BaCeO_3$* . Solid State Ionics, 1993. **61**(1-3): p. 93-98.

## **Selbstständigkeitserklärung**

Mit dieser Erklärung versichere ich an Eides statt, dass ich die vorliegende Arbeit selbstständig angefertigt und ohne fremde Hilfe verfasst habe, keine außer den von mir angegebenen Hilfsmitteln und Quellen dazu verwendet habe und die den benutzten Werken inhaltlich und wörtlich entnommenen Stellen als solche gekennzeichnet habe.

Greifswald, 15.10.2020